UNIVERSITÀ
DEGLI STUDI
DI PADOVA

Sede Amministrativa: Università degli Studi di Padova

Dipartimento di Scienze Chimiche

CORSO DI DOTTORATO DI RICERCA IN SCIENZE MOLECOLARI
CURRICOLO SCIENZE CHIMICHE
XXXV CICLO

MODELS AND QUANTUM ALGORITHMS FOR OPEN SYSTEM DYNAMICS: THE CASE STUDY OF EXCITON TRANSPORT IN MOLECULAR NETWORKS

Coordinatore: Ch.mo Prof. Leonard Prins
Supervisore: Ch.ma Prof.ssa Barbara Fresch

Dottorando: Federico Gallina

Table of contents

Abstract

As physical systems of chemical interest are rarely isolated, molecular processes should always be intended within the framework of open system dynamics. Notable examples are charge and energy transfer in molecular networks, for which intense theoretical and experimental research has highlighted the central role of the interplay between the system Hamiltonian and decoherences due to the interaction with the environment. At intermediate system-environment interaction strengths, the cooperation between coherent and incoherent dynamics can result in a prototypical effect called environment-assisted quantum transport (ENAQT), which consists of the enhancement of transport efficiency. ENAQT is believed to play a primary part in the high efficiency of natural light-harvesting complexes. A comprehensive understanding and powerful simulation strategies for these dynamical phenomena could help us, for example, in the design of artificial devices, based on the engineering of materials and their environment, for high-performance cells for photovoltaic applications. However, the simulation of open quantum systems poses the theoretical challenge of devising an adequate equation of motion for the dynamics and a computational strategy for its solution, which becomes prohibitively difficult for classical computers when handling large quantum systems.

Thanks to the theoretical and experimental scientific advances of the last decades, we are now at the dawn of the so-called second quantum revolution that promises novel technological tools based on harnessing quantum coherence. Quantum computers, *i.e.*, physical systems manipulated at the quantum level with high precision, are concrete examples. In recent years, quantum computers have already demonstrated they can tackle some complex problems considered intractable by classical computers: the so-called quantum advantage. The simulation of quantum systems has always been a strong motivation behind the development of quantum computers, as they are expected to provide advantages in dealing with large systems based on their huge computational space. However, despite its importance, the simulation of open system dynamics has received relatively little attention. One of the reasons is the non-trivial challenge of reproducing the evolution of open quantum systems in the framework of quantum circuits.

In this thesis, we approach the study of open system dynamics by drawing two parallel paths. On the one hand, we intend to explore in detail some salient features of quantum transport in molecular networks. To do so, we will critically analyse existing models for open system dynamics, ranging from Markovian to non-Markovian regime, from weak to strong coupling and from infinite to finite temperature. On the other hand, we consider the problem of simulating the dynamics underlying ENAQT with digital quantum computers. An algorithmic package is developed to implement the dynamics in different conditions. The algorithms are designed with two different strategies, the first one based on stochastic Hamiltonians and the second one based on a collision model. We discuss the algorithmic quantum trajectories generated during the execution of the algorithms showing that they realize distinct *unravellings* of the dynamics of the open system. We demonstrate the potentiality of our algorithms by simulating ENAQT on a quantum computer emulator and provide a comparative analysis of the two approaches. Both algorithmic strategies can be implemented in a memory-efficient encoding with the number of required qubits scaling logarithmically with the size of the simulated system, while the number of gates scales polynomially depending on the target environmental conditions. The potential quantum advantage over classical simulations stems from the efficient memory encoding and from the possibility to efficiently implement quantum dynamics of many-body local systems (multiple excitons), unleashing the inherent power of the quantum simulation.

Chapter I

Introduction

Since its introduction about a century ago, quantum mechanics has proven to be a powerful theory capable of explaining the behaviour of matter at the nanoscale and beyond. It has enabled us to better understand natural phenomena, such as the interaction between atoms or molecules, and, consequently, to use the knowledge to design technologies that have now come into common use, like lasers, semiconductors, GPS and magnetic resonance imaging. This is often referred to as the *first quantum revolution*. Now scientific and technological progress has paved the way for the direct manipulation of quantum systems, which combined with the interpenetration of quantum theory and information science brings us to the dawn of a *second quantum revolution* [1], promising a new generation of quantum technologies capable of outperforming current solutions in selected fields. These include for example advanced quantum sensors, quantum cryptography, quantum internet and quantum computing. Quantum computers (QCs) are believed to have disruptive power for solving certain classes of problems, and this has been recently supported by experimental demonstrations [2–5]. One of the areas thought to benefit from the use of QCs is the simulation of quantum systems, a notoriously difficult problem for classical computers when the size of the system under consideration is large. This is true for the dynamics of isolated systems but is especially valid for open quantum systems, where the effects of the environment must be included in the computation.

The broad scope of the present work is to test the paradigm of quantum computation for the simulation of non-trivial quantum dynamics in molecular processes, including the effects of the interaction with the environment. Therefore, our first goal is to start from specific models and design quantum algorithms to simulate them (from models to algorithms). As a case study, we have selected the dynamics of energy transport in multi-chromophore complexes, which is also an important process involved in the light-harvesting step of photosynthesis. In these systems, photoexcitation populates partially delocalized states, known as excitons, which must reach a reaction centre to initiate the series of chemical reactions involved in photosynthesis. A decade of theoretical and experimental research in the field has highlighted that the presence of the

environment, represented by the molecular vibrational surrounding, plays a role that is not only non-negligible but fundamental for the efficiency of the transfer. Consequently, the system must be described in the framework of the open system dynamics, which poses important theoretical challenges. In particular, although nowadays the dynamics of not too large systems can be solved by "numerically exact" techniques, we are still far from a complete understanding of how the transport properties of these molecular systems are influenced by particular combinations of local or non-local environmental fluctuations, their temporal and spatial correlations, the spectral properties of the system, the vibrational structure, the coupling pattern in the multi-chromophore network, the coherence lifetime and the thermal relaxation, to name a few. To reach such an understanding, reduced models for the dynamics which are able to highlight the effect of selected feature are highly valuable. In this sense, this thesis hits a second goal, which is to critically reconsider several existing models of exciton transfer dynamics to point out the relation between their basic assumptions and the resulting dynamics (in some sense starting from the quantum algorithm to go back to the assessment of the model). We want to stress that having theoretical models for describing the dynamics and algorithms for their simulation is the key to understanding the properties of natural and artificial systems, making predictions, and designing functionalized materials for synthetic light-harvesting and photovoltaic applications [6].

In the following, we discuss some background notions that will be useful for the rest of the work. Section I.1 is intended to provide a brief introduction to quantum simulators. In section I.2, we start by discussing the dynamics of quantum systems and in particular we introduce two cornerstones of the theory of open quantum system: the Lindblad equation for Markovian dynamics and the Redfield theory of relaxation. We also provide an overview of previous results about the quantum simulations of open system dynamics. In section I.3, we cast the exciton dynamics in a multi-chromophore aggregate as a quantum walk over a molecular network. This idea will be used also in the rest of the thesis. We will also introduce the phenomenology of the environment assisted quantum transport (ENAQT) and present the state of the art about its quantum simulation in digital QCs. We briefly present the main theoretical approaches we will use for the formulation of our quantum algorithms in section I.4. Finally, the structure of the thesis is detailed in section I.5.

I.1 Quantum simulators

The idea of QCs originated in the last decades of the 20th century, thanks to the works of Benioff [7], Feynman [8] and Deutsch [9], among others.[1] Feynman, in particular, was concerned with the inherent difficulty of dealing with the complexity of quantum systems using classical computers [8]. A striking example is an exponential demand of computational resources for the simulation of many-body systems, which becomes harder as the size of the problem increases. This is not only related to the storage space, but also to the number

[1] For the reader interested in quantum computing, we recommend the textbook by Nielsen and Chuang [59], over 20 years old, but still the bible of quantum computing, and the well-designed and constantly-updated webpage of Qiskit [156]. Other interesting sources are textbooks in refs [157,158]. While, for more curious readers, we indicate Shor's recently released memoirs on the early days of quantum computing [159].

of operations required to perform the computation. Feynman, therefore, wondered whether an exact simulation of nature was possible, in which the computer follows the same laws as the simulated system, leading to the birth of a new and successful idea: quantum simulators.

Using a quantum system to efficiently simulate another quantum system is the idea behind quantum simulation. To do this, the state and Hamiltonian of a target system must be accurately mapped into the ones of the simulator. Then, after a certain evolution, the quantities of interest are measured and traced back to the reference system with an inverse mapping. There exist essentially two ways to achieve the task, *i.e.*, using analogue or digital quantum simulators [10].

An analogue quantum simulator (AQS) is a highly controllable quantum system whose dynamics can be tuned to reproduce the dynamics of the target system. For example, recently, energy transport in molecular networks has been simulated with analogue quantum devices using photonic setups [6,11] ultracold atoms [12], superconducting circuits [13–15], nuclear spin systems [16] and trapped atoms [17]. The power of AQSs, in this case, is to offer a controlled environment to test the effects of noise and interactions in quantum transport. As a drawback, AQSs can simulate only a restricted class of problems according to the possibility of designing a mapping between the system and the simulator, and their accuracy depends on the degree to which the simulator is able to reproduce the target dynamics. Until a few years ago, AQSs were the most advanced type of simulator, as they were built on an extensive body of knowledge developed during decades of research. However, thanks to rapid technological advancement (also due to substantial funding) and the possibility of using devices *via* the cloud, the creation and use of digital quantum simulators (DQSs) is constantly growing.

DQSs are usually composed of independent two-level systems, called *qubits*, implemented with various physical systems: superconducting circuits [18], photons [19], trapped ions [20] and Rydberg atoms [21] are some of the most common. Running a quantum simulation requires several steps, as depicted in Figure 1. The first point is to set the target of the simulation by identifying the quantity of interest and developing a physical model of the system. What a DQS does, is transform its initial state $|\psi_0\rangle$ into a final state $|\psi_f\rangle$ through a series of operations (the *quantum gates*) dictated by a suitable *quantum algorithm*. The ordered sequence of gates applied to the qubits takes the name of *quantum circuit*, in analogy with classical computing. In digital quantum simulation, a strategy has to be found to encode the state of the target system into the *quantum register* (*i.e.*, an ensemble of qubits used for the computation) and the algorithm has to be designed inspired by the physical model, so that the final state contains the information about the relevant properties of the target system. Once the algorithmic strategy is defined, a code is prepared on a local machine with the instructions to build the quantum circuit. Unlike classical computing, for which one is used to programming at a high level, the programming of DQS is done similarly to assembly language, in which one specifies the individual operations (gates) to be performed by the quantum processor. Various libraries can be used for the scope, among the most popular are Qiskit [22] (which has been used for this thesis) and Cirq [23]. Using online platforms, the user selects a quantum machine on which to run the circuit. Before the data is sent, the circuit

must be *transpiled*, *i.e.*, the quantum gates must be decomposed into simple 1- or 2-qubit operations from a universal gate set that can be physically implemented by the required device. A control apparatus receives the instructions and prepare the experiment that will be executed on the quantum processor. Finally, the state of the quantum register is measured and it represents the solution of the algorithm. Differently from AQSs, DQSs are *universal* simulators, *i.e.*, by choosing the right mapping and algorithm, a DQS can simulate any other quantum system.

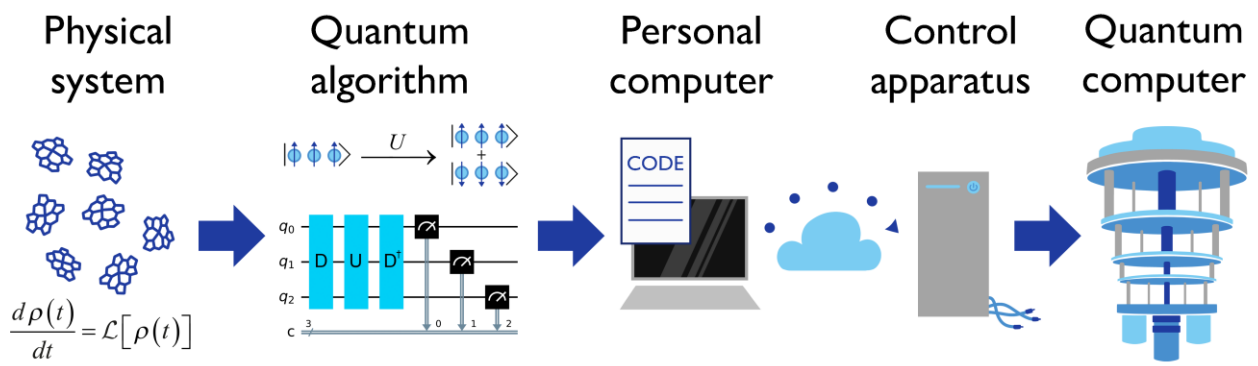

Figure 1. Picturing digital quantum simulation. From the study of a physical system, we extract a theoretical model to describe its properties. An algorithmic strategy is designed to reproduce the system using only unitary operations and measurement: this is the quantum algorithm. The algorithm is translated into a code using dedicated libraries, and run on our local PC. The instructions pass *via* the cloud to a control apparatus that interprets and translates them into physical operations performed on a quantum register inside the quantum processor. The state of the qubits is sampled through measurements and sent back to the user, where it is elaborated to obtain the results of the simulation.

Quantum algorithms are not limited to simulation but have been proposed for various applications in science, economy, cryptography and informatics. In this case, we refer generically to digital QCs (or just QCs).[2] Today's QCs are known to be noisy intermediate-scale quantum (NISQ) devices [24], as they are characterized by a limited size (up to a few hundreds of qubits) and a non-negligible interaction with their environment, which limit the coherence time of the quantum processor. For this reason, only short circuits can be successfully executed. To test quantum algorithms that are too demanding for current QCs, one can use quantum computer emulators, *i.e.*, classical software that emulates the execution on a QC. Clearly, the computational space of the emulators is limited by their classical hardware and therefore the test must be

[2] An alternative paradigm is offered by analogue quantum computing, that exploits the mathematical similarities between the problem to be solved and the physical evolution of the QC [160]. Examples are adiabatic quantum computing and quantum annealing [161,162]. In this thesis, we do not consider this form of quantum computing.

performed on small systems. In this thesis, we will use Qiskit QASM simulator and Qiskit statevector simulator [22] for this purpose.

Albeit their limitations, NISQ devices have already shown some notable results. In 2019, for example, Google announced the first implementation of a computational problem which is not tractable by classical computers [2], the so-called *quantum supremacy* or *quantum advantage* [25,26]. Quantum supremacy was claimed for the execution of a random quantum circuit of a size infeasible for simulation with any available classical computer. The problem was solved with Sycamore, a 53-qubit superconducting processor, that allows a computational space of 2^{53} states. Google argued that, to sample the output of the quantum circuit, the best classical computer (IBM Summit) would need 10 thousand years, whilst Sycamore took only 200 seconds. Although the task was admittedly of not much use and IBM (Google's main competitor in the field) expressed perplexities on the significance of the result [27], Google's demonstration accelerated both hardware and algorithm research in the last years. Now the demand for algorithms for a new generation of quantum computers is constantly growing.

Chemistry has long been considered among the fields that will benefit the most from the use of QCs [28–33]. A prominent example is quantum chemistry, where the many-electron wavefunction of molecules becomes quickly intractable for classical computers. Currently, electronic structure calculation is one of the most studied problems in quantum computing, and quantum algorithms have been proposed that have also demonstrated their potential in real hardware implementations [34–45]. Quantum algorithms for chemical applications have also been presented for elucidating reaction mechanisms [46], drug discovery [47,48], simulation of material properties [49–52], molecular vibrations [53,54], protein folding [55,56] and even for the solution of classical stochastic processes [57].

Despite its importance, the simulation of dynamical molecular processes has received relatively less attention than the electronic problem. This is related to some non-trivial aspects in the implementation, that will be analysed in the following.

I.2 The dynamics of quantum systems

I.2.1 Hamiltonian dynamics

The state of *isolated* or *closed* quantum systems[3] can be described by a pure state $|\psi(t)\rangle = \sum_\alpha c_\alpha(t)|\alpha\rangle$ that is a linear combination of states of a basis set that composes the Hilbert space $\mathcal{H}$ of the system. The dynamics of such systems is driven by the Hamiltonian H and ruled by the Schrödinger equation [58], which reads

[3] Here, we refer to an isolated quantum system when there is no exchange of information (energy and matter) with any other system. Isolated systems have time-independent Hamiltonians. Closed quantum systems can be driven by a classical field in a known way and thus can have time-dependent Hamiltonians.

$$\frac{d\left|\psi(t)\right\rangle}{dt} = -\mathrm{i}H\left|\psi(t)\right\rangle, \tag{I.1}$$

where we have set $\hbar = 1$. When the Hamiltonian is time-independent, the evolution of the statevector has an analytical solution in the form[4]

$$\left|\psi(t)\right\rangle = e^{-\mathrm{i}H(t-t_0)}\left|\psi(t_0)\right\rangle = U(t-t_0)\left|\psi(t_0)\right\rangle, \tag{I.2}$$

where $U(t-t_0)$ is the Hamiltonian propagator with initial condition $U(0) = \mathbb{I}$, where $\mathbb{I}$ the identity operator. The Hamiltonian propagator has the special property of being a *unitary* operator, which means that its inverse $U^{-1}(t-t_0)$ exits and corresponds to the adjoint operator $U^{\dagger}(t-t_0)$, so that the relation $U^{\dagger}(t-t_0)U(t-t_0) = \mathbb{I}$ holds. Because of this, the evolution described by the Schrödinger equation can always be inverted to recover a valid past state, *i.e.*, it is time *reversible*.
The qubits of a QC form, in ideal conditions, a closed quantum system that communicates only with the control apparatus. The user, by choosing the quantum gates to apply, modifies the Hamiltonian of the quantum register, and controls the Schrödinger evolution of the qubits. Therefore, we have to keep in mind that quantum gates correspond to Hamiltonian propagators and are thus unitary operations.[5] Interestingly, the relation applies also in the other direction, *i.e.*, every unitary operation represents a valid quantum gate [59].

The Schrödinger equation (I.1), which can be taken as a postulate of quantum mechanics (like Newton's laws for classical mechanics) [60], gives a deterministic description of the time behaviour of the statevector: if I know the state of the system and the Hamiltonian, I know the evolution. The inherently probabilistic nature of quantum mechanics is related to the interpretation of the squared norm of the coefficients $c_\alpha(t)$. Because of this, the observables of the quantum system can be accessed only as a statistical average of measurements carried out on an *ensemble* of independent systems described by the same state [61].
This also happens in QCs, where to read the state of the qubits, that correspond to the output of the quantum algorithm, it is necessary to repeat the execution of the circuit many times and accumulate statistics.

Sometimes, however, the state of a system is not perfectly known, or, following another vision, individual systems composing an ensemble can assume different states [62,63]. So let us say the state $\left|\psi(t)\right\rangle$ is not certain but is $\left|\psi_k(t)\right\rangle$ with the (positive) probability p_k. The sum of the probabilities is taken normalized to 1. Then,

---

[4] The solution for time-dependent Hamiltonian reads $U(t-t_0) = \underline{\mathcal{T}}\exp\left[-\mathrm{i}\int_{t_0}^{t} H(t')dt'\right]$, where $\underline{\mathcal{T}}$ is the chronological time-ordering operator [61].

[5] The measurement and reset gates represent exceptions to this rule since the collapse of the wavefunction is involved.

we can write what is known as the density matrix of the system as the appropriate weighted sum of the matrix for each state k [61]:

$$\rho(t)=\sum_k p_k \left|\psi_k(t)\right\rangle\left\langle\psi_k(t)\right|. \tag{I.3}$$

If $p_k \neq 1$, the state of the system is said to be mixed, and the evolution is described by the so-called von Neumann (or Liouville-von Neumann) equation, which derives directly from the Schrödinger equation and reads

$$\frac{d\rho(t)}{dt}=-\mathrm{i}\left[H,\rho(t)\right], \tag{I.4}$$

where $\left[A,B\right]=AB-BA$ is the commutator. Eq. (I.4) has the formal solution

$$\rho(t)=U(t-t_0)\rho(t_0)U^{\dagger}(t-t_0)=\mathcal{U}_{t-t_0}\left[\rho(t_0)\right], \tag{I.5}$$

where $\mathcal{U}_{t-t_0}$ is called the dynamical map of the evolution [61]. Since the von Neumann equation is the equivalent of the Schrödinger equation for the density matrix, it retains all the aforementioned properties.

When we study molecular processes, most of the time, we are only interested in a small portion of a large system that includes all the molecular plus solvent degrees of freedom and external fields with which the molecules interact. In this case, we refer to the portion of interest as the *open system* (or *reduced system*), while the remaining part takes the name of the *environment*. The whole system, composed of the open system and its environment, is called the *universe system* and can, in principle, be taken large enough to include all the interactions involving its components. So, the universe system can be regarded as an isolated or closed system, and thus its dynamics is generically dictated by the von Neumann equation. The upper path in the commutative diagram in Figure 2 represents the evolution of the system: starting typically (but not necessarily) from an initial separated state of the open system $\rho_{\mathrm{S}}(0)$ and environment $\rho_{\mathrm{E}}(0)$, the unitary dynamical map $\mathcal{U}_t$ produces the state of the universe system $\rho_{\mathrm{SE}}(t)$ at time t. Then, the state of the reduced system can be obtained as a trace over the environmental degrees of freedom

$$\rho_{\mathrm{S}}(t)=\mathrm{Tr}_{\mathrm{E}}\left\{\rho_{\mathrm{SE}}(t)\right\}=\mathrm{Tr}_{\mathrm{E}}\left\{\mathcal{U}_t\left[\rho_{\mathrm{S}}(0)\otimes\rho_{\mathrm{E}}(0)\right]\right\}. \tag{I.6}$$

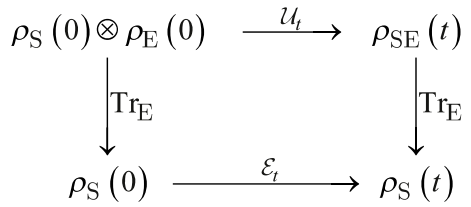

Figure 2. Commutative diagram of the dynamics of an open system. The initial state of the reduced system $\rho_{\mathrm{S}}(0)$ is usually assumed to be separated from the state of the environment $\rho_{\mathrm{E}}(0)$. Then, two paths are shown: the Hamiltonian evolution of the universe system $\mathcal{U}_t$, followed by the trace over the environmental degrees of freedom, or the evolution $\mathcal{E}_t$ of the reduced system alone parametrically influenced by the environment.

I.2.2 The quest for a quantum master equation for the dynamics of open systems

In realistic situations, however, the environment is often composed of a huge number of degrees of freedom, so even if one knows the initial state and the interactions occurring between the subparts, the simulation of the universe system dynamics proves intractable. For this reason, theoretical and computational physicists and chemists have developed, over the years, several techniques to circumvent the problem and allow an effective description of the underlying dynamics of open systems. Among these methods, *Quantum Master Equations* have found fertile ground, especially in the interpretation of the response of optical and magnetic spectroscopies. The strength of master equations is that one only focuses on the subsystem of interest, while the environment enters through some effective parameters. The equation of motion of the reduced density matrix generally reads

$$\frac{d\rho_{\mathrm{S}}(t)}{dt} = -\mathrm{i}\left[H_{\mathrm{S}}, \rho_{\mathrm{S}}(t)\right] + \mathcal{D}\left[\rho_{\mathrm{S}}(t)\right], \tag{I.7}$$

and includes the contributions that characterize the evolution of the reduced dynamics, *i.e.*, the coherent evolution, dictated by the self-Hamiltonian of the open system H_{S}, which reflects the dynamics of the isolated/closed system (cf. eq. (I.4)) and the relaxations and dephasings due to the interaction with the environment, represented by the superoperator [64] $\mathcal{D}$ known as the *dissipator*. Because of the dissipator, information initially contained in the open system is constantly exchanged with the environment and dispersed as time proceeds. As a consequence, the solution of eq. (I.7) results in a non-unitary dynamical map $\rho_{\mathrm{S}}(t) = \mathcal{E}_t\left[\rho_{\mathrm{S}}(0)\right]$ (lower path in the commutative diagram in Figure 2), and the dynamics is no longer time reversible. Striking evidence is that the final equilibrium state of the system is often completely independent of the initial state, which cannot be recovered by inverting the map.

Quantum master equations can be roughly divided into two groups depending on the approach taken for their definition, whether phenomenological or constructive. In phenomenological master equations, the operatorial form of the dissipator is usually assumed *ad hoc*, based on physical intuition, or seldom can be somehow justified by the microscopic interactions with the environment, while the parameters defining the

relaxation processes are chosen phenomenologically by fitting experimental data [65–71]. Under the assumption of a Markovian environment, the reference equation for the open system dynamics is described by the celebrated Gorini-Kossakowski-Sudarshan-Lindblad (or just Lindblad) master equation [72,73]. In the Lindblad form, it reads

$$\frac{d\rho_{\mathrm{S}}(t)}{dt} = -\mathrm{i}\left[H_{\mathrm{S}}, \rho_{\mathrm{S}}(t)\right] + \sum_k \gamma_k \left\{ L_k \rho_{\mathrm{S}}(t) L_k^{\dagger} - \frac{1}{2}\left[L_k^{\dagger} L_k, \rho_{\mathrm{S}}(t) \right]_+ \right\}, \tag{I.8}$$

where $\gamma_k > 0$ are the relaxation rates, L_k are the so-called Lindblad operators and $\left[A,B\right]_+ = AB + BA$ is the anticommutator.[6] The advantage of dealing with a Lindblad dissipator is that the associated dynamical map $\mathcal{E}_t$ satisfies the semigroup property $\mathcal{E}_{t_2}\left[\mathcal{E}_{t_1}\left[\rho_{\mathrm{S}}(0)\right]\right] = \mathcal{E}_{t_1+t_2}\left[\rho_{\mathrm{S}}(0)\right]$, and it preserves the trace, Hermiticity and positivity of the reduced density matrix at any time, *i.e.*, it always guarantees physical evolutions [61]. Eq. (I.8) stems from an axiomatic approach, it represents the most general evolution equation ensuring well-behaved dynamics in the Markovian limit.

On the other hand, one can derive an equation of motion for the reduced density matrix of the system by following a constructive route starting from first principles [60,61]. To do this, a *microscopic* model is necessary for the description of the system-environment interaction. Then, by taking assumptions on the environment, typically treated as a large reservoir described by a thermal equilibrium state (commonly called a *bath*), and tracing over its degrees of freedom, a master equation is derived with solid theoretical foundations. Using sophisticated techniques, like the Nakajima-Zwanzig projection formalism [74,75], quantum master equations can in principle be derived at any order of the system-environment interaction. However, their structure is usually prohibitive to tackle, such that obtaining an exact description is a challenging task. For this reason, frequently, quantum master equations are derived under the assumption of perturbative interactions and often rely on the Markovian approximation, which excludes any memory effect of the environment. In this pool of equations, the Redfield master equation, independently developed by Redfield and Bloch in 1957 [76,77], is one of the most used and useful. Within Redfield theory, the environment influences the dynamics of the system through its spectral function and relaxations occur on the basis of the system eigenstates. The microscopically derived master equation maintains the Hermiticity and trace of the reduced density matrix, however, it cannot be written in the Lindblad form, which means that it does not guarantee positivity. It is commonly accepted that non-positivity is not an issue when the Redfield equation is used inside its regime of validity (*i.e.*, when the weak coupling and Markovian approximations are valid), but clear boundaries can be difficult to establish. For this reason, often further approximations are applied to the Redfield equation that can influence the outcome of the simulations, which will be detailed in a dedicated section of the thesis (Chapter IV).

[6] The system Hamiltonian can also present some kind of modulation, but it is not relevant for the discussion.

Both the Lindblad and the standard form of the Redfield master equations are confined to the realm of Markovian dynamics, meaning they underlie the assumption that the environment is able to relax quickly on the timescale of the system dynamics. Although this is undoubtedly a strong assumption, it can be met by a careful choice of the boundary defining the system-environment separation (which may require redefining the system by including all the "slow" coordinates). The alternative approach is to enter the difficult landscape of non-Markovian or post-Markovian master equations, see *e.g.* [67,71,78–80], characterized by "memory kernels" that bring into the evolution the dependence on previous states of the dynamics. Although a comprehensive analysis of non-Markovian effects is not amongst our intentions, we do face a particular instance of this problem in Chapter III.

From a computational point of view, a common characteristic of all master equations is that they propagate the density matrix, whose dimension is quadratic in the number of states of the system N, and therefore the representation of the dynamical maps scales as N^4. For large systems, this can result in a resource-demanding simulation for classical computers, and that is where QCs could help with their large computational space. However, as we have highlighted before, QCs only allow for the implementation of pure states and unitary quantum gates, which poses the problem of designing quantum algorithms to simulate the dynamics of the quantum master equation.

I.2.3 Quantum algorithms for open system dynamics: an overview

Two main aspects may explain the relatively little attention given to the simulation of open quantum system dynamics using QCs. One is common to many other applications and stems from the technical limitations of NISQ devices in executing long circuits usually required to simulate any dynamical process. The second is specific to the simulation of open quantum systems, and it is the inherent difficulty of mapping non-unitary evolutions into the framework of unitary gates. Nevertheless, several approaches to this problem have been developed and here we give an overview of them.

The first theoretical demonstration of Feynman's intuition [8] that quantum computers can efficiently simulate the dynamics of locally interacting physical systems was given by Lloyd in ref [81]. In this seminal work, Lloyd shows that the Hamiltonian dynamics of isolated systems can be decomposed in simpler operations *via* the Trotter decomposition [82,83], $e^{-\mathrm{i}Ht} = \lim_{m\to\infty}\left(e^{-\mathrm{i}H_0 t/m}e^{-\mathrm{i}H_1 t/m}...e^{-\mathrm{i}H_n t/m}\right)^m$ (see Chapter II for more details), so that it can be directly translated into the gates of the QC, resulting in an efficient implementation when each term represents local interactions. Even if his primary focus was the simulation of unitary quantum dynamics (isolated/closed systems), already in this work the importance of an extension to open systems was discussed. For open quantum systems, Lloyd suggested the use of Hilbert space dilation to circumvent the problem of non-unitary operators. In fact, according to the Stinespring dilation theorem [84], any completely positive and trace-preserving dynamical map can always be embedded in a Hamiltonian (*i.e.*, unitary) dynamics on a larger Hilbert space. This is done by introducing an ancillary system whose dimension is the square of the system size in the general case. After propagation, which can be performed with

Trotterization, the (generally mixed) state of the open system is then obtained by tracing over the ancillary degrees of freedom. This original idea was successively developed by several authors. Recently, it was shown that other dilation theorems, such as the Sz.-Nagy dilation, can be used to further reduce the dimension of the ancillary system, reducing also the computational cost [85]. Since the enlarged system is always in a pure state, these techniques are also known with the name of *purifications* and still represent one of the main strategies for addressing the problem both for Markovian and non-Markovian dynamics [85–91]. The weak points of these approaches are the necessity of a computational space that is larger than what is required by the system alone, and, more importantly, that the global unitary dynamics is not necessarily ruled by a physical (*i.e.*, local) Hamiltonian and therefore it may not be simulated efficiently.

Another general strategy for open system simulation relies on time-dependent variational principles [92–94]. Instead of solving explicitly the dynamics, one assumes that the solution at a certain time can be written as a parametrized function. Then, using a class of algorithms called variational hybrid algorithms [93,95], one decomposes the problem in two parts: a variational routine that generates the parameters for the minimization of a cost function, which is in charge of a classical computer, and the preparation of the trial states and computation of the cost function, assigned to a quantum computer. As they usually rely on shallow circuits, variational algorithms are promising for the implementation on NISQ devices, however, they are heavily affected by the quality of the classical optimization [96].

A third interesting approach, which is also close to the view expressed in this thesis, aims at encoding explicitly the quantum environment into the quantum computer by an effective representation. The idea was pioneered by Nori et al in ref [97] who proposed a procedure directly inspired by the microscopic derivation of the master equation.

In addition, efficient quantum circuits have been devised for the simulation of quantum channels with the potential of representing general open quantum system dynamics [98–105]. In any case, these methods give a framework for the evolution of generic physical systems, and, they need to be revised and adapted to the particular case, for which specific algorithms can be designed to provide some benefits based on the characteristics of the system under consideration.

I.3 Our case study: a quantum walk on molecular networks

It is now time to say something more about the process that will be the target of this thesis investigation. During the light-harvesting process, specialized antenna chromophores present in photosynthetic organisms absorb the sunlight, creating partially delocalized excited states, known as excitons, which are formed by an (excited) electron-hole pair [106]. To lead to the formation of biochemical energy reservoirs, excitons must traverse networks of coupled chromophores to reach a reaction centre where the charge separation occurs, initiating the series of chemical reactions involved in photosynthesis. A prototypical example of a molecular network involved in the process is the Fenna-Matthews-Olson (FMO) complex of green sulfur bacteria. The FMO complex is composed of three identical subunits in which a set of pigments is embedded in a protein

scaffold as depicted in Figure 3. Pigments are coupled each other via Coulomb interactions, enhanced by the presence of a dielectric environment [107]. Despite the natural variety in the structure and composition of the chromophoric networks connecting the antennae to the reaction centre in photosynthetic bacteria, algae and plants [116–124], the exciton transport is generally known to be universally highly efficient [111–115]. It is precisely because of its efficiency that the transport process is much studied for applications in artificial photosynthesis and photovoltaics.

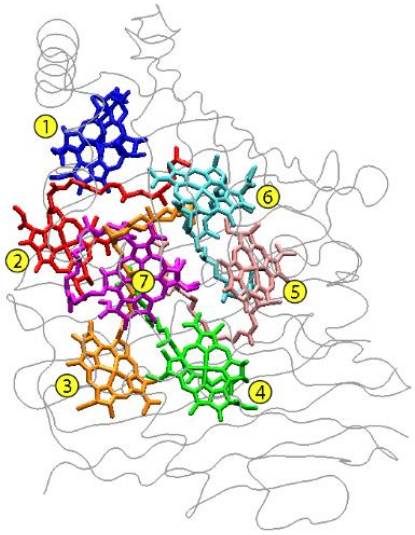

Figure 3. The spatial structure of one of the three identical pigment-protein subunits forming the Fenna-Matthews-Olson (FMO) molecular trimer is reported. Chromophores, that are immerse in the protein environment (grey line), act as a molecular wire for the energy transfer from the chlorosome to the reaction centre of green sulfur bacteria. The numbering of the chromophores corresponds to the Fenna original numbering [108]. Figure is obtained using open data from ref [109,110] (PDB ID: 3ENI).

Thinking about molecules and excitons is part of the chemist's intuition. However, in the following, we will discuss how such a process can be translated in terms of a random walk on a network. This more abstract picture will prove useful to visualise the problem and defining its algorithmic implementation.

A large variety of mathematical and physical problems can be translated into a *graph* and solved by a walker moving randomly from one node to another connected node. Energy and charge transfer processes in molecular networks are prominent examples. A graph is a mathematical structure made of a set of vertices connected by edges according to a certain topology, which can be described by the Laplacian matrix

$$L = \sum_{j=1}^{N} d_j |j\rangle\langle j| - \sum_{\langle j,j'\rangle} \left(|j'\rangle\langle j| + |j\rangle\langle j'| \right), \tag{I.9}$$

where N is the number of vertices of the graph represented by the basis $|j\rangle$, d_j is the number of links to other vertices (the degree of vertex j) and $\langle j, j'\rangle$ indicates an edge between two connected vertices. Random walks define a family of probabilistic models providing a general paradigm for sampling and exploring extended networks by using a sequence of simple local transitions [125–128]. Notably, the Continuous-Time

Quantum Walk (QW) was introduced by Farhi and Gutmann as the quantum analogue of the classical random walk algorithm [129] and it assures a quantum advantage with respect to the classical counterpart in several computational tasks like traversing decision trees [129,130], searching unstructured databases [131,132] and solving hard satisfiability problems [133]. The continuous-time QW is defined by building a quantum Hamiltonian according to the topology of the underlying graph $H = -\nu L$, where the coefficient ν set the rate of transport in the network. Then the walker placed at node j moves among the other nodes following the rules of quantum dynamics dictated by the Schrödinger equation

$$\left|\psi(t)\right\rangle = e^{-\mathrm{i}Ht}\left|\psi(0)\right\rangle = e^{\mathrm{i}\nu Lt}\left|j\right\rangle. \tag{I.10}$$

By its definition, QW computation is intimately related to the dynamics of quantum transport and it offers an efficient simulation routine for the coherent transport over a network of quantum states [134]. The relation also applies in the opposite direction, and any physical system whose Hamiltonian can be cast in the required form can implement an analogue quantum simulation of the QW algorithm. A straightforward analogy with eq. (I.9) can be found in the tight-binding Hamiltonian used in solid-state physics [135] and the Hückel model for molecular orbitals [136], but also with the Frenkel exciton Hamiltonian used to model excitation on chromophore networks [137] and in general with the model Hamiltonians built to describe charge and energy transfer in weakly interacting molecular aggregates and nanostructures [138]. In all these cases, we define a set of quantum sites $\{j\}$ and, when there is one quantum state at each site, the Hamiltonian can be written as

$$H = \sum_{j=1}^{N} \varepsilon_j \left|j\right\rangle\left\langle j\right| + \sum_{\langle j,j'\rangle} V_{j,j'}\left(\left|j\right\rangle\left\langle j'\right| + \left|j'\right\rangle\left\langle j\right|\right), \tag{I.11}$$

with ε_j being the site energy and $V_{j,j'}$ the coupling constant between two sites.

Because the exponential speedup in traversing certain graph topologies arises from constructive interference effects, one might expect that the purely unitary quantum transport described by the QW algorithm is the fastest and the most efficient way to propagate through a network of quantum sites. However, such an expectation turns out to be wrong. Indeed, a rather general scenario is that the presence of a dephasing environment coupled to the system can enhance quantum transport, in a phenomenon named Environment-Assisted Quantum Transport [139] (ENAQT). Although ENAQT can occur on ordered lattices [139,140], transport enhancement was first characterized in disordered systems in the context of exciton transfer in light-harvesting complexes where the process of site-decoherence is physically motivated by the interaction of the electronic states of the chromophores (*i.e.*, the quantum sites) with the vibrational environment. The high efficiency of the energy transfer and the long-living coherent beatings that were experimentally measured with advanced (two-dimensional) electronic spectroscopies (see for example refs [141–143] and references therein), triggered a lively debate on the interplay between Hamiltonian dynamics, static disorder and decoherence in affecting the energy transport dynamics. Substantial theoretical work demonstrated that an intermediate level of environmental-induced dephasing can indeed explain the high efficiency and partial coherent character of the transport [144,145].

The basic phenomenology of ENAQT is described by a Lindblad master equation in which the Hamiltonian describes the coupling between different quantum sites and local dephasing terms account for the decoherences induced by the surrounding environment with δ-approximated correlation functions. However, contributions from memory time and the temperature of the environment can play a non-trivial role as well. For this reason, it is necessary to have a pool of algorithms that can simulate the dynamics of the open system in the widest possible range of scenarios.

I.3.1 Quantum algorithms for ENAQT: state of the art

Taking advantage of the favourable scaling of memory requirements, quantum simulations of mesoscopic chromophore networks might be possible on quantum computers. At the moment, only a few quantum algorithms have been proposed for the simulation of environment-assisted quantum transport in molecular networks: in reference [86], Kais and coworkers implemented the aforementioned dephasing Lindblad master equation (also adding recombination of the exciton to ground state and transfer to the reaction centre) by means of the Sz.-Nagy dilation approach they introduced in [85]. In [146], Mahdian and Yeganeh analysed the same master equation by decomposing the unitary and non-unitary parts of the Lindblad generator into generators belonging to the universal set discussed in [105], and propose a circuital implementation on an NMR quantum computer [147]. Gupta and Chandrashekar cast the solution of a secular Redfield equation, which can be written as a Lindblad master equation, in the form of an operator sum representation for the evolution of the density matrix during discrete time steps and sketched a quantum algorithm that implements the coherent dynamics and the transitions between different excitonic states [148].

As far as we know, all the proposed quantum algorithms are able to handle only the Markovian dynamics, while quantum algorithms simulating ENAQT in the presence of memory effects have not been proposed yet.

I.4 Methodologies

To simulate ENAQT in a vast range of conditions of the environment, we propose a quantum algorithmic package for the simulation of the dynamics of the open system based on stochastic Hamiltonian propagation [149] or the recently emerging collision models [150]. The peculiarity of both methods is that they rely on an effective representation of the environment, which we will exploit to overcome the problem of mapping the non-unitary dynamics into quantum gates. In the thesis, we will demonstrate that both approaches can be implemented efficiently on a quantum computer and that their execution realizes different *unravellings* of the open system dynamics in terms of trajectories of pure states.

The stochastic Hamiltonian propagation consists of devising an effective Hamiltonian for the dynamics, which is composed of the Hamiltonian of the isolated system and a fluctuating term due to the interaction with the environment, which acts as a classical field. A single stochastic propagation is called a trajectory and evolves through the Schrödinger equation equivalently to the dynamics of a closed system. Then, the exact dynamics of the open system is obtained as the average over an infinite number of trajectories. For white noise fluctuations, it can be shown that the resulting averaged dynamics reproduces a Lindblad master equation.

Differently, with coloured fluctuations, a correspondent master equation cannot be always derived explicitly. Thus, the method can be used to "perform experiments" through the quantum computer, meaning to simulate open system dynamics which are not known *a priori* but rather generated in the computer by explicitly controlling the features of the effective environment. On the other hand, it is known that dynamics generated as the average of a stochastic Hamiltonian propagation corresponds to the simulation of infinite temperature quantum environments [151].

To go beyond this limit, we also propose quantum algorithms based on collision models. Collision models offer a framework for the simulation of open system dynamics which is obtained through repeated interactions with a minimum model of environment, often represented by a single qubit. After the interaction, the environment is traced out and the state of the reduced system is recovered. In the quantum transposition of this method, the trace procedure can be substituted with a measure of the ancillary qubit. To the best of our knowledge, the first proposal of a quantum simulation algorithm that could be interpreted as a collision model has been presented in ref [97] for Markovian dynamics. Notably, the authors also illustrate a tentative extension to embed memory effects, without however giving a rigorous framework. Recently, collision model implementations have been tested on real quantum hardware for small systems [152,153]. More details on collision models will be given in the thesis.

In the Chapters, we will compare and discuss the differences between our algorithm and the previous proposals both in terms of the approach and in terms of scalability. Thanks to the effective representation of the environment, we will demonstrate that our algorithms can cover a wide spectrum of situations. In particular, we will propose quantum algorithms valid in the following environmental conditions:

1. A Markovian environment with δ-approximated time correlation functions, in all the range of system-environment coupling strengths (Chapter II);
2. An environment with classical correlation functions with finite memory time, in all the range of system-environment coupling strengths (Chapter III);
3. An environment with quantum correlation function, in the Markovian and weak-coupling regime (Chapter V).

Being described by classical correlation functions, the first two classes of algorithms correspond to the case of a quantum environment at infinite temperature.

We would like to anticipate few ingredients of our work by briefly discussing an example of exciton transport dynamics on the FMO molecular complex, also used as a prototypical example in Chapters IV and V, and depicted in Figure 3. The importance of the FMO stems from the fact that it was one of the first light-harvesting complexes for which long-living (electronic and/or vibronic) coherences were experimentally measured [141]. For this reason, it is often used as a prototypical model to test which are the most relevant ingredients of a (vibrational) environment that affects exciton transport. The excitation is assumed to enter the complex from chromophore 1 and we pose in a (theoretically) difficult regime of non-negligible memory time

and non-perturbative coupling strength of the system-environment interaction. The reference dynamics (Figure 4a) is obtained using a numerically exact method, namely HEOM [154] (see Chapter III), which can be used to calculate the time evolution exactly, at the expense of a high computational cost. In Figure 4b, we approximate the correlation functions of the environment as classical and use, as an example, the quantum algorithms based on the stochastic Hamiltonian propagation devised in Chapter III to solve the dynamics. While in Figure 4c, we neglect the memory of the environment and use the quantum algorithm of Chapter V to implement the secular Redfield dynamics by means of a collision model.

Our algorithms are not meant to reproduce the exact dynamics in this regime. However, it is interesting to point out how each dynamical model can be considered a "good" or "bad" approximation of the reference dynamics depending on the aspect of interest. For example, the stochastic Hamiltonian model in Figure 4b well reproduces the coherent oscillation of the population at early time failing the long-time thermal distribution. Conversely, the weak coupling master equation in Figure 4c underestimates the coherent oscillation at early times, but become accurate at longer time. So, we are confident that by combining the results of our algorithms, one will be able to recover much of the information about the exact dynamics. Furthermore, for small systems there are exact methods to compute the dynamics, but what happens when the system is a mesoscopic aggregate formed by dozens of chromophores? We think that this could be the area of application where our quantum algorithms could provide an advantage over classical methods and give information that is otherwise difficult to obtain.

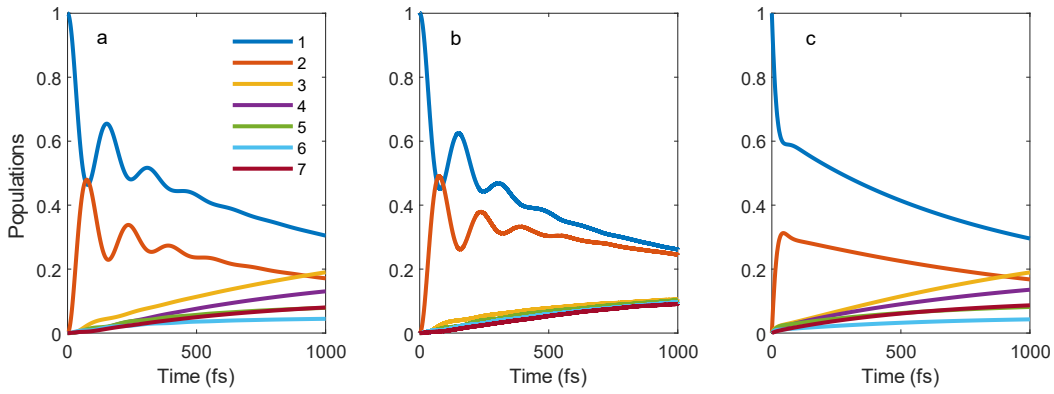

Figure 4. Exciton transport between the chromophores of the Fenna-Matthews-Olson molecular complex. Y-axis represents the probability to find the excitation on a certain chromophore. The reference dynamics of the open system is obtained with a computationally-demanding numerically-exact method (a). Alternative computational strategies presented in this thesis are reported in (b) and (c). Both strategies can reproduce some salient aspects of the exact dynamics while sacrificing others.

I.5 Structure of the thesis

This work couples a systematic analysis of open system dynamics applied to exciton transfer to the implementation of the corresponding algorithms suitable for quantum computers. The landscape is rather wide and rich of assumptions defining the significance of different dynamical models. Figure 5 reports a conceptual

map presenting an overview of the theoretical models used in the thesis, their assumptions, results, and connections. Inside the circles, different dynamical models are defined based on how they describe the environment which in turn characterizes the resulting master equation (Markovian, non-Markovian, weak-coupling results etc..). The blue arrows denote the main connections between the theoretical models. The dashed grey line divides the models in two groups: above the line we find theories that can describe the whole range of coupling-strength but cannot account for finite temperature effects. Below we find dynamical models that rely on the weak-coupling assumption but include thermal effects leading to correct detailed balance solutions at finite temperature. Finally, orange and blue borders enclose the theoretical models which can be simulated by quantum algorithms based on a classical noise (orange) or collisional (blue) approach.

The thesis is organized according to such conceptual categorization of the different dynamical models, indeed each circle of figure 5 is also the subject of a specific Chapter.

In more details: in Chapter II (adapted from our publication [155]), we formally introduce the transport problem in the simple case of a Markovian environment with no temporal correlations and define the efficiency of transport. The mapping of the network to the states of a quantum computer and the two quantum algorithmic strategies are described in detail. We will then demonstrate that this minimal model of the environment is already sufficient to describe the characteristic timescales of the relaxation and the effect of ENAQT. Since the simulation of our algorithms is still prohibitive using the quantum computers at our disposal, we will give a proof of concept of their performance using a quantum computer simulator, namely Qiskit QASM simulator [22].

Thanks to the effective representation of the environment in our algorithmic strategies, in Chapter III, we will be able to introduce non-Markovian effects in the simulation of the open system dynamics. This is particularly interesting because we will be able to explore the dynamics in environmental conditions in which an explicit master equation is not easy to derive (*e.g.*, for strong coupling). We will give an outlook of the effects of non-Markovianity in the evolution of the open system, finding, for example, that the memory time of the environment can help sustain the coherences of the system.

In Chapter IV, we will momentarily pause the development of algorithms to devote ourselves to a review of the description of exciton transport in molecular systems in terms of the Redfield equation. Often acclaimed, the Redfield equation is a powerful tool for describing the dynamics of open systems in perturbative regimes of coupling with the environment. However, the Redfield approach has also been criticised for not guaranteeing the positivity of the density matrix of the system during the dynamics, and is often used with further approximations that can modify its behaviour. In the Chapter, we will discuss its use and limitations in light-harvesting molecular systems starting from a microscopical derivation.

The algorithms introduced in Chapters II and III cover the entire spectrum of coupling strength and can be used for Markovian and non-Markovian situations. However, they correspond to infinite temperature situations of a quantum environment. To cover this gap, in Chapter V, we will propose a version of the collision algorithm

that accounts for the finite temperature, but is restricted to the Markovian and weak-coupling regime. In this case, we will need to define some target equations to be reproduced. Although the Redfield equation would be the perfect reference, its possible non-positivity is not suited to a quantum implementation. We will therefore refer to a set of other equations that preserve positivity by giving similar results to Redfield in its same range of validity.

To the best of our knowledge, the quantum algorithms discussed in this work have not been previously analysed. In Chapter IV, the first two sections recall well-known derivations and models for exciton dynamics in the presence of molecular vibrations, while the comparative analysis presented in the third section is an original result of the research conducted during the doctoral period.

Although all the Chapters are interconnected, each one is designed to be as self-explanatory as possible and can be consulted separately. The conclusions are separately reported at the end of each Chapter together with the dedicated bibliography.

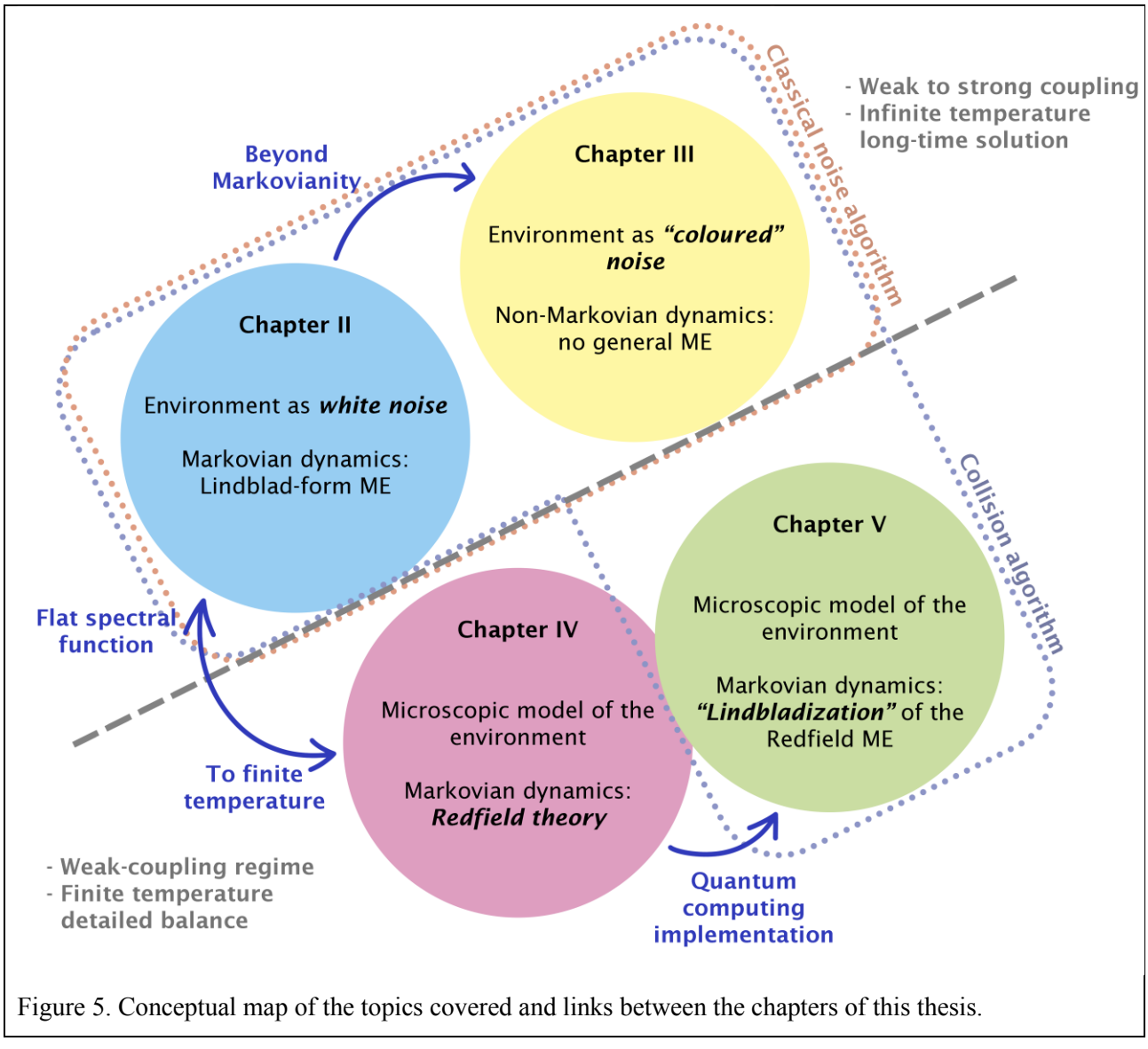

Figure 5. Conceptual map of the topics covered and links between the chapters of this thesis.

I.6 References

[1] I.H. Deutsch, Harnessing the Power of the Second Quantum Revolution, PRX Quantum. 1 (2020) 020101. https://doi.org/10.1103/PRXQuantum.1.020101.

[2] F. Arute, K. Arya, R. Babbush, D. Bacon, J.C. Bardin, R. Barends, R. Biswas, S. Boixo, F.G.S.L. Brandao, D.A. Buell, B. Burkett, Y. Chen, Z. Chen, B. Chiaro, R. Collins, W. Courtney, A. Dunsworth, E. Farhi, B. Foxen, A. Fowler, C. Gidney, M. Giustina, R. Graff, K. Guerin, S. Habegger, M.P. Harrigan, M.J. Hartmann, A. Ho, M. Hoffmann, T. Huang, T.S. Humble, S. V. Isakov, E. Jeffrey, Z. Jiang, D. Kafri, K. Kechedzhi, J. Kelly, P. V. Klimov, S. Knysh, A. Korotkov, F. Kostritsa, D. Landhuis, M. Lindmark, E. Lucero, D. Lyakh, S. Mandrà, J.R. McClean, M. McEwen, A. Megrant, X. Mi, K. Michielsen, M. Mohseni, J. Mutus, O. Naaman, M. Neeley, C. Neill, M.Y. Niu, E. Ostby, A. Petukhov, J.C. Platt, C. Quintana, E.G. Rieffel, P. Roushan, N.C. Rubin, D. Sank, K.J. Satzinger, V. Smelyanskiy, K.J. Sung, M.D. Trevithick, A. Vainsencher, B. Villalonga, T. White, Z.J. Yao, P. Yeh, A. Zalcman, H. Neven, J.M. Martinis, Quantum supremacy using a programmable superconducting processor, Nature. 574 (2019) 505–510. https://doi.org/10.1038/s41586-019-1666-5.

[3] Y. Wu, W.-S. Bao, S. Cao, F. Chen, M.-C. Chen, X. Chen, T.-H. Chung, H. Deng, Y. Du, D. Fan, M. Gong, C. Guo, C. Guo, S. Guo, L. Han, L. Hong, H.-L. Huang, Y.-H. Huo, L. Li, N. Li, S. Li, Y. Li, F. Liang, C. Lin, J. Lin, H. Qian, D. Qiao, H. Rong, H. Su, L. Sun, L. Wang, S. Wang, D. Wu, Y. Xu, K. Yan, W. Yang, Y. Yang, Y. Ye, J. Yin, C. Ying, J. Yu, C. Zha, C. Zhang, H. Zhang, K. Zhang, Y. Zhang, H. Zhao, Y. Zhao, L. Zhou, Q. Zhu, C.-Y. Lu, C.-Z. Peng, X. Zhu, J.-W. Pan, Strong Quantum Computational Advantage Using a Superconducting Quantum Processor, Phys. Rev. Lett. 127 (2021) 180501. https://doi.org/10.1103/PhysRevLett.127.180501.

[4] L.S. Madsen, F. Laudenbach, M.F. Askarani, F. Rortais, T. Vincent, J.F.F. Bulmer, F.M. Miatto, L. Neuhaus, L.G. Helt, M.J. Collins, A.E. Lita, T. Gerrits, S.W. Nam, V.D. Vaidya, M. Menotti, I. Dhand, Z. Vernon, N. Quesada, J. Lavoie, Quantum computational advantage with a programmable photonic processor, Nature. 606 (2022) 75–81. https://doi.org/10.1038/s41586-022-04725-x.

[5] H.-S. Zhong, H. Wang, Y.-H. Deng, M.-C. Chen, L.-C. Peng, Y.-H. Luo, J. Qin, D. Wu, X. Ding, Y. Hu, P. Hu, X.-Y. Yang, W.-J. Zhang, H. Li, Y. Li, X. Jiang, L. Gan, G. Yang, L. You, Z. Wang, L. Li, N.-L. Liu, C.-Y. Lu, J.-W. Pan, Quantum computational advantage using photons, Science. 370 (2020) 1460–1463. https://doi.org/10.1126/science.abe8770.

[6] H. Park, N. Heldman, P. Rebentrost, L. Abbondanza, A. Iagatti, A. Alessi, B. Patrizi, M. Salvalaggio, L. Bussotti, M. Mohseni, F. Caruso, H.C. Johnsen, R. Fusco, P. Foggi, P.F. Scudo, S. Lloyd, A.M. Belcher, Enhanced energy transport in genetically engineered excitonic networks, Nat. Mater. 15 (2016) 211–216. https://doi.org/10.1038/nmat4448.

[7] P. Benioff, The computer as a physical system: A microscopic quantum mechanical Hamiltonian model of computers as represented by Turing machines, J. Stat. Phys. 22 (1980) 563–591. https://doi.org/10.1007/BF01011339.

[8] R.P. Feynman, Simulating physics with computers, Int. J. Theor. Phys. 21 (1982) 467–488. https://doi.org/10.1007/BF02650179.

[9] D. Deutsch, Quantum theory, the Church–Turing principle and the universal quantum computer, Proc. R. Soc. London. A. Math. Phys. Sci. 400 (1985) 97–117. https://doi.org/10.1098/rspa.1985.0070.

[10] I. Buluta, F. Nori, Quantum Simulators, Science. 326 (2009) 108–111. https://doi.org/10.1126/science.1177838.

[11] D.N. Biggerstaff, R. Heilmann, A.A. Zecevik, M. Gräfe, M.A. Broome, A. Fedrizzi, S. Nolte, A. Szameit, A.G. White, I. Kassal, Enhancing coherent transport in a photonic network using controllable decoherence, Nat. Commun. 7 (2016) 11282. https://doi.org/10.1038/ncomms11282.

[12] R. Dorner, J. Goold, V. Vedral, Towards quantum simulations of biological information flow, Interface Focus. 2 (2012) 522–528. https://doi.org/10.1098/rsfs.2011.0109.

[13] S. Mostame, P. Rebentrost, A. Eisfeld, A.J. Kerman, D.I. Tsomokos, A. Aspuru-Guzik, Quantum simulator of an open quantum system using superconducting qubits: exciton transport in photosynthetic complexes, New J. Phys. 14 (2012) 105013. https://doi.org/10.1088/1367-2630/14/10/105013.

[14] S. Mostame, J. Huh, C. Kreisbeck, A.J. Kerman, T. Fujita, A. Eisfeld, A. Aspuru-Guzik, Emulation of complex open quantum systems using superconducting qubits, Quantum Inf. Process. 16 (2017) 44. https://doi.org/10.1007/s11128-016-1489-3.

[15] A. Potočnik, A. Bargerbos, F.A.Y.N. Schröder, S.A. Khan, M.C. Collodo, S. Gasparinetti, Y. Salathé, C. Creatore, C. Eichler, H.E. Türeci, A.W. Chin, A. Wallraff, Studying light-harvesting models with superconducting circuits, Nat. Commun. 9 (2018) 904. https://doi.org/10.1038/s41467-018-03312-x.

[16] B.-X. Wang, M.-J. Tao, Q. Ai, T. Xin, N. Lambert, D. Ruan, Y.-C. Cheng, F. Nori, F.-G. Deng, G.-L. Long,

Efficient quantum simulation of photosynthetic light harvesting, Npj Quantum Inf. 4 (2018) 52. https://doi.org/10.1038/s41534-018-0102-2.

[17] C. Maier, T. Brydges, P. Jurcevic, N. Trautmann, C. Hempel, B.P. Lanyon, P. Hauke, R. Blatt, C.F. Roos, Environment-Assisted Quantum Transport in a 10-qubit Network, Phys. Rev. Lett. 122 (2019) 050501. https://doi.org/10.1103/PhysRevLett.122.050501.

[18] M.H. Devoret, R.J. Schoelkopf, Superconducting Circuits for Quantum Information: An Outlook, Science. 339 (2013) 1169–1174. https://doi.org/10.1126/science.1231930.

[19] S. Barz, Quantum computing with photons: introduction to the circuit model, the one-way quantum computer, and the fundamental principles of photonic experiments, J. Phys. B At. Mol. Opt. Phys. 48 (2015) 083001. https://doi.org/10.1088/0953-4075/48/8/083001.

[20] J.I. Cirac, P. Zoller, Quantum Computations with Cold Trapped Ions, Phys. Rev. Lett. 74 (1995) 4091–4094. https://doi.org/10.1103/PhysRevLett.74.4091.

[21] L. Henriet, L. Beguin, A. Signoles, T. Lahaye, A. Browaeys, G.-O. Reymond, C. Jurczak, Quantum computing with neutral atoms, Quantum. 4 (2020) 327. https://doi.org/10.22331/q-2020-09-21-327.

[22] G. Aleksandrowicz, T. Alexander, P. Barkoutsos, L. Bello, Y. Ben-Haim, D. Bucher, F.J. Cabrera-Hernández, J. Carballo-Franquis, A. Chen, C.-F. Chen, J.M. Chow, A.D. Córcoles-Gonzales, A.J. Cross, A. Cross, J. Cruz-Benito, C. Culver, S.D.L.P. González, E.D. La Torre, D. Ding, E. Dumitrescu, I. Duran, P. Eendebak, M. Everitt, I.F. Sertage, A. Frisch, A. Fuhrer, J. Gambetta, B.G. Gago, J. Gomez-Mosquera, D. Greenberg, I. Hamamura, V. Havlicek, J. Hellmers, Ł. Herok, H. Horii, S. Hu, T. Imamichi, T. Itoko, A. Javadi-Abhari, N. Kanazawa, A. Karazeev, K. Krsulich, P. Liu, Y. Luh, Y. Maeng, M. Marques, F.J. Martín-Fernández, D.T. McClure, D. McKay, S. Meesala, A. Mezzacapo, N. Moll, D.M. Rodríguez, G. Nannicini, P. Nation, P. Ollitrault, L.J. O'Riordan, H. Paik, J. Pérez, A. Phan, M. Pistoia, V. Prutyanov, M. Reuter, J. Rice, A.R. Davila, R.H.P. Rudy, M. Ryu, N. Sathaye, C. Schnabel, E. Schoute, K. Setia, Y. Shi, A. Silva, Y. Siraichi, S. Sivarajah, J.A. Smolin, M. Soeken, H. Takahashi, I. Tavernelli, C. Taylor, P. Taylour, K. Trabing, M. Treinish, W. Turner, D. Vogt-Lee, C. Vuillot, J.A. Wildstrom, J. Wilson, E. Winston, C. Wood, S. Wood, S. Wörner, I.Y. Akhalwaya, C. Zoufal, Qiskit: An Open-source Framework for Quantum Computing, Zenodo. (2019). https://doi.org/10.5281/ZENODO.2562111.

[23] Cirq-Developers, Cirq, Zenodo. (2022). https://doi.org/10.5281/ZENODO.6599601.

[24] J. Preskill, Quantum Computing in the NISQ era and beyond, Quantum. 2 (2018) 79. https://doi.org/10.22331/q-2018-08-06-79.

[25] J. Preskill, Quantum computing and the entanglement frontier, (2012) 1–18. http://arxiv.org/abs/1203.5813.

[26] C. Palacios-Berraquero, L. Mueck, D.M. Persaud, Instead of 'supremacy' use 'quantum advantage,' Nature. 576 (2019) 213–213. https://doi.org/10.1038/d41586-019-03781-0.

[27] E. Pednault, J. Gunnels, D. Maslov, J.M. Gambetta, On "Quantum Supremacy," (2019). https://www.ibm.com/blogs/research/2019/10/on-quantum-supremacy/ (accessed September 12, 2022).

[28] I.M. Georgescu, S. Ashhab, F. Nori, Quantum simulation, Rev. Mod. Phys. 86 (2014) 153–185. https://doi.org/10.1103/RevModPhys.86.153.

[29] J. Olson, Y. Cao, J. Romero, P. Johnson, P.-L. Dallaire-Demers, N. Sawaya, P. Narang, I. Kivlichan, M. Wasielewski, A. Aspuru-Guzik, Quantum Information and Computation for Chemistry, 2017. http://arxiv.org/abs/1706.05413.

[30] S. McArdle, S. Endo, A. Aspuru-Guzik, S.C. Benjamin, X. Yuan, Quantum computational chemistry, Rev. Mod. Phys. 92 (2020) 015003. https://doi.org/10.1103/RevModPhys.92.015003.

[31] Y. Cao, J. Romero, J.P. Olson, M. Degroote, P.D. Johnson, M. Kieferová, I.D. Kivlichan, T. Menke, B. Peropadre, N.P.D. Sawaya, S. Sim, L. Veis, A. Aspuru-Guzik, Quantum Chemistry in the Age of Quantum Computing, Chem. Rev. 119 (2019) 10856–10915. https://doi.org/10.1021/acs.chemrev.8b00803.

[32] I. Kassal, J.D. Whitfield, A. Perdomo-Ortiz, M.-H. Yung, A. Aspuru-Guzik, Simulating Chemistry Using Quantum Computers, Annu. Rev. Phys. Chem. 62 (2011) 185–207. https://doi.org/10.1146/annurev-physchem-032210-103512.

[33] A. Aspuru-Guzik, R. Lindh, M. Reiher, The Matter Simulation (R)evolution, ACS Cent. Sci. 4 (2018) 144–152. https://doi.org/10.1021/acscentsci.7b00550.

[34] A. Aspuru-Guzik, Simulated Quantum Computation of Molecular Energies, Science. 309 (2005) 1704–1707. https://doi.org/10.1126/science.1113479.

[35] J.D. Whitfield, J. Biamonte, A. Aspuru-Guzik, Simulation of electronic structure Hamiltonians using quantum computers, Mol. Phys. 109 (2011) 735–750. https://doi.org/10.1080/00268976.2011.552441.

[36] M. Rossmannek, P.K. Barkoutsos, P.J. Ollitrault, I. Tavernelli, Quantum HF/DFT-embedding algorithms for electronic structure calculations: Scaling up to complex molecular systems, J. Chem. Phys. 154 (2021) 114105.

https://doi.org/10.1063/5.0029536.

[37] F. Arute, K. Arya, R. Babbush, D. Bacon, J.C. Bardin, R. Barends, S. Boixo, M. Broughton, B.B. Buckley, D.A. Buell, B. Burkett, N. Bushnell, Y. Chen, Z. Chen, B. Chiaro, R. Collins, W. Courtney, S. Demura, A. Dunsworth, E. Farhi, A. Fowler, B. Foxen, C. Gidney, M. Giustina, R. Graff, S. Habegger, M.P. Harrigan, A. Ho, S. Hong, T. Huang, W.J. Huggins, L. Ioffe, S. V. Isakov, E. Jeffrey, Z. Jiang, C. Jones, D. Kafri, K. Kechedzhi, J. Kelly, S. Kim, P. V. Klimov, A. Korotkov, F. Kostritsa, D. Landhuis, P. Laptev, M. Lindmark, E. Lucero, O. Martin, J.M. Martinis, J.R. McClean, M. McEwen, A. Megrant, X. Mi, M. Mohseni, W. Mruczkiewicz, J. Mutus, O. Naaman, M. Neeley, C. Neill, H. Neven, M.Y. Niu, T.E. O'Brien, E. Ostby, A. Petukhov, H. Putterman, C. Quintana, P. Roushan, N.C. Rubin, D. Sank, K.J. Satzinger, V. Smelyanskiy, D. Strain, K.J. Sung, M. Szalay, T.Y. Takeshita, A. Vainsencher, T. White, N. Wiebe, Z.J. Yao, P. Yeh, A. Zalcman, Hartree-Fock on a superconducting qubit quantum computer, Science. 369 (2020) 1084–1089. https://doi.org/10.1126/science.abb9811.

[38] A. Peruzzo, J. McClean, P. Shadbolt, M.-H. Yung, X.-Q. Zhou, P.J. Love, A. Aspuru-Guzik, J.L. O'Brien, A variational eigenvalue solver on a photonic quantum processor, Nat. Commun. 5 (2014) 4213. https://doi.org/10.1038/ncomms5213.

[39] A. Kandala, A. Mezzacapo, K. Temme, M. Takita, M. Brink, J.M. Chow, J.M. Gambetta, Hardware-efficient variational quantum eigensolver for small molecules and quantum magnets, Nature. 549 (2017) 242–246. https://doi.org/10.1038/nature23879.

[40] B.P. Lanyon, J.D. Whitfield, G.G. Gillett, M.E. Goggin, M.P. Almeida, I. Kassal, J.D. Biamonte, M. Mohseni, B.J. Powell, M. Barbieri, A. Aspuru-Guzik, A.G. White, Towards quantum chemistry on a quantum computer, Nat. Chem. 2 (2010) 106–111. https://doi.org/10.1038/nchem.483.

[41] C. Hempel, C. Maier, J. Romero, J. McClean, T. Monz, H. Shen, P. Jurcevic, B.P. Lanyon, P. Love, R. Babbush, A. Aspuru-Guzik, R. Blatt, C.F. Roos, Quantum Chemistry Calculations on a Trapped-Ion Quantum Simulator, Phys. Rev. X. 8 (2018) 31022. https://doi.org/10.1103/PhysRevX.8.031022.

[42] A. Kandala, K. Temme, A.D. Córcoles, A. Mezzacapo, J.M. Chow, J.M. Gambetta, Error mitigation extends the computational reach of a noisy quantum processor, Nature. 567 (2019) 491–495. https://doi.org/10.1038/s41586-019-1040-7.

[43] J.I. Colless, V. V. Ramasesh, D. Dahlen, M.S. Blok, M.E. Kimchi-Schwartz, J.R. McClean, J. Carter, W.A. de Jong, I. Siddiqi, Computation of Molecular Spectra on a Quantum Processor with an Error-Resilient Algorithm, Phys. Rev. X. 8 (2018) 011021. https://doi.org/10.1103/PhysRevX.8.011021.

[44] F. Benfenati, G. Mazzola, C. Capecci, P.K. Barkoutsos, P.J. Ollitrault, I. Tavernelli, L. Guidoni, Improved Accuracy on Noisy Devices by Nonunitary Variational Quantum Eigensolver for Chemistry Applications, J. Chem. Theory Comput. 17 (2021) 3946–3954. https://doi.org/10.1021/acs.jctc.1c00091.

[45] L. Ratini, C. Capecci, F. Benfenati, L. Guidoni, Wave Function Adapted Hamiltonians for Quantum Computing, J. Chem. Theory Comput. 18 (2022) 899–909. https://doi.org/10.1021/acs.jctc.1c01170.

[46] M. Reiher, N. Wiebe, K.M. Svore, D. Wecker, M. Troyer, Elucidating reaction mechanisms on quantum computers, Proc. Natl. Acad. Sci. 114 (2017) 7555–7560. https://doi.org/10.1073/pnas.1619152114.

[47] Y. Cao, J. Romero, A. Aspuru-Guzik, Potential of quantum computing for drug discovery, IBM J. Res. Dev. 62 (2018) 6:1-6:20. https://doi.org/10.1147/JRD.2018.2888987.

[48] S. Mensa, E. Sahin, F. Tacchino, P.K. Barkoutsos, I. Tavernelli, Quantum Machine Learning Framework for Virtual Screening in Drug Discovery: a Prospective Quantum Advantage, (2022) 1–16. http://arxiv.org/abs/2204.04017.

[49] J. Schuhmacher, G. Mazzola, F. Tacchino, O. Dmitriyeva, T. Bui, S. Huang, I. Tavernelli, Extending the reach of quantum computing for materials science with machine learning potentials, (2022) 1–17. http://arxiv.org/abs/2203.07219.

[50] N. Yoshioka, T. Sato, Y.O. Nakagawa, Y. Ohnishi, W. Mizukami, Variational quantum simulation for periodic materials, Phys. Rev. Res. 4 (2022) 013052. https://doi.org/10.1103/PhysRevResearch.4.013052.

[51] R. Babbush, N. Wiebe, J. McClean, J. McClain, H. Neven, G.K.L. Chan, Low-Depth Quantum Simulation of Materials, Phys. Rev. X. 8 (2018) 11044. https://doi.org/10.1103/PhysRevX.8.011044.

[52] P.K. Barkoutsos, F. Gkritsis, P.J. Ollitrault, I.O. Sokolov, S. Woerner, I. Tavernelli, Quantum algorithm for alchemical optimization in material design, Chem. Sci. 12 (2021) 4345–4352. https://doi.org/10.1039/D0SC05718E.

[53] P.J. Ollitrault, A. Baiardi, M. Reiher, I. Tavernelli, Hardware efficient quantum algorithms for vibrational structure calculations, Chem. Sci. 11 (2020) 6842–6855. https://doi.org/10.1039/D0SC01908A.

[54] S. McArdle, A. Mayorov, X. Shan, S. Benjamin, X. Yuan, Digital quantum simulation of molecular vibrations,

Chem. Sci. 10 (2019) 5725–5735. https://doi.org/10.1039/C9SC01313J.

[55] M. Fingerhuth, T. Babej, C. Ing, A quantum alternating operator ansatz with hard and soft constraints for lattice protein folding, (2018) 1–12. http://arxiv.org/abs/1810.13411.

[56] A. Robert, P.K. Barkoutsos, S. Woerner, I. Tavernelli, Resource-efficient quantum algorithm for protein folding, Npj Quantum Inf. 7 (2021) 38. https://doi.org/10.1038/s41534-021-00368-4.

[57] P. Pravatto, D. Castaldo, F. Gallina, B. Fresch, S. Corni, G.J. Moro, Quantum computing for classical problems: variational quantum eigensolver for activated processes, New J. Phys. 23 (2021) 123045. https://doi.org/10.1088/1367-2630/ac3ff9.

[58] E. Schrödinger, An Undulatory Theory of the Mechanics of Atoms and Molecules, Phys. Rev. 28 (1926) 1049–1070. https://doi.org/10.1103/PhysRev.28.1049.

[59] M.A. Nielsen, I.L. Chuang, Quantum Computation and Quantum Information, 10th ed., Cambridge University Press, 2000. http://www.tandfonline.com/doi/abs/10.1080/00107514.2011.587535.

[60] A. Rivas, S.F. Huelga, Open Quantum Systems, Springer Berlin Heidelberg, Berlin, Heidelberg, 2012. https://doi.org/10.1007/978-3-642-23354-8.

[61] H.-P. Breuer, F. Petruccione, The Theory of Open Quantum Systems, Oxford University Press, Oxford, 2007. https://doi.org/10.1093/acprof:oso/9780199213900.001.0001.

[62] U. Fano, Description of States in Quantum Mechanics by Density Matrix and Operator Techniques, Rev. Mod. Phys. 29 (1957) 74–93. https://doi.org/10.1103/RevModPhys.29.74.

[63] L.E. Ballentine, The Statistical Interpretation of Quantum Mechanics, Rev. Mod. Phys. 42 (1970) 358–381. https://doi.org/10.1103/RevModPhys.42.358.

[64] J.A. Gyamfi, Fundamentals of quantum mechanics in Liouville space, Eur. J. Phys. 41 (2020) 063002. https://doi.org/10.1088/1361-6404/ab9fdd.

[65] B. Palmieri, D. Abramavicius, S. Mukamel, Lindblad equations for strongly coupled populations and coherences in photosynthetic complexes, J. Chem. Phys. 130 (2009) 204512. https://doi.org/10.1063/1.3142485.

[66] E. Kleinherbers, N. Szpak, J. König, R. Schützhold, Relaxation dynamics in a Hubbard dimer coupled to fermionic baths: Phenomenological description and its microscopic foundation, Phys. Rev. B. 101 (2020) 125131. https://doi.org/10.1103/PhysRevB.101.125131.

[67] L. Mazzola, E.-M. Laine, H.-P. Breuer, S. Maniscalco, J. Piilo, Phenomenological memory-kernel master equations and time-dependent Markovian processes, Phys. Rev. A. 81 (2010) 062120. https://doi.org/10.1103/PhysRevA.81.062120.

[68] G. Kiršanskas, M. Franckié, A. Wacker, Phenomenological position and energy resolving Lindblad approach to quantum kinetics, Phys. Rev. B. 97 (2018) 035432. https://doi.org/10.1103/PhysRevB.97.035432.

[69] M. Scala, B. Militello, A. Messina, J. Piilo, S. Maniscalco, Microscopic derivation of the Jaynes-Cummings model with cavity losses, Phys. Rev. A. 75 (2007) 013811. https://doi.org/10.1103/PhysRevA.75.013811.

[70] T. Yu, L. Diósi, N. Gisin, W.T. Strunz, Post-Markov master equation for the dynamics of open quantum systems, Phys. Lett. A. 265 (2000) 331–336. https://doi.org/10.1016/S0375-9601(00)00014-1.

[71] A. Shabani, D.A. Lidar, Completely positive post-Markovian master equation via a measurement approach, Phys. Rev. A. 71 (2005) 020101. https://doi.org/10.1103/PhysRevA.71.020101.

[72] V. Gorini, A. Kossakowski, E.C.G. Sudarshan, Completely positive dynamical semigroups of N-level systems, J. Math. Phys. 17 (1976) 821. https://doi.org/10.1063/1.522979.

[73] G. Lindblad, On the generators of quantum dynamical semigroups, Commun. Math. Phys. 48 (1976) 119–130. https://doi.org/10.1007/BF01608499.

[74] S. Nakajima, On Quantum Theory of Transport Phenomena, Prog. Theor. Phys. 20 (1958) 948–959. https://doi.org/10.1143/PTP.20.948.

[75] R. Zwanzig, Ensemble Method in the Theory of Irreversibility, J. Chem. Phys. 33 (1960) 1338–1341. https://doi.org/10.1063/1.1731409.

[76] A.G.G. Redfield, On the Theory of Relaxation Processes, IBM J. Res. Dev. 1 (1957) 19–31. https://doi.org/10.1147/rd.11.0019.

[77] F. Bloch, Generalized Theory of Relaxation, Phys. Rev. 105 (1957) 1206–1222. https://doi.org/10.1103/PhysRev.105.1206.

[78] S. Maniscalco, F. Petruccione, Non-Markovian dynamics of a qubit, Phys. Rev. A. 73 (2006) 012111. https://doi.org/10.1103/PhysRevA.73.012111.

[79] H.-J. Briegel, B.-G. Englert, Quantum optical master equations: The use of damping bases, Phys. Rev. A. 47

(1993) 3311–3329. https://doi.org/10.1103/PhysRevA.47.3311.

[80] S. Maniscalco, Complete positivity of a spin-1/2 master equation with memory, Phys. Rev. A. 75 (2007) 062103. https://doi.org/10.1103/PhysRevA.75.062103.

[81] S. Lloyd, Universal Quantum Simulators, Science. 273 (1996) 1073–1078. https://doi.org/10.1126/science.273.5278.1073.

[82] M. Suzuki, Generalized Trotter's formula and systematic approximants of exponential operators and inner derivations with applications to many-body problems, Commun. Math. Phys. 51 (1976) 183–190. https://doi.org/10.1007/BF01609348.

[83] H.F. Trotter, On the Product of Semi-Groups of Operators, Proc. Am. Math. Soc. 10 (1959) 545. https://doi.org/10.2307/2033649.

[84] W.F. Stinespring, Positive functions on C*-algebras, Proc. Am. Math. Soc. 6 (1955) 211–216. https://doi.org/10.1090/S0002-9939-1955-0069403-4.

[85] Z. Hu, R. Xia, S. Kais, A quantum algorithm for evolving open quantum dynamics on quantum computing devices, Sci. Rep. 10 (2020) 3301. https://doi.org/10.1038/s41598-020-60321-x.

[86] Z. Hu, K. Head-Marsden, D.A. Mazziotti, P. Narang, S. Kais, A general quantum algorithm for open quantum dynamics demonstrated with the Fenna-Matthews-Olson complex, Quantum. 6 (2022) 726. https://doi.org/10.22331/q-2022-05-30-726.

[87] B.M. Terhal, I.L. Chuang, D.P. DiVincenzo, M. Grassl, J.A. Smolin, Simulating quantum operations with mixed environments, Phys. Rev. A. 60 (1999) 881–885. https://doi.org/10.1103/PhysRevA.60.881.

[88] S.-J. Wei, D. Ruan, G.-L. Long, Duality quantum algorithm efficiently simulates open quantum systems, Sci. Rep. 6 (2016) 30727. https://doi.org/10.1038/srep30727.

[89] R. Sweke, M. Sanz, I. Sinayskiy, F. Petruccione, E. Solano, Digital quantum simulation of many-body non-Markovian dynamics, Phys. Rev. A. 94 (2016) 022317. https://doi.org/10.1103/PhysRevA.94.022317.

[90] K. Head-Marsden, S. Krastanov, D.A. Mazziotti, P. Narang, Capturing non-Markovian dynamics on near-term quantum computers, Phys. Rev. Res. 3 (2021) 013182. https://doi.org/10.1103/PhysRevResearch.3.013182.

[91] Y. Wang, E. Mulvihill, Z. Hu, N. Lyu, S. Shivpuje, Y. Liu, M.B. Soley, E. Geva, V.S. Batista, S. Kais, Simulation of open quantum system dynamics based on the generalized quantum master equation on quantum computing devices, (2022) 1–31. http://arxiv.org/abs/2209.04956.

[92] S. Endo, J. Sun, Y. Li, S.C. Benjamin, X. Yuan, Variational Quantum Simulation of General Processes, Phys. Rev. Lett. 125 (2020) 010501. https://doi.org/10.1103/PhysRevLett.125.010501.

[93] X. Yuan, S. Endo, Q. Zhao, Y. Li, S.C. Benjamin, Theory of variational quantum simulation, Quantum. 3 (2019) 191. https://doi.org/10.22331/q-2019-10-07-191.

[94] P. Kramer, A review of the time-dependent variational principle, J. Phys. Conf. Ser. 99 (2008) 012009. https://doi.org/10.1088/1742-6596/99/1/012009.

[95] J.R. McClean, J. Romero, R. Babbush, A. Aspuru-Guzik, The theory of variational hybrid quantum-classical algorithms, New J. Phys. 18 (2016) 023023. https://doi.org/10.1088/1367-2630/18/2/023023.

[96] Y. Li, S.C. Benjamin, Efficient Variational Quantum Simulator Incorporating Active Error Minimization, Phys. Rev. X. 7 (2017) 021050. https://doi.org/10.1103/PhysRevX.7.021050.

[97] H. Wang, S. Ashhab, F. Nori, Quantum algorithm for simulating the dynamics of an open quantum system, Phys. Rev. A. 83 (2011) 062317. https://doi.org/10.1103/PhysRevA.83.062317.

[98] D.-S. Wang, B.C. Sanders, Quantum circuit design for accurate simulation of qudit channels, New J. Phys. 17 (2015) 043004. https://doi.org/10.1088/1367-2630/17/4/043004.

[99] D.-S. Wang, D.W. Berry, M.C. de Oliveira, B.C. Sanders, Solovay-Kitaev Decomposition Strategy for Single-Qubit Channels, Phys. Rev. Lett. 111 (2013) 130504. https://doi.org/10.1103/PhysRevLett.111.130504.

[100] R. Sweke, I. Sinayskiy, F. Petruccione, Simulation of single-qubit open quantum systems, Phys. Rev. A. 90 (2014) 022331. https://doi.org/10.1103/PhysRevA.90.022331.

[101] D. Bacon, A.M. Childs, I.L. Chuang, J. Kempe, D.W. Leung, X. Zhou, Universal simulation of Markovian quantum dynamics, Phys. Rev. A. 64 (2001) 062302. https://doi.org/10.1103/PhysRevA.64.062302.

[102] T. Barthel, M. Kliesch, Quasilocality and Efficient Simulation of Markovian Quantum Dynamics, Phys. Rev. Lett. 108 (2012) 230504. https://doi.org/10.1103/PhysRevLett.108.230504.

[103] S. Lloyd, L. Viola, Engineering quantum dynamics, Phys. Rev. A. 65 (2001) 010101. https://doi.org/10.1103/PhysRevA.65.010101.

[104] T. Rybár, S.N. Filippov, M. Ziman, V. Bužek, Simulation of indivisible qubit channels in collision models, J.

Phys. B At. Mol. Opt. Phys. 45 (2012) 154006. https://doi.org/10.1088/0953-4075/45/15/154006.

[105] R. Sweke, I. Sinayskiy, D. Bernard, F. Petruccione, Universal simulation of Markovian open quantum systems, Phys. Rev. A. 91 (2015) 062308. https://doi.org/10.1103/PhysRevA.91.062308.

[106] A.S. Davydov, Theory of Molecular Excitons, Springer US, Boston, MA, 1971. https://doi.org/10.1007/978-1-4899-5169-4.

[107] J. Adolphs, T. Renger, How Proteins Trigger Excitation Energy Transfer in the FMO Complex of Green Sulfur Bacteria, Biophys. J. 91 (2006) 2778–2797. https://doi.org/10.1529/biophysj.105.079483.

[108] R.E. Fenna, B.W. Matthews, Chlorophyll arrangement in a bacteriochlorophyll protein from Chlorobium limicola, Nature. 258 (1975) 573–577. https://doi.org/10.1038/258573a0.

[109] D.E. Tronrud, A. Camara-Artigas, R.E. Blankenship, J.P. Allen, Crystal structure of the Fenna-Matthews-Olson Protein from Chlorobaculum Tepidum, (2009). https://doi.org/10.2210/pdb3ENI/pdb.

[110] D.E. Tronrud, J. Wen, L. Gay, R.E. Blankenship, The structural basis for the difference in absorbance spectra for the FMO antenna protein from various green sulfur bacteria, Photosynth. Res. 100 (2009) 79–87. https://doi.org/10.1007/s11120-009-9430-6.

[111] T. Polívka, H.A. Frank, Molecular Factors Controlling Photosynthetic Light Harvesting by Carotenoids, Acc. Chem. Res. 43 (2010) 1125–1134. https://doi.org/10.1021/ar100030m.

[112] R.K. Chain, D.I. Arnon, Quantum efficiency of photosynthetic energy conversion., Proc. Natl. Acad. Sci. 74 (1977) 3377–3381. https://doi.org/10.1073/pnas.74.8.3377.

[113] H.J.M. Kramer, R. van Grondelle, C.N. Hunter, W.H.J. Westerhuis, J. Amesz, Pigment organization of the B800–850 antenna complex of Rhodopseudomonas sphaeroides, Biochim. Biophys. Acta - Bioenerg. 765 (1984) 156–165. https://doi.org/10.1016/0005-2728(84)90009-4.

[114] H. van Amerongen, R. van Grondelle, L. Valkunas, Photosynthetic Excitons, World Scientific, Singapore, 2000. https://doi.org/10.1142/3609.

[115] J. Dostál, J. Pšenčík, D. Zigmantas, In situ mapping of the energy flow through the entire photosynthetic apparatus, Nat. Chem. 8 (2016) 705–710. https://doi.org/10.1038/nchem.2525.

[116] G.J. Wedemayer, D.G. Kidd, D.E. Wemmer, A.N. Glazer, Phycobilins of cryptophycean algae. Occurrence of dihydrobiliverdin and mesobiliverdin in cryptomonad biliproteins, J. Biol. Chem. 267 (1992) 7315–7331. https://doi.org/10.1016/s0021-9258(18)42521-5.

[117] A.B. Doust, C.N.J. Marai, S.J. Harrop, K.E. Wilk, P.M.G. Curmi, G.D. Scholes, Developing a Structure–Function Model for the Cryptophyte Phycoerythrin 545 Using Ultrahigh Resolution Crystallography and Ultrafast Laser Spectroscopy, J. Mol. Biol. 344 (2004) 135–153. https://doi.org/10.1016/j.jmb.2004.09.044.

[118] D.E. Chandler, J. Strümpfer, M. Sener, S. Scheuring, K. Schulten, Light Harvesting by Lamellar Chromatophores in Rhodospirillum photometricum, Biophys. J. 106 (2014) 2503–2510. https://doi.org/10.1016/j.bpj.2014.04.030.

[119] G. McDermott, S.M. Prince, A.A. Freer, A.M. Hawthornthwaite-Lawless, M.Z. Papiz, R.J. Cogdell, N.W. Isaacs, Crystal structure of an integral membrane light-harvesting complex from photosynthetic bacteria, Nature. 374 (1995) 517–521. https://doi.org/10.1038/374517a0.

[120] A.W. Roszak, T.D. Howard, J. Southall, A.T. Gardiner, C.J. Law, N.W. Isaacs, R.J. Cogdell, Crystal Structure of the RC-LH1 Core Complex from Rhodopseudomonas palustris, Science. 302 (2003) 1969–1972. https://doi.org/10.1126/science.1088892.

[121] N. Nelson, C.F. Yocum, Structure and function of photosystems I and II, Annu. Rev. Plant Biol. 57 (2006) 521–565. https://doi.org/10.1146/annurev.arplant.57.032905.105350.

[122] Y. Umena, K. Kawakami, J.-R. Shen, N. Kamiya, Crystal structure of oxygen-evolving photosystem II at a resolution of 1.9 Å, Nature. 473 (2011) 55–60. https://doi.org/10.1038/nature09913.

[123] P. Jordan, P. Fromme, H.T. Witt, O. Klukas, W. Saenger, N. Krauß, Three-dimensional structure of cyanobacterial photosystem I at 2.5 Å resolution, Nature. 411 (2001) 909–917. https://doi.org/10.1038/35082000.

[124] G.T. Oostergetel, H. van Amerongen, E.J. Boekema, The chlorosome: a prototype for efficient light harvesting in photosynthesis, Photosynth. Res. 104 (2010) 245–255. https://doi.org/10.1007/s11120-010-9533-0.

[125] R. Kutner, J. Masoliver, The continuous time random walk, still trendy: fifty-year history, state of art and outlook, Eur. Phys. J. B. 90 (2017) 50. https://doi.org/10.1140/epjb/e2016-70578-3.

[126] B. Fresch, F. Remacle, R.D. Levine, Implementation of Probabilistic Algorithms by Multi-chromophoric Molecular Networks with Application to Multiple Travelling Pathways, ChemPhysChem. 18 (2017) 1782–1789. https://doi.org/10.1002/cphc.201700228.

[127] T.J. Lane, G.R. Bowman, K. Beauchamp, V.A. Voelz, V.S. Pande, Markov State Model Reveals Folding and Functional Dynamics in Ultra-Long MD Trajectories, J. Am. Chem. Soc. 133 (2011) 18413–18419.

https://doi.org/10.1021/ja207470h.

[128] B. Pruvost, H. Mizuta, S. Oda, Voltage-limitation-free analytical single-electron transistor model incorporating the effects of spin-degenerate discrete energy states, J. Appl. Phys. 103 (2008) 054508. https://doi.org/10.1063/1.2838491.

[129] E. Farhi, S. Gutmann, Quantum computation and decision trees, Phys. Rev. A - At. Mol. Opt. Phys. 58 (1998) 915–928. https://doi.org/10.1103/PhysRevA.58.915.

[130] A.M. Childs, R. Cleve, E. Deotto, E. Farhi, S. Gutmann, D.A. Spielman, Exponential algorithmic speedup by quantum walk, in: Proc. 36th ACM Symp. Theory Comput., 2002: pp. 59–68. https://doi.org/10.1145/780542.780552.

[131] A.M. Childs, J. Goldstone, Spatial search by quantum walk, Phys. Rev. A - At. Mol. Opt. Phys. 70 (2004) 1–11. https://doi.org/10.1103/PhysRevA.70.022314.

[132] M. Cattaneo, M.A.C. Rossi, M.G.A. Paris, S. Maniscalco, Quantum spatial search on graphs subject to dynamical noise, Phys. Rev. A. 98 (2018) 052347. https://doi.org/10.1103/PhysRevA.98.052347.

[133] E. Campos, S.E. Venegas-Andraca, M. Lanzagorta, Quantum tunneling and quantum walks as algorithmic resources to solve hard K-SAT instances, Sci. Rep. 11 (2021) 1–18. https://doi.org/10.1038/s41598-021-95801-1.

[134] O. Mülken, A. Blumen, Continuous-time quantum walks: Models for coherent transport on complex networks, Phys. Rep. 502 (2011) 37–87. https://doi.org/10.1016/j.physrep.2011.01.002.

[135] I. Foulger, S. Gnutzmann, G. Tanner, Quantum walks and quantum search on graphene lattices, Phys. Rev. A. 91 (2015) 062323. https://doi.org/10.1103/PhysRevA.91.062323.

[136] E. Estrada, The electron density function of the Hückel (tight-binding) model, Proc. R. Soc. A Math. Phys. Eng. Sci. 474 (2018) 20170721. https://doi.org/10.1098/rspa.2017.0721.

[137] S. Hoyer, M. Sarovar, K. Birgitta Whaley, Limits of quantum speedup in photosynthetic light harvesting, New J. Phys. 12 (2010) 065041. https://doi.org/10.1088/1367-2630/12/6/065041.

[138] L. Cuadra, J.C. Nieto-Borge, Modeling Quantum Dot Systems as Random Geometric Graphs with Probability Amplitude-Based Weighted Links, Nanomaterials. 11 (2021) 375. https://doi.org/10.3390/nano11020375.

[139] I. Kassal, A. Aspuru-Guzik, Environment-assisted quantum transport in ordered systems, New J. Phys. 14 (2012) 053041. https://doi.org/10.1088/1367-2630/14/5/053041.

[140] E. Zerah-Harush, Y. Dubi, Universal Origin for Environment-Assisted Quantum Transport in Exciton Transfer Networks, J. Phys. Chem. Lett. 9 (2018) 1689–1695. https://doi.org/10.1021/acs.jpclett.7b03306.

[141] G.S. Engel, T.R. Calhoun, E.L. Read, T.-K. Ahn, T. Mančal, Y.-C. Cheng, R.E. Blankenship, G.R. Fleming, Evidence for wavelike energy transfer through quantum coherence in photosynthetic systems, Nature. 446 (2007) 782–786. https://doi.org/10.1038/nature05678.

[142] E. Collini, C.Y. Wong, K.E. Wilk, P.M.G. Curmi, P. Brumer, G.D. Scholes, Coherently wired light-harvesting in photosynthetic marine algae at ambient temperature, Nature. 463 (2010) 644–647. https://doi.org/10.1038/nature08811.

[143] H. Lee, Y.-C. Cheng, G.R. Fleming, Coherence Dynamics in Photosynthesis: Protein Protection of Excitonic Coherence, Science. 316 (2007) 1462–1465. https://doi.org/10.1126/science.1142188.

[144] M.B. Plenio, S.F. Huelga, Dephasing-assisted transport: quantum networks and biomolecules, New J. Phys. 10 (2008) 113019. https://doi.org/10.1088/1367-2630/10/11/113019.

[145] P. Rebentrost, M. Mohseni, I. Kassal, S. Lloyd, A. Aspuru-Guzik, Environment-assisted quantum transport, New J. Phys. 11 (2009) 033003. https://doi.org/10.1088/1367-2630/11/3/033003.

[146] M. Mahdian, H.D. Yeganeh, Quantum Simulation of FMO Complex Using One-Parameter Semigroup of Generators, Brazilian J. Phys. 50 (2020) 807–813. https://doi.org/10.1007/s13538-020-00804-4.

[147] M. Mahdian, H.D. Yeganeh, A. Dehghani, Quantum simulation dynamics and circuit synthesis of FMO complex on an NMR quantum computer, Int. J. Quantum Inf. 18 (2020) 2050034. https://doi.org/10.1142/S0219749920500343.

[148] P. Gupta, C.M. Chandrashekar, Digital quantum simulation framework for energy transport in an open quantum system, New J. Phys. 22 (2020) 123027. https://doi.org/10.1088/1367-2630/abcdc9.

[149] H. Haken, G. Strobl, An exactly solvable model for coherent and incoherent exciton motion, Zeitschrift Für Phys. A Hadron. Nucl. 262 (1973) 135–148. https://doi.org/10.1007/BF01399723.

[150] F. Ciccarello, S. Lorenzo, V. Giovannetti, G.M. Palma, Quantum collision models: Open system dynamics from repeated interactions, Phys. Rep. 954 (2022) 1–70. https://doi.org/10.1016/j.physrep.2022.01.001.

[151] B.J. West, K. Lindenberg, Stochastic model for exciton lineshapes at finite temperatures, in: AIP Conf. Proc., AIP, 1984: pp. 111–132. https://doi.org/10.1063/1.34342.

[152] G. García-Pérez, M.A.C. Rossi, S. Maniscalco, IBM Q Experience as a versatile experimental testbed for simulating open quantum systems, Npj Quantum Inf. 6 (2020) 1. https://doi.org/10.1038/s41534-019-0235-y.

[153] M. Cattaneo, M.A.C. Rossi, G. García-Pérez, R. Zambrini, S. Maniscalco, Quantum simulation of dissipative collective effects on noisy quantum computers, (2022) 1–25. http://arxiv.org/abs/2201.11597.

[154] Y. Tanimura, R. Kubo, Time Evolution of a Quantum System in Contact with a Nearly Gaussian-Markoffian Noise Bath, J. Phys. Soc. Japan. 58 (1989) 101–114. https://doi.org/10.1143/JPSJ.58.101.

[155] F. Gallina, M. Bruschi, B. Fresch, Strategies to simulate dephasing-assisted quantum transport on digital quantum computers, New J. Phys. 24 (2022) 023039. https://doi.org/10.1088/1367-2630/ac512f.

[156] Qiskit, Qiskit Textbook, (2019). https://qiskit.org/learn/ (accessed September 9, 2022).

[157] B. Coecke, A. Kissinger, Picturing Quantum Processes, Cambridge University Press, Cambridge, 2017. https://doi.org/10.1017/9781316219317.

[158] T.G. Wong, Introduction to Classical and Quantum Computing, Second Edi, Rooted Grove, Omaha, 2022.

[159] P.W. Shor, The Early Days of Quantum Computation, (2022) 1–10. http://arxiv.org/abs/2208.09964.

[160] M. Zak, Quantum Analog Computing, Chaos, Solitons & Fractals. 10 (1999) 1583–1620. https://doi.org/10.1016/S0960-0779(98)00215-X.

[161] T. Kadowaki, H. Nishimori, Quantum annealing in the transverse Ising model, Phys. Rev. E. 58 (1998) 5355–5363. https://doi.org/10.1103/PhysRevE.58.5355.

[162] E. Farhi, J. Goldstone, S. Gutmann, M. Sipser, Quantum Computation by Adiabatic Evolution, (2000). http://arxiv.org/abs/quant-ph/0001106.

Chapter II

Quantum algorithms for dephasing-assisted dynamics in the Markovian limit

In this Chapter, we consider the problem of simulating dephasing environment-assisted quantum transport (ENAQT) [1] on a gate-based (*i.e.*, digital) quantum computer and we explicitly formulate, discuss and test two different algorithms. ENAQT represents a moderately sophisticated quantum dynamical process, and the comparison of different quantum simulation algorithms offers a fresh view of the underlying mechanism. In particular, we will discuss how different algorithms provide different *unravellings* of the average evolution corresponding to the solution of the site-dephasing master equation. The design of the algorithms is inspired by the underlying idea of devising *effective* representations of the environment.
Following the stochastic approach to exciton dynamics pioneered by Haken and Strobl [2], in the first algorithm the environment is represented by a stochastic noise in the Hamiltonian of the system, we will refer to this scheme as the *classical noise algorithm*. The second algorithm is based on a quantum collisional model [3] and we will show how a single ancilla qubit is sufficient to encode the dephasing role of the environment, we will refer to this implementation as the *collision algorithm.* We test both algorithms by demonstrating ENAQT in a system of four sites with nearest-neighbour interactions (cyclic topology network).

The Chapter is organized as follows: in section II.1, we introduce ENAQT in terms of a Lindblad master equation corresponding to the Haken-Strobl model for exciton diffusion. The Hamiltonian part of the model accounts for the coupling between different quantum sites while the role of the environment is to induce decoherence between different sites. We define the transport efficiency and discuss how the molecular network can be encoded in the quantum computer. Section II.2 is dedicated to the development of the classical noise algorithm based on a stochastic Hamiltonian with diagonal disorder. The solution of the master equation is

obtained by an explicit average of the Schrödinger dynamics corresponding to different realizations of the noise. In section II.3, we discuss an algorithm based on a collision model and we demonstrate how a single ancilla qubit is sufficient to encode the effect of the environment. Both algorithms can be run encoding each site of the network in a qubit (physical mapping) or by encoding each site of the network into an element of the computational basis (algorithmic mapping). A comparative analysis of the computational resources required by the two algorithms using the two mappings is detailed in section II.4. The analysis is supplemented with the results obtained by running the algorithms on a quantum computer emulator, namely the IBM Qiskit QASM simulator [4]. Because of the necessity of repeating the quantum circuit to accumulate measurement statistics, each execution of the circuit realizes a quantum trajectory, which we analyse in section II.5, followed by conclusions and perspectives.

II.1 Dephasing-assisted quantum transport with a quantum computer

We have seen in Chapter I that systems described by a tight-binding Hamiltonian realises an instance of the Quantum Walk (QW) scheme [5]. Such an Hamiltonian reads

$$H = \sum_{j=1}^{N} \varepsilon_j |j\rangle\langle j| + \sum_{\langle j,j'\rangle} V_{j,j'} \left(|j\rangle\langle j'| + |j'\rangle\langle j| \right), \tag{II.1}$$

where we have a set on quantum sites $\{j\}$, with site energy ε_j and coupled to the nearest-neighbour, according to a certain topology, with strength $V_{j,j'}$. By looking at the Hamiltonian structure in eq. (II.1), in principle, we can implement a Quantum Walk on, *e.g.*, a cyclic lattice by considering a ring of tunnel coupled quantum dots [6] or a chromophore ring of the LH2 antenna complex [7]. However, since nanostructures are rarely free of imperfections and molecular systems have a multitude of degrees of freedom, the effects of static and dynamic disorder on the dynamics of the quantum walk become of central interest. A common feature is the presence of (static) energy disorder in the diagonal terms of the Hamiltonian. If disorder is high, quantum transport can be suppressed by Anderson localization with detrimental effects on the quantum advantage provided by the QW algorithm respect to the classical counterpart [8–10]. Localization is destroyed in the presence of a dephasing environment which in this case acts by enhancing transport efficiency. To give an intuition on the mechanisms underlying the enhancement in ENAQT, a good example is an environment that acts on the system by causing fluctuations $\delta\varepsilon_j(t)$ in the site energies. We assume $\delta\varepsilon_j(t)$ to be independent white noise on each site, that is

$$\overline{\delta\varepsilon_j(t)} = 0, \tag{II.2}$$

$$\overline{\delta\varepsilon_j(t)\delta\varepsilon_{j'}(t')} = \gamma_j \delta_{j,j'} \delta(t-t'), \tag{II.3}$$

where the overbar indicates the average over the noise realizations, γ_j is the variance of the noise, $\delta_{j,j'}$ and $\delta(t-t')$ are respectively the Kronecker and Dirac delta functions, meaning that noise is spatially and dynamically uncorrelated. Under these assumptions, we define a stochastic time-dependent Hamiltonian as

$$H_{\mathrm{HS}}(t) = H + H_{\mathrm{fluc}}(t) = \sum_{j=1}^{N}\left(\varepsilon_j + \delta\varepsilon_j(t)\right)|j\rangle\langle j| + \sum_{\langle j,j'\rangle} V_{j,j'}\left(|j\rangle\langle j'| + |j'\rangle\langle j|\right) . \qquad \text{(II.4)}$$

This model was introduced by Haken and Strobl [2] to describe the effects of the phonons on the dynamics of triplet excitons in molecular crystals. When the exciton bandwidth is smaller than the phonon bandwidth, the coupling with the phonon can be modelled by Gaussian white-noise modulation of the site energies, specified by the statistical properties in eqs. (II.2)-(II.3). The fluctuations cause instantaneous and stochastic resonances of the site energies, overcoming localization and facilitating exciton transport. The state of the system acquires a random character, and the density matrix is recovered as the average over the noise realizations, $\rho(t) = \overline{|\psi(t)\rangle\langle\psi(t)|}$. The following master equation in the Lindblad form [11] is derived for the time evolution

$$\dot{\rho}(t) = -\mathrm{i}\left[H, \rho(t)\right] + \sum_{j=1}^{N}\gamma_j\left(L_j\rho(t)L_j^{\dagger} - \frac{1}{2}L_j^{\dagger}L_j\rho(t) - \frac{1}{2}\rho(t)L_j^{\dagger}L_j\right), \qquad \text{(II.5)}$$

where the Lindblad operators are simply the projectors on the site basis, $L_j = |j\rangle\langle j|$, and the dissipation rates describing decoherence between different sites are controlled by the (positive) fluctuation amplitudes, γ_j. It was shown that the simple site-dephasing dynamics as described by eq. (II.5) captures qualitatively the transition from a purely coherent to an incoherent regime of energy transfer as a function of the dephasing rates [12] and allows studying how the transport efficiency may be enhanced in the presence of a dephasing environment [1,13,14]. On the other hand, eq. (II.5) corresponds to the high-temperature limit of dephasing quantum dynamics. Indeed, the long-time asymptotic solution implies an equal occupation of all quantum sites (and all eigenstates) independently of their energy (cf. Chapter IV).

II.1.1 Transport efficiency

The common setting to evaluate the effect of dephasing on quantum transport is to consider the dynamical evolution of an initially localized state. In the network, a target site is identified, and the transport efficiency depends on the probability of the quantum walker visiting the target site. Often, non-Hermitian contributions to the Hamiltonian are included to model recombination of the exciton (loss of the walker) and the trapping of the exciton at the target site [15,16]. Because here we want to consider the simplest model where decoherence is the only non-unitary dynamics included in the system evolution, we define the transport efficiency like in Maier *et al.* [17], as the cumulative probability of finding the walker at the target site j within a finite time T

$$\eta_j(T) \equiv \int_0^T p(j,t\,|\,j_0)\,dt\,, \qquad \text{(II.6)}$$

where $p(j,t\,|\,j_0)=\langle j|\rho(t)|j\rangle$ is the probability to find the walker at site j at time t if the dynamics started at site j_0 at time $t=0$. If the walker represents the exciton transport in molecular complexes, T should be chosen long enough to observe ENAQT, but shorter than the typical lifetime of the exciton as recombination is not included in the dynamics.

Because the digital simulation requires discretizing the dynamics in time steps Δt, we will approximate the integral in eq. (II.6) with the sum

$$\eta_j(T)\approx\sum_{s=0}^{S}p(j,s\Delta t\,|\,j_0)\Delta t\,, \tag{II.7}$$

where s is an integer indexing the time step of the simulated dynamics ranging from zero to S, where S indicates the maximum number of time steps and $T=S\Delta t$. Below, we will calculate the transport efficiency through different quantum algorithms by starting from an initially localized state. However, the algorithms are general, and they may be used to simulate the dynamics of any localized or diffuse, pure or mixed, initial state.

II.1.2 Mappings

The problem of simulating the quantum dynamics of a quantum molecular network as described above can be mapped in two different ways into a quantum register. We call them the *physical mapping* and the *algorithmic mapping*. Let us assume we want to simulate a chromophore network with N sites. The physical mapping is inspired by the direct representation of each chromophore by a qubit of the register and it is commonly employed in analogue quantum simulators [17–23]. In the simple case where each chromophore is modelled as a two-level system, the mapping on a digital quantum computer is straightforward since each chromophore corresponds to a qubit of the register. The Frenkel exciton Hamiltonian of eq. (II.1) is written in terms of the qubit Hamiltonian as

$$H_{\mathrm{ex}}=-\sum_{j=1}^{N}\frac{\varepsilon_j}{2}\sigma_z^j+\sum_{\langle j,j'\rangle}\frac{V_{j,j'}}{2}\left(\sigma_x^j\sigma_x^{j'}+\sigma_y^j\sigma_y^{j'}\right), \tag{II.8}$$

where ε_j is the energy gap between the ground and the excited state of the chromophore j when it is isolated, and $\sigma_\alpha^j=\mathbb{I}^{\otimes j-1}\otimes\sigma_\alpha\otimes\mathbb{I}^{\otimes N-j}$ denotes a Pauli operator acting on the qubit in position j, with $\mathbb{I}$ the two-dimensional identity matrix. The populations of the states of a qubit correspond to the populations of the chromophores, and the coupling between two chromophores is realized by coupling the qubits. Within this mapping, the master equation in eq. (II.5) is written as

$$\dot{\rho}(t)=-\mathrm{i}\left[H_{\mathrm{ex}},\rho(t)\right]+\sum_{j=1}^{N}\Gamma_j\left(\sigma_z^j\rho(t)\sigma_z^j-\rho(t)\right), \tag{II.9}$$

where $\Gamma_j=\gamma_j/4$. In this case, we identify the basis vector $|j\rangle$ in eq. (II.1) as the state where all the qubits are in the ground state, except qubit j that is excited, namely

$$|j\rangle \equiv |0\rangle_1 \otimes |0\rangle_2 \otimes ... \otimes |1\rangle_j \otimes ... \otimes |0\rangle_N \equiv |00...1_j...0\rangle . \quad \text{(II.10)}$$

The number of qubits required for this encoding scales linearly with the size of the system N, but the vectors that correspond to useful states of the system are only a small subset of the entire computational basis. Although this mapping offers a vivid physical representation, it is not advantageous in terms of memory requirements. Indeed, the Hamiltonian (II.8) and the site-dephasing master equation (II.9) do not mix different exciton manifolds, and therefore to represent the single-exciton manifold a Hilbert space of dimension N is sufficient, much smaller than the 2^N dimensional Hilbert space which is generated by the physical mapping. The exponential scaling of the computational space can be harnessed by adopting the algorithmic mapping which is usually required for a resource-efficient implementation of the quantum walk algorithm. A graph with N nodes can be encoded by using only $\lceil \log_2(N) \rceil$ qubits by using the binary representation of the node index in the computational basis, that is $|j\rangle = |\mathrm{bin}(j-1)\rangle$ for j running from 1 to N. For example, a four-site network is efficiently encoded by two qubits as

$$|1\rangle \equiv |00\rangle \quad |2\rangle \equiv |01\rangle \quad |3\rangle \equiv |10\rangle \quad |4\rangle \equiv |11\rangle \quad \text{(II.11)}$$

From the perspective of a chromophore network, this mapping only represents the single-exciton manifold. Because of the exponential saving in memory obtained by encoding the position as a binary number in a quantum computer, the algorithmic mapping will always win eventually as the molecular network we want to simulate gets larger. On the other hand, because each site of the network is represented by multiple qubits, the Hamiltonian evolution requires the implementation of unitary operations over multiple qubits (eventually decomposed in a series of elementary gates) and reading the population of a single site requires measuring all the qubits. The interplay between memory advantage and circuit complexity is a key factor for estimating the scaling of the algorithmic efficiency with the size of the simulated system. The algorithms we present below can be realized by using both mappings. To illustrate both possibilities, we will discuss explicitly the classical noise algorithm in an algorithmic mapping while we will move to a physical mapping to present the collision algorithm. In section II.4.1 the algorithmic scaling in the two cases will be analysed in detail.

II.2 Classical noise algorithm

The non-unitary time evolution described by eq. (II.5) physically arises from tracing out degrees of freedom which are part of the global system evolving unitarily. However, the same incoherent dynamics can also arise as a consequence of an averaging procedure over distinct autonomous evolutions (*i.e.*, trajectories). This point of view was taken by Haken and Strobl to model the effect of the phonon coupling on the excitonic transport in molecular crystals. The dephasing master equation is then obtained by averaging over the noise realizations. The first algorithm we consider is based on the simulation of the unitary dynamics ruled by the Haken-Strobl stochastic Hamiltonian in eq. (II.4), where the stochastic part is a classical Gaussian stochastic process specified by eqs. (II.2)-(II.3). The non-unitary evolution is then recovered by averaging over the different realizations of the circuit.

For the numerical solution of the Schrödinger equation, we first discretize the evolution time from $t=0$ to T into S small time intervals $\Delta t = T/S$. A trajectory ξ is obtained by evolving the initial state through the time-ordered propagator

$$U_\xi(t,0) = \overleftarrow{\mathcal{T}} \exp\left[-\mathrm{i}\int_0^t H_{\mathrm{HS}}(\tau)\,d\tau\right] \approx \overleftarrow{\mathcal{T}} \prod_{s=1}^{S} U_\xi(s\Delta t,(s-1)\Delta t), \tag{II.12}$$

where $\overleftarrow{\mathcal{T}}$ is the time-ordering operator [24]. On the right-hand side, the operator is evaluated as the product of short-time evolutions governed by the average Hamiltonian in the corresponding time interval, *i.e.*,

$$U_\xi(s\Delta t,(s-1)\Delta t) = \exp\left[-\mathrm{i}\int_{(s-1)\Delta t}^{s\Delta t} H_{\mathrm{HS}}(\tau)\,d\tau\right] = \exp\left[-\mathrm{i}H\Delta t - \mathrm{i}\int_{(s-1)\Delta t}^{s\Delta t} H_{\mathrm{fluc},\xi}(\tau)\,d\tau\right]. \tag{II.13}$$

The integral of the fluctuating part of the Hamiltonian requires some care because it implies integrating Gaussian white noises

$$\int_{(s-1)\Delta t}^{s\Delta t} H_{\mathrm{fluc},\xi}(\tau)\,d\tau = \sum_{j=1}^{N} |j\rangle\langle j| \int_{(s-1)\Delta t}^{s\Delta t} \delta\varepsilon_{j,\xi}(\tau)\,d\tau\,. \tag{II.14}$$

Each integral is a Gaussian random variable with zero mean and variance $\gamma_j \Delta t$ [25]. By defining the fluctuating Hamiltonian for each time interval s by a set of normally distributed energies $\delta\varepsilon_{j,\xi,s}$ with zero mean and variance γ_j

$$H_{\mathrm{fluc},\xi,s} = \sum_{j=1}^{N} \delta\varepsilon_{j,\xi,s} |j\rangle\langle j|, \tag{II.15}$$

the short-time evolution operator (II.13) explicitly reads

$$U_\xi(s\Delta t,(s-1)\Delta t) = \exp\left[-\mathrm{i}H\Delta t - \mathrm{i}H_{\mathrm{fluc},\xi,s}\sqrt{\Delta t}\right]. \tag{II.16}$$

In Appendix A, we show that the dephasing master equation (II.5) can be recovered from the average of the trajectories generated by the evolution operator (II.12) for different realizations of the noise ξ in the limit of vanishing time step $\Delta t \to 0^+$ and for an infinite number of trajectories, *i.e.*, $\Xi \to \infty$.

Before running the algorithm, the following parameters need to be set: the time step Δt, the number of trajectories Ξ, the fluctuation amplitude at each site γ_j and the number of samples (*shots*) that are taken during measurement. In the following, we detail the algorithmic steps to propagate the dynamics and to

calculate the transport efficiency, eq. (II.7). Figure 1 depicts the structure of the algorithm using three qubits which can encode a network with a maximum of $2^3 = 8$ sites:

1. Initialize the quantum register to the initial state of the dynamics $|j_0\rangle$;
2. Draw N independent real random numbers from a Gaussian distribution with zero mean and variance γ_j. Each random number represents the site-energy fluctuation $\delta\varepsilon_{j,\xi,s}$;
3. Apply the unitary gate corresponding to the operator $U_\xi\left(s\Delta t,(s-1)\Delta t\right)$, eq. (II.16);
4. Create a copy of the circuit, so that one has two identical objects: a quantum circuit $\mathcal{A}$ that will be the lead and its copy $\mathcal{B}$ to which the measurement gates will be appended;
5. Add measurement gates to circuit $\mathcal{B}$ and execute it to obtain a finite-sampling estimator $\pi_\xi\left(j,s\Delta t\,|\,j_0\right)$ of $p_\xi\left(j,s\Delta t\,|\,j_0\right)$, which is the probability of being at the target site during the trajectory generated by ξ;
6. Discard circuit $\mathcal{B}$ and continue with circuit $\mathcal{A}$;
7. Repeat steps 2-6 for $s \in \{0,1,...,S\}$. In the end, a trajectory is embedded in the gates of circuit $\mathcal{A}$. Each time point of the trajectory is recorded in $\pi_\xi\left(j,s\Delta t\,|\,j_0\right)$;
8. Repeat steps 1-7 for $\xi \in \{1,2,...,\Xi\}$ to obtain a swarm of trajectories;
9. Estimate the transport efficiency as

$$\eta_j(T) \approx \sum_{s=0}^{S} p\left(j,s\Delta t\,|\,j_0\right)\Delta t \approx \frac{1}{\Xi}\sum_{s=0}^{S}\sum_{\xi=1}^{\Xi} p_\xi\left(j,s\Delta t\,|\,j_0\right)\Delta t \approx \frac{1}{\Xi}\sum_{s=0}^{S}\sum_{\xi=1}^{\Xi} \pi_\xi\left(j,s\Delta t\,|\,j_0\right)\Delta t\,, \qquad \text{(II.17)}$$

where each term in the equation evidences an approximation made in the estimation. Namely, the discretization of time into intervals Δt, the finite number of trajectories Ξ and the finite number of sampling shots in the final measurement of the qubits.

Notice that the initialization, evolution and measurement gates act in general on the whole quantum register as a consequence of the algorithmic mapping. Executing and measuring a clone of the circuit (step 4 of the algorithm) is important to guarantee the correct evolution of the unitary trajectory. In fact, applying measurements after every evolution gate would destroy the quantum coherence of the register, resulting in our case in a localization of the walker at some site at each time step. In step 5, a good estimator of the site population $p_\xi\left(j,s\Delta t\,|\,j_0\right)$ is obtained by collecting a large statistical sample. However, if one is not interested in individual trajectories but only in the simulation of the master equation, it is fair to set the number of sampling shots equal to 1 to lower the execution time.

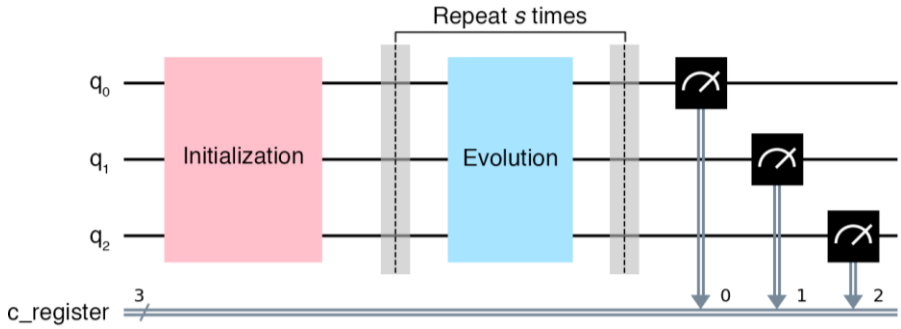

Figure 1. Scheme of the classical noise algorithm to simulate the dephasing dynamics of a molecular network with a maximum of 8 sites (algorithmic mapping). The circuit generates the state corresponding to $|j_0\rangle = |\mathrm{bin}(j_0 - 1)\rangle$ with the initialization gate, then the evolution gate propagates the dynamics up to the time $t = s\Delta t$ before measuring the state of the system. The gate decomposition of the evolution gate depends on the specific realization of the stochastic Hamiltonian. We refer to the main text for further details.

II.2.1 Stochastic trajectories and average evolution

The classical noise algorithm is implemented for the simulation of the dynamics in a $N = 4$ cyclic network with diagonal static disorder. The site energies were obtained from a Gaussian distribution centred at zero and parametrized by its standard deviation $\sigma/V = 2$, where we assume the nearest-neighbour interaction strength V as the energy unit. The result is the following set of energies: $\varepsilon_1/V \simeq 0.44$, $\varepsilon_2/V \simeq 0.24$, $\varepsilon_3/V \simeq -3.22$ and $\varepsilon_4/V \simeq 0.36$, which is used for all the simulations discussed hereafter. The dynamics was initialized at the site $j_0 = 1$ and we set the target site at $j = 3$ so that we aim at computing the probability of finding the walker at the target site as a function of time. The amplitudes of the stochastic fluctuations in the Haken-Strobl Hamiltonian were set equal for every site resulting in a (scaled) dephasing rate of $\gamma_j/V = \gamma/V = 10^{-1}\hbar^{-1}$.

First, let us look at a single stochastic trajectory, this can be obtained by setting $\Xi = 1$ in the algorithm and by choosing an appropriate number of shots in step 5 to determine the average population of the target site. Figure 2a shows such a stochastic trajectory (blue line) compared with the dynamics of the isolated system (green line), that is in the absence of white noise. Note how the single trajectory evolves differently from the isolated system from the very beginning of the dynamics. However, as for the isolated system, the single trajectory never reaches an equilibrium constant value. A swarm of $\Xi = 200$ unitary stochastic trajectories obtained from different realizations of the noise is reported in Figure 2b (blue lines in transparency). The trajectory of the open system is then obtained as an average of them (solid blue), and it is in very good agreement with the direct solution of the master equation (orange dotted line). The decay of the site coherences and the emergence of a constant equilibrium value for the site population are not a direct consequence of the presence of the noise, but rather emerge because of the averaging procedure.

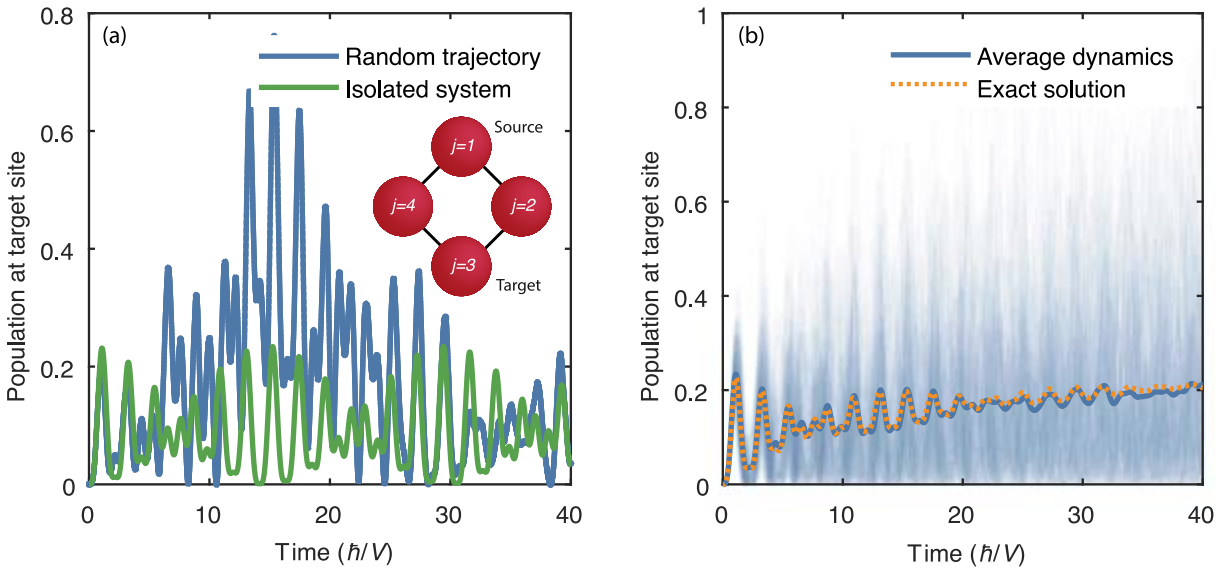

Figure 2. Time evolution of the population at site $j=3$ on a disordered four-site cyclic network initially populated at site $j_0=1$. The dynamics of a single stochastic trajectory obtained with the classical noise algorithm (blue) is compared with the dynamics of the isolated system (green) in panel (a). A swarm of $\Xi=200$ different stochastic trajectories (blue lines in transparency) is reported in panel (b). Their average (solid blue) approximates the open system dynamics obtained with an exact propagation of the Lindblad equation (orange). All the trajectories are obtained by running the classical noise algorithm in the Qiskit Statevector simulator, the Statevector mode corresponds to a single execution of the circuit and returns the statevector of the quantum register. The time step for the algorithmic evolution is $\Delta t=10^{-2}\,\hbar/V$, and the (scaled) dephasing rate is $\gamma/V=10^{-1}\hbar^{-1}$.

As we will show in the next Chapter, the classical noise algorithm can be readily adapted to other models of stochastic modulation of the Hamiltonian (coloured noise) to investigate the role of the environment correlation time in the decoherence dynamics and energy transfer rates in molecular systems. In this case, the average dynamics is not known *a priori* because stochastic modulations different from white noise do not lead in general to a Lindblad form of the master equation [26–28].

II.3 Collision algorithm

Quantum collision models have recently emerged as a powerful and versatile tool to describe the dynamics of open quantum systems. The basic idea is to induce decoherence and relaxation in the dynamics of an open system by repeated interactions (*collisions*) between the system and a set of ancillae that represents an effective environment. Currently, collision models are used in the study of quantum thermodynamics [29–31], quantum non-Markovian dynamics [32–34], quantum optics [35] and foundational issues such as quantum Darwinism [36]. Ref. [37] gives a perspective on the application of collision models in quantum physics. Recently, a stochastic version of a collision model has been applied to the study of ENAQT [38]. Besides being widely

used both for theoretical investigations and simulations on classical computers, collision models are particularly suitable to be translated into quantum algorithms. Literature in this sense is very recent and limited to the dynamics of few qubits [39,40]. In this section, we discuss a quantum algorithm for the simulation of dephasing-enhanced quantum transport based on collisions between the system and the ancillae representing the environment.

To introduce the underlying idea, imagine we associate at each site of the molecular network a reservoir of ancilla systems. As in the classical noise algorithm, we first discretize the evolution time. During each time step Δt (collision time), each site interacts with one ancilla of its reservoir. The dynamics proceeds through successive pairwise collisions between the system and the bath ancillae, each collision involving a unitary evolution of the system and the colliding ancilla. If the ancillae are initially uncorrelated and each of them collides with the system only once, then it can be shown that the dynamics of the system is described by the solution of a Lindblad master equation in the continuous-time limit [3,41].

The concept of a reservoir of independent ancillae is used in the framework of collision models and we will use it to give the theoretical basis of the algorithm. However, we will show later that for the algorithm a single ancilla-qubit is sufficient to represent the whole environment.

We will work in a physical mapping of the system, where each qubit represents a site of the network and the system Hamiltonian is translated into the qubit Hamiltonian of eq. (II.8). During a time interval Δt, we define the Hamiltonian of the collision model acting on the system-ancillae state as

$$\begin{aligned} H_{\mathrm{CM}} &= H_{\mathrm{ex}} \otimes \mathbb{I}^{\otimes N} + H_{\mathrm{int}} = \\ &= \sum_{j=1}^{N} \frac{\varepsilon_j}{2} \sigma_z^j \otimes \mathbb{I}^{\otimes N} + \sum_{\langle j,j' \rangle} \frac{V_{j,j'}}{2} \left(\sigma_x^j \sigma_x^{j'} \otimes \mathbb{I}^{\otimes N} + \sigma_y^j \sigma_y^{j'} \otimes \mathbb{I}^{\otimes N} \right) + \sum_{j=1}^{N} c_j \sigma_z^j \otimes \sigma_x^{a_j} \end{aligned} \tag{II.18}$$

where H_{int} is the interaction Hamiltonian between the sites and the corresponding ancillae and $\sigma_x^{a_j}$ is the Pauli X-operator acting on the environment ancilla assigned to site j. We emphasise the separation between the system $\mathcal{S}$ and the ancillary a subspaces by the explicit tensor product $\otimes$. The choice of the interaction Hamiltonian is crucial to recover a specific dynamics of the system $\mathcal{S}$. By assuming a $\sigma_z^j \otimes \sigma_x^{a_j}$ form of the interaction, we obtain the dephasing dynamics described by eq. (11) when the initial state of the ancilla system is any state which is diagonal in the computational basis (see eq. (34) in Appendix B). For convenience, we set the initial state of each ancilla as the qubits' ground state, $\rho_a = \left(|0\rangle\langle 0| \right)^{\otimes N}$. After the interaction, the ancillae are discarded and no longer affect the dynamics of the system, therefore we trace over their degrees of freedom to obtain the reduced density matrix of the system. Thus, the dynamical map of a collision event can be written as

$$\rho_{\mathcal{S}}(t + \Delta t) = \Phi\left[\rho_{\mathcal{S}}(t) \right] = \mathrm{Tr}_a \left\{ U \left(\rho_{\mathcal{S}}(t) \otimes \rho_a \right) U^{\dagger} \right\}, \tag{II.19}$$

where Tr_a is the trace over the ancillary degrees of freedom and $U = \exp\left(-\mathrm{i}H_{\mathrm{CM}}\Delta t\right)$ is the evolution operator. By sequentially repeating the interaction step with new ancillae from the reservoir, the reduced dynamics of the system at later times is obtained

$$\rho_{\mathcal{S}}\left(s\Delta t\right) = \Phi_s\left[\rho_{\mathcal{S}}\left(0\right)\right] = \Phi\left[\Phi\left[...\Phi\left[\rho_{\mathcal{S}}\left(0\right)\right]...\right]\right]. \tag{II.20}$$

In Appendix B we show that, in the limit $\Delta t \to 0^+$, the dynamical map of eq. (II.20) approximates the solution of the target master equation (II.9) with dephasing rates $\Gamma_j = c_j^2\Delta t$. The dephasing rates are therefore determined by the strength of the interaction and the collision time, conveying the intuition that the system undergoes decoherence when it interacts strongly for a short time as well as when the interaction is weaker, but it lasts longer. Note that the dependence of the interaction strength on the collision time $c_j = \sqrt{\Gamma_j/\Delta t}$ is a typical relation in quantum collision models [35,42].

We are now in the position of translating the collision model described above into an algorithm that simulates the site-dephasing master equation. Given the decoherence rate, the user must choose the time step Δt and the coupling strengths with the ancillae c_j accordingly. Let us first translate the model into an algorithm that uses two quantum registers of the same size to represent the system and the ancillae in a physical mapping; keeping in mind that we will then shrink the register of the ancillae to a single qubit. The algorithm implements the following steps, graphically represented in Figure 3a:

1. Initialize the system quantum register to the initial state of the dynamics $\left|j_0\right\rangle$ (*i.e.*, apply an X-gate to the qubit representing the initial site of the dynamics in the physical mapping);
2. Apply the gates corresponding to the evolution operator U of the collision model Hamiltonian eq. (II.18) to both the system and environment quantum registers;
3. Reset the environment quantum register;
4. Create a copy of the circuit, so that you have two identical objects: a quantum circuit $\mathcal{A}$ that will be the lead and its copy $\mathcal{B}$ to which the measurement gate will be appended;
5. Add a measurement gate to circuit $\mathcal{B}$, in correspondence with the qubit encoding the target site and read the population of state 1 to obtain the estimator $\pi\left(j,s\Delta t\,|\,j_0\right)$ of $p\left(j,s\Delta t\,|\,j_0\right)$;
6. Discard circuit $\mathcal{B}$ and continue with circuit $\mathcal{A}$;
7. Repeat steps 2-6 for $s \in \left\{0,1,...,S\right\}$;
8. Approximate the transport efficiency as $\eta_j\left(T\right) \approx \sum_{s=0}^{S} p\left(j,s\Delta t\,|\,j_0\right)\Delta t \approx \sum_{s=0}^{S} \pi\left(j,s\Delta t\,|\,j_0\right)\Delta t$.

The evolution operator in step 2 which identifies the evolution gate in Figure 3a needs to be decomposed into elementary (one and two-qubit) gates. A generic unitary operation on n qubits may imply an impractical

exponential scaling of the length of the circuit. However, the physical mapping suggests the implementation of a Trotter-Suzuki decomposition which at the first order in the interaction reads

$$
\begin{aligned}
U &= \exp\left\{-\mathrm{i}\left[\sum_{j=1}^{N}\frac{\varepsilon_j}{2}\sigma_z^j\otimes\mathbb{I}^{\otimes N}+\sum_{\langle j,j'\rangle}\frac{V_{j,j'}}{2}\left(\sigma_x^j\sigma_x^{j'}\otimes\mathbb{I}^{\otimes N}+\sigma_y^j\sigma_y^{j'}\otimes\mathbb{I}^{\otimes N}\right)+\sum_{j=1}^{N}c_j\sigma_z^j\otimes\sigma_x^{a_j}\right]\Delta t\right\} \\
&\approx\left(e^{-\mathrm{i}\frac{\Delta t}{m}\sum_{j=1}^{N}c_j\sigma_z^j\otimes\sigma_x^{a_j}}\,e^{-i\frac{\Delta t}{m}\sum_{\langle j,j'\rangle}\frac{V_{j,j'}}{2}\left(\sigma_x^j\sigma_x^{j'}\otimes\mathbb{I}^{\otimes N}+\sigma_y^j\sigma_y^{j'}\otimes\mathbb{I}^{\otimes N}\right)}\,e^{-i\frac{\Delta t}{m}\sum_{j=1}^{N}\frac{\varepsilon_j}{2}\sigma_z^j\otimes\mathbb{I}^{\otimes N}}\right)^m+O\left(\frac{\Delta t^2}{m^2}\right) \\
&=\left(\prod_{j=1}^{N}e^{-\mathrm{i}\frac{\Delta t}{m}c_j\sigma_z^j\sigma_x^{a_j}}\prod_{\langle j,j'\rangle}e^{-i\frac{\Delta t}{m}\frac{V_{j,j'}}{2}\left(\sigma_x^j\sigma_x^{j'}+\sigma_y^j\sigma_y^{j'}\right)}\prod_{j=1}^{N}e^{-i\frac{\Delta t}{m}\frac{\varepsilon_j}{2}\sigma_z^j}\right)^m+O\left(\frac{\Delta t^2}{m^2}\right)
\end{aligned}
\tag{II.21}
$$

with $m\in\mathbb{N}$. The unitary operator is eventually approximated by the sequential application of one and two-qubit operators, where the approximation improves for large m. We note that this form of the evolution operator is particularly convenient because each site-ancilla interaction occurs as a standalone process and therefore one ancilla qubit which is reset after each interaction suffices to implement the whole environment (as represented in Figure 4). Moreover, as the collision model is shown to converge to the solution of the Lindblad master equation in the limit of small collision time Δt, a suitable choice of the time step can be made to ensure the approximation of eq. (II.21) is already satisfactory for $m=1$. The effects of the time step will be discussed later in section II.4. The application of the Trotter-Suzuki decomposition allows us to further specify the circuit of the evolution gate in step 2 by reducing the ancilla system to a single qubit, as follows:[1]

2a. Apply the $\mathrm{RZ}\left(-\varepsilon_j\Delta t/m\right)$ gates to all the qubits of the system quantum register;

2b. Apply the $\mathrm{RXX}\left(V_{j,j'}\Delta t/m\right)$ and $\mathrm{RYY}\left(V_{j,j'}\Delta t/m\right)$ gates to all the system qubits representing coupled sites of the network;

2c. Apply the $\mathrm{RZX}\left(2c_j\Delta t/m\right)$ to the j-th system qubit and the ancilla;

2d. Reset the state of the ancilla;

2e. Repeat steps 2c-2d for $j\in\{1,2,...,N\}$;

2f. Repeat steps 2a-2e m times.

---

[1] Brief guide to the reported gates: the 1-qubit gate is defined by $\mathrm{RZ}(\theta)=\exp\left(-\mathrm{i}\theta\sigma_z/2\right)$, where σ_z is the Pauli Z-operator, while a 2-qubit gate is, for example, $\mathrm{RXX}(\theta)=\exp\left(-\mathrm{i}\theta\sigma_x^a\sigma_x^b/2\right)$, where the Pauli X-operators act on two different qubits a and b. The other 2-qubit gates RYY and RZX are defined accordingly.

The circuit which realizes the evolution operations by employing a single ancilla qubit is reported in Figure 3b for $m=1$. As mentioned before, the collision algorithm can be applied also when the system is encoded in the quantum computer through an algorithmic mapping. In that case, the most convenient form of the interaction Hamiltonian and the state of the ancilla are different and are discussed in Appendix C.

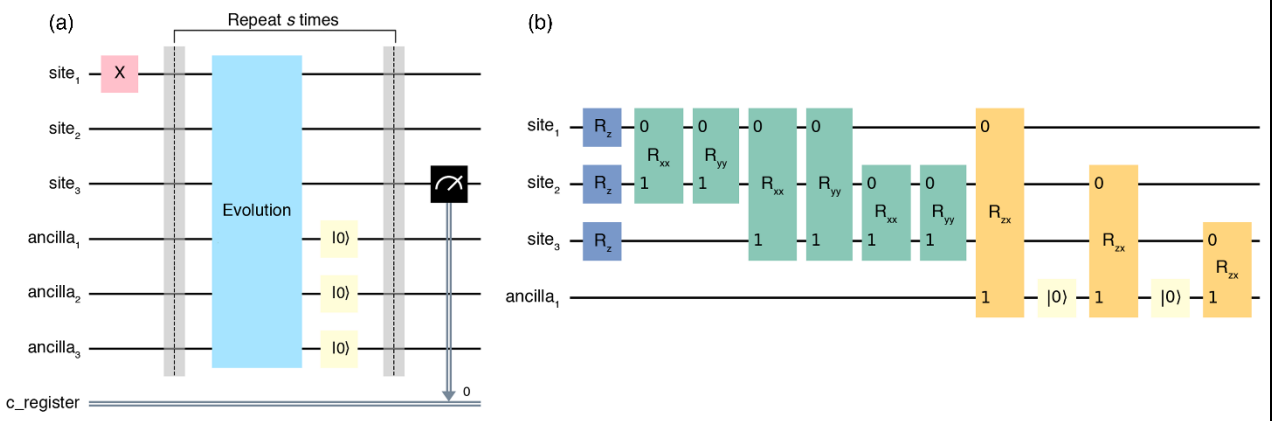

Figure 3. Scheme of the collision algorithm for a system with 3 sites (physical mapping) (a). The initial state is generated with an X-gate on a qubit, site_1 in the example, then the evolution-reset gates propagate the dynamics up to the time $t=s\Delta t$ before measuring the population of the target qubit, site_3. In the limit of a small collision time, the evolution gate can be decomposed into one and two-qubit gates (b) using only one ancilla qubit.

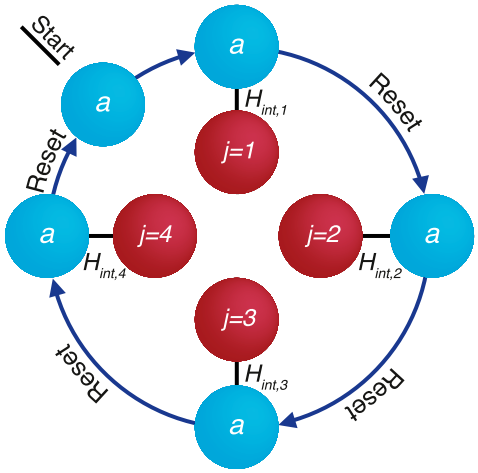

Figure 4. Schematic representation of the sequential interaction between a single ancilla and a four-site network (in the physical mapping) resulting from a first-order Trotter-Suzuki decomposition. The ancilla is reset after each interaction. When the algorithm is formulated in the algorithmic mapping, the reset is followed by reinitialization of the ancilla to a suitable state (see Appendix C).

II.4 Comparative analysis of the two algorithms

We now test both the classical noise algorithm and the collision algorithm by simulating the open system dynamics of the disordered four-site network already introduced in section II.2.1. The implementation of the classical noise algorithm in the algorithmic mapping requires two qubits, which are sufficient to encode the four states of the network. In contrast, the collision algorithm is run on five qubits, four qubits to encode the network in the physical mapping and one ancilla qubit encoding the dephasing environment. By comparing the circuits shown in Figure 1 (classical noise algorithm) and Figure 3 (collision algorithm), first note the differences imposed by the different mappings. The algorithmic mapping requires the preparation of the initial state (initialization of the circuit) and the readout of the population of the target site to be implemented by multiple qubit gates. In the physical mapping, the same operations are performed by simpler single-qubit gates. Starting from site $j_0 = 1$, the population of the target site $j = 3$ is calculated as a function of time and the results are shown in Figure 5 together with the numerical solution of the Lindblad dynamics for the set of parameters specified in the legend. For the classical noise algorithm (Figure 5a) we generated $\Xi = 8000$ trajectories, measuring each one with a single shot for each time point of the dynamics. The results for the collision algorithm (Figure 5b) were obtained with 8000 shots from the same circuit for each time point. For both algorithms, we used a time step $\Delta t = 10^{-2}\,\hbar/V$. The algorithms were executed on the noiseless Qiskit QASM simulator.

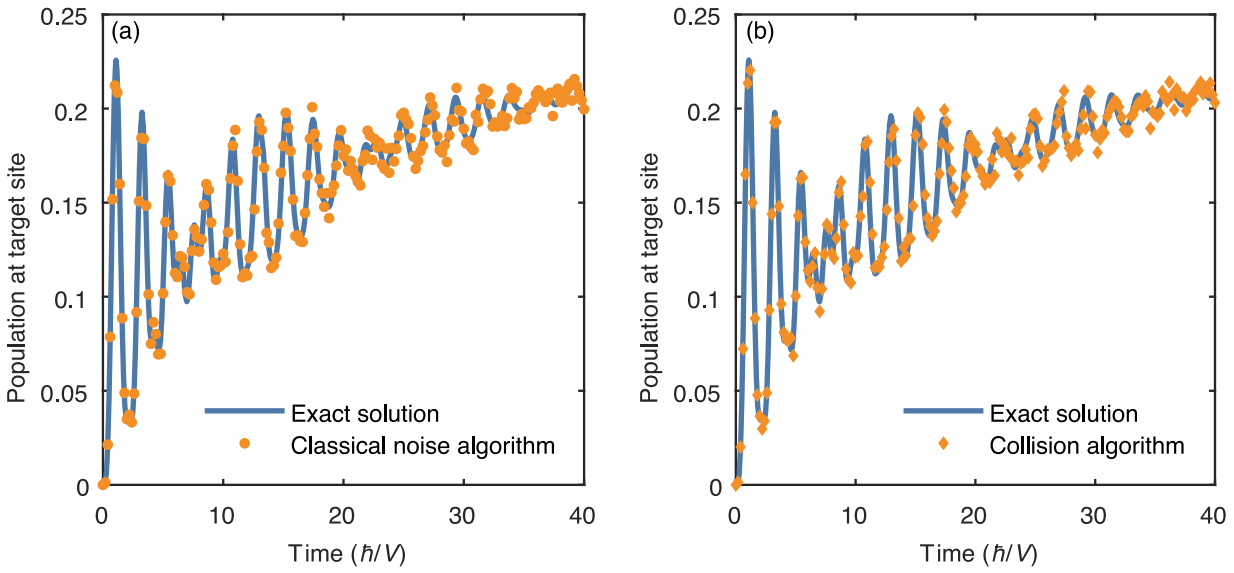

Figure 5. Time evolution of the population at site $j = 3$ on a disordered four-site cyclic network initially populated at site $j_0 = 1$. Exact numerical solution (blue line) refers to the solution of the Lindblad master equation. Results for the classical noise algorithm (a) and collision algorithms (b) are acquired by running the algorithms with the Qiskit QASM simulator. The time step for the algorithmic evolution is $\Delta t = 10^{-2}\,\hbar/V$, and the (scaled) dephasing rate is $\gamma/V = 10^{-1}\hbar^{-1}$.

By simulating the dynamics changing the decoherent environment, we then recover the phenomenology of ENAQT in terms of transport efficiency. Figure 6 reports the transport efficiency $\eta_{j=3}\left(T=40\hbar/V\right)$ obtained from the quantum simulations as a function of the ratio between the decoherence rate and the site coupling, γ/V. Simulations were performed under the same conditions already described in Figure 5, only tuning the fluctuation amplitudes in the classical noise algorithm and the strength of the site-ancilla interaction in the collision algorithm. The results are in very good agreement with the curve obtained by solving the Lindblad master equation (blue line), with errors ranging from 0.027% to 2.7% for the classical noise algorithm and from 0.086% to 1.6% for the collision algorithm. The transport efficiency as a function of the decoherence rate presents a maximum in the intermediate regime of coupling with the environment, which is the hallmark of ENAQT. Low transport efficiency in the weak decoherence limit can be understood as the prevailing of the static disorder, indeed the average population on the target site would be very low in the absence of decoherence. The walker tends to be trapped in the initial site and the efficiency drops also in the strong decoherence limit, although the mechanism is different. In this case, the coherent transfer from site to site (induced by the system Hamiltonian) is suppressed by the fast decay of the site coherences. In the limit of an infinite decoherence rate, the walker would never leave the initial site and the efficiency would be zero, a limit that is often associated with the quantum Zeno paradox [43].

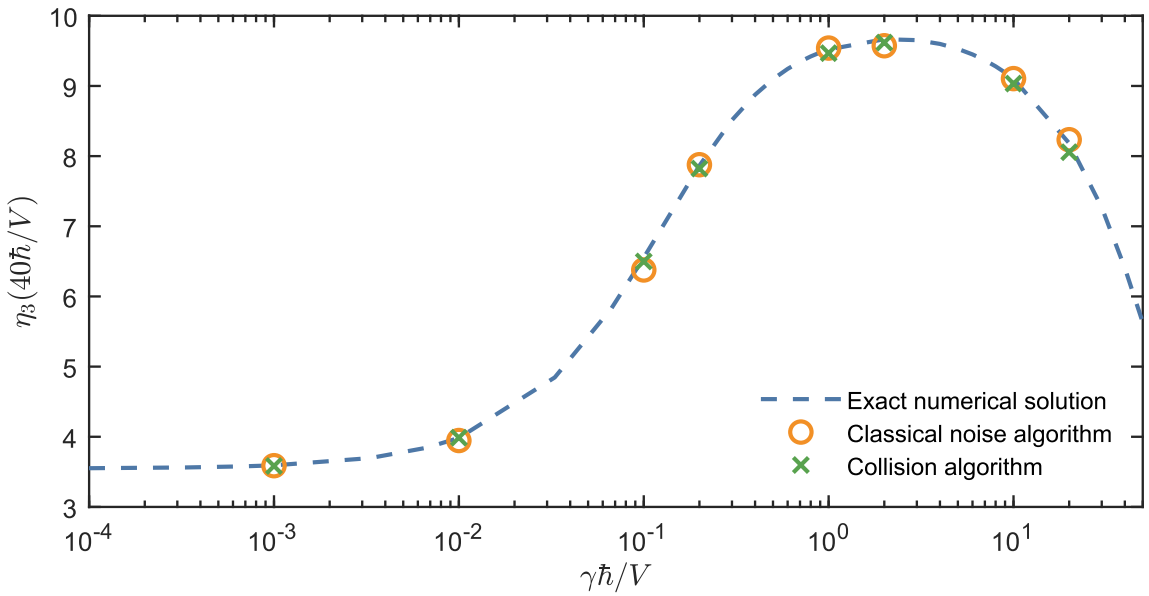

Figure 6. Transport efficiency on a disordered four-site cyclic network as a function of the ratio between the dephasing rate and the site coupling. The excitation is initially localized at site $j_0=1$ and we measure the population at the target site $j=3$ within the fixed reference time $T=40\hbar/V$. The algorithmic time step is $\Delta t=10^{-2}\,\hbar/V$. The results obtained with the classical noise algorithm (circles) and collision algorithms (crosses) using the Qiskit QASM simulator are compared with the expected result obtained by solving directly the master equation (blue dashed line).

The accuracy of the simulations performed with both the algorithms critically depends on the time step Δt chosen to discretize the continuous dynamics. As the time interval decreases, the simulated dynamics approximates the exact solution of the master equation with increasing accuracy (cf. Appendix A and B). On the other hand, the execution time of the circuit grows significantly and a reasonable trade-off between accuracy and simulation time must be found also considering the specific parameters of the simulated system (Hamiltonian spectrum, decoherence rate and simulation length T). For example, it is worth noting that as the dephasing rate increases, smaller time steps are required to maintain the accuracy of the simulated dynamics. In general, a reasonable guess is to use a Δt which is at least one order of magnitude smaller than any characteristic timescale of the system dynamics. Operationally, the obtained result can be validated by checking that the observable of interest remains practically unchanged by halving the time step.

Another parameter to consider is the number of circuit repetitions, which assume a different meaning in the two algorithms. For the classical noise algorithm to reproduce the dynamics of the master equation, the statistics must be accumulated from different trajectories. This means that to accumulate a given number of shots, *e.g.* 8000 shots as used for the dynamics of Figure 5 and Figure 6, one needs to generate the same number of quantum circuits and perform a single-shot measurement on each of them. Each circuit is composed of different gates depending on the specific sequence of random numbers characterizing the noise of the specific trajectory. In contrast, with the collision algorithm, the same circuit is executed and measured 8000 times (*i.e.*, 8000 shots). For both algorithms, the finite number of circuit repetitions introduces a statistical error in the estimation of populations that is expected to decrease with the square root of the inverse of this number. Therefore, more trajectories/shots will lead to a more accurate estimate of the site population. It is also worth noting that once the results of the algorithms have been obtained, if we want to further improve accuracy, it will be sufficient to submit new circuits and mediate the new data with those already collected.
Although this difference in the statistic accumulation of the two algorithms does not affect the analysis of the scaling of the resources presented in the next section, one should consider that the generation of multiple circuits implies a (classical) computational overhead in the *transpilation* procedure, which is the decomposition of the circuit in elementary (1- and 2-qubit) gates.

II.4.1 Scaling of memory and algorithmic resources

In this section, we will analyse how the number of qubits and gates required by the algorithms scale with the size of the simulated system N when using the algorithmic and the physical mappings. Since actually the number of gates strictly depends on the specific machine one is using and which gates can physically

implement, the established procedure is to count the number of 2-qubit operations (*e.g.*, the CNOT gates)[2] required by the circuit. The results are summarized in Table 1.

As already reported above, the algorithmic scaling implies an exponential advantage in terms of memory resources as the number of qubits required to encode the system scales only logarithmically with its size, $n = \lceil \log_2 N \rceil$. However, this mapping complicates the gate decomposition of the simulation procedure. The classical noise algorithm in the formulation of an algorithmic mapping consists of two operations that potentially act on the whole quantum register of size n: the initialization and the evolution (see Figure 1). If the initial state is completely localized on one site, the initialization process translates into a series of X-gates, whose impact on the scaling analysis is negligible. This is not the case for the evolution gate. Consisting in a unitary transformation acting on $\lceil \log_2 N \rceil$ qubits, in the general case it requires a number of CNOT gates that scales exponentially with the number of qubits of the register, and therefore quadratically with the size of the network: $\mathcal{O}\left(4^{\lceil \log_2 N \rceil}\right) \approx \mathcal{O}\left(N^2\right)$. Since the dynamics is obtained by a series of different evolution gates (because the system is subject to random fluctuations), each gate requires a dedicated decomposition. Although this does not compromise quadratic scaling, it involves a classical computational effort in transpilation which adds up to the effort already required to simulate different trajectories. This overhead can be slightly mitigated by adopting a suitably small time step for the dynamics. Indeed, in the limit of a vanishing time step, we can assume

$$\lim_{\Delta t \to 0^+} e^{-\mathrm{i}\left(H\Delta t + H_{\mathrm{fluc},s}\sqrt{\Delta t}\right)} \approx e^{-\mathrm{i}H\Delta t} e^{-\mathrm{i}H_{\mathrm{fluc},s}\sqrt{\Delta t}} . \tag{II.22}$$

The first term on the right-hand side is common for the evolution at each time step and for each trajectory and therefore it can be decomposed once for all. The second term, which changes in each evolution operator, is a diagonal unitary, therefore admitting a more performant gate decomposition scaling linearly with the size of the problem, which is $\mathcal{O}\left(2^{\lceil \log_2 N \rceil}\right) \approx \mathcal{O}\left(N\right)$ gates. Overall, the leading term in the scaling remains quadratic. The analysis of the collision algorithm in the algorithmic mapping is reported in Appendix C. It turns out that

[2] The CNOT (which is read *controlled-not*) gate is the most popular 2-qubit operation. The first qubit takes the name of the control, while the second is the target qubit. Its effect is the following: if the state of the control is $|0\rangle$ then nothing happens, if the state of the control is $|1\rangle$ then an X gate is applied to the target, which corresponds to the NOT gate for classical computing. For example, it transforms a state $a|00\rangle + b|10\rangle$ into $a|00\rangle + b|11\rangle$. Since 2-qubit gates take more time and introduce more errors in the computation than 1-qubit gates, they are used as a metric for circuit complexity.

the depth of the circuit grows also quadratically with the size of the system, while it requires $\lceil \log_2 N \rceil$ qubits and an extra ancilla qubit to represent the environment.

The physical mapping, on the other hand, is not memory efficient as it requires a number of qubits that grows linearly with the size of the network, that is N for the classical noise algorithm and $N+1$ for the collision algorithm. On the other hand, it greatly simplifies the gate decomposition procedure. As we have shown in section II.3, it is possible to perform the initialization of the circuit by the application of a single X-gate, while the evolution gate, which is repeated during the algorithm, can be easily reduced to 1- and 2-qubits gates. In this case, the interaction Hamiltonian between adjacent sites gives the leading term for the scaling of the algorithm: in a network where all sites are coupled, $\mathcal{O}\left(N^2\right)$ two-qubit gates are required to account for the unitary evolution. When the connectivity is restricted (as in tight-binding graphs), the resulting scaling is usually sub-quadratic (*e.g.*, linear for a cyclic topology).
Although the scaling with the size of the network results similar for the two mappings, the classical effort required by the algorithmic mapping for gate decomposition partially contrasts the stunning advantage in terms of memory. This "classical" overhead is further amplified in the classical noise algorithm by the need of creating a different circuit for each time step of each trajectory.

Let us now compare the scaling of the algorithms discussed above with the other quantum algorithms discussed in literature for the simulation of environment-assisted quantum transport. We find a slightly more favourable scaling than the algorithmic strategy proposed by Gupta and Chandrashekar in ref. [44], which provides a scaling of $\mathcal{O}\left(N^2 \log_2 N\right)$ by employing an algorithmic mapping with some extra ancillae. On the other hand, the model of ref. [44] allows the introduction of the effect of the temperature at the cost of working in the exciton basis, thus requiring a preparatory step involving the diagonalization of the Hamiltonian. The algorithm discussed by Hu *et al.* in ref. [45], which is based on a dilation approach, is characterized by a remarkable sub-polynomial scaling of $\mathcal{O}\left(\log_2^2 N\right)$. However, the authors also discuss an exponential scaling with the number of time steps of the dynamics which can be probably reduced by circuit optimization in the simulations of specific systems.

Table 1. Comparative analysis of the scaling of the memory resources and circuit depth for the classical noise and the collision algorithm with the size N of the simulated system in the two different mappings. The first term refers to the number of qubits needed for the simulation while the second term refers to the gate count.

	Classical noise algorithm	Collision algorithm
Physical mapping	N, $\mathcal{O}\left(N^2\right)$	$N+1$, $\mathcal{O}\left(N^2\right)$
Algorithmic mapping	$\lceil \log_2 N \rceil$, $\mathcal{O}\left(N^2\right)$	$\lceil \log_2 N \rceil + 1$, $\mathcal{O}\left(N^2\right)$

II.5 Algorithmic quantum trajectories

Unravelling the master equation for the system density matrix amounts to considering an ensemble of pure states whose average gives the desired dynamics. Each system, described by a wavefunction, evolves stochastically in time defining a so-called quantum trajectory [46]. Unravelling approaches originate from the quantum optics community [47,48], when technological advancements allowed for monitoring individual quantum systems. Quantum trajectories were proved to be tightly connected with the measurement protocol used to monitor quantum states [49] providing an effective framework to describe different detection schemes, as photon-counting and homodyne detection, for which ensemble descriptions based on the density matrix does not offer a straightforward interpretation. Subsequently, quantum trajectories have been used in many other fields as a numerical technique to solve the open system dynamics with the number of variables being linear with the dimension of the Hilbert space rather than quadratic as the dimension of the density matrix [50–53]. In this section, we want to characterize the *algorithmic quantum trajectories*, which are quantum trajectories generated by a given algorithm in a quantum computer as the result of the different operations on the computer state, both in terms of gates (classical noise algorithm) and measurements on the ancillae (collision algorithm).

The very working principle of digital quantum simulations requires the accumulation of measurement statistics to evaluate the expectation value of interest, which for our purpose is the population of the target site at different times, *i.e.*, $p(j,t\,|\,j_0)=\langle j|\rho(t)|j\rangle$. This implies that the quantum circuits must be executed many times and the simulated open system dynamics can be naturally understood as the average of different realizations of underlying stochastic dynamics. This observation implies that different quantum algorithms realize different unravellings of the master equation.

The classical noise algorithm is based on an explicit average over trajectories which are generated by the stochastic terms in the Hamiltonian which are mapped into the gates of the quantum circuit. When the algorithmic time step is small enough each trajectory is a good approximation of a stochastic Schrödinger equation where the stochastic part is given by a Wiener increment [25]

$$d|\psi(t)\rangle=\left(-\mathrm{i}H-\frac{1}{2}\sum_{j=1}^{N}\gamma_j L_j^{\dagger}L_j\right)|\psi(t)\rangle dt-\mathrm{i}\sum_{j=1}^{N}\sqrt{\gamma_j}L_j|\psi(t)\rangle dW_j(t),$$

where $L_j=|j\rangle\langle j|$, $\overline{dW_j(t)}=0$ and $\overline{dW_j(t)^2}=dt$. The stochastic differential introduces small but frequent deviations from the evolution of the isolated system ruled by the average Hamiltonian, resulting in the noisy trajectories already shown in Figure 2.

Trajectories obtained by the collision model algorithm are qualitatively different. In this case, the stochastic nature of the evolution can be more easily understood as resulting from the quantum probabilities for the outcomes of measurements performed on the ancilla environment. Indeed, at each time step after the interaction

with the system, the state of the ancilla is reset. The reset gate acts as a measurement of the ancilla qubit and its subsequent reinitialization to state $|0_a\rangle$. One thus goes from an entangled system-ancilla state $|\psi\rangle = c_0|\psi_{0,\mathcal{S}}\rangle\otimes|0_a\rangle + c_1|\psi_{1,\mathcal{S}}\rangle\otimes|1_a\rangle$ to a product state that is $|\psi_{0,\mathcal{S}}\rangle\otimes|0_a\rangle$ with probability $|c_0|^2$ or $|\psi_{1,\mathcal{S}}\rangle\otimes|0_a\rangle$ with probability $|c_1|^2$. Performing this operation multiple times reproduces the effect of tracing out the ancilla's degrees of freedom, resulting in a statistical density matrix for the system $\rho_{\mathcal{S}} = |c_0|^2|\psi_{0,\mathcal{S}}\rangle\langle\psi_{0,\mathcal{S}}| + |c_1|^2|\psi_{1,\mathcal{S}}\rangle\langle\psi_{1,\mathcal{S}}|$. However, a single run of the circuit of the collision algorithm realizes a single quantum trajectory. The specific character of the trajectory depends on the form of the interaction between the system and the ancilla environment. Let us look closer into the algorithm steps discussed in section II.3 and reported in Figure 3: suppose we have initialized the state and executed the first block of RZ, RXX and RYY in the system register. After this evolution block, the state of the quantum register will be generically $|\psi\rangle = |\psi_{\mathcal{S}}\rangle\otimes|0_a\rangle$. The interaction between the first qubit of the system, $j=1$, and the ancilla is through an RZX gate, which is

$$\exp\left(-\mathrm{i}c_1\sigma_z^1\otimes\sigma_x^a\Delta t\right) = \cos(c_1\Delta t)\mathbb{I}^1\otimes\mathbb{I}^a - \mathrm{i}\sin(c_1\Delta t)\sigma_z^1\otimes\sigma_x^a . \tag{II.23}$$

By applying it to the state $|\psi\rangle$ we explicitly get

$$\begin{aligned}|\psi'\rangle &= \cos(c_1\Delta t)\mathbb{I}^1\otimes\mathbb{I}^a|\psi\rangle - \mathrm{i}\sin(c_1\Delta t)\sigma_z^1\otimes\sigma_x^a|\psi\rangle \\ &= \cos(c_1\Delta t)|\psi_{\mathcal{S}}\rangle\otimes|0_a\rangle - \mathrm{i}\sin(c_1\Delta t)\sigma_z^1|\psi_{\mathcal{S}}\rangle\otimes\sigma_x^a|0_a\rangle \\ &= \cos(c_1\Delta t)|\psi_{\mathcal{S}}\rangle\otimes|0_a\rangle - \mathrm{i}\sin(c_1\Delta t)\sigma_z^1|\psi_{\mathcal{S}}\rangle\otimes|1_a\rangle\end{aligned} \tag{II.24}$$

The next step of the algorithm is the reset, *i.e.*, measure and reinitialization of the ancilla. Since the ancilla and the system are in an entangled state, the measurement of the ancilla affects the state of the system. In particular, if state 0 is measured, then the system will be in state $|\psi_{\mathcal{S}}\rangle$, while if state 1 is measured the system will be in $\sigma_z^1|\psi_{\mathcal{S}}\rangle$. These states correspond respectively to an *avoided* collision, in which the system remains in the same state, or an *occurred* collision, in which the phase of the interacting qubit (site) is flipped. In practice, the operation "interaction and reset" acts on the system-qubit as a probabilistic Z-gate which reverses the phase of the system-qubit with probability $\left|\sin\left(c_j\Delta t\right)\right|^2$. Notice that for $\Delta t \ll 1$, which is a condition to approximate the Lindblad master equation, the collision event is unlikely and most of the reset gates have the only effect of erasing the correlation created between the system and the ancilla qubit. Because the result of the measurement on the ancilla is stochastic at each repetition of the circuit, we devise a modified algorithm that replicates a single quantum trajectory. To do this, we simply save on a separate classical register the sequence of the outcomes obtained from the measurement of the ancilla. This is a string, let us say $\mathbf{b}$, of NSm bits, where N is the number of sites, S is the number of time steps and m is the number of Trotter steps. Once the history of the outcomes is accessible, the same trajectory can be generated multiple times by using only the quantum

register encoding the system. In the execution circuit of Figure 3b, the 2-qubit gates involving system and ancilla are then replaced with the I-gate (identity-gate), if the corresponding bit in string **b** is 0, and with the Z-gate if the bit is 1; this is shown in Figure 7.

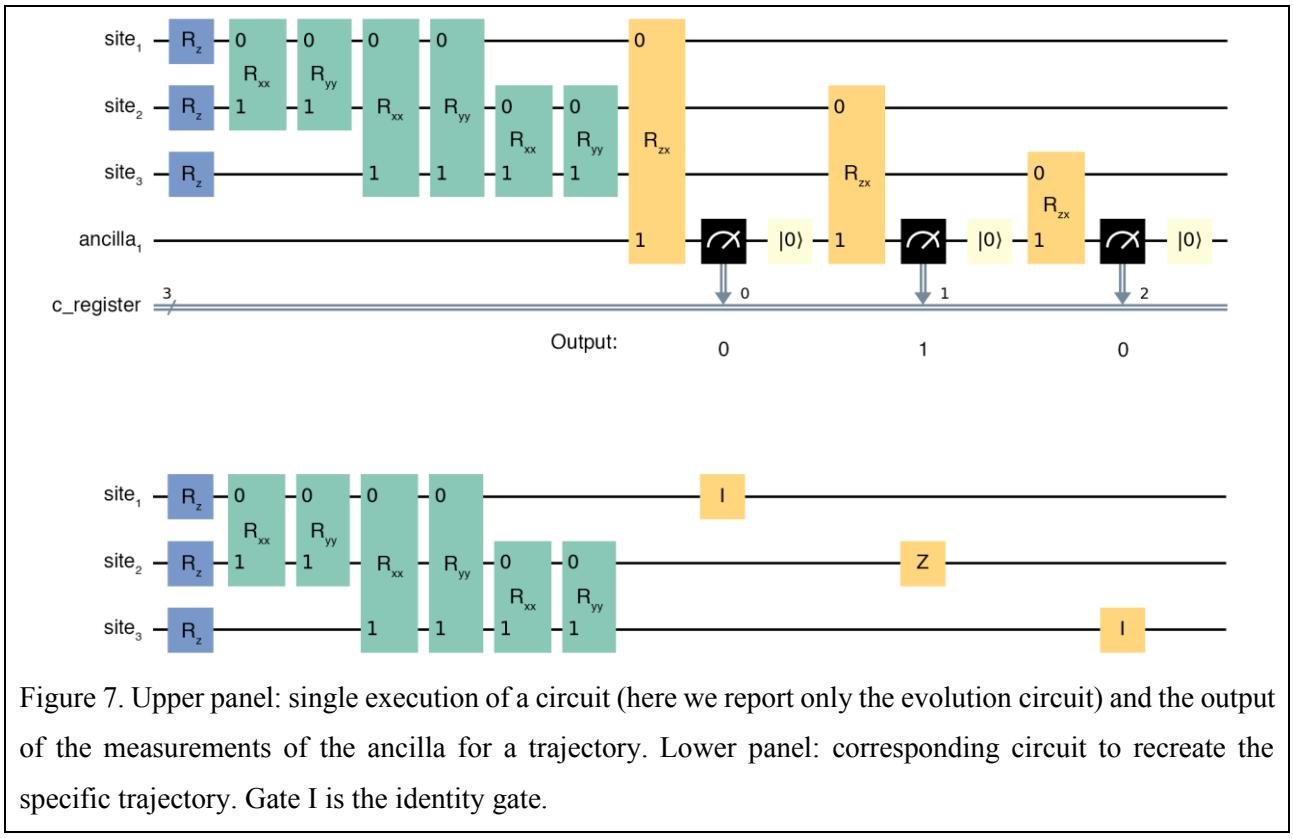

Figure 7. Upper panel: single execution of a circuit (here we report only the evolution circuit) and the output of the measurements of the ancilla for a trajectory. Lower panel: corresponding circuit to recreate the specific trajectory. Gate I is the identity gate.

Figure 8a shows a single trajectory (blue line) generated by the procedure described above together with the dynamics of the isolated system (green line). Because the probability of the system-ancilla collision is low, the two dynamics coincide for the initial time interval until an effective collision happens. The waiting time until the first effective collision has naturally a random character as we can see by looking at the swarm of trajectories reported in Figure 8b. Initially, the dynamics of the isolated system is clearly reproduced by the overlay of multiple trajectories (blue lines in transparency) and gradually fades as the probability to have observed an effective collision increases with time. The solid blue line represents the dynamics of the open system obtained as an average of 200 trajectories while the orange dotted line is the solution of the corresponding master equation. By comparing the trajectories of the collision algorithm in Figure 8 with those of the classical noise algorithm shown in Figure 2, it is evident that they generate a different distribution of the observable despite providing the same average value. Other algorithms can be devised based on a different unravelling of the master equation, for example by realizing the trajectories obtained with the traditional *quantum jump* approach to open system dynamics as used by Govia *et al.* in ref. [54].

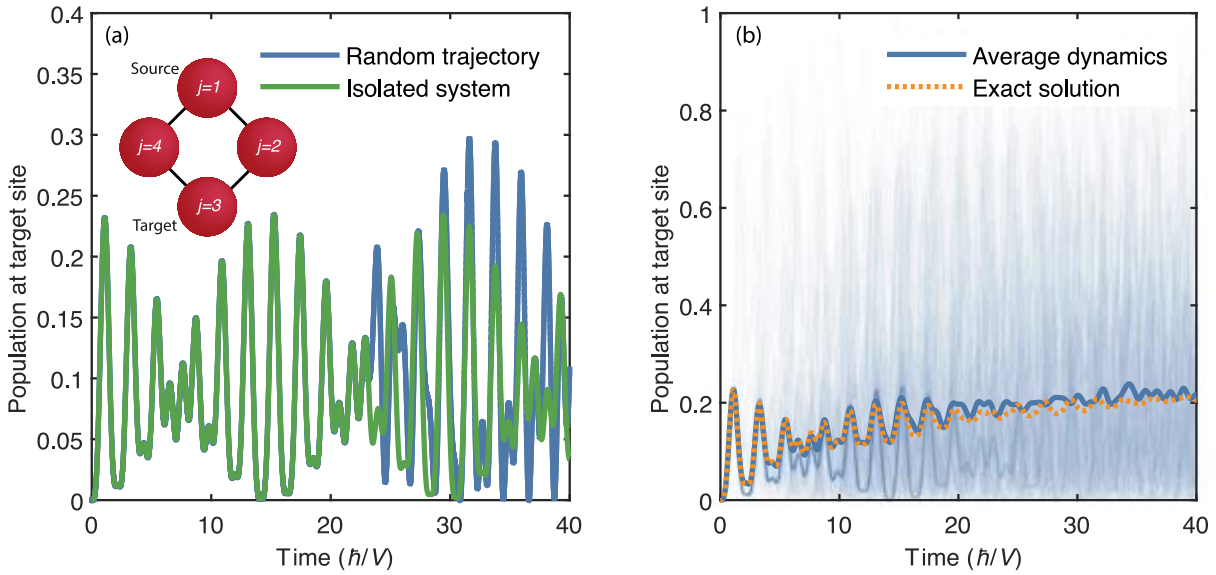

Figure 8. Time evolution of the population at site $j=3$ on a disordered four-site cyclic network initially populated at site $j_0=1$. The dynamics of a single trajectory is obtained with the collision algorithm (blue) and it is compared with the dynamics of the isolated system (green) in panel (a). A swarm of $\Xi=200$ different trajectories (blue lines in transparency) is reported in panel (b). Their overlay allows observing the shade of the dynamics of the isolated system fading as simulation time increases. The average of the trajectories (solid blue) approximates the open system dynamics obtained by the solution of the Lindblad master equation (orange). All the trajectories are obtained by running the algorithms in the Qiskit Statevector simulator, the Statevector mode corresponds to a single execution of the circuit and returns the statevector of the quantum register. The time step for the algorithmic evolution is $\Delta t=10^{-2}\,\hbar/V$, and the (scaled) dephasing rate is $\gamma/V=10^{-1}\hbar^{-1}$.

II.6 Conclusions

Simulating quantum dynamics in molecular networks necessarily requires taking into account the role of the environment in an effective way as it induces qualitatively different phenomena as the environment-assisted quantum transport. We have analysed in detail two different quantum algorithms for the simulation of dephasing-assisted quantum transport in digital quantum computers, focusing on the solution of the Lindblad master equation where site decoherence is included in the dissipator. The first algorithm is based on an explicit average over dynamics obtained by solving the Schrödinger equation with a stochastic Hamiltonian while the second algorithm is based on a collision scheme. Both algorithms can be applied with a physical mapping of the network, where each site is encoded in a qubit, and with an algorithmic mapping in which each site is encoded in an element of the computational basis. The circuit complexity is the same in the two cases and for both algorithms, and it scales quadratically with the number of quantum sites in the network. The two encodings provide different advantages: the algorithmic mapping allows an exponential saving of memory

resources as it requires only $\lceil \log_2 N \rceil$ qubits to represent an N-site network. On the other hand, it entails a larger computational effort for the gate decomposition of the Hamiltonian part of the dynamics. The physical mapping does not bring a memory advantage for simulations confined to the single exciton manifold, but it can straightforwardly accommodate more excitons unleashing the quantum advantage of simulating many-body dynamics.

We test the algorithms on the Qiskit QASM simulator by calculating the dynamics and the transfer efficiency in a disordered four-site ring with different strengths of the environment-induced site decoherence. Our simulations find that an intermediate level of decoherence enhances the transport efficiency which is the hallmark of environment-assisted quantum transport. We have further analysed the two algorithms in the framework of quantum trajectories and found that quantum computers are versatile testbeds for unravelling-based implementations. In fact, while the approaches based on quantum trajectories in classical computers imply the overhead of generating a statistical sample which is not necessary in principle, quantum trajectories appear a natural tool to analyse quantum dynamical simulations because of the inherent necessity of repeating the circuit to extract expectation values.

We should point out that the specific type of open system dynamics considered in this contribution is a simple instance of the possible effect of the environment, only considering decoherence between different sites. Because of its structure, the site-dephasing master equation does not describe the effects of the temperature (indeed it corresponds to a high-temperature limit) and being in the Lindblad form, it cannot describe environments beyond the Markovian assumption underlying the semigroup theory. However, both the algorithms have been designed to include an effective representation of the environment, in the form of a stochastic process (classical noise algorithm) or additional degrees of freedom (collision algorithm). This is because we aim at algorithmic strategies which allow building different environments to simulate their effects on the dynamics of a target system. For example, in the next Chapter, we will expand the current algorithms to coloured noise environments, for which an equation for the average dynamics is not analytically available in general. Moreover, in Chapter V the collision scheme allows us to include temperature effects [55], by designing the states of the ancillae and the interaction with the system's subunits [33,56]. Therefore, this work serves as a benchmark of these algorithmic strategies by demonstrating their reliability in the simulation of a well-defined open-system dynamics whose master equation is known.

II.7 Appendix A

We show that the classical noise algorithm approximates on average the site-dephasing master equation. The state of the system at time $s\Delta t$ is obtained by applying the evolution operator $U_{\xi,s}\left(s\Delta t,(s-1)\Delta t\right)=\exp\left(-\mathrm{i}H\Delta t-\mathrm{i}H_{\mathrm{fluc},\xi,s}\sqrt{\Delta t}\right)$ to the state at $(s-1)\Delta t$,

$$\left|\psi(t+\Delta t)\right\rangle\left\langle\psi(t+\Delta t)\right|=U_{\xi,s}\left(s\Delta t,(s-1)\Delta t\right)\left|\psi(t)\right\rangle\left\langle\psi(t)\right|U_{\xi,s}^{\dagger}\left(s\Delta t,(s-1)\Delta t\right), \tag{II.25}$$

where $t+\Delta t = s\Delta t$ for simplicity. By assuming the integration step Δt to be small enough, we can expand the evolution operator to the first order in Δt,

$$U_{\xi,s}\left(s\Delta t,(s-1)\Delta t\right) \approx \mathbb{I}^{\otimes\lceil \log_2 N\rceil} - \mathrm{i}H\Delta t - \mathrm{i}H_{\mathrm{fluc},\xi,s}\sqrt{\Delta t} - \frac{1}{2}H^2_{\mathrm{fluc},\xi,s}\Delta t\,. \tag{II.26}$$

Thus, eq. (II.25) can be written as

$$\begin{aligned}\left|\psi(t+\Delta t)\right\rangle\!\left\langle\psi(t+\Delta t)\right| \approx & \left|\psi(t)\right\rangle\!\left\langle\psi(t)\right| + \\ & -\mathrm{i}\left[H,\left|\psi(t)\right\rangle\!\left\langle\psi(t)\right|\right]\Delta t - \mathrm{i}\left[H_{\mathrm{fluc},\xi,s},\left|\psi(t)\right\rangle\!\left\langle\psi(t)\right|\right]\sqrt{\Delta t} + \\ & +H_{\mathrm{fluc},\xi,s}\left|\psi(t)\right\rangle\!\left\langle\psi(t)\right|H_{\mathrm{fluc},\xi,s}\Delta t - \frac{1}{2}\left[H^2_{\mathrm{fluc},\xi,s},\left|\psi(t)\right\rangle\!\left\langle\psi(t)\right|\right]_+\Delta t\end{aligned} \tag{II.27}$$

where we have used $H_{\mathrm{fluc},\xi,s} = H^{\dagger}_{\mathrm{fluc},\xi,s}$ to simplify the notation.

Recalling that $H_{\mathrm{fluc},\xi,s} = \sum_{j=1}^{N}\delta\varepsilon_{j,\xi,s}\left|j\right\rangle\!\left\langle j\right| = \sum_{j=1}^{N}\delta\varepsilon_{j,\xi,s}L_j$ and $\rho(t) = \overline{\left|\psi(t)\right\rangle\!\left\langle\psi(t)\right|}$, by taking the average over the realizations of the stochastic process, one obtains

$$\begin{aligned}\rho(t+\Delta t) \approx & \rho(t) + \\ & -\mathrm{i}\left[H,\rho(t)\right]\Delta t - \mathrm{i}\sum_{j=1}^{N}\left[L_j,\overline{\delta\varepsilon_{j,\xi,s}\left|\psi(t)\right\rangle\!\left\langle\psi(t)\right|}\right]\sqrt{\Delta t} + \\ & +\sum_{j=1}^{N}L_j\,\overline{\delta\varepsilon^2_{j,\xi,s}\left|\psi(t)\right\rangle\!\left\langle\psi(t)\right|}L_j\Delta t - \frac{1}{2}\sum_{j=1}^{N}\left[L_jL_j,\overline{\delta\varepsilon^2_{j,\xi,s}\left|\psi(t)\right\rangle\!\left\langle\psi(t)\right|}\right]_+\Delta t\end{aligned} \tag{II.28}$$

Because of the statistical properties of the white noise, the following relations hold

$$\begin{aligned}\overline{\delta\varepsilon_{j,\xi,s}\left|\psi(t)\right\rangle\!\left\langle\psi(t)\right|} &= \overline{\delta\varepsilon_{j,\xi,s}}\,\rho(t) = 0\,,\\ \overline{\delta\varepsilon^2_{j,\xi,s}\left|\psi(t)\right\rangle\!\left\langle\psi(t)\right|} &= \overline{\delta\varepsilon^2_{j,\xi,s}}\,\rho(t) = \gamma_j\rho(t)\,.\end{aligned}$$

Thus, eq. (II.28) reduces to the following difference quotient

$$\frac{\rho(t+\Delta t)-\rho(t)}{\Delta t} \approx -\mathrm{i}\left[H,\rho(t)\right] + \sum_{j=1}^{N}\gamma_j\left(L_j\rho(t)L_j - \frac{1}{2}\left[L_jL_j,\rho(t)\right]_+\right), \tag{II.29}$$

that gives the master equation (II.5) in the limit of $\Delta t \to 0^+$.

II.8 Appendix B

In its most common microscopic derivation, the Lindblad dynamics of an open quantum system is generated by a weak interaction with a fast thermal environment [14]. The environment is assumed to be large enough so that the thermal state is not affected by the interaction with the system and its relaxation time is assumed to be shorter than the typical evolution of the system due to the interaction with the bath. All microscopic

derivations of Markovian master equations implicitly set a characteristic time under which the needed assumptions are violated. As such quantum Markovian dynamics imply a *coarse-graining* of time. To derive the master equation from a collision scheme, we identify the time scale of the coarse-graining Δt with the collision time. In the limit of small Δt, we can expand the time evolution operator $U = \exp\left(-iH_{CM}\delta\tau\right)$ as

$$U \approx \mathbb{I}^{\otimes N} \otimes \mathbb{I}^{\otimes N} - \mathrm{i}H_{\mathrm{ex}} \otimes \mathbb{I}^{\otimes N}\Delta t - \mathrm{i}H_{\mathrm{int}}\Delta t - \frac{1}{2}H_{\mathrm{int}}^2\Delta t^2 . \tag{II.30}$$

The need of expanding the interaction Hamiltonian to second-order will become clear in the following. By substituting the above expression into the dynamical map in eq. (II.19) and keeping linear terms in $H_{\mathrm{ex}} \otimes \mathbb{I}^{\otimes N}$ and quadratic terms in H_{int}, one gets

$$\begin{aligned}\rho_{\mathcal{S}}\left(t+\Delta t\right) \approx \rho_{\mathcal{S}}\left(t\right) + \\ -\mathrm{i}\,\mathrm{Tr}_a\left\{\left[H_{\mathrm{ex}} \otimes \mathbb{I}^{\otimes N}, \rho_{\mathcal{S}}\left(t\right) \otimes \rho_a\right]\right\}\Delta t - \mathrm{i}\,\mathrm{Tr}_a\left\{\left[H_{\mathrm{int}}, \rho_{\mathcal{S}}\left(t\right) \otimes \rho_a\right]\right\}\Delta t + \\ + \mathrm{Tr}_a\left\{H_{\mathrm{int}}\left(\rho_{\mathcal{S}}\left(t\right) \otimes \rho_a\right)H_{\mathrm{int}}^{\dagger}\right\}\Delta t^2 - \frac{1}{2}\mathrm{Tr}_a\left\{\left[H_{\mathrm{int}}^2, \rho_{\mathcal{S}}\left(t\right) \otimes \rho_a\right]_+\right\}\Delta t^2\end{aligned} \tag{II.31}$$

By assuming that the density matrix of the ancilla subspace is diagonal in the computational basis, the following equalities hold

$$\begin{aligned}\mathrm{Tr}_a\left\{\sigma_x^{a_j}\rho_a\right\} = 0 \\ \mathrm{Tr}_a\left\{\sigma_x^{a_j}\sigma_x^{a_{j'}}\rho_a\right\} = \begin{cases}1 & j = j' \\ 0 & \text{otherwise}\end{cases}\end{aligned} \tag{II.32}$$

and eq. (II.31) can be written as

$$\rho_{\mathcal{S}}\left(t+\Delta t\right) \approx \rho_{\mathcal{S}}\left(t\right) - \mathrm{i}\left[H_{\mathrm{ex}}, \rho_{\mathcal{S}}\left(t\right)\right]\Delta t + \sum_{j=1}^{N} c_j^2\Delta t^2\left(\sigma_z^j\rho_{\mathcal{S}}\left(t\right)\sigma_z^j - \rho_{\mathcal{S}}\left(t\right)\right), \tag{II.33}$$

By transforming into a difference quotient during the collision time one obtains

$$\frac{\rho_{\mathcal{S}}\left(t+\Delta t\right) - \rho_{\mathcal{S}}\left(t\right)}{\Delta t} \approx -\mathrm{i}\left[H_{\mathrm{ex}}, \rho_{\mathcal{S}}\left(t\right)\right] + \sum_{j=1}^{N} c_j^2\Delta t\left(\sigma_z^j\rho_{\mathcal{S}}\left(t\right)\sigma_z^j - \rho_{\mathcal{S}}\left(t\right)\right). \tag{II.34}$$

To recover the master equation, the next step is to apply the limit $\Delta t \to 0^+$. However, if the coupling constants c_j are assumed independent of Δt, the summation on the right-hand side of eq. (II.34) vanishes in the limit. It is, therefore, appropriate to define the coupling terms as $c_j^2 = \Gamma_j/\Delta t$, where Γ_j are constants. In this way, eq. (II.9) is obtained. Note that, with this definition of c_j, the second-order expansion in eq. (II.30) corresponds to a first-order term in Δt.

II.9 Appendix C

In this Appendix, we briefly discuss the collision algorithm for an algorithmic mapping. The algorithmic mapping should be applied only to the quantum register of the system since it is not advantageous in the single ancilla register. In this framework, the Hamiltonian of the system is the same as in eq. (II.1), while for the interaction of each site j with the ancilla, the form $c_j |j\rangle\langle j| \otimes \sigma_z^a$ can be assumed, where the first operator acts on the site of the system and the second on the ancilla. Note that this form of interaction differs from what we used for the algorithm in the physical mapping, eq. (II.18), because of the σ_z on the ancilla qubit. This form is convenient because the operator associated with the site-ancilla interaction Hamiltonian becomes diagonal on the computational basis, and thus it can be decomposed into a smaller number of gates (see section II.4.1). However, to simulate the site-dephasing master equation with this form of interaction, the ancilla system must be prepared in the state $\rho_a = \left(|0\rangle\langle 0| + |1\rangle\langle 1|\right)/2$. Although this mixed state cannot be directly implemented on a quantum computer, the same effect is obtained by randomly initializing the ancilla to state $|0\rangle$ or $|1\rangle$ with probability $1/2$.

The algorithm can be divided into two main parts: the initialization of the system which is typical for the algorithmic mapping, and the dynamics through evolution gates. Assuming a small collision time Δt, each evolution gate can be factorized into an evolution acting only on the system, $\exp(-\mathrm{i}H\Delta t)$, which is decomposed into $\mathcal{O}\left(4^{\lceil \log_2 N \rceil}\right) \approx \mathcal{O}\left(N^2\right)$ CNOT gates (see section II.4.1), and N interactions between the sites and the ancilla, driven by the gate associated with operator $\exp\left(-\mathrm{i}c_j |j\rangle\langle j| \otimes \sigma_z^a \Delta t\right)$, each one followed by the reset and reinitialization of the state of the ancilla. The (diagonal) evolution operator of the interaction can be decomposed into $\mathcal{O}(N)$ CNOT gates. The number of CNOT gates thus scales as $\mathcal{O}\left(N^2\right)$ when all the interactions are taken into account. The collision algorithm in the algorithmic mapping thus scales logarithmically in the number of qubits required for the implementation of the system $\lceil \log_2 N \rceil$ with the addition of one ancilla qubit, and it scales quadratically with respect to the number of CNOT gates.

II.10 References

[1] P. Rebentrost, M. Mohseni, I. Kassal, S. Lloyd, A. Aspuru-Guzik, Environment-assisted quantum transport, New J. Phys. 11 (2009) 033003. https://doi.org/10.1088/1367-2630/11/3/033003.

[2] H. Haken, G. Strobl, An exactly solvable model for coherent and incoherent exciton motion, Zeitschrift Für Phys. A Hadron. Nucl. 262 (1973) 135–148. https://doi.org/10.1007/BF01399723.

[3] M. Ziman, P. Štelmachovič, V. Bužek, Description of Quantum Dynamics of Open Systems Based on Collision-Like Models, Open Syst. Inf. Dyn. 12 (2005) 81–91. https://doi.org/10.1007/s11080-005-0488-0.

[4] G. Aleksandrowicz, T. Alexander, P. Barkoutsos, L. Bello, Y. Ben-Haim, D. Bucher, F.J. Cabrera-Hernández, J. Carballo-Franquis, A. Chen, C.-F. Chen, J.M. Chow, A.D. Córcoles-Gonzales, A.J. Cross, A. Cross, J. Cruz-Benito, C. Culver, S.D.L.P. González, E.D. La Torre, D. Ding, E. Dumitrescu, I. Duran, P. Eendebak, M. Everitt, I.F. Sertage, A. Frisch, A. Fuhrer, J. Gambetta, B.G. Gago, J. Gomez-Mosquera, D. Greenberg, I. Hamamura, V. Havlicek, J. Hellmers, Ł. Herok, H. Horii, S. Hu, T. Imamichi, T. Itoko, A. Javadi-Abhari, N. Kanazawa, A.

Karazeev, K. Krsulich, P. Liu, Y. Luh, Y. Maeng, M. Marques, F.J. Martín-Fernández, D.T. McClure, D. McKay, S. Meesala, A. Mezzacapo, N. Moll, D.M. Rodríguez, G. Nannicini, P. Nation, P. Ollitrault, L.J. O'Riordan, H. Paik, J. Pérez, A. Phan, M. Pistoia, V. Prutyanov, M. Reuter, J. Rice, A.R. Davila, R.H.P. Rudy, M. Ryu, N. Sathaye, C. Schnabel, E. Schoute, K. Setia, Y. Shi, A. Silva, Y. Siraichi, S. Sivarajah, J.A. Smolin, M. Soeken, H. Takahashi, I. Tavernelli, C. Taylor, P. Taylour, K. Trabing, M. Treinish, W. Turner, D. Vogt-Lee, C. Vuillot, J.A. Wildstrom, J. Wilson, E. Winston, C. Wood, S. Wood, S. Wörner, I.Y. Akhalwaya, C. Zoufal, Qiskit: An Open-source Framework for Quantum Computing, Zenodo. (2019). https://doi.org/10.5281/ZENODO.2562111.

[5] E. Farhi, S. Gutmann, Quantum computation and decision trees, Phys. Rev. A - At. Mol. Opt. Phys. 58 (1998) 915–928. https://doi.org/10.1103/PhysRevA.58.915.

[6] D. Solenov, L. Fedichkin, Continuous-time quantum walks on a cycle graph, Phys. Rev. A - At. Mol. Opt. Phys. 73 (2006) 1–5. https://doi.org/10.1103/PhysRevA.73.012313.

[7] Y.C. Cheng, R.J. Silbey, Coherence in the B800 Ring of Purple Bacteria LH2, Phys. Rev. Lett. 96 (2006) 028103. https://doi.org/10.1103/PhysRevLett.96.028103.

[8] P.W. Anderson, Absence of Diffusion in Certain Random Lattices, Phys. Rev. 109 (1958) 1492–1505. https://doi.org/10.1103/PhysRev.109.1492.

[9] J.P. Keating, N. Linden, J.C.F. Matthews, A. Winter, Localization and its consequences for quantum walk algorithms and quantum communication, Phys. Rev. A - At. Mol. Opt. Phys. 76 (2007) 1–5. https://doi.org/10.1103/PhysRevA.76.012315.

[10] G.J. Moro, G. Dall'Osto, B. Fresch, Signatures of Anderson localization and delocalized random quantum states, Chem. Phys. 514 (2018) 141–149. https://doi.org/10.1016/j.chemphys.2018.03.006.

[11] V. Gorini, A. Kossakowski, E.C.G. Sudarshan, Completely positive dynamical semigroups of N-level systems, J. Math. Phys. 17 (1976) 821. https://doi.org/10.1063/1.522979.

[12] J.M. Moix, M. Khasin, J. Cao, Coherent quantum transport in disordered systems: I. The influence of dephasing on the transport properties and absorption spectra on one-dimensional systems, New J. Phys. 15 (2013) 085010. https://doi.org/10.1088/1367-2630/15/8/085010.

[13] K.M. Gaab, C.J. Bardeen, The effects of connectivity, coherence, and trapping on energy transfer in simple light-harvesting systems studied using the Haken-Strobl model with diagonal disorder, J. Chem. Phys. 121 (2004) 7813. https://doi.org/10.1063/1.1786922.

[14] M.B. Plenio, S.F. Huelga, Dephasing-assisted transport: quantum networks and biomolecules, New J. Phys. 10 (2008) 113019. https://doi.org/10.1088/1367-2630/10/11/113019.

[15] G.G. Giusteri, F. Mattiotti, G.L. Celardo, Non-Hermitian Hamiltonian approach to quantum transport in disordered networks with sinks: Validity and effectiveness, Phys. Rev. B. 91 (2015) 094301. https://doi.org/10.1103/PhysRevB.91.094301.

[16] G.G. Giusteri, F. Recrosi, G. Schaller, G.L. Celardo, Interplay of different environments in open quantum systems: Breakdown of the additive approximation, Phys. Rev. E. 96 (2017) 012113. https://doi.org/10.1103/PhysRevE.96.012113.

[17] C. Maier, T. Brydges, P. Jurcevic, N. Trautmann, C. Hempel, B.P. Lanyon, P. Hauke, R. Blatt, C.F. Roos, Environment-Assisted Quantum Transport in a 10-qubit Network, Phys. Rev. Lett. 122 (2019) 050501. https://doi.org/10.1103/PhysRevLett.122.050501.

[18] H. Park, N. Heldman, P. Rebentrost, L. Abbondanza, A. Iagatti, A. Alessi, B. Patrizi, M. Salvalaggio, L. Bussotti, M. Mohseni, F. Caruso, H.C. Johnsen, R. Fusco, P. Foggi, P.F. Scudo, S. Lloyd, A.M. Belcher, Enhanced energy transport in genetically engineered excitonic networks, Nat. Mater. 15 (2016) 211–216. https://doi.org/10.1038/nmat4448.

[19] R. Dorner, J. Goold, V. Vedral, Towards quantum simulations of biological information flow, Interface Focus. 2 (2012) 522–528. https://doi.org/10.1098/rsfs.2011.0109.

[20] S. Mostame, P. Rebentrost, A. Eisfeld, A.J. Kerman, D.I. Tsomokos, A. Aspuru-Guzik, Quantum simulator of an open quantum system using superconducting qubits: exciton transport in photosynthetic complexes, New J. Phys. 14 (2012) 105013. https://doi.org/10.1088/1367-2630/14/10/105013.

[21] S. Mostame, J. Huh, C. Kreisbeck, A.J. Kerman, T. Fujita, A. Eisfeld, A. Aspuru-Guzik, Emulation of complex open quantum systems using superconducting qubits, Quantum Inf. Process. 16 (2017) 44. https://doi.org/10.1007/s11128-016-1489-3.

[22] A. Potočnik, A. Bargerbos, F.A.Y.N. Schröder, S.A. Khan, M.C. Collodo, S. Gasparinetti, Y. Salathé, C. Creatore, C. Eichler, H.E. Türeci, A.W. Chin, A. Wallraff, Studying light-harvesting models with superconducting circuits, Nat. Commun. 9 (2018) 904. https://doi.org/10.1038/s41467-018-03312-x.

[23] B.-X. Wang, M.-J. Tao, Q. Ai, T. Xin, N. Lambert, D. Ruan, Y.-C. Cheng, F. Nori, F.-G. Deng, G.-L. Long,

Efficient quantum simulation of photosynthetic light harvesting, Npj Quantum Inf. 4 (2018) 52. https://doi.org/10.1038/s41534-018-0102-2.

[24] H.-P. Breuer, F. Petruccione, The Theory of Open Quantum Systems, Oxford University Press, Oxford, 2007. https://doi.org/10.1093/acprof:oso/9780199213900.001.0001.

[25] C.W. Gardiner, Handbook of Stochastic Methods for Physics, Chemistry and the Natural Sciences, 3rd ed., Springer-Verlag, Berlin, 1997.

[26] A.A. Budini, A.K. Chattah, M.O. Cáceres, On the quantum dissipative generator: weak-coupling approximation and stochastic approach, J. Phys. A. Math. Gen. 32 (1999) 631–646. https://doi.org/10.1088/0305-4470/32/4/007.

[27] A.A. Budini, Non-Markovian Gaussian dissipative stochastic wave vector, Phys. Rev. A. 63 (2000) 012106. https://doi.org/10.1103/PhysRevA.63.012106.

[28] A. Chenu, M. Beau, J. Cao, A. del Campo, Quantum Simulation of Generic Many-Body Open System Dynamics Using Classical Noise, Phys. Rev. Lett. 118 (2017) 140403. https://doi.org/10.1103/PhysRevLett.118.140403.

[29] J.M. Horowitz, J.M.R. Parrondo, Entropy production along nonequilibrium quantum jump trajectories, New J. Phys. 15 (2013) 085028. https://doi.org/10.1088/1367-2630/15/8/085028.

[30] B. Çakmak, A. Manatuly, Ö.E. Müstecaplıoğlu, Thermal production, protection, and heat exchange of quantum coherences, Phys. Rev. A. 96 (2017) 032117. https://doi.org/10.1103/PhysRevA.96.032117.

[31] L. Li, J. Zou, H. Li, B.-M. Xu, Y.-M. Wang, B. Shao, Effect of coherence of nonthermal reservoirs on heat transport in a microscopic collision model, Phys. Rev. E. 97 (2018) 022111. https://doi.org/10.1103/PhysRevE.97.022111.

[32] S. Kretschmer, K. Luoma, W.T. Strunz, Collision model for non-Markovian quantum dynamics, Phys. Rev. A. 94 (2016) 012106. https://doi.org/10.1103/PhysRevA.94.012106.

[33] S. Campbell, F. Ciccarello, G.M. Palma, B. Vacchini, System-environment correlations and Markovian embedding of quantum non-Markovian dynamics, Phys. Rev. A. 98 (2018) 012142. https://doi.org/10.1103/PhysRevA.98.012142.

[34] S. Lorenzo, F. Ciccarello, G.M. Palma, Composite quantum collision models, Phys. Rev. A. 96 (2017) 032107. https://doi.org/10.1103/PhysRevA.96.032107.

[35] F. Ciccarello, Collision models in quantum optics, Quantum Meas. Quantum Metrol. 4 (2017) 53–63. https://doi.org/10.1515/qmetro-2017-0007.

[36] G. García-Pérez, D.A. Chisholm, M.A.C. Rossi, G.M. Palma, S. Maniscalco, Decoherence without entanglement and quantum Darwinism, Phys. Rev. Res. 2 (2020) 1–5. https://doi.org/10.1103/physrevresearch.2.012061.

[37] S. Campbell, B. Vacchini, Collision models in open system dynamics: A versatile tool for deeper insights?, EPL (Europhysics Lett.). 133 (2021) 60001. https://doi.org/10.1209/0295-5075/133/60001.

[38] D.A. Chisholm, G. García-Pérez, M.A.C. Rossi, G.M. Palma, S. Maniscalco, Stochastic collision model approach to transport phenomena in quantum networks, New J. Phys. 23 (2021) 033031. https://doi.org/10.1088/1367-2630/abd57d.

[39] G. García-Pérez, M.A.C. Rossi, S. Maniscalco, IBM Q Experience as a versatile experimental testbed for simulating open quantum systems, Npj Quantum Inf. 6 (2020) 1. https://doi.org/10.1038/s41534-019-0235-y.

[40] M. Cattaneo, M.A.C. Rossi, G. García-Pérez, R. Zambrini, S. Maniscalco, Quantum simulation of dissipative collective effects on noisy quantum computers, (2022) 1–25. http://arxiv.org/abs/2201.11597.

[41] M. Ziman, V. Bužek, All (qubit) decoherences: Complete characterization and physical implementation, Phys. Rev. A. 72 (2005) 022110. https://doi.org/10.1103/PhysRevA.72.022110.

[42] F. Ciccarello, S. Lorenzo, V. Giovannetti, G.M. Palma, Quantum collision models: Open system dynamics from repeated interactions, Phys. Rep. 954 (2022) 1–70. https://doi.org/10.1016/j.physrep.2022.01.001.

[43] B. Misra, E.C.G. Sudarshan, The Zeno's paradox in quantum theory, J. Math. Phys. 18 (1977) 756–763. https://doi.org/10.1063/1.523304.

[44] P. Gupta, C.M. Chandrashekar, Digital quantum simulation framework for energy transport in an open quantum system, New J. Phys. 22 (2020) 123027. https://doi.org/10.1088/1367-2630/abcdc9.

[45] Z. Hu, K. Head-Marsden, D.A. Mazziotti, P. Narang, S. Kais, A general quantum algorithm for open quantum dynamics demonstrated with the Fenna-Matthews-Olson complex, Quantum. 6 (2022) 726. https://doi.org/10.22331/q-2022-05-30-726.

[46] T.A. Brun, A simple model of quantum trajectories, Am. J. Phys. 70 (2002) 719–737. https://doi.org/10.1119/1.1475328.

[47] H.M. Wiseman, G.J. Milburn, Interpretation of quantum jump and diffusion processes illustrated on the Bloch

sphere, Phys. Rev. A. 47 (1993) 1652–1666. https://doi.org/10.1103/PhysRevA.47.1652.

[48] M.B. Plenio, P.L. Knight, The quantum-jump approach to dissipative dynamics in quantum optics, Rev. Mod. Phys. 70 (1998) 101–144. https://doi.org/10.1103/RevModPhys.70.101.

[49] H.M. Wiseman, Quantum trajectories and quantum measurement theory, Quantum Semiclassical Opt. J. Eur. Opt. Soc. Part B. 8 (1996) 205–222. https://doi.org/10.1088/1355-5111/8/1/015.

[50] O. Linden, V. May, Quantum master equation, Lindblad-type of dissipation and temperature dependent Monte Carlo wave-function propagation, Eur. Phys. J. D. 12 (2000) 473–485. https://doi.org/10.1007/s100530070008.

[51] G. Dall'Osto, E. Coccia, C.A. Guido, S. Corni, Investigating ultrafast two-pulse experiments on single DNQDI fluorophores: a stochastic quantum approach, Phys. Chem. Chem. Phys. 22 (2020) 16734–16746. https://doi.org/10.1039/D0CP02557G.

[52] E. Coccia, F. Troiani, S. Corni, Probing quantum coherence in ultrafast molecular processes: An ab initio approach to open quantum systems, J. Chem. Phys. 148 (2018) 204112. https://doi.org/10.1063/1.5022976.

[53] I. Kondov, U. Kleinekathöfer, M. Schreiber, Stochastic unraveling of Redfield master equations and its application to electron transfer problems, J. Chem. Phys. 119 (2003) 6635–6646. https://doi.org/10.1063/1.1605095.

[54] L.C.G. Govia, B.G. Taketani, P.K. Schuhmacher, F.K. Wilhelm, Quantum simulation of a quantum stochastic walk, Quantum Sci. Technol. 2 (2017) 015002. https://doi.org/10.1088/2058-9565/aa540b.

[55] H. Wang, S. Ashhab, F. Nori, Quantum algorithm for simulating the dynamics of an open quantum system, Phys. Rev. A. 83 (2011) 062317. https://doi.org/10.1103/PhysRevA.83.062317.

[56] M. Cattaneo, G. De Chiara, S. Maniscalco, R. Zambrini, G.L. Giorgi, Collision Models Can Efficiently Simulate Any Multipartite Markovian Quantum Dynamics, Phys. Rev. Lett. 126 (2021) 130403. https://doi.org/10.1103/PhysRevLett.126.130403.

Chapter III

Quantum transport assisted by a coloured environment: Algorithms and phenomenology

In the previous Chapter, we focused on quantum transport mediated by a memoryless environment causing dephasing of inter-site coherences in the dynamics of the open system. For their simple but non-trivial formulation, the quantum algorithms we proposed can be used as a good starting point to demonstrate the enhancement of transport efficiency in the dynamics assisted by a dephasing environment. However, because of the Markovian assumption, the underlying model is not sufficient to describe the effects induced by an environment whose relaxation is comparable with the characteristic timescale of the system evolution.

Here, we cover this part by studying the phenomenology of more structured environments with a finite correlation time, in order to include non-Markovian (memory) effects into the quantum dynamics. In section III.1, we present the Ornstein-Uhlenbeck process for describing the site-energy fluctuations of the network. This process has been proposed for example in [1,2] to describe the effects of the overdamped vibrations in the exciton transport on chromophoric networks. The peculiarity of non-Markovian models is that, outside the weak-coupling regime, it is not always possible to derive a master equation for the dynamics of the open system. So, alternative techniques must be used. Here, we address this problem by proposing quantum algorithms based on the same principles as the classical noise algorithm (section III.2) and collision algorithm (section III.3). The result of the algorithms as well as the study of the transport efficiency in presence of a coloured environment are discussed in section III.4. Finally, we give our conclusions in section III.5.

III.1 The Ornstein-Uhlenbeck process for energy fluctuations

Let us take the classical noise algorithm introduced in the previous Chapter. In this case, the evolution of the open system is obtained as an ensemble average over unitary Schrödinger dynamics with a stochastic Hamiltonian. We have seen that white noise fluctuations of the site energies $\delta\varepsilon_j(t)$ generate a dynamics that can be described by a Lindblad master equation. A simple generalization to correlated noise is offered by the stationary Ornstein-Uhlenbeck (OU) process [3,4], a Gaussian-Markovian process with exponential damping of correlations (see Appendix A)

$$c_{\mathrm{OU}}(t) = \overline{\delta\varepsilon_j(t)\delta\varepsilon_{j'}(0)} = \gamma\delta_{j,j'}\exp\left(-|t|/\tau\right), \tag{III.1}$$

where the overbar indicates the average over noise realizations, γ is the fluctuation amplitude, $\delta_{j,j'}$ is the Kronecker delta function and τ is the correlation time of the fluctuations. Such a correlation function is related to a Lorentzian spectral density in the form

$$J_{\mathrm{OU}}(\omega) = \int_{-\infty}^{\infty} c_{\mathrm{OU}}(t)e^{\mathrm{i}\omega t}dt = 2\gamma\frac{\Omega}{\omega^2+\Omega^2}, \tag{III.2}$$

where $\Omega = 1/\tau$ is the inverse of the characteristic memory time τ of the environment, and ω is in the frequency range of the open system.

In Figure 1, we report an example of the trajectories generated by the OU process with $\tau = 1$ ps, as well as the exponentially-damped correlation function calculated from the trajectories, compared with the theoretical one given in eq. (III.1).

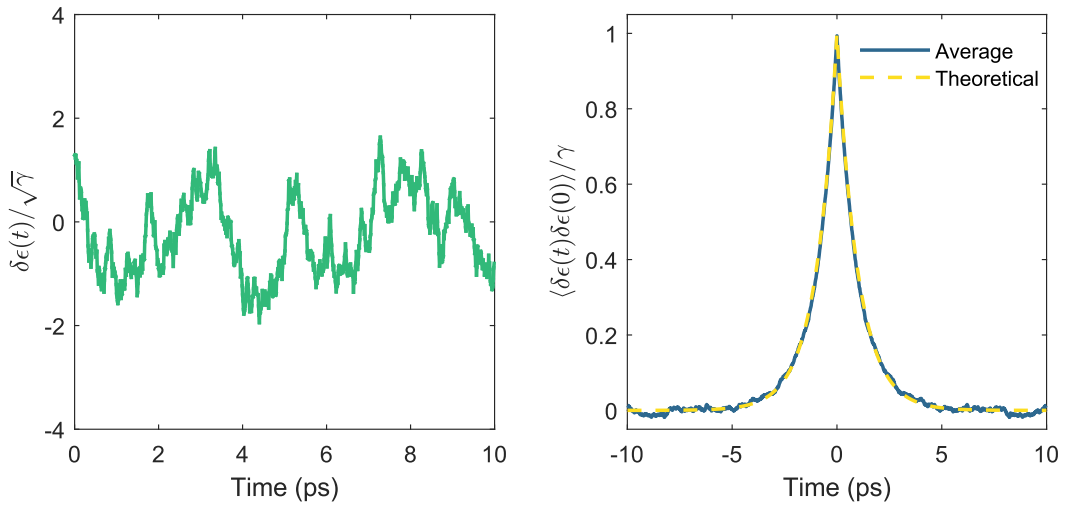

Figure 1. Left panel: a single realization (trajectory) of the stochastic energy fluctuation generated by the Ornstein-Uhlenbeck process. Right panel: the correlation function of the energy fluctuations calculated as the ensemble average over 10^4 trajectories (blue line) is compared with the theoretical one given in eq. (III.1) (yellow line).

When the fluctuations are very slow, *i.e.*, in the limit of $\tau \to \infty$, the effect is that of a static disorder on the energies of the network. The effects of this disorder have been studied for example in [5–11]. On the other hand, in the limit of vanishing correlation time $\tau \to 0$, that is when the environment relaxation time is way faster than the system evolution, the correlation function approaches the white noise limit

$$\begin{aligned} c_{\mathrm{w}}(t) &= \lim_{\tau\to 0} \gamma\delta_{j,j'} \exp\left(-|t|/\tau\right) \\ &= 2\gamma\tau\delta_{j,j'} \lim_{\tau\to 0} \frac{\exp\left(-|t|/\tau\right)}{2\tau} \\ &= 2\gamma\tau\delta_{j,j'}\delta(t) \end{aligned} \tag{III.3}$$

where for the second equivalence the product $\gamma\tau$ must be kept constant, and in the last equivalence we used a definition of the Dirac delta function $\delta(t)$. The spectral density, in this case, becomes constant (flat) in the frequency range of the system

$$J_{\mathrm{w}}(\omega) = 2\gamma\tau\,. \tag{III.4}$$

Note that this type of Markovian environment is the one we studied in the previous Chapter (it produces eq. I.7 by identifying the relaxation rates with $2\gamma\tau$) and can be obtained as a limiting case of the more general OU process. In section III.4.1, parameter $\gamma\tau$ will allow us to compare the efficiency of transport mediated by the white noise and OU processes. Because of its role as a comparison quantity, we will call it the *equivalent noise strength* (where the word "equivalent" refers to the white noise case).

We report in Figure 2 a stochastic trajectory generated by the white noise process, and the correlation function generated as the ensemble average over various realizations of the process, along with the theoretical one given in eq. (III.3). Form a qualitative comparison with the OU process, one can appreciate how the complete absence of correlation in the values at close time instants influences the trajectory.

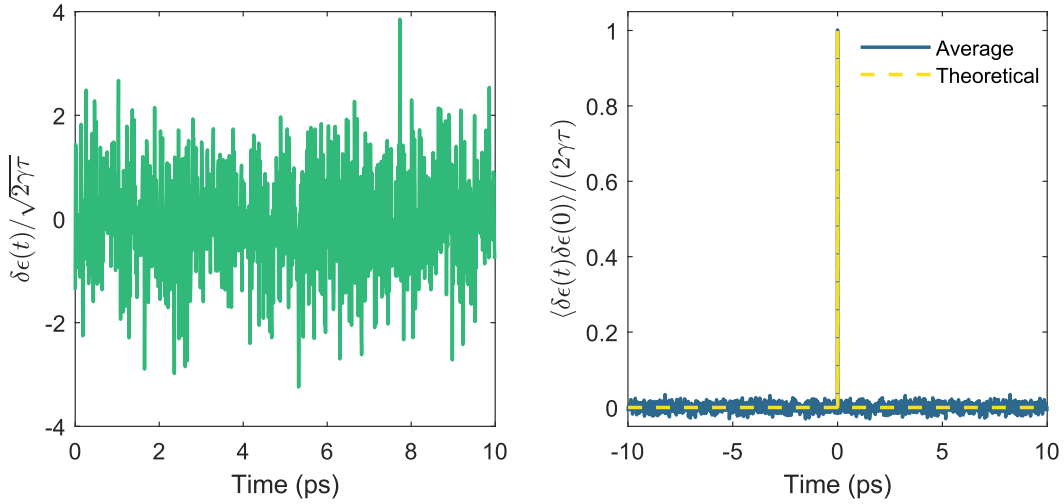

Figure 2. Left panel: a single realization (trajectory) of the stochastic energy fluctuation generated by the white noise process. Right panel: the correlation function of the energy fluctuations calculated as the ensemble average over 10^4 trajectories (blue line) is compared with the theoretical one given in eq. (III.3) (yellow line).

In general, it can be demonstrated that when site energy fluctuations follow an OU process with a finite correlation time, the average dynamics of the open system becomes non-trivial and clearly displays non-Markovian signatures, as proved in Appendix B. If the interaction with the environment is perturbative and the correlation time of the fluctuating environment is short compared to the system timescale, one can use the Redfield treatment to obtain a Markovian master equation for the reduced open system (see Chapters IV). In another case, when only the perturbative interaction holds, one can derive, under the Born approximation, a master equation with a memory kernel describing the effects of the correlated environment fluctuations on the dynamics of the reduced system [12,13]. However, there is not a general form of quantum master equation describing the average dynamics resulting from such a process [14,15].

Since our algorithms aim to reproduce the full range of interaction strengths, including intermediate and strong coupling, this poses the problem of an external benchmark to validate the results of our algorithms, that, even if they rely on theoretically exact methods, are still subjected to a numerical (*i.e.*, approximated) implementation.

Exact numerical methods exist for the solution of open quantum system dynamics in the intermediate, or even strong, coupling regimes such as the *Quasi Adiabatic Path Integral* method (QUAPI) [16,17], the *Time-Evolving Density matrix using the Orthogonal Polynomials Algorithm* (TEDOPA) [18,19] or the *Hierarchy of stochastic Pure States* (HOPS) [20–22]. In our case, we opt for the *Hierarchical Equation Of Motion* (HEOM), introduced by Tanimura and Kubo [23]. The method is based on a stochastic Liouville approach in which the system density matrix is coupled to an infinite hierarchical series of density matrices that accounts for the non-Markovian interactions with the environment. In the last decade, HEOM gained a lot of attention in the study of exciton transport in molecular aggregates, becoming the “gold standard” method to study such dynamics [1,24–28]. For the implementation of HEOM, we used the BoFiN-HEOM package [29,30] integrated with the

popular QuTip library for Python [31,32]. The HEOM solver requires to know only the system Hamiltonian, the system interaction operator with the environment and the correlation functions of the environment, which makes it a perfect candidate to be the benchmark. For the results shown in this Chapter, we adopted an iterative procedure to truncate the hierarchy depth once convergence was found (truncation is required for the numerical implementation since an infinite series is impossible to handle). It must be stressed that even if these exact approaches exist, they are computationally expensive and their use is limited to small systems.

III.2 Classical noise algorithm

For the classical noise algorithm, the generalization to the new environment is straightforward. The idea is to propagate a stochastic Schrödinger equation where the stochastic process is no more a white-noise fluctuation of the site energies of the network but follows an OU process [33].

We need a method for the propagation of a trajectory ξ described by the time-dependent Hamiltonian

$$H_{\mathrm{OU}}(t) = H + H_{\mathrm{fluct},\xi}(t) = \sum_{j=1}^{N}\left(\varepsilon_j + \delta\varepsilon_{j,\xi}(t)\right)|j\rangle\langle j| + \sum_{\langle j,j'\rangle} V_{jj'}\left(|j\rangle\langle j'| + |j'\rangle\langle j|\right). \tag{III.5}$$

The Schrödinger equation for the evolution has the formal solution

$$|\psi(t)\rangle = U_\xi(t,0)|\psi(0)\rangle, \tag{III.6}$$

where the exact propagator can be formally written by mean of the time ordering operator $\underleftarrow{\mathcal{T}}$

$$U_\xi(t,0) = \underleftarrow{\mathcal{T}}\exp\left[-\mathrm{i}\int_0^t H_{\mathrm{OU}}(t)\,dt\right]. \tag{III.7}$$

This formal solution must be implemented numerically to simulate the dynamics of the system. Here we proceed as in the previous chapter by dividing the dynamics into small time steps Δt, so that the propagator to time $t = S\Delta t$ can be approximated as

$$U_\xi(t,0) \approx \underleftarrow{\mathcal{T}}\prod_{s=1}^{S} U_\xi\left(s\Delta t,(s-1)\Delta t\right) = \underleftarrow{\mathcal{T}}\prod_{s=1}^{S}\exp\left[-\mathrm{i}\int_{(s-1)\Delta t}^{s\Delta t} H_{\mathrm{OU}}(t)\,dt\right]. \tag{III.8}$$

This method corresponds to a first-order Magnus expansion [34–37].

As for the white noise case, the integral in eq. (III.8) can be decomposed into two contributions

$$\int_{(s-1)\Delta t}^{s\Delta t} H_{\mathrm{OU}}(t)\,dt = H\Delta t + \int_{(s-1)\Delta t}^{s\Delta t} H_{\mathrm{fluc},\xi}(t)\,dt, \tag{III.9}$$

where in the stochastic part,

$$\int_{(s-1)\Delta t}^{s\Delta t} H_{\mathrm{fluc},\xi}(t)\,dt = \sum_{j=1}^{N}|j\rangle\langle j|\int_{(s-1)\Delta t}^{s\Delta t}\delta\varepsilon_{j,\xi}(t)\,dt, \tag{III.10}$$

it appears the time integral of the OU process, defined as the process that satisfies

$$Y_{j,\xi}\left(t+dt\right)=Y_{j,\xi}\left(t\right)+\delta\varepsilon_{j,\xi}\left(t\right)dt\,. \tag{III.11}$$

$Y_{j,\xi}\left(t\right)$ is known to be a Gaussian random variable [3,4] whose statistical properties are different from the Wiener process seen in the previous Chapter, *i.e.*,

$$\overline{Y_{j,\xi}\left(t\right)}=Y_{j,\xi}\left(t_0\right)+\delta\varepsilon_{j,\xi}\left(t_0\right)e^{-\left(t-t_0\right)/\tau}\,, \tag{III.12}$$

$$\mathrm{var}\left\{Y_{j,\xi}\left(t\right)\right\}=2\gamma\tau^2\left[\frac{t-t_0}{\tau}-2\left(1-e^{-\left(t-t_0\right)/\tau}\right)+\frac{1}{2}\left(1-e^{-2\left(t-t_0\right)/\tau}\right)\right], \tag{III.13}$$

$$\mathrm{cov}\left\{\delta\varepsilon_{j,\xi}\left(t\right),Y_{j,\xi}\left(t\right)\right\}=\gamma\tau\left(1-2e^{-\left(t-t_0\right)/\tau}+e^{-2\left(t-t_0\right)/\tau}\right). \tag{III.14}$$

In order to solve integral in eq. (III.10), we look for an updating formula that gives $Y_{j,\xi}\left(s\Delta t\right)$ from $Y_{j,\xi}\left(\left(s-1\right)\Delta t\right)$, so that

$$Y_{j,\xi}\left(s\Delta t\right)-Y_{j,\xi}\left(\left(s-1\right)t\right)=\int_{\left(s-1\right)\Delta t}^{s\Delta t}\delta\varepsilon_{j,\xi}\left(t\right)dt\,. \tag{III.15}$$

A first-order approximation of such an updating formula can be obtained by replacing the infinitesimal dt in eq. (III.11) with the finite time step Δt [3]

$$Y_{j,\xi}\left(s\Delta t\right)\approx Y_{j,\xi}\left(\left(s-1\right)\Delta t\right)+\delta\varepsilon_{j,\xi}\left(\left(s-1\right)\Delta t\right)\Delta t\,. \tag{III.16}$$

This equation must be propagated together with the updating formula for the OU process [3], which is known to be

$$\delta\varepsilon_{j,\xi}\left(s\Delta t\right)=\delta\varepsilon_{j,\xi}\left(\left(s-1\right)\Delta t\right)e^{-\Delta t/\tau}+n_{j,\xi,s}^{(1)}\sqrt{\gamma\left(1-e^{-2\Delta t/\tau}\right)}\,, \tag{III.17}$$

where $n_{j,\xi,s}^{(1)}$ is a random number sampled from a normal distribution with mean zero and unit variance. The initial condition corresponds to $\delta\varepsilon_{j,\xi}\left(0\right)=n_{j,\xi,0}^{(1)}$ (cf. Appendix A). Note that this first-order approximation is equivalent to not solving the integral and simply assuming that $\delta\varepsilon_{j,\xi}\left(\left(s-1\right)\Delta t\right)$ remains constant during the time interval Δt, as done for example in the Numerical Integration of the Schrödinger Equation (NISE) method proposed by Jansen *et al* [1,38,39].

An exact update formula is also known for $Y\left(t\right)$ [3,4]

$$
\begin{aligned}
Y_{j,\xi}\left(s\Delta t\right) &= Y_{j,\xi}\left(\left(s-1\right)\Delta t\right) \\
&+\delta\varepsilon_{j,\xi}\left(\left(s-1\right)\Delta t\right)\tau\left(1-e^{-\Delta t/\tau}\right) \\
&+n^{(2)}_{j,\xi,s}\sqrt{2\gamma\tau^2\left[\frac{\Delta t}{\tau}-\left(\frac{3}{2}-2e^{-\Delta t/\tau}+\frac{1}{2}e^{-2\Delta t/\tau}\right)-\frac{1}{2}\frac{\left(1-e^{-\Delta t/\tau}\right)^4}{\left(1-e^{-2\Delta t/\tau}\right)}\right]} \\
&+n^{(1)}_{j,\xi,s}\sqrt{\gamma\tau^2\frac{\left(1-e^{-\Delta t/\tau}\right)^4}{\left(1-e^{-2\Delta t/\tau}\right)}}
\end{aligned}
\qquad \text{(III.18)}
$$

that must be propagated together with eq. (III.17). In this case, $n^{(1)}_{j,\xi,s}$ is the same number in both updating formulas, while $n^{(2)}_{j,\xi,s}$ is another normal random number independent from $n^{(1)}_{j,\xi,s}$.

Eq. (III.18) should give more accurate results for the integral (III.15). However, since the time step Δt must be kept small to satisfy equation (III.8), we did not notice any benefit in using the exact update formula, so for the rest of the Chapter, we will use the first-order approximation to propagate the dynamics.

The algorithmic scheme of the Classical Noise algorithm is equivalent to the one already introduced in the previous Chapter, so we will not repeat the instructions of the algorithm here. The results of the quantum algorithm and the effect of non-Markovianity, due to the finite memory of the environment, on the dynamics of the walker will be analysed in detail in section III.4.

III.2.1 Stochastic trajectories and average evolution

Before moving to the next method, it is worth investigating the trajectories obtained by a (classical) numerical computation of the Schrödinger dynamics. To do so, we start with the simplest system, *i.e.*, a network composed of two linked sites. Such a network can model for example the single exciton manifold of an excitonic dimer. We use the following parameters for the system: an homodimer with site energy $\varepsilon_1=\varepsilon_2=0$, coupling $V=1\ \text{ps}^{-1}$, fluctuation amplitude $\gamma=1\ \text{ps}^{-2}$ and memory time of the environment fluctuations $\tau=1\ \text{ps}$. The Schrödinger equations were propagated with a time step $\Delta t=50\ \text{fs}$, that must be lower than the timescale of the system and the environment dynamics. In Figure 3, we show the results obtained by the algorithm. In the left panel, we report a single random trajectory for the population of the initial site of the dynamics. As can be noted, the population smoothly change in time without presenting any sudden variation or discontinuity (jump). This evolution resembles the one observed in the previous Chapter for the trajectory of the classical noise algorithm for the white noise. In the right panel, we show the population of the initial site obtained for a swarm of 10^4 trajectories (here we represent 200 of them as green lines in transparency) generated by solving different Schrödinger equations for each one of them. The ensemble average (solid blue line) is a population with damped oscillations that relaxes to the equilibrium value, $P_1^{\text{eq}}=0.5$, at around 15 ps.

From a comparison with HEOM, we can confirm that the classical noise method can successfully reproduce the non-Markovian dynamics when the coloured spectral density used. We conclude with a remark. For this simple system, the HEOM solver was faster in the computation than the generation of 10^4 stochastic unitary trajectories. However, we noted that a HEOM treatment becomes soon intractable in terms of computational time when the dimension of the system increases or the environment has long correlations [40]. Moreover, HEOM is known to have a very bad scaling with the system-environment coupling strength.

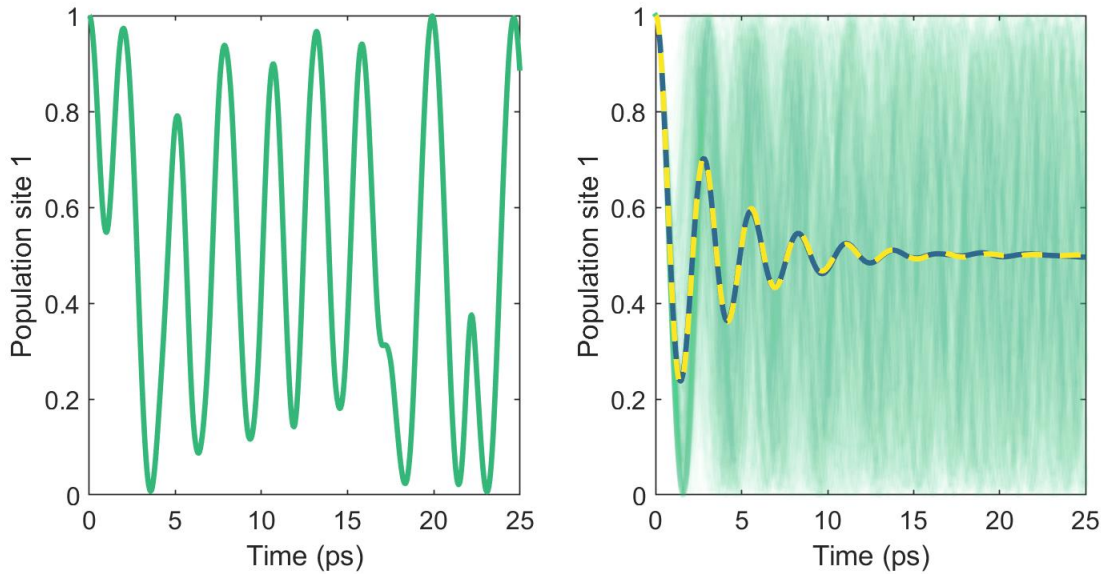

Figure 3. Left panel: the stochastic dynamics of a single trajectory obtained monitoring the initially populated site of a dimeric open system obtained by the classical noise algorithm. Right panel: an ensemble of 200 trajectories (green). The average dynamics over 10^4 trajectories (blue) fits precisely the result by HEOM (yellow).

III.3 Collision algorithm

Collision models for non-Markovian processes have been proposed in various forms using ancilla-ancilla interactions [41,42], correlating the initial states of the ancillae [43,44], generating collisions at stochastic times [45,46], allowing multiple collisions between the ancillae and the system [47] or *dressing* the system with permanent ancillae [48,49]. In all these models, the common idea is to have the system interact with ancillae that have "memory" of the collisions that occurred at past times. For those who would like to learn more about collision models, we recommend the extensive review of ref. [50]. Here, we propose an implementation inspired by the composite collision model of ref. [48], which was proved to be efficient for the simulation of the (Markovian) dynamics of a dressed system [51]. To do so we will introduce the pseudomodes method [48,52–57], adapt it to our transport problem and propose the corresponding collision algorithm that can be used for a quantum computer simulation. To the best of our knowledge, this implementation scheme for quantum algorithms involving pseudomodes has not been presented in the literature so far.

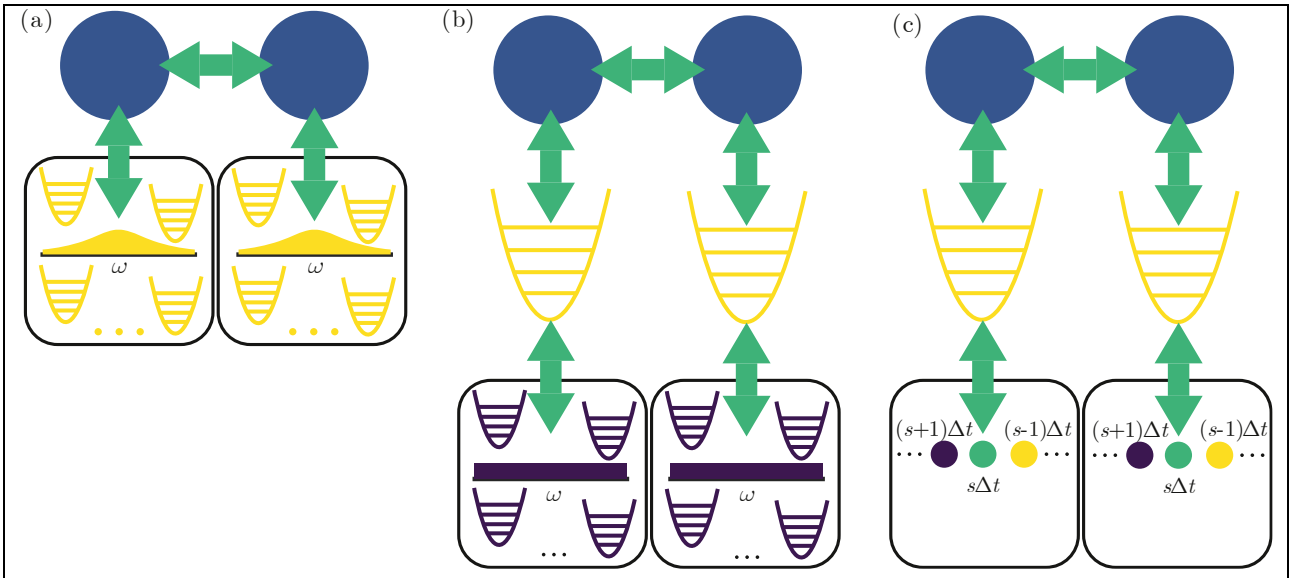

Figure 4. Interaction of a two-site system with various forms of environment gives the same reduced dynamics. (a) Each site of the network interacts with a bosonic reservoir characterized by a Lorentzian spectral density causing site dephasing. The reduced dynamics of the system is non-Markovian. (b) Pseudomodes, one for each site of the network, are inserted between the open system and the bosonic reservoir, whose spectral density becomes flat (white noise). The dynamics of the enlarged system composed of the network plus the pseudomodes becomes Markovian. The reduced dynamics of the open system is obtained by tracing over the pseudomodes degrees of freedom. (c) In the collision model implementation, the reservoir with flat spectral density is substituted by ancillae qubits that interact with the pseudomodes at different time instants.

So let us take a step back and look at the problem from a different perspective. We anticipate that in the next Chapter, we will introduce a model for the study of the exciton transport mediated by molecular vibrations in the Fenna-Matthews-Olson complex that recall several aspects of the treatment discussed in the following. Let us consider the case of a network where sites are coupled to each other and (individually) with a collection of harmonic oscillators, *i.e.*, a bosonic bath (Figure 4a)

$$H^{\mathrm{s+e}} = H + \sum_{j=1}^{N}\sum_{k=0}^{\infty} \omega_k b_{jk}^{\dagger} b_{jk} + \sum_{j=1}^{N} |j\rangle\langle j| \sum_{k=0}^{\infty} \sqrt{\gamma}\left(b_{jk} + b_{jk}^{\dagger}\right). \tag{III.19}$$

Here, $\sqrt{\gamma}$ is the strength of the coupling between the sites and the modes of its environment [56], ω_k is the frequency of the mode and $b_{jk}^{\dagger}$ (b_{jk}) represents the creation (annihilation) operator for the harmonic oscillator in second quantization, defined as

$$b_{jk}^{\dagger}\left|n_{jk}^{\mathrm{b}}\right\rangle = \sqrt{n+1}\left|(n+1)_{jk}^{\mathrm{b}}\right\rangle, \quad b_{jk}\left|n_{jk}^{\mathrm{b}}\right\rangle = \sqrt{n}\left|(n-1)_{jk}^{\mathrm{b}}\right\rangle \tag{III.20}$$

with $\left|n_{jk}^{\mathrm{b}}\right\rangle$ denoting the presence of an excitation on the n-th level of mode k.

To implement the same open system dynamics that we have seen with the fluctuating environment, it is necessary for the baths relative to different sites to be uncorrelated and for the correlation function of the bath interacting operators, $\left(b_{jk}+b_{jk}^{\dagger}\right)$, to have an exponential decay (see Chapter IV for a more detailed discussion). Then, the solution of the Von Neumann equation with Hamiltonian (III.19) gives the exact (desired) dynamics of the universe system (open system plus environment) when the initial state corresponds to the factorized state $\rho^{\mathrm{s+b}}(0)=\rho(0)\otimes\rho^{\mathrm{b}}(0)$, and $\rho^{\mathrm{b}}(0)$ is Gaussian. In our case for simplicity, we can take it in the vacuum state [56]

$$\rho^{\mathrm{b}}(0)=\bigotimes_{j=1}^{N}\bigotimes_{k=0}^{\infty}\left|0_{jk}^{\mathrm{b}}\right\rangle\left\langle 0_{jk}^{\mathrm{b}}\right|. \tag{III.21}$$

However, it is clear that the computational resources required for the simulation of the complete model are not available as the Hilbert space of each oscillator is formally infinite, as infinite is the number of oscillators per site. To use this framework for a numerical simulation, it is thus imperative to reduce the size of the problem. Two main questions need to be faced: how many oscillator *per* site sufficiently describe a "continuum" environment? And what is an effective truncation of the oscillator Hilbert space? This observation explains why the theory of open quantum systems has so much success. In fact, most of the universe system is composed of the degrees of freedom of the environment, which give us extra information that we do not need to know for our purposes. Therefore, the opportunity to focus only on a master equation for the reduced system (with some approximations), by incorporating the effects of the environment on some effective parameters, has a potentially great computational advantage. Unfortunately, as already mentioned, writing an explicit master equation for the reduced system alone is not easy (or even possible) in all the range parameters we want to explore in this Chapter.

Here, we use the so-called pseudomode method [52,53] to overcome the problem. The first step is to insert a fictitious layer that separate the bosonic bath from the system. This layer is represented by some harmonic modes (the pseudomodes [53]) associated to the sites. The pseudomodes act as an intermediate system, interacting both with the open system and with external bosonic reservoirs. One might ask why we are increasing the size of the universe system instead of reducing it. But here is the point. We can use the pseudomode as a memory kernel and treat the bosonic reservoir as a bath with vanishing correlation time $c_{\mathrm{a}}(t)=2\Omega\delta(t)$ [52] (Figure 4b). In this way, the dynamics of the enlarged open system plus pseudomodes can be described by a Markovian Lindblad master equation, which can be conveniently implemented with a collision model.[1] Then, it can be demonstrated [52,53] that, after tracing over the pseudomode degrees of freedom, each site experiences an effective spectral density composed of a combination of Lorentzian functions centred at the oscillation frequency of the pseudomodes with which it interacts. Since our target spectral density

[1] Note that this does not contradict our previous statement that it is not possible to derive a general master equation for the reduced system, since in this case we are expanding the system with additional terms.

is made of a single Lorentzian centred at $\omega = 0$, we will need only one pseudomode for each site with zero oscillation frequency.

The new Hamiltonian reads

$$H = H^{\mathrm{s+p}} + \sum_{j=1}^{N}\sum_{k=0}^{\infty} \omega_k a_{jk}^{\dagger} a_{jk} + \sum_{j=1}^{N}\sum_{k=0}^{\infty} \sqrt{\frac{\Omega}{\pi}} \left(c_j^{\dagger} a_{jk} + c_j a_{jk}^{\dagger} \right) \tag{III.22}$$

where

$$H^{\mathrm{s+p}} = H + \sum_{j=1}^{N} \sqrt{\gamma} \left| j \right\rangle\!\left\langle j \right| \left(c_j + c_j^{\dagger} \right) \tag{III.23}$$

is the system plus pseudomodes Hamiltonian, and $\sqrt{\Omega/\pi}$ is the coupling strength of the interaction between a pseudomode and the k-th mode of the related external reservoir [56]. c_j and a_{jk} represent the annihilation operators of the pseudomodes and the reservoirs, respectively.

In the case of exciton transport in a molecular network, a pseudomode can be seen as an effective phonon mode dressing the electronic level of a chromophore [52,58]. Fixing the initial condition $\rho^{\mathrm{s+p+a}}(0) = \rho(0) \otimes \rho^{\mathrm{p}}(0) \otimes \rho^{a}(0)$, where

$$\rho^{\mathrm{p}}(0) = \bigotimes_{j=1}^{N} \left| 0_j^{\mathrm{p}} \right\rangle\!\left\langle 0_j^{\mathrm{p}} \right|, \quad \rho^{\mathrm{a}}(0) = \bigotimes_{j=1}^{N} \bigotimes_{k=0}^{\infty} \left| 0_{jk}^{\mathrm{a}} \right\rangle\!\left\langle 0_{jk}^{\mathrm{a}} \right| \tag{III.24}$$

(cf. eq. (III.21)), the global exciton plus phonon (*polaron* [52]) density matrix $\rho^{\mathrm{s+p}}(t)$ can be demonstrated to evolve according to an exact Markovian master equation in Lindblad form [56]

$$\frac{d\rho^{\mathrm{s+p}}(t)}{dt} = -\mathrm{i}\left[H^{\mathrm{s+p}}, \rho^{\mathrm{s+p}}(t) \right] + \Omega \sum_{j=1}^{N} \left(2 c_j \rho^{\mathrm{s+p}}(t) c_j^{\dagger} - c_j^{\dagger} c_j \rho^{\mathrm{s+p}}(t) - \rho^{\mathrm{s+p}}(t) c_j^{\dagger} c_j \right). \tag{III.25}$$

At this point, to recover the equation of motion for the open system it is sufficient to trace out the pseudomode degrees of freedom $\rho(t) = \mathrm{Tr}_{\mathrm{p}}\left(\rho^{\mathrm{s+p}}(t) \right)$.

III.3.1 Collision algorithm and mapping for digital quantum computers

Eq. (III.25) will be our reference master equation for the implementation of the Markovian collision model of the enlarged system (Figure 4c). For this purpose, the dynamics is divided into time intervals of length Δt, during which the evolution of $\rho^{\mathrm{s+p}}$ occurs according to the following dynamical map

$$\rho^{\mathrm{s+p}}(s\Delta t) = \mathrm{Tr}_{\bar{\mathrm{a}}} \left\{ U \rho^{\mathrm{s+p}}\left((s-1)\Delta t \right) \otimes \rho^{\bar{\mathrm{a}}} U^{\dagger} \right\}. \tag{III.26}$$

At every instant of time, a group of N ancilla qubits, always initialized in the uncorrelated state

$$\rho^{\bar{\mathrm{a}}} = \bigotimes_{j=1}^{N} \left| 0_j^{\bar{\mathrm{a}}} \right\rangle\!\left\langle 0_j^{\bar{\mathrm{a}}} \right| \tag{III.27}$$

(cf. eq. (III.24)), interacts pairwise with the pseudomodes. The interaction Hamiltonian specific for the evolution is described by

$$H_j^{\mathrm{p}+\bar{\mathrm{a}}} = \sqrt{\frac{2\Omega}{\Delta t}}\left(c_j^\dagger \sigma_j^- + c_j \sigma_j^+\right), \tag{III.28}$$

where σ_j^+ (σ_j^-) is the raising (lowering) operator for the ancilla qubit associated with pseudomode j, and for the collision model to be valid, it must hold that $\Delta t \ll (2\Omega)^{-1} = \tau/2$ (perturbative pseudomode-ancilla interaction during time-step evolution).

Finally, the unitary evolution operator of eq. (III.26) reads

$$U = \exp\left\{-\mathrm{i}\left(H^{\mathrm{s}+\mathrm{p}} + \sum_{j=1}^{N} H_j^{\mathrm{p}+\bar{\mathrm{a}}}\right)\Delta t\right\}. \tag{III.29}$$

In a quantum computer implementation, the operator (III.29) is translated into a multiple-qubit gate acting simultaneously on three quantum registers encoding the system, the pseudomodes and the ancillae, respectively. This large gate must be transpiled into smaller one- or two-qubits operations depending on the physical gates available on the device and its topology. The process of decomposing the multi-qubit gate can produce some overhead that can easily be reduced. Before doing it, let us say something more about the quantum registers involved in the algorithm. The register of the system will contain information about the state of the sites of our network and consists of q qubits, which can be either $q = \lceil \log_2 N \rceil$ or $q = N$, depending on the type of mapping chosen (algorithmic or physical, respectively. Cf. section II.1.2 of the previous Chapter). For the simulations in this Chapter, we will always use the more performing algorithmic one. The system register must be initialized at the beginning of the circuit to the desired initial state of the system; we choose $|j_0 = 1\rangle$ in the examples reported in this Chapter. Then, there must be a register where the states of the pseudomodes are stored. It is clear at this point that we need to build a finite dimensional approximation for the pseudomodes. To do so, we approximate each pseudomode with 2^p levels (states), where p is the number of qubits dedicated to a specific pseudomode, so that the state $|n_j\rangle$ of the j-th pseudomode is mapped into state $\left|\mathrm{bin}(n)_j\right\rangle$ of the j-th "partition" in the pseudomode quantum register. Thus, the total number of qubits for the pseudomode register is pN, that is N pseudomodes implemented by p qubits each. Accordingly, the pseudomode creation and annihilation operators must be properly adapted to the truncation of the proper Hilbert space. For better visualization, we report here the finite-dimensional matrices implementing the redefined operators

$$c_j^\dagger = \begin{pmatrix} 0 & 0 & 0 & 0 & \cdots & 0 \\ 1 & 0 & 0 & 0 & \cdots & 0 \\ 0 & \sqrt{2} & 0 & 0 & \cdots & 0 \\ 0 & 0 & \sqrt{3} & 0 & \cdots & 0 \\ \vdots & \vdots & \vdots & \ddots & \ddots & \cdots \\ 0 & 0 & 0 & \cdots & \sqrt{2^p} & 0 \end{pmatrix}, \quad c_j = \begin{pmatrix} 0 & 1 & 0 & 0 & \cdots & 0 \\ 0 & 0 & \sqrt{2} & 0 & \cdots & 0 \\ 0 & 0 & 0 & \sqrt{3} & \cdots & 0 \\ 0 & 0 & 0 & 0 & \ddots & \vdots \\ \vdots & \vdots & \vdots & \vdots & \ddots & \sqrt{2^p} \\ 0 & 0 & 0 & 0 & \cdots & 0 \end{pmatrix}. \tag{III.30}$$

Then, in the last quantum register, we store the state of the ancillae. In principle, this is composed of N qubits that should be reset after every interaction to guarantee the Markovianity of the evolution of the system plus pseudomodes state. However, it is possible to reduce the size of the ancilla register to a single qubit by adopting a proper decomposition of the propagator. In fact, as we have shown in the previous Chapter, for a small enough Δt we can apply Trotterization to (III.29) that reads

$$\lim_{\Delta t\to 0} U \approx e^{-\mathrm{i}H\Delta t}\prod_{j=1}^{N} e^{-\mathrm{i}\sqrt{\gamma}|j\rangle\langle j|\left(c_j+c_j^\dagger\right)\Delta t} e^{-\mathrm{i}H_j^{\mathrm{p}+\bar{\mathrm{a}}}\Delta t} = U^{\mathrm{s}}\prod_{j=1}^{N} U_j^{\mathrm{s}+\mathrm{p}} U_j^{\mathrm{p}+\bar{\mathrm{a}}}\,, \tag{III.31}$$

where we have separated the free-evolution of the system, the system-pseudomode interaction and the pseudomode-ancilla collision. Now every collision event occurs as an individual process, so a single qubit (opportunely reset after every interaction) is sufficient to implement the whole ancilla space. Trotterization has another advantage, namely, it allows for easier transpilation. Indeed, because the dimension of the unitary operators in (III.31) is smaller than the full propagator (III.29), the decomposition into the basis-gate set is facilitated. The steps of the resulting collision algorithm are reported in Appendix C.

III.3.2 Setting the pseudomode representation

To discuss the trajectories and results obtained by the collision algorithm, we need first to discuss the crucial issue of setting an effective representation of the pseudomodes. The key parameter here is the number of qubits p used to approximate each pseudomode. In Figure 5, we show the results obtained for the dynamics of a dimer system using $p=1,2$ qubits (blue and green lines, respectively) to implement the pseudomodes in the quantum register. HEOM is used as the benchmark method to compare the results (yellow line). The system is described by site-energy $\varepsilon_1=\varepsilon_2=0$ and coupling strength $V=1\ \mathrm{ps}^{-1}$, while we show the results of several values of the memory time and fluctuation amplitude. By looking at the results, the factor that most influences the quality of the finite-state approximation of the pseudomodes is the (dimensionless) product $\tau\sqrt{\gamma}$. In particular, we observed that when $\tau\sqrt{\gamma}\lesssim 1$ for $p=1$ and $\tau\sqrt{\gamma}\lesssim\sqrt{2}$ for $p=2$ the results of the collision model well reproduce the exact dynamics. A simple justification of this rule can be derived on a physical ground. The square of the fluctuation amplitude $\sqrt{\gamma}$ regulates the interaction between the system and the pseudomodes, see eq. (III.23). This interaction promotes population in the states $|n>0\rangle$ of pseudomodes, initially in state $|0\rangle$. Stemming from the Hamiltonian contribution to the dynamics, the characteristic transfer

frequency is proportional to the coupling strength $\sqrt{\gamma}$. In contrast, τ represents the relaxation time of the pseudomodes due to the collisions with the Markovian environment. Its effect is to transfer back population to states with low n, with a characteristic time τ. When $\tau\sqrt{\gamma}$ is sufficiently small, the pseudomode relaxation is fast enough to maintain non-negligible populations only in the first $2^{p=1}=2$ or $2^{p=2}=4$ states of the pseudomodes.

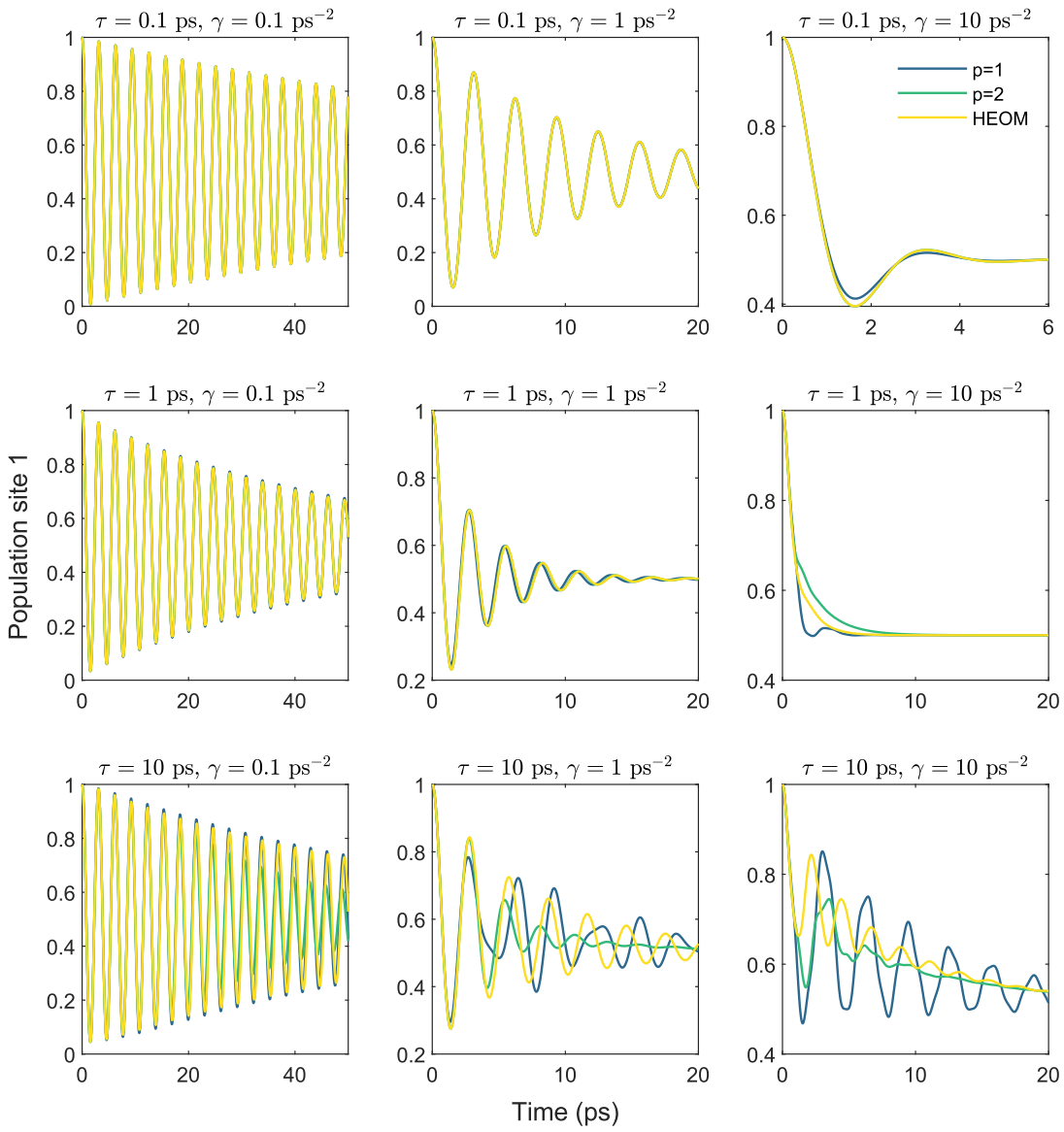

Figure 5. Dynamics of a homodimer system in a wide range of environment parameters. The results of the collision model with $p=1$ (blue) and $p=2$ (green) approximations for the pseudomodes are compared with the solution of HEOM (yellow).

We report Figure 6 to illustrate the populations of the energy levels of the approximated pseudomode coupled to site 1 in the case of $\gamma=1\ \mathrm{ps}^{-2}$ and $\tau=1\ \mathrm{ps}$. As can be seen, in this case, the addition of 2 extra

states in the approximation, *i.e.*, passing from $p=1$ (left panel) to $p=2$ (right panel), has an overall small reorganization effect. That is why the $p=1$ approximation still works with these parameters.

On the other hand, as $\tau\sqrt{\gamma}$ grows there are increasingly discrepancies in the results of Figure 5, showing the limit of the finite-dimensional approximation. In this regard, concerning the dynamics with parameters $\tau=10$ ps and $\gamma=0.1$ ps^{-2}, it is worth noting that similarities between the HEOM solution and the collision model with $p=1$ are only fortuitous. The situation can be improved by increasing the dimension of the Hilbert space of the implemented pseudomodes, that is, by using more states. This poses limitations in the case of a simulation on a classical computer in terms of the resources required. However, from the perspective of a quantum computer, each time we add a qubit for implementing a pseudomode, the number of available states doubles, leading to the well-known and desirable exponential scaling.

Because a rigorous guide for an optimal choice of the parameter p is still lacking, a practical procedural solution is to check for the convergence of the dynamics in the presence of an additional pseudomode qubit on a minimal model.

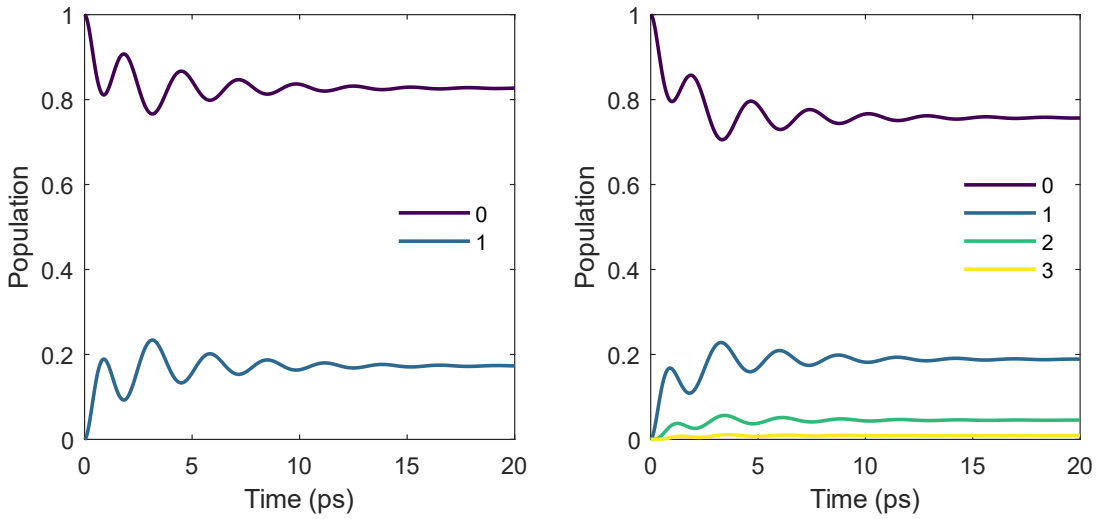

Figure 6. Populations of the pseudomode that is associated to site 1 of a homodimer system. The dynamics is obtained with a collision model with $p=1$ (left panel) and $p=2$ (right panel) approximations for the pseudomodes.

III.3.3 Collisional trajectories and average evolution

Now that we have explored the implementational aspects of the method, let us look closer at the trajectories generated by the collision algorithm. Again, for this purpose, we take the homodimer system with environment parameters $\gamma=1$ ps^{-2} and $\tau=1$ ps, in order to compare the results with the classical noise algorithm. The algorithm was propagated with a time step $\Delta t=50$ fs and we approximated every pseudomode with only one qubit, $p=1$. The procedure is tested through a classical simulation of the quantum algorithm.

In Figure 7, we report in the left panel a single random trajectory for the population of the initial site of the dynamics. Unlike the smooth trajectory of the classical noise algorithm, the population dynamics generated by the collision algorithm has various discontinuities at random times, *e.g.*, at $t \approx 5$ ps. At first glance, one might think that these kinds of jumps are the same as those observed in the previous Chapter for the collision algorithm for the Markovian dynamics of the open system. However, since the collision schemes are completely different in the two cases, the resulting similarities are not obvious at all. In the first place, the collision does not occur directly between the system and the ancilla as in Chapter II, but it is mediated by the pseudomode, and the system is affected only because of the coherent interaction with the latter. Secondly, the interaction operators with the ancillary Markovian environment are completely different. We do not want to go into too much detail here in order not to get off topic. Therefore, we refer the interested reader to Chapter V, where we offer a more in-depth analysis of how this type of interaction method works.

Coming back to the comparison with the classical noise algorithm, consequently to the difference of the trajectories, also the swarm of 200 trajectories of the collision algorithm (green lines in transparency), reported in the right panel, has a completely different distribution. Therefore, in straight analogy with what we have shown in the previous Chapter, we can state that the two algorithms implement different unravellings of the same open dynamics, obtained as the ensemble average over the trajectories.[2]

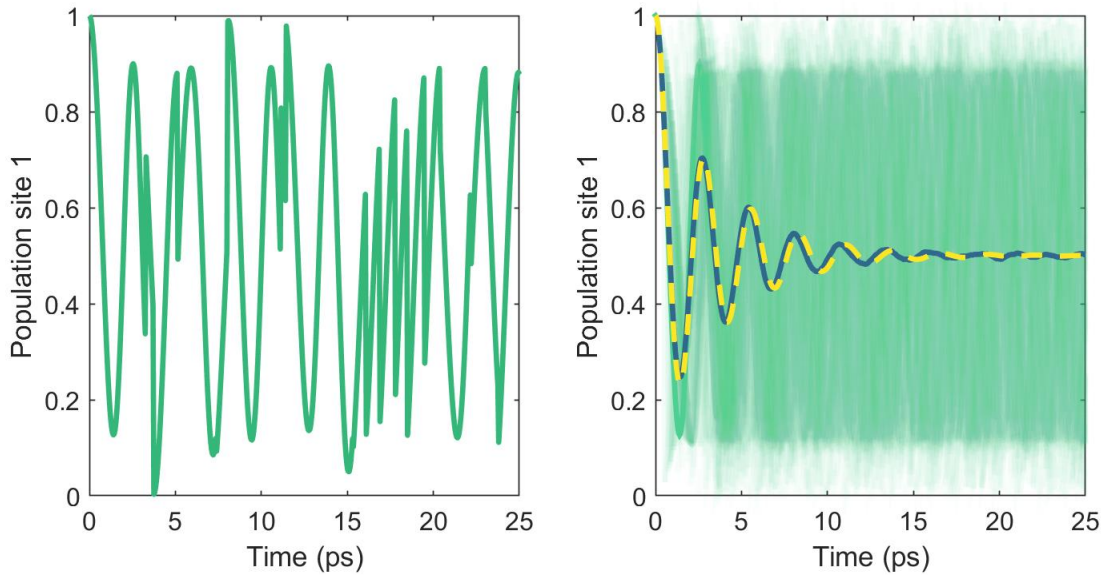

Figure 7. Left panel: the stochastic dynamics of a single trajectory obtained monitoring the initially populated site of a dimeric open system obtained by the collision algorithm with a 2-level approximation for each pseudomode. Right panel: an ensemble of 200 trajectories (green). The average dynamics over 10^4 trajectories (blue) fits precisely the results by HEOM (yellow).

[2] Note that there is a slight detuning of the coherent beatings between the dynamics produced by the collision algorithm and the one originating from HEOM. As discussed above, this is due to the finite-state approximation of the pseudomodes (see Figure 5).

III.4 Results and discussion

III.4.1 Effects of the memory time

We have seen so far that coloured noise can be implemented in simulation algorithms to account for the memory time of the environment. Now, by exploiting the simulation routines and the HEOM reference, we examine the effects of the resulting non-Markovianity on the dynamics of an open system and in particular on the efficiency profile. The equivalent noise strength $\gamma\tau$ will be here the control parameter, as it defines the Markovian evolution and all the shades of non-Markovian dynamics through eqs. (III.1) and (III.3). Our case-study for this section will be the 4-site cyclic network used in the previous Chapter. For completeness, we recall the site energies $\varepsilon_1 \approx 0.44\ \text{ps}^{-1}$, $\varepsilon_2 \approx 0.24\ \text{ps}^{-1}$, $\varepsilon_3 \approx -3.22\ \text{ps}^{-1}$ and $\varepsilon_4 \approx 0.36\ \text{ps}^{-1}$, and coupling between adjacent sites $V = 1\ \text{ps}^{-1}$. The dynamics starts with the excitation localized at site 1, and we monitor the population at site 3 to calculate the transport efficiency, defined as (cf. Chapter II)

$$\eta_{j=3}(t) = \int_0^t \rho_{33}(t')dt', \tag{III.32}$$

where $\rho_{33}(t)$ is the value of the third diagonal entry of the system density matrix (*i.e.*, the population at site 3).

In Figure 8, we report the transport efficiency at time $t = 40\ \text{ps}$ as a function of the equivalent noise strength $\gamma\tau$. The various curves have been calculated for growing memory time of the environment, from $\tau \to 0$ (Markovian limit) to $\tau = 1\ \text{ps}$ (where the environment has a relaxation time comparable with the site coupling). The Markovian transport efficiency is simulated by solving the relative Lindblad master equations (see the previous Chapter), while continuous lines are the results of HEOM computations for finite correlation times. We set $\gamma\tau = 20\ \text{ps}^{-1}$ as the upper limit of the equivalent noise strength, as deep hierarchical series and long computational time are required for higher values, especially when τ increases. Results from simulations of our quantum algorithms using Qiskit QASM simulator [59] are also shown for $\tau = 1\ \text{ps}$ (circles), and will be discussed in a dedicated paragraph below.

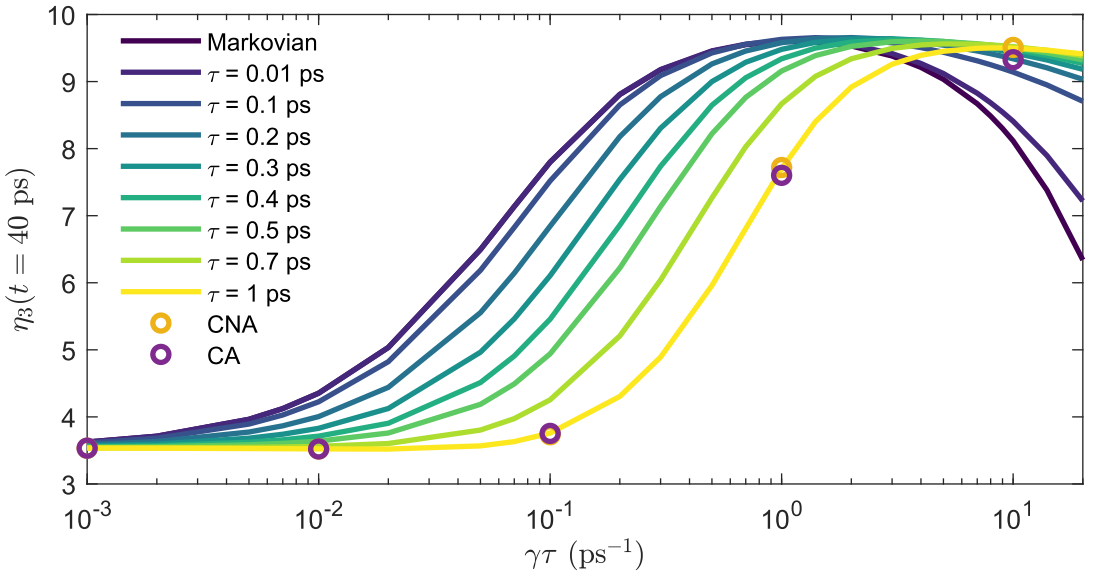

Figure 8. The efficiency of transport in a 4-site cyclic network. Lines represent different memory times of the environment ranging from $\tau \to 0$ (Markovian limit, obtained solving a Lindblad master equation) to $\tau = 1$ ps (calculated using HEOM). For $\tau = 1$ ps, we also report the transport efficiency computed by a Qiskit QASM simulation of our Classical Noise Algorithm (CNA, orange circles) and Collision Algorithm (CA, violet circles). Each circle is the ensemble average over 10^4 samples. For the CA, we used a single qubit to approximate a pseudomode. The time step for the simulations was set at $\Delta t = 50$ fs.

The first thing to notice is that in all cases the efficiencies of transport exhibit a phenomenology similar to the Markovian one, first increasing thanks to the interaction with the environment and finally dropping in a slow diffusion regime, which is the hallmark of ENAQT. At low values of $\gamma\tau$, *i.e.*, when the interaction with the environment is weak and the relaxation dynamics is slow, we have low efficiency. This is because our network has an energetic static disorder, due in particular to a prominent energy gap between site 3 and its neighbours. So, a weak interaction with the environment is not sufficient to overcome localization in the system within the time limit chosen to measure efficiency.

Then, there is an intermediate range of parameters where the noise and the coherences of the system cooperate to enhance transport. Here, $\gamma\tau$ is strong enough for the decoherence effect to play a role. We observe that longer correlation times, therefore slower environments, requires a higher equivalent noise strength to induce the enhancement. This is shown by the drift of the efficiency profile going from the violet line (Markovian) to the yellow line (slowest environment) in Figure 8.

Enhanced efficiency stems from a balance between the coherent and incoherent contributions to the overall quantum dynamics. Therefore, to rationalize the effect of a finite correlation time, let us analyse the population dynamics at site 3 for an equivalent noise strength of $\gamma\tau = 0.1\,\text{ps}^{-1}$ and $1\,\text{ps}^{-1}$ for various τ (Figure 9). From Figure 8, we can see that in these cases the Markovian dynamics is closed to the maximum efficiency, while the efficiency decreases as the environment gets slower. Interestingly, for the same $\gamma\tau$, longer memory times

of the environment have the effect of sustaining the system coherences, as reflected by the persistent coherent beating of the site population (see green and yellow traces). Notice that such coherent beating will necessarily die out following the complete relaxation of the dynamics which admit equally distributed site populations as stationary solution.

By comparing dynamics with similar efficiency (Figure 10), we notice that the beatings are damped faster for longer correlation times τ, while the relaxation to the asymptotic population is comparable between Markovian and non-Markovian dynamics. This suggests that, for the considered system, the efficiency is primarily determined by the timescale of the relaxation. A striking evidence that longer living coherences does not imply higher transfer efficiency. Figure 9 shows that this timescale of the relaxation is heavily dependent on the environment correlation time. Indeed, the coherence between different sites, sustained by τ, keeps the system far from the asymptotic solution. An higher equivalent noise strength is thus needed to get the same efficiency, which is the cause of the right-drift of the transport efficiency curve with increasing memory time τ.

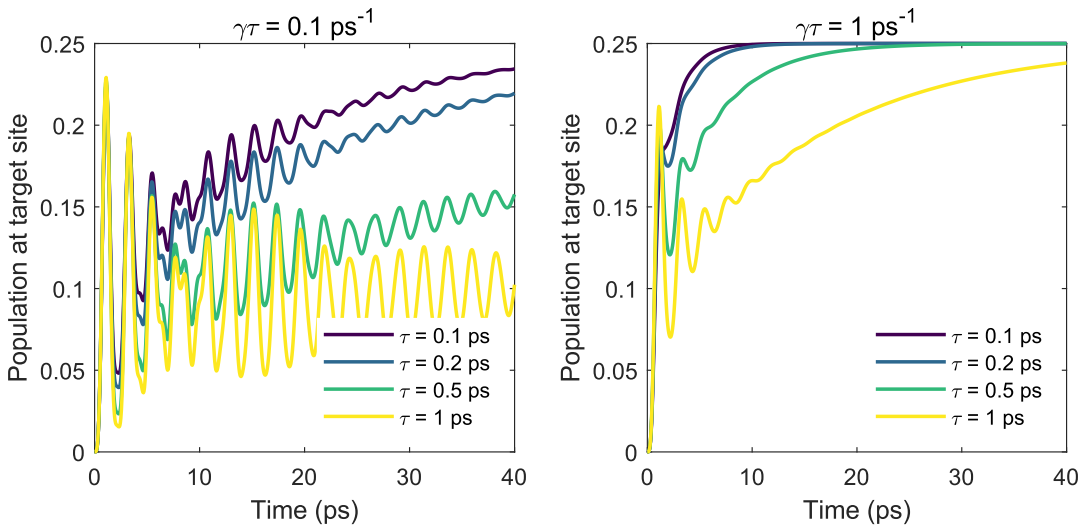

Figure 9. Comparison of the dynamics of the target site population for environments with equivalent noise strength $\gamma\tau = 0.1\ \mathrm{ps}^{-1}$ (left panel) and $\gamma\tau = 1\ \mathrm{ps}^{-1}$ (right panel). Differences in the memory time of the environment, $\tau = 0.1$ ps (violet), $\tau = 0.2$ ps (blue), $\tau = 0.5$ ps (green) and $\tau = 1$ ps (yellow), lead to different damping of the coherent beating and relaxation.

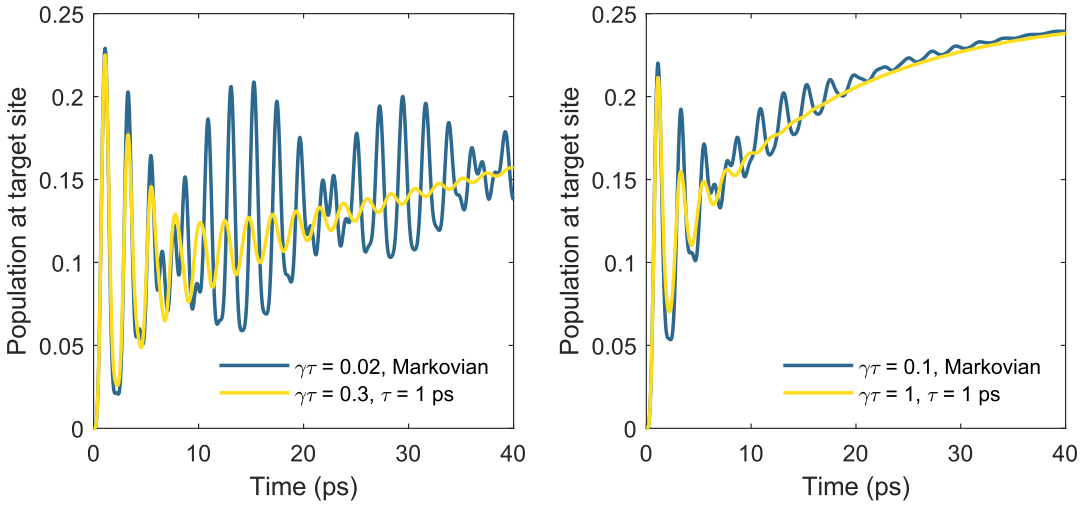

Figure 10. Comparison of the dynamics of the target site population for efficiency $\eta_3(t = 40\ \text{ps}) \approx 5.00$ (left panel) and $\eta_3(t = 40\ \text{ps}) \approx 7.80$ (right panel). Differences in the correlation time of the environment, vanishing (blue line) and $\tau = 1\ \text{ps}$ (yellow line), lead to the same thermalization rate but different dephasing rates.

The last regime to consider is when ENAQT is suppressed by the strong decohering effect of the environment, *i.e.*, in the limit of large $\gamma\tau$. It is known that in this limit the dynamics is largely controlled by the dissipative dynamics and transport becomes incoherent. In this conditions, the coupling V_{jl} between sites can be treated as a perturbation and the evolution of the site populations is well-described by a hopping mechanism where the transfer rates are calculated via the Fermi golden rule (leading to Förster theory in exciton transport, see Appendix B of Chapter IV for further details) [2,24,60–62]. In our case, the kinetic equation reads

$$\frac{dP_j(t)}{dt} = \sum_l \kappa_{jl} P_l(t), \tag{III.33}$$

where $P_j(t) = \rho_{jj}(t)$ are the site populations and the transfer rates can be demonstrated to be [2,60]

$$\kappa_{j\neq l} = 2V_{jl}^2\,\text{Re}\left\{\int_0^\infty \exp\left[\text{i}\left(\varepsilon_j - \varepsilon_l\right)t - 2\gamma\tau + 2\gamma\tau^2\left(1 - \exp\left(-t/\tau\right)\right)\right]dt\right\}, \quad \kappa_{jj} = -\sum_{l\neq j}\kappa_{jl}\,. \tag{III.34}$$

The transfer rates are suppressed in the limit $\gamma \to \infty$, causing the decrease of the efficiency (as in the quantum Zeno effect discussed in the previous Chapter). Moreover, eq. (III.34) suggests that there should be a threshold value of $\gamma\tau$ over which the differences of the site energies become irrelevant. Above such a critical value, we expect that the topology of the network, V_{ij}, γ and τ become the only significant parameters for the dynamics. To prove this point, we generate a representative ensemble of Hamiltonians for a 4-site cyclic topology. Hamiltonians present static disorder on the site energies with standard deviation $2\ \text{ps}^{-1}$ (cf. Chapter

II). In Figure 11, we show the profile of the transport efficiency generated by the ensemble for different memory times of the environment, from memoryless to $\tau = 1$ ps. To obtain the profiles, we solve the dynamics with HEOM for points up to $\gamma\tau = 50$ ps^{-1} (except for the Markovian case, for which we used the correspondent Lindblad equation), while for higher values of the equivalent noise strength we solve directly the incoherent master equation for the dynamics of the populations. As can be noted, the two parts match smoothly. However, to have further proof that the incoherent hopping gives a reliable description, we also report some values of the transport efficiency at high $\gamma\tau$ for $\tau = 1$ ps obtained by a classical simulation of the classical noise algorithm (average over 10^4 trajectories). Contrary to HEOM, whose hierarchical depth becomes intractable in this regime, the classical noise algorithm maintains the same computational scaling allowing for a comparison with the incoherent master equation.
The results verify both the transport suppression at high $\gamma\tau$ and the predicted convergence of the profiles in the same limit due to the vanishing influence of the static disorder.

Besides confirming the independence of the transport efficiency from the particular realization of the site energies in the incoherent regime, Figure 11 offers another interesting evidence. In most cases, the maximum value of the efficiency, for this molecular network topology, is not much affected by the non-Markovianity of the environment (even if the maximum is shifted toward an higher value of the equivalent noise strength as noted above). However, in some cases (see for example the curve with a pronounced peak at $\gamma\tau = 0.3$ ps^{-1} for $\tau = 1$ ps), longer environment correlation times can result in a significant improvement of the efficiency, with clear advantages over the Markovian situation. This phenomenology is clearly linked to spectral features realized in that particular instance of the static disorder, but a full rationalization is still missing and will be the object of future investigations.

We conclude this part with a final remark. The incoherent equation (III.33) is evidently Markovian and this might seem bizarre given that we were starting from dynamics with clear non-Markovian signatures. However, this is absolutely in line with what is shown in Appendix B, where the degree of non-Markovianity goes to zero in the limit of $\gamma \to \infty$.

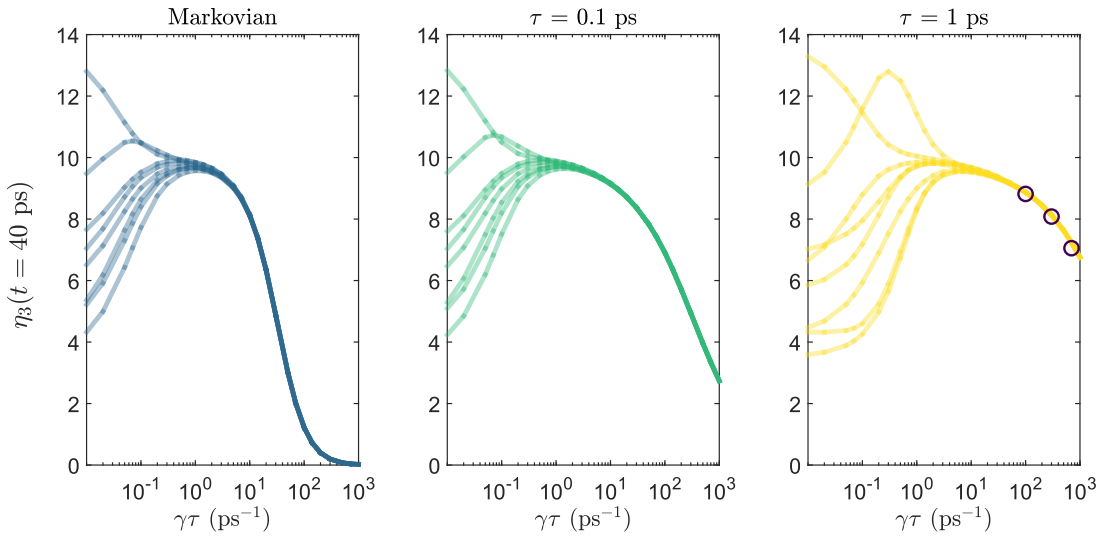

Figure 11. Transport efficiency generated by a representative ensemble of 4-site cyclic networks with different static disorders on the site energies. Results have been obtained by solving the correspondent dynamics using the Lindblad master equation ($\tau \to 0$, blue lines) or HEOM ($\tau = 0.1$ ps, green lines, and $\tau = 1$ ps, yellow lines) for $\gamma\tau < 50$ ps^{-1}, while the incoherent master equation (III.33) was used for the rest. As a benchmark for the incoherent master equation, some values of transport efficiency at high $\gamma\tau$ have been computer with a simulation of the classical noise algorithm (violet circles for $\tau = 1$ ps).

III.4.2 Qiskit QASM simulations and comparison of the algorithms

In the previous paragraph, we showed that a finite memory time for the environment can strongly affect the dynamics of the system and change some fundamental quantities such as the dephasing time and transport efficiency. This requires reliable algorithms that can simulate the dynamics of even large systems, preferably with short computational times. The quantum algorithms we propose are designed with this aim.

However, quantum computers are not yet ready for interesting simulations of non-trivial quantum dynamics. Tentative implementations of collision models on real (noisy) digital quantum devices have been recently reported in refs. [44,63] for small systems. In particular, Cattaneo *et al* report a collision model to study the super- and sub-radiance between two qubits emitting in the same environment, showing theoretical and experimental error bounds [63]. From their "experiments" it is evident that, even if their collision model is propagated for a few time steps, the amount of noise from gate error is still considerably high. Furthermore, in their implementation, they had to replace the ancilla qubits with a new qubit after every interaction, as they found that the use of the reset gate introduces too many decoherences in today's quantum computer.

While waiting for a new generation of more noise-resilient quantum computers, which would actually allow the execution of interesting circuits, we simulate our algorithms with the IBM Qiskit QASM simulator. The dynamics are executed for $\tau = 1$ ps with time step $\Delta t = 50$ fs and using $p = 1$ qubit to implement each

pseudomode in the collision algorithm. For the classical noise algorithm, the results are the average over 10^4 independent circuits, each one representing a unique realization of the noise trajectories and sampled with a single measure (single shot). For the collision algorithm, we run and measure 10^4 times the same circuit, because the trajectories naturally emerge from the reset of the ancilla qubit. Results of the transport efficiency are shown in Figure 8 as circles. The classical noise algorithm fits very well the transport efficiency calculated by HEOM in all the range of parameters, while the collision algorithm underestimates the values at $\gamma\tau = 1$ ps and $\gamma\tau = 10$ ps^{-1}. However, this is in complete accordance with the analysis reported in section III.3.2 related to the number of states included in pseudomode representation.

For completeness, in Figure 12, we show the output of the algorithms for the dynamics with $\gamma\tau = 1$ ps^{-1}. Yellow dots represent the population measured at site 3. Despite some noise due to finite sampling, here we see that the classical noise algorithm faithfully follows the exact dynamics, as expected. On the other hand, the collision algorithm displays a slightly underestimation of the average population which explains the small deviation in the efficiency.

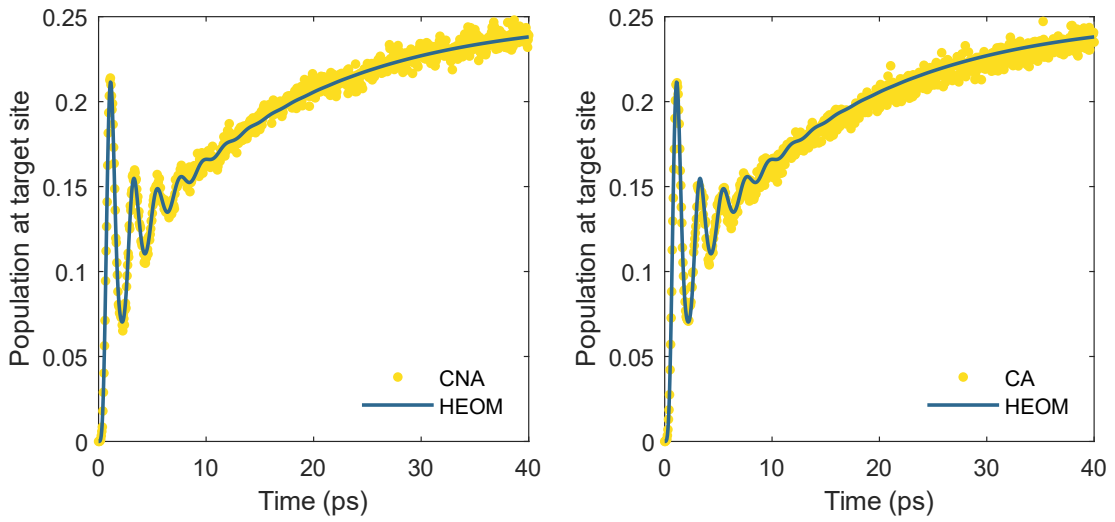

Figure 12. Time evolution of the population at site 3. Results for the Classical Noise Algorithm (CNA, left panel) and Collision Algorithm (CA, right panel) are obtained with Qiskit QASM simulator. The exact numerical solution is calculated with HEOM (blue line). The time step for the algorithmic evolution is $\Delta t = 50$ fs, and the environment parameters are $\gamma\tau = 1$ ps^{-1} and $\tau = 1$ ps. Pseudomodes in the collision algorithm are implemented using one qubit.

Unlike the Markovian dynamics seen in the previous Chapter, in which the quantum versions of both the classical noise and collision algorithms gave comparable results and scaling, in this case, the differences are such that the choice should be directed toward the classical noise algorithm for most applications. Indeed, this algorithm allows accurate results to be obtained over a wide range of parameters, without the need to expand the quantum register beyond the number of qubits required for the system. Moreover, it maintains the same

algorithmic scaling of $\mathcal{O}\left(N^2\right)$ found for the white noise implementation. In contrast, for the collision algorithm, it is necessary to include a quantum register for the pseudomodes and one for the ancilla. In addition, to achieve the same results as the classical noise algorithm at high $\tau\sqrt{\gamma}$, it may be necessary to further expand the pseudomode register, *i.e.*, add more qubits.

Although these inconveniences, the collision algorithm has great potential as it offers the possibility to study entanglement and thermodynamic quantities affecting the open system and its environment (see for example [64]). In this regard, running the collision algorithm on a quantum computer is expected to give advantages over a classical simulation. In fact, the collision model presented here requires 2^{pN} degrees of freedom for the implementation of the N pseudomodes approximated with 2^p levels each. On a classical computer, the problem becomes soon expensive for large N (also in the case of $p=1$), due to the exponential scaling. But a quantum computer requires only pN qubits for the pseudomodes, which is an exponential saving of resources. Regarding the circuit depht, the number of gates required to solve the problem scales polynomially with N and with the number of states of each pseudomode (see Appendix C). This means that quantum computers could in principle efficiently manage the problem and offer a quantum advantage with respect to classical computation.

III.5 Conclusions

In this Chapter, we have explored the phenomenology of quantum transport on networks assisted by a coloured environment. We showed that a site-dephasing environment with exponentially damped time-correlations can lead to non-negligible non-Markovian signatures in the dynamics of the open system.

At the same equivalent noise strength $\gamma\tau$, non-Markovian dynamics were found to have more persistent coherences in the examined situations. This observation is in line with what is found in refs. [24,65,66] for the Drude-Lorentz spectral density and in ref. [65] for an Ohmic spectral density with an exponential cutoff.

Non-Markovianity also affects some important quantities such as the transport efficiency. However, the effect of a slower environment can be both detrimental or beneficial depending on the specific realization of the Hamiltonian, confirming a non-trivial interplay between the coherent and the incoherent contributions to the quantum dynamics in determining the overall efficiency. A general rationalization of such an interplay is still missing to the best of out knowledge and it is an intriguing issue which is left for future works.

At high $\gamma\tau$, we found that the dynamics of the open system becomes incoherent and can be described by a kinetic master equation where the transfer rates are calculated via the Fermi golden rule assuming perturbative coupling between sites. In this regime, at certain values of $\gamma\tau$, the static disorder in the site energies of the network becomes irrelevant and all the networks with the same topology and coupling strength have similar dynamics.

As finite memory time for the environment can strongly affect the dynamics of the open system we expanded the quantum algorithmic package introduced in the previous Chapter in order to account for the non-

Markovian effects. Both algorithms rely on an effective representation of the environment for their implementation. For the classical noise algorithm, the generalization is straightforward, while for the collision algorithm we opted for the inclusion of external degrees of freedom (the pseudomodes) to account for the memory effects. In straight analogy with what we have shown in the previous Chapter, the two algorithms implement different unravellings of the same open system dynamics.

The resource and algorithmic scaling of the classical noise algorithm proved to be advantageous with respect to the collision one. However, the collision algorithm offers the possibility to analyse the thermodynamics of the interaction with the environment with a quantum advantage over a classical simulation of the same algorithm.

In our proposal, the algorithms are designed to simulate the effect of an environment with a Lorentzian spectral density centred in $\omega = 0$. However, both algorithms can be easily adapted to simulate more general spectral densities that can be decomposed as a sum of non-negative Lorentzian contributions. In one case, this can be done by adding more fluctuations as reported in [2]. In the other case, it is sufficient to insert new pseudomodes that are harmonic oscillators whose frequencies correspond to the central frequencies of the Lorentzian peaks [52–54].

III.6 Appendix A

Here we revise the statistical properties of the Ornstein-Uhlenbeck process by adapting Gillespie notation [3,4] for our purposes. The mean of the fluctuations describing the process is defined as

$$\overline{\delta\varepsilon_j(t)} = \delta\varepsilon_j(t_0)\, e^{-(t-t_0)/\tau} + \overline{\delta\varepsilon_j(t\to\infty)}\left(1 - e^{-(t-t_0)/\tau}\right), \tag{III.35}$$

where $\delta\varepsilon_j(t_0)$ is the initial value of the fluctuation at time $t_0 = 0$, τ is the correlation time of the fluctuation, while $\overline{\delta\varepsilon_j(t\to\infty)}$ is the mean value at long times, $t \gg \tau$. Here, we assume fluctuations to oscillate around zero at long times, *i.e.*, $\overline{\delta\varepsilon_j(t\to\infty)} = 0$.

The variance of the fluctuation is given by

$$\begin{aligned} \mathrm{var}\left\{\delta\varepsilon_j(t)\right\} &= \overline{\delta\varepsilon_j^2(t)} - \overline{\delta\varepsilon_j(t)}^2 \\ &= \gamma\left(1 - e^{-2(t-t_0)/\tau}\right) \end{aligned} \tag{III.36}$$

where γ is the fluctuation amplitude, and the auto-covariance is

$$\begin{aligned} \mathrm{cov}\left\{\delta\varepsilon_j(t_2), \delta\varepsilon_j(t_1)\right\} &= \overline{\delta\varepsilon_j(t_2)\,\delta\varepsilon_j(t_1)} - \overline{\delta\varepsilon_j(t_2)}\cdot\overline{\delta\varepsilon_j(t_1)} \\ &= \gamma\left(e^{-|t_2-t_1|/\tau} - e^{-(t_2+t_1-2t_0)/\tau}\right) \end{aligned} \tag{III.37}$$

The process, as introduced above, depends on the specific initial condition $\delta\varepsilon_j(t_0)$, which has no particular meaning in our case as there is no reason why our system should be initialized to a specific value of the

fluctuation at the beginning of the dynamics. This problem is solved when the process becomes stationary, that is in two cases: for long times, so that

$$\min\{t_2,t_1\}-t_0 \gg \tau\,, \tag{III.38}$$

or by randomly sorting the initial value $\delta\varepsilon_j(t_0)$ for every different realization of the process. The first case reconducts to the second if one takes an initial time of the fluctuations $t_0 \to -\infty$ different from the initial time of the dynamics $t=0$. In this way, the condition (III.38) is always valid for $t_1,t_2 \geq 0$. For the stationary process, the moments become independent on t

$$\overline{\delta\varepsilon_j(t)} = \overline{\delta\varepsilon_j(t\to\infty)} = 0, \quad \mathrm{var}\{\delta\varepsilon_j(t)\} = \gamma \tag{III.39}$$

and the covariance becomes equal to the correlation function

$$\mathrm{cov}\{\delta\varepsilon_j(t_2),\delta\varepsilon_j(t_1)\} = \overline{\delta\varepsilon_j(t_2)\delta\varepsilon_j(t_1)} = \gamma e^{-|t_2-t_1|/\tau}\,. \tag{III.40}$$

III.7 Appendix B

In ref. [67], Breuer and coworkers proposed an indicator for the degree of non-Markovianity in the dynamics of open quantum systems. They pointed out that all positive and trace-preserving dynamical maps $\Phi(t)$ are contractions [68] for the trace distance [69]

$$D(\rho_1,\rho_2) = \frac{1}{2}\mathrm{Tr}|\rho_1-\rho_2|, \tag{III.41}$$

with $|A| = \sqrt{A^\dagger A}$, measuring the distinguishability of two quantum states ρ_1 and ρ_2. Practically, the condition

$$D(\Phi(t)[\rho_1],\Phi(t)[\rho_2]) \leq D(\rho_1,\rho_2) \tag{III.42}$$

holds for Markovian master equations as Lindblad-form master equations, even with time-dependent Lindblad operators and relaxation rates (as long as they are ≥ 0 at all times). Time intervals in which eq. (III.42) is not valid are interpreted as a backflow of information from the environment to the system, enhancing the distinguishability of the states. Looking at the slope of D, *i.e.*

$$\sigma(t,\rho_{1,2}(0)) = \frac{d}{dt}D(\rho_1(t),\rho_2(t))\,, \tag{III.43}$$

these time intervals are characterized by $\sigma(t,\rho_{1,2}(0)) > 0$. The degree of non-Markovianity $\mathcal{N}$ of the process $\Phi(t)$ is then defined as

$$\mathcal{N} = \max_{\rho_{1,2}(0)} \int_{\sigma>0} \sigma(t,\rho_{1,2}(0))\,dt\,, \tag{III.44}$$

where the time integral is over all the time intervals satisfying $\sigma(t,\rho_{1,2}(0)) > 0$, and the maximum is taken over all pairs of pure and mixed initial states $\rho_1(0)$ and $\rho_2(0)$.

In Figure 13, we tested the non-Markovianity in the dynamics of a dimer system with site-energy fluctuations described by OU processes. The dynamics were simulated with HEOM (see section III.2) using the following parameters for the dimer system: $\varepsilon_1 = \varepsilon_2 = 0$ and $V = 1\ \text{ps}^{-1}$. In the left panel, we keep $\gamma = 1\ \text{ps}^{-2}$ fixed and vary the memory time. As one could expect, non-Markovianity $\mathcal{N}$ increases with τ, meaning that the longer the memory time of the environment, the more the backflow of information to the system [67]. The increase seems to be exponential for high τ. In the right panel, we do the opposite by fixing $\tau = 1\ \text{ps}$ and changing γ. Here, we identify three different behaviours. In the limit of $\gamma \to 0$ we see vanishing non-Markovianity. This is expected since small values of γ mean weak interactions with the environment. At high γ, transport becomes incoherent and it can be described approximated by a proper Pauli master equation as discussed in section III.4.1. As Pauli master equations are Markovian, $\mathcal{N}$ decrease until it vanishes as $\gamma \to \infty$. Consequently, in the intermediate region, the expected increase and decrease are observed, leading to a maximum degree of non-Markovianity $\mathcal{N}$ in the region $0.1\ \text{ps}^{-2} < \gamma < 1\ \text{ps}^{-2}$.

Similar results were observed by Rebentrost and Aspuru-Guzik for the Drude-Lorentz spectral density [70]. However, caution must be observed in generalizing the results to other forms of Hamiltonian. For example, it is known that for a diagonal Hamiltonian with OU fluctuations, *i.e.*, by assuming no coupling between sites, the dynamics is purely Markovian [71].

It is worth mentioning that the definition of witnesses of non-Markovianity is still an open problem. This type of measure of non-Markovianity is limited to some classes of non-Markovian maps and it excludes, for example, non-Markovian dynamics that represent a contraction of trace-distance, such as those reported in ref. [72]. Other metrics have been designed based on the refinement of the degree of non-Markovianity (see for example [73]), but the topic is beyond the scope of this thesis.

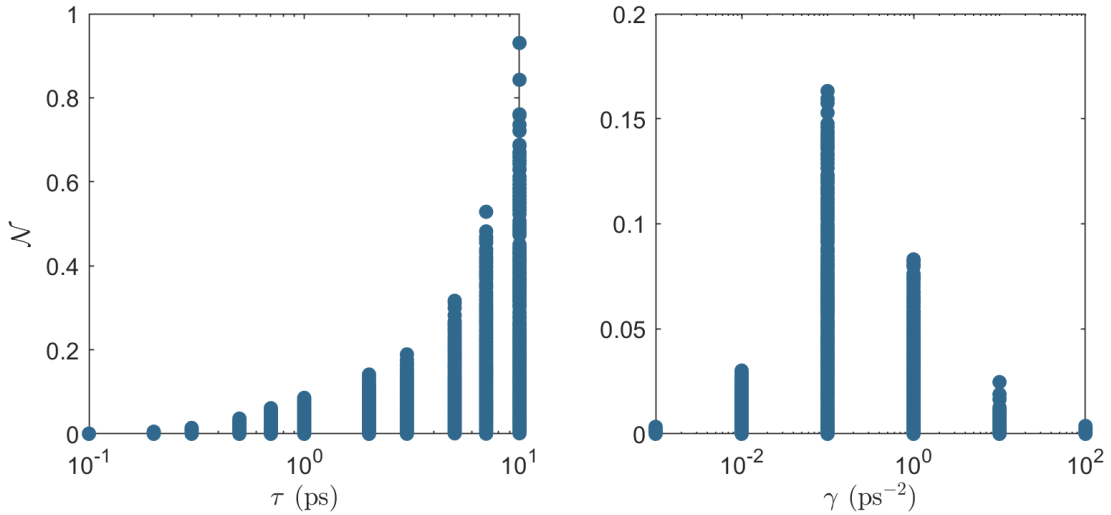

Figure 13. Measures of non-Markovianity in the dynamics of a dimer system as a function of the memory time of the environment τ (left panel) and fluctuation amplitude γ (right panel). For each set of parameters (γ,τ), we sampled 500 randomly-drawn pairs of initial states whose values of non-Markovianity are represented as dots in the figures.

III.8 Appendix C

Steps of the collision algorithm for the quantum simulation of transport in a network with an exponentially correlated site-dephasing:

a) Initialize the system quantum register to the initial state of the dynamics $|j_0\rangle$;

b) Apply gate corresponding to operator U^{S} to the system register;

c) Sequentially apply gates corresponding to operators $U_j^{\mathrm{s+p}}$ and $U_j^{\mathrm{p+\bar{a}}}$ to the system plus pseudomode registers and to the pseudomode plus ancilla register, respectively;

d) Reset the ancilla;

e) Repeat steps c) and d) for $j\in\{1,2,...,N\}$;

f) Create a copy of the circuit, so that you have two identical objects: a quantum circuit $\mathcal{A}$ that will be the lead and its copy $\mathcal{B}$ to which the measurement gate will be appended;

g) Add measurement gates to the clone of the system register in circuit $\mathcal{B}$ to read the populations of the system;

h) Discard circuit $\mathcal{B}$ and continue with circuit $\mathcal{A}$;

i) Repeat steps from b) to h) for $s\in\{0,1,...,S=t/\Delta t\}$, where t is the final time of the dynamics.

We now briefly discuss the scaling of the collision algorithm for both mappings presented in the previous Chapter. In the algorithmic mapping, the system quantum register contains $\lceil \log_2 N \rceil$ qubits, so that the system

operator U^{s} is decomposed using $\mathcal{O}\left(4^{\lceil \log_2 N \rceil}\right) = \mathcal{O}\left(N^2\right)$ CNOT gates. Then, each interaction operator $U_j^{\mathrm{s+p}}$ acts on a Hilbert space that includes the system plus a pseudomode, leading to a gate count of $\mathcal{O}\left(4^{\lceil \log_2 N \rceil + p}\right) = \mathcal{O}\left(N^2 4^p\right)$ CNOT gate. The last element is the pseudomode-ancilla interaction, implemented with $\mathcal{O}\left(4^{p+1}\right) = \mathcal{O}\left(4^p\right)$ CNOT gates for each $U_j^{\mathrm{p+\bar{a}}}$ operator. Since there are N system-pseudomode and pseudomode-ancilla interactions, we have a $\mathcal{O}\left(N^3 4^p\right)$ and $\mathcal{O}\left(N 4^p\right)$ scaling, respectively. Thus, the final CNOT gate count is $\mathcal{O}\left(N^3 4^p\right)$, *i.e.*, cubic with respect to the system dimension and quadratic with respect to the number of states for the implementation of a pseudomode (which we recall to be 2^p).

In the physical mapping, every site of the network is mapped as the state $|1\rangle$ of a qubit, requiring N qubits for the implementation of the system. The system Hamiltonian and the system-pseudomode interaction must be redefined accordingly. See the previous Chapter for the details. The new system operator U^{s} scales differently based on network connectivity, from $\mathcal{O}\left(N^2\right)$ for fully connected systems to $\mathcal{O}(N)$ for linear or cyclic chains. The system-pseudomode operator $U_j^{\mathrm{p+\bar{a}}}$ becomes an interaction between a single qubit implementing a site and the pseudomode qubits, needing $\mathcal{O}\left(4^{p+1}\right) = \mathcal{O}\left(4^p\right)$ CNOT gates for the implementation. Since there are N system-pseudomode interactions, the count is $\mathcal{O}\left(N 4^p\right)$ CNOTs, exactly the same as for the interactions between the pseudomodes and the ancilla. Therefore, for the physical mapping, we have a polynomial scaling ($\mathcal{O}\left(N^2\right)$ in the worst case) with the system dimension and quadratic with the number of states for the implementation of a pseudomode.

In addition, with both types of mapping, we need to apply N times the reset gate to the ancilla per time step (*i.e.*, after every interaction).

III.9 References

[1] A.S. Bondarenko, J. Knoester, T.L.C. Jansen, Comparison of methods to study excitation energy transfer in molecular multichromophoric systems, Chem. Phys. 529 (2020) 110478. https://doi.org/10.1016/j.chemphys.2019.110478.

[2] A.G. Dijkstra, C. Wang, J. Cao, G.R. Fleming, Coherent Exciton Dynamics in the Presence of Underdamped Vibrations, J. Phys. Chem. Lett. 6 (2015) 627–632. https://doi.org/10.1021/jz502701u.

[3] D.T. Gillespie, Exact numerical simulation of the Ornstein-Uhlenbeck process and its integral, Phys. Rev. E. 54 (1996) 2084–2091. https://doi.org/10.1103/PhysRevE.54.2084.

[4] D.T. Gillespie, The mathematics of Brownian motion and Johnson noise, Am. J. Phys. 64 (1996) 225–240. https://doi.org/10.1119/1.18210.

[5] P.W. Anderson, Absence of Diffusion in Certain Random Lattices, Phys. Rev. 109 (1958) 1492–1505. https://doi.org/10.1103/PhysRev.109.1492.

[6] P.W. Anderson, Local Moments and Localized States, Science. 201 (1978) 307–316. https://doi.org/10.1126/science.201.4353.307.

[7] G.J. Moro, G. Dall'Osto, B. Fresch, Signatures of Anderson localization and delocalized random quantum states, Chem. Phys. 514 (2018) 141–149. https://doi.org/10.1016/j.chemphys.2018.03.006.

[8] G. Dall'Osto, Localizzazione di Anderson: Fenomenologia e modelli, Università degli Studi di Padova, 2017.

[9] F. Gallina, Effetti del disordine sull'equilibrazione dell'algoritmo di quantum walk: Studio teorico di un'implementazione nanoscopica, Università degli Studi di Padova, 2019.

[10] M. Bruschi, Stochastic Models of Disorder in Excitonic Systems : Localization , Decoherence and Optical Response, Università degli Studi di Padova, 2020.

[11] A. Schreiber, K.N. Cassemiro, V. Potoček, A. Gábris, I. Jex, C. Silberhorn, Decoherence and Disorder in Quantum Walks: From Ballistic Spread to Localization, Phys. Rev. Lett. 106 (2011) 180403. https://doi.org/10.1103/PhysRevLett.106.180403.

[12] H.-P. Breuer, F. Petruccione, The Theory of Open Quantum Systems, Oxford University Press, Oxford, 2007. https://doi.org/10.1093/acprof:oso/9780199213900.001.0001.

[13] A. Rivas, S.F. Huelga, Open Quantum Systems, Springer Berlin Heidelberg, Berlin, Heidelberg, 2012. https://doi.org/10.1007/978-3-642-23354-8.

[14] A.A. Budini, Quantum systems subject to the action of classical stochastic fields, Phys. Rev. A. 64 (2001) 052110. https://doi.org/10.1103/PhysRevA.64.052110.

[15] A. Chenu, M. Beau, J. Cao, A. del Campo, Quantum Simulation of Generic Many-Body Open System Dynamics Using Classical Noise, Phys. Rev. Lett. 118 (2017) 140403. https://doi.org/10.1103/PhysRevLett.118.140403.

[16] N. Makri, Numerical path integral techniques for long time dynamics of quantum dissipative systems, J. Math. Phys. 36 (1995) 2430–2457. https://doi.org/10.1063/1.531046.

[17] N. Makri, D.E. Makarov, Tensor propagator for iterative quantum time evolution of reduced density matrices. I. Theory, J. Chem. Phys. 102 (1995) 4611–4618. https://doi.org/10.1063/1.469509.

[18] A.W. Chin, Á. Rivas, S.F. Huelga, M.B. Plenio, Exact mapping between system-reservoir quantum models and semi-infinite discrete chains using orthogonal polynomials, J. Math. Phys. 51 (2010) 092109. https://doi.org/10.1063/1.3490188.

[19] J. Prior, A.W. Chin, S.F. Huelga, M.B. Plenio, Efficient Simulation of Strong System-Environment Interactions, Phys. Rev. Lett. 105 (2010) 050404. https://doi.org/10.1103/PhysRevLett.105.050404.

[20] D. Suess, A. Eisfeld, W.T. Strunz, Hierarchy of Stochastic Pure States for Open Quantum System Dynamics, Phys. Rev. Lett. 113 (2014) 150403. https://doi.org/10.1103/PhysRevLett.113.150403.

[21] R. Hartmann, W.T. Strunz, Exact Open Quantum System Dynamics Using the Hierarchy of Pure States (HOPS), J. Chem. Theory Comput. 13 (2017) 5834–5845. https://doi.org/10.1021/acs.jctc.7b00751.

[22] P.-P. Zhang, A. Eisfeld, Non-Perturbative Calculation of Two-Dimensional Spectra Using the Stochastic Hierarchy of Pure States, J. Phys. Chem. Lett. 7 (2016) 4488–4494. https://doi.org/10.1021/acs.jpclett.6b02111.

[23] Y. Tanimura, R. Kubo, Time Evolution of a Quantum System in Contact with a Nearly Gaussian-Markoffian Noise Bath, J. Phys. Soc. Japan. 58 (1989) 101–114. https://doi.org/10.1143/JPSJ.58.101.

[24] A. Ishizaki, G.R. Fleming, Unified treatment of quantum coherent and incoherent hopping dynamics in electronic energy transfer: Reduced hierarchy equation approach, J. Chem. Phys. 130 (2009) 234111. https://doi.org/10.1063/1.3155372.

[25] Y. Tanimura, Numerically "exact" approach to open quantum dynamics: The hierarchical equations of motion (HEOM), J. Chem. Phys. 153 (2020) 020901. https://doi.org/10.1063/5.0011599.

[26] M. Aghtar, J. Liebers, J. Strümpfer, K. Schulten, U. Kleinekathöfer, Juxtaposing density matrix and classical path-based wave packet dynamics, J. Chem. Phys. 136 (2012) 214101. https://doi.org/10.1063/1.4723669.

[27] J. Zhu, S. Kais, P. Rebentrost, A. Aspuru-Guzik, Modified Scaled Hierarchical Equation of Motion Approach for the Study of Quantum Coherence in Photosynthetic Complexes, J. Phys. Chem. B. 115 (2011) 1531–1537. https://doi.org/10.1021/jp109559p.

[28] G. Ritschel, J. Roden, W.T. Strunz, A. Eisfeld, An efficient method to calculate excitation energy transfer in light-harvesting systems: application to the Fenna–Matthews–Olson complex, New J. Phys. 13 (2011) 113034. https://doi.org/10.1088/1367-2630/13/11/113034.

[29] N. Lambert, T. Raheja, S. Ahmed, A. Pitchford, F. Nori, BoFiN-HEOM: A bosonic and fermionic numerical hierarchical-equations-of-motion library with applications in light-harvesting, quantum control, and single-molecule electronics, (2020) 1–15. http://arxiv.org/abs/2010.10806.

[30] N. Lambert, T. Raheja, S. Ahmed, A. Pitchford, F. Nori, https://github.com/tehruhn/bofin, (2020). https://github.com/tehruhn/bofin.

[31] J.R. Johansson, P.D. Nation, F. Nori, QuTiP: An open-source Python framework for the dynamics of open quantum systems, Comput. Phys. Commun. 183 (2012) 1760–1772. https://doi.org/10.1016/j.cpc.2012.02.021.

[32] J.R. Johansson, P.D. Nation, F. Nori, QuTiP 2: A Python framework for the dynamics of open quantum systems, Comput. Phys. Commun. 184 (2013) 1234–1240. https://doi.org/10.1016/j.cpc.2012.11.019.

[33] F. Gallina, M. Bruschi, B. Fresch, Strategies to simulate dephasing-assisted quantum transport on digital quantum computers, New J. Phys. 24 (2022) 023039. https://doi.org/10.1088/1367-2630/ac512f.

[34] W. Magnus, On the exponential solution of differential equations for a linear operator, Commun. Pure Appl. Math. 7 (1954) 649–673. https://doi.org/10.1002/cpa.3160070404.

[35] A. Iserles, H.Z. Munthe-Kaas, S.P. Nørsett, A. Zanna, Lie-group methods, Acta Numer. 9 (2000) 215–365. https://doi.org/10.1017/S0962492900002154.

[36] K. Kormann, S. Holmgren, H.O. Karlsson, Accurate time propagation for the Schrödinger equation with an explicitly time-dependent Hamiltonian, J. Chem. Phys. 128 (2008) 184101. https://doi.org/10.1063/1.2916581.

[37] D.J. Tannor, Introduction to Quantum Mechanics: A Time-Dependent Perspective, University Science Books, Sausalito, 2006.

[38] T.L.C. Jansen, J. Knoester, Nonadiabatic Effects in the Two-Dimensional Infrared Spectra of Peptides: Application to Alanine Dipeptide, J. Phys. Chem. B. 110 (2006) 22910–22916. https://doi.org/10.1021/jp064795t.

[39] C. Liang, T.L.C. Jansen, An Efficient N 3 -Scaling Propagation Scheme for Simulating Two-Dimensional Infrared and Visible Spectra, J. Chem. Theory Comput. 8 (2012) 1706–1713. https://doi.org/10.1021/ct300045c.

[40] C. Kreisbeck, T. Kramer, M. Rodríguez, B. Hein, High-Performance Solution of Hierarchical Equations of Motion for Studying Energy Transfer in Light-Harvesting Complexes, J. Chem. Theory Comput. 7 (2011) 2166–2174. https://doi.org/10.1021/ct200126d.

[41] F. Ciccarello, V. Giovannetti, A quantum non-Markovian collision model: incoherent swap case, Phys. Scr. T153 (2013) 014010. https://doi.org/10.1088/0031-8949/2013/T153/014010.

[42] F. Ciccarello, G.M. Palma, V. Giovannetti, Collision-model-based approach to non-Markovian quantum dynamics, Phys. Rev. A. 87 (2013) 040103. https://doi.org/10.1103/PhysRevA.87.040103.

[43] T. Rybár, S.N. Filippov, M. Ziman, V. Bužek, Simulation of indivisible qubit channels in collision models, J. Phys. B At. Mol. Opt. Phys. 45 (2012) 154006. https://doi.org/10.1088/0953-4075/45/15/154006.

[44] G. García-Pérez, M.A.C. Rossi, S. Maniscalco, IBM Q Experience as a versatile experimental testbed for simulating open quantum systems, Npj Quantum Inf. 6 (2020) 1. https://doi.org/10.1038/s41534-019-0235-y.

[45] G. García-Pérez, D.A. Chisholm, M.A.C. Rossi, G.M. Palma, S. Maniscalco, Decoherence without entanglement and quantum Darwinism, Phys. Rev. Res. 2 (2020) 1–5. https://doi.org/10.1103/physrevresearch.2.012061.

[46] D.A. Chisholm, G. García-Pérez, M.A.C. Rossi, G.M. Palma, S. Maniscalco, Stochastic collision model approach to transport phenomena in quantum networks, New J. Phys. 23 (2021) 033031. https://doi.org/10.1088/1367-2630/abd57d.

[47] B. Vacchini, H.-P. Breuer, A. Bassi, Advances in Open Systems and Fundamental Tests of Quantum Mechanics, Springer International Publishing, Cham, 2019. https://doi.org/10.1007/978-3-030-31146-9.

[48] S. Lorenzo, F. Ciccarello, G.M. Palma, Composite quantum collision models, Phys. Rev. A. 96 (2017) 032107. https://doi.org/10.1103/PhysRevA.96.032107.

[49] S. Campbell, F. Ciccarello, G.M. Palma, B. Vacchini, System-environment correlations and Markovian embedding of quantum non-Markovian dynamics, Phys. Rev. A. 98 (2018) 012142. https://doi.org/10.1103/PhysRevA.98.012142.

[50] F. Ciccarello, S. Lorenzo, V. Giovannetti, G.M. Palma, Quantum collision models: Open system dynamics from repeated interactions, Phys. Rep. 954 (2022) 1–70. https://doi.org/10.1016/j.physrep.2022.01.001.

[51] M. Cattaneo, G. De Chiara, S. Maniscalco, R. Zambrini, G.L. Giorgi, Collision Models Can Efficiently Simulate Any Multipartite Markovian Quantum Dynamics, Phys. Rev. Lett. 126 (2021) 130403. https://doi.org/10.1103/PhysRevLett.126.130403.

[52] A. Imamoglu, Stochastic wave-function approach to non-Markovian systems, Phys. Rev. A. 50 (1994) 3650–3653. https://doi.org/10.1103/PhysRevA.50.3650.

[53] B.M. Garraway, Nonperturbative decay of an atomic system in a cavity, Phys. Rev. A. 55 (1997) 2290–2303. https://doi.org/10.1103/PhysRevA.55.2290.

[54] L. Mazzola, S. Maniscalco, J. Piilo, K.-A. Suominen, B.M. Garraway, Pseudomodes as an effective description of memory: Non-Markovian dynamics of two-state systems in structured reservoirs, Phys. Rev. A. 80 (2009) 012104. https://doi.org/10.1103/PhysRevA.80.012104.

[55] G. Pleasance, F. Petruccione, Pseudomode description of general open quantum system dynamics: non-perturbative master equation for the spin-boson model, (2021) 1–9. http://arxiv.org/abs/2108.05755.

[56] G. Pleasance, B.M. Garraway, F. Petruccione, Generalized theory of pseudomodes for exact descriptions of non-Markovian quantum processes, Phys. Rev. Res. 2 (2020) 043058. https://doi.org/10.1103/PhysRevResearch.2.043058.

[57] R. Hartmann, W.T. Strunz, Accuracy assessment of perturbative master equations: Embracing nonpositivity, Phys. Rev. A. 101 (2020) 012103. https://doi.org/10.1103/PhysRevA.101.012103.

[58] A. Imamoğlu, Y. Yamamoto, Quantum Monte Carlo wave-function approach to dissipative processes in mesoscopic semiconductors, Phys. Lett. A. 191 (1994) 425–430. https://doi.org/10.1016/0375-9601(94)90798-6.

[59] G. Aleksandrowicz, T. Alexander, P. Barkoutsos, L. Bello, Y. Ben-Haim, D. Bucher, F.J. Cabrera-Hernández, J. Carballo-Franquis, A. Chen, C.-F. Chen, J.M. Chow, A.D. Córcoles-Gonzales, A.J. Cross, A. Cross, J. Cruz-Benito, C. Culver, S.D.L.P. González, E.D. La Torre, D. Ding, E. Dumitrescu, I. Duran, P. Eendebak, M. Everitt, I.F. Sertage, A. Frisch, A. Fuhrer, J. Gambetta, B.G. Gago, J. Gomez-Mosquera, D. Greenberg, I. Hamamura, V. Havlicek, J. Hellmers, Ł. Herok, H. Horii, S. Hu, T. Imamichi, T. Itoko, A. Javadi-Abhari, N. Kanazawa, A. Karazeev, K. Krsulich, P. Liu, Y. Luh, Y. Maeng, M. Marques, F.J. Martín-Fernández, D.T. McClure, D. McKay, S. Meesala, A. Mezzacapo, N. Moll, D.M. Rodríguez, G. Nannicini, P. Nation, P. Ollitrault, L.J. O'Riordan, H. Paik, J. Pérez, A. Phan, M. Pistoia, V. Prutyanov, M. Reuter, J. Rice, A.R. Davila, R.H.P. Rudy, M. Ryu, N. Sathaye, C. Schnabel, E. Schoute, K. Setia, Y. Shi, A. Silva, Y. Siraichi, S. Sivarajah, J.A. Smolin, M. Soeken, H. Takahashi, I. Tavernelli, C. Taylor, P. Taylour, K. Trabing, M. Treinish, W. Turner, D. Vogt-Lee, C. Vuillot, J.A. Wildstrom, J. Wilson, E. Winston, C. Wood, S. Wood, S. Wörner, I.Y. Akhalwaya, C. Zoufal, Qiskit: An Open-source Framework for Quantum Computing, Zenodo. (2019). https://doi.org/10.5281/ZENODO.2562111.

[60] J. Wu, J. Cao, Higher-order kinetic expansion of quantum dissipative dynamics: Mapping quantum networks to kinetic networks, J. Chem. Phys. 139 (2013) 044102. https://doi.org/10.1063/1.4812781.

[61] J. Wu, F. Liu, J. Ma, R.J. Silbey, J. Cao, Efficient energy transfer in light-harvesting systems: Quantum-classical comparison, flux network, and robustness analysis, J. Chem. Phys. 137 (2012) 174111. https://doi.org/10.1063/1.4762839.

[62] M. Yang, G.R. Fleming, Influence of phonons on exciton transfer dynamics: comparison of the Redfield, Förster, and modified Redfield equations, Chem. Phys. 275 (2002) 355–372. https://doi.org/10.1016/S0301-0104(01)00540-7.

[63] M. Cattaneo, M.A.C. Rossi, G. García-Pérez, R. Zambrini, S. Maniscalco, Quantum simulation of dissipative collective effects on noisy quantum computers, (2022) 1–25. http://arxiv.org/abs/2201.11597.

[64] A. Pedram, B. Çakmak, Ö.E. Müstecaplıoğlu, Environment-Assisted Modulation of Heat Flux in a Bio-Inspired System Based on Collision Model, Entropy. 24 (2022) 1162. https://doi.org/10.3390/e24081162.

[65] A. Ishizaki, G.R. Fleming, Theoretical examination of quantum coherence in a photosynthetic system at physiological temperature, Proc. Natl. Acad. Sci. 106 (2009) 17255–17260. https://doi.org/10.1073/pnas.0908989106.

[66] M. Mohseni, A. Shabani, S. Lloyd, H. Rabitz, Energy-scales convergence for optimal and robust quantum transport in photosynthetic complexes, J. Chem. Phys. 140 (2014) 035102. https://doi.org/10.1063/1.4856795.

[67] H.-P. Breuer, E.-M. Laine, J. Piilo, Measure for the Degree of Non-Markovian Behavior of Quantum Processes in Open Systems, Phys. Rev. Lett. 103 (2009) 210401. https://doi.org/10.1103/PhysRevLett.103.210401.

[68] M.B. Ruskai, Beyond strong subadditivity? Improved bounds on the contraction of generalized relative entropy, Rev. Math. Phys. 06 (1994) 1147–1161. https://doi.org/10.1142/S0129055X94000407.

[69] M.A. Nielsen, I.L. Chuang, Quantum Computation and Quantum Information, 10th ed., Cambridge University Press, 2000. http://www.tandfonline.com/doi/abs/10.1080/00107514.2011.587535.

[70] P. Rebentrost, A. Aspuru-Guzik, Communication: Exciton–phonon information flow in the energy transfer process of photosynthetic complexes, J. Chem. Phys. 134 (2011) 101103. https://doi.org/10.1063/1.3563617.

[71] S. Cialdi, M.A.C. Rossi, C. Benedetti, B. Vacchini, D. Tamascelli, S. Olivares, M.G.A. Paris, All-optical quantum simulator of qubit noisy channels, Appl. Phys. Lett. 110 (2017) 081107. https://doi.org/10.1063/1.4977023.

[72] N.K. Bernardes, A.R.R. Carvalho, C.H. Monken, M.F. Santos, Environmental correlations and Markovian to non-Markovian transitions in collisional models, Phys. Rev. A. 90 (2014) 032111. https://doi.org/10.1103/PhysRevA.90.032111.

[73] D. Chruściński, S. Maniscalco, Degree of Non-Markovianity of Quantum Evolution, Phys. Rev. Lett. 112 (2014) 120404. https://doi.org/10.1103/PhysRevLett.112.120404.

Chapter IV

A microscopic model for the environment: the Redfield master equation

In the vast panorama of quantum master equations, it is hard to overstate the conceptual and practical importance of Redfield derivation [1,2]. It provides a route to open system dynamics starting from the full specification of the system-environment Hamiltonian with the possibility of specifying the conditions of validity for each assumption made on the way. From a more practical point of view, it gives a receipt to completely characterized the dissipative part of the system evolution solely based on the spectral density of the environment. In the standard derivation, also used in this Chapter, the Redfield equation stems from a second-order truncation on the system-environment interaction and the Born-Markov approximation. The price to pay at the end, is the requirement of complete positivity, because the Redfield equation may generate non-physical negative probabilities during time evolution. The adequacy of the Redfield equation for describing excitonic transport dynamics in light-harvesting complexes is a long-standing debate in the literature. On the one hand, by emphasising its weak-coupling nature, some authors seem to advise against its use in favour of more computationally demanding exact equations [3]. On the other hand, other authors approve of its conscious use, meaning being aware of its range of validity and thus employing a physically grounded definition of the environment [4]. Some papers see non-positivity as a problem [5], while others suggest that, since it happens only outside the range of validity of the approach, non-positivity should be regarded as a powerful indicator [6]. The debate is further complicated by the use of the equation with additional approximations, like the often-invoked secular form of the Redfield tensor.

We believe that, although this equation cannot describe the full spectrum of coupling regimes and it is limited to Markovian conditions, it is nevertheless extremely useful for providing information on the dynamics

that can then be refined using more advanced methods. With this in mind, in section IV.1 we first give a derivation of the Redfield equation for a generic system in contact with its environment. The purpose of the section is to establish the language used thereafter and to highlight the approximations introduced and the limitations they pose. Once we get the equation, we discuss two well-known "variants" often used for the excitonic dynamics: the secular equation and the equation for δ-correlated environments.

In section IV.2, the derivation is contextualised for a light-harvesting system interacting with its overdamped vibrational environment. We assume a Drude-Lorentz spectral function for the environment, corresponding to the overdamped Brownian oscillator model, and study how it depends on the three characterising parameters (reorganization energy, cutoff frequency and temperature), finding the limiting cases that reproduce the classical spectral densities used in Chapters II and III.

In the last section IV.3, we use the established framework to conduct an original comparative analysis on the dynamics produced by the Redfield equation and some variants used in the literature. In particular, we will test the behaviour, validity limits and effectiveness of the Redfield treatment over a wide range of parameters. Although the Redfield equation is much studied in the literature, we are not aware of an extensive comparative analysis as the one presented in this chapter. The Fenna-Matthews-Olson molecular complex will be our testbed. As a result, we find that, where the Born-Markov approximation is valid, there are no substantial differences between the dynamics produced by the Redfield equation, its secular version or Redfield equation without imaginary part (where the contribution of the dispersion function is neglected). On the contrary, where the approximation fails there can be large differences in the dynamics of both populations and coherences. We also explicitly show cases where the non-positivity issue becomes relevant. Although this problem is well known and much analysed from the theoretical point of view, it is not common to encounter concrete simulation cases in which it occurs. In this regard, we verified that the positivity of the density matrix, not guaranteed by the Redfield equation, is a useful indicator of the range of validity of the equation itself, in agreement with [6].

We conclude in section IV.4 with some remarks.

IV.1 A microscopic derivation of the equation of motion

Consider an open quantum system with a time-independent Hamiltonian H_s and an environment described by H_b coupled together via an interaction Hamiltonian H_sb, that we assume to be in the form

$$H_{sb} = \sum_i S_i B_i \,, \tag{IV.1}$$

where S_i and B_i are operators acting on the system and environment subspace, respectively. The Hamiltonian for the universe system reads

$$H = H_0 + H_\mathrm{sb} = H_\mathrm{s} + H_\mathrm{b} + H_\mathrm{sb} \,, \tag{IV.2}$$

with H_0 the Hamiltonian of the non-interacting systems.

The Von Neumann equation that regulates the dynamics of the universe system density matrix $\rho_{\mathrm{sb}}(t)$ in the interaction picture reads

$$\frac{d\tilde{\rho}_{\mathrm{sb}}(t)}{dt} = -\mathrm{i}\left[\tilde{H}_{\mathrm{sb}}(t), \tilde{\rho}_{\mathrm{sb}}(t)\right], \tag{IV.3}$$

where the interaction picture is related to the Schrödinger picture by the unitary transformation

$$\tilde{O}(t) = U_0^{\dagger}(t) O U_0(t), \tag{IV.4}$$

with $U_0(t) = \exp(-\mathrm{i}H_0 t) = \exp(-\mathrm{i}H_{\mathrm{s}} t)\exp(-\mathrm{i}H_{\mathrm{b}} t)$, that is the free-evolution operator of the global non-interacting system. In the following, we set $\hbar = 1$ for simplicity.

Integrating eq. (IV.3) leads to

$$\tilde{\rho}_{\mathrm{sb}}(t) = \rho_{\mathrm{sb}}(0) - \mathrm{i}\int_0^t dt'\left[\tilde{H}_{\mathrm{sb}}(t'), \tilde{\rho}_{\mathrm{sb}}(t')\right], \tag{IV.5}$$

where we have used the identity $\tilde{\rho}_{\mathrm{sb}}(0) = \rho_{\mathrm{sb}}(0)$.

Now we substitute eq. (IV.5) in the right-hand side of the Von Neumann eq. (IV.3) and trace over the bath degrees of freedom since we are interested in an equation of motion for the reduced density matrix of the open system, defined as $\rho_{\mathrm{s}}(t) \equiv \mathrm{Tr}_{\mathrm{b}}\left\{\rho_{\mathrm{sb}}(t)\right\}$. The result reads

$$\frac{d\,\mathrm{Tr}_{\mathrm{b}}\left\{\tilde{\rho}_{\mathrm{sb}}(t)\right\}}{dt} = \frac{d\tilde{\rho}_{\mathrm{s}}(t)}{dt} = -\mathrm{i}\,\mathrm{Tr}_{\mathrm{b}}\left[\tilde{H}_{\mathrm{sb}}(t), \rho_{\mathrm{sb}}(0)\right] - \int_0^t dt'\,\mathrm{Tr}_{\mathrm{b}}\left[\tilde{H}_{\mathrm{sb}}(t), \left[\tilde{H}_{\mathrm{sb}}(t'), \tilde{\rho}_{\mathrm{sb}}(t')\right]\right]. \tag{IV.6}$$

As we have not made any approximation yet, this equation is an exact equation of motion for the density matrix of the system.

IV.1.1 Mean-field effect

The first assumption, common to nearly all the developments in open system theory, is that at time $t = 0$ the system and the environment are in a product state $\rho_{\mathrm{sb}}(0) = \rho_{\mathrm{s}}(0) \otimes \rho_{\mathrm{b}}(0)$. Although there is not a truly valid justification of this assumption, one may argue that the system and the environment are initially non-interacting, and then a Hamiltonian quench occurs turning on the coupling. Alternatively, one may argue that the uncorrelated state stems from a rapid variation of the state of the system, as in the case of a photon excitation of the electronic degrees of freedom of a molecule surrounded by a vibronic environment.

In addition, we make another common assumption that is that the environment is initially in its thermal (Gibbs) state, $\rho_{\mathrm{b}}(0) = \rho_{\mathrm{b}}^{\mathrm{eq}}$, associated with H_{b}, that is

$$\rho_{\mathrm{b}}(0) = \rho_{\mathrm{b}}^{\mathrm{eq}} = \frac{\exp(-H_{\mathrm{b}}\beta)}{Z}, \tag{IV.7}$$

where $Z = \mathrm{Tr_b}\left\{\exp\left(-H_\mathrm{b}\beta\right)\right\}$ is the partition function, $\beta = \left(k_\mathrm{B}T\right)^{-1}$ the inverse temperature, k_B the Boltzmann constant and T the temperature of the environment. As a consequence, we have that the commutation relation $\left[H_0, \rho_\mathrm{b}^\mathrm{eq}\right] = 0$ holds, and thus $U_0^\dagger(t)\rho_\mathrm{b}^\mathrm{eq}U_0(t) = \rho_\mathrm{b}^\mathrm{eq}$.

Now, we look at the first term on the right-hand side of eq. (IV.6). For initially separated states, this can be written as

$$\begin{aligned}\mathrm{Tr_b}\left[\tilde{H}_\mathrm{sb}(t), \rho_\mathrm{sb}(0)\right] &= \sum_i \left[\tilde{S}_i(t), \rho_\mathrm{s}(0)\right]\mathrm{Tr_b}\left\{\tilde{B}_i(t)\rho_\mathrm{b}^\mathrm{eq}\right\} \\ &= \sum_i \left[\tilde{S}_i(t), \rho_\mathrm{s}(0)\right]\left\langle B_i\right\rangle_\mathrm{eq}\end{aligned} \tag{IV.8}$$

where we have defined the expectation value of the environment interacting operators at the equilibrium as $\left\langle B_i\right\rangle_\mathrm{eq} = \mathrm{Tr_b}\left\{\tilde{B}_i(t)\rho_\mathrm{b}^\mathrm{eq}\right\}$. Often, one naturally gets that $\left\langle B_i\right\rangle_\mathrm{eq} = 0$. However, in general, the first-order term gives a so-called mean-field effect that can be taken into account by simply redefining the system and interaction Hamiltonians as

$$H_\mathrm{s} = H_\mathrm{s} + \sum_i S_i \left\langle B_i\right\rangle_\mathrm{eq}, \tag{IV.9}$$

$$H_\mathrm{sb} = \sum_i S_i \left(B_i - \left\langle B_i\right\rangle_\mathrm{eq}\right). \tag{IV.10}$$

In the end, eq. (IV.6) can thus be rewritten as

$$\frac{d\tilde{\rho}_\mathrm{s}(t)}{dt} = -\int_0^t dt' \mathrm{Tr_b}\left[\tilde{H}_\mathrm{sb}(t), \left[\tilde{H}_\mathrm{sb}(t'), \tilde{\rho}_\mathrm{sb}(t')\right]\right]. \tag{IV.11}$$

IV.1.2 Born approximation

Eq. (IV.11) depends on the universe density matrix $\tilde{\rho}_\mathrm{sb}(t)$, which is in general a mixed state difficult to handle. However, if the environment can be treated as a large reservoir and the coupling with the open system is small enough[1] (weak coupling approximation, see [7–9] for some definitions), then the *Born approximation* can be applied. This consists in neglecting the entanglement between the system and the environment, with the justification that the environment is negligibly perturbed by the interaction, resulting in a density matrix for the universe system that is always described by the product state $\tilde{\rho}_\mathrm{sb}(t) = \tilde{\rho}_\mathrm{s}(t) \otimes \tilde{\rho}_\mathrm{b}(t)$. Now, as a further step of the approximation, we assume the bath relaxation τ_b to be fast compared to the time scale Δt we use

[1] The strength of the interaction can be evaluated through the operator 1-norm of the interaction Hamiltonian, which is defined as $\left\|H_\mathrm{sb}\right\|_1 \equiv \max_\alpha \lambda_\alpha\left(\left|H_\mathrm{sb}\right|\right)$, where the maximum is taken over the eigenvalues λ_α of the matrix $\left|H_\mathrm{sb}\right| \equiv \sqrt{H_\mathrm{sb}^\dagger H_\mathrm{sb}} = \sqrt{H_\mathrm{sb}^2}$, where in the last equivalence we use the Hermiticity of H_sb.

to look at the system evolution (*i.e.*, $\Delta t \ll \tau_{\mathrm{b}}$). In this case, the state of the environment always results relaxed in its equilibrium state, *i.e.*, $\tilde{\rho}_{\mathrm{sb}}(t) = \tilde{\rho}_{\mathrm{s}}(t) \otimes \rho_{\mathrm{b}}^{\mathrm{eq}}$.

The new integrodifferential equation of motion for the density matrix under Born approximation reads

$$\frac{d\tilde{\rho}_{\mathrm{s}}(t)}{dt} = -\int_0^t dt' \mathrm{Tr}_{\mathrm{b}}\left[\tilde{H}_{\mathrm{sb}}(t), \left[\tilde{H}_{\mathrm{sb}}(t'), \tilde{\rho}_{\mathrm{s}}(t')\rho_{\mathrm{b}}^{\mathrm{eq}}\right]\right]. \tag{IV.12}$$

Note that, although the validity of the Born approximation is strictly related both to the weak coupling and to the existence of a *coarse-grained* timescale Δt, whose limit is dictated by τ_{b}, the only visible effect in eq. (IV.12) is the state separation, while the coarse-graining remains implicit in the derivation.

IV.1.3 The correlation functions of the environment

Since we are interested in the evolution of the reduced system, it would be convenient to condensate all the information regarding the environment into some effective functions. To do this, let us expand the nested commutators inside the time integral of eq. (IV.12) as

$$\begin{aligned}\mathrm{Tr}_{\mathrm{b}}\left[\tilde{H}_{\mathrm{sb}}(t), \left[\tilde{H}_{\mathrm{sb}}(t'), \tilde{\rho}_{\mathrm{s}}(t')\rho_{\mathrm{b}}^{\mathrm{eq}}\right]\right] = &\mathrm{Tr}_{\mathrm{b}}\left\{\tilde{H}_{\mathrm{sb}}(t)\tilde{H}_{\mathrm{sb}}(t')\tilde{\rho}_{\mathrm{s}}(t')\rho_{\mathrm{b}}^{\mathrm{eq}}\right\} \\ &- \mathrm{Tr}_{\mathrm{b}}\left\{\tilde{H}_{\mathrm{sb}}(t')\tilde{\rho}_{\mathrm{s}}(t')\rho_{\mathrm{b}}^{\mathrm{eq}}\tilde{H}_{\mathrm{sb}}(t)\right\} \\ &+ \mathrm{h.c.}\end{aligned} \tag{IV.13}$$

Now we want to write explicitly the interaction Hamiltonian H_{sb} is terms of operators S_i and B_i. Here, we assume for simplicity that they are Hermitian, however, if they are not, it is always possible to redefine them as Hermitian (see the appendix of ref. [10]). For Hermitian operators, the identity $H_{\mathrm{sb}} = \sum_i S_i B_i = \sum_i S_i^{\dagger} B_i^{\dagger}$ holds, and it holds also in the interaction picture. Making use of it, we write the trace in eq. (IV.13) by inserting $\tilde{S}_i(t')$ and $\tilde{B}_i(t')$ for $\tilde{H}_{\mathrm{sb}}(t')$, while $\tilde{S}_i^{\dagger}(t)$ and $\tilde{B}_i^{\dagger}(t)$ for $\tilde{H}_{\mathrm{sb}}(t)$

$$\begin{aligned}\mathrm{Tr}_{\mathrm{b}}\left[\tilde{H}_{\mathrm{sb}}(t), \left[\tilde{H}_{\mathrm{sb}}(t'), \tilde{\rho}_{\mathrm{s}}(t')\rho_{\mathrm{b}}^{\mathrm{eq}}\right]\right] = &\sum_{i,j} \tilde{S}_i^{\dagger}(t)\tilde{S}_j(t')\tilde{\rho}_{\mathrm{s}}(t')\mathrm{Tr}_{\mathrm{b}}\left\{\tilde{B}_i^{\dagger}(t)\tilde{B}_j(t')\rho_{\mathrm{b}}^{\mathrm{eq}}\right\} \\ &- \sum_{i,j} \tilde{S}_j(t')\tilde{\rho}_{\mathrm{s}}(t')\tilde{S}_i^{\dagger}(t)\mathrm{Tr}_{\mathrm{b}}\left\{\tilde{B}_i^{\dagger}(t)\tilde{B}_j(t')\rho_{\mathrm{b}}^{\mathrm{eq}}\right\} \\ &+ \mathrm{h.c.}\end{aligned} \tag{IV.14}$$

Since S_i and B_i are Hermitian operators, this choice does not affect the result, but the dagger sign will help us identify the terms in the following.

We recognize that the equilibrium two-point correlation functions of the environment appear in eq. (IV.14)

$$\mathrm{Tr}_{\mathrm{b}}\left\{\tilde{B}_i^{\dagger}(t)\tilde{B}_j(t')\rho_{\mathrm{b}}^{\mathrm{eq}}\right\} = \left\langle \tilde{B}_i^{\dagger}(t)\tilde{B}_j(t')\right\rangle_{\mathrm{eq}} = \left\langle \tilde{B}_i^{\dagger}(t-t')B_j\right\rangle_{\mathrm{eq}} = c_{ij}(t-t'). \tag{IV.15}$$

For a quantum environment, the correlation functions of Hermitian operators are in general complex, and satisfy both the symmetry relation

$$c_{ij}^{*}(t-t') = \mathrm{Tr_b}\left\{\left(\tilde{B}_i^{\dagger}(t)\tilde{B}_j(t')\rho_{\mathrm{b}}^{\mathrm{eq}}\right)^{\dagger}\right\} = \mathrm{Tr_b}\left\{\tilde{B}_j^{\dagger}(t')\tilde{B}_i(t)\rho_{\mathrm{b}}^{\mathrm{eq}}\right\} = c_{ji}(t'-t), \tag{IV.16}$$

and the Kubo-Martin-Schwinger (KMS) condition that ensures the detail balance at finite temperature[2]

$$c_{ij}^{*}(t-t') = c_{ij}(t-t'-\mathrm{i}\beta). \tag{IV.17}$$

Using the new notation for the correlation functions, eq. (IV.12) can be written in terms of the system operators only, as

$$\frac{d\tilde{\rho}_{\mathrm{s}}(t)}{dt} = -\int_0^t dt' \sum_{i,j} c_{ij}(t-t')\left[\tilde{S}_i^{\dagger}(t), \tilde{S}_j(t')\tilde{\rho}_s(t')\right] + \mathrm{h.c.}. \tag{IV.18}$$

IV.1.4 Markov approximation

It is convenient to introduce the time difference $\tau = t - t'$ to facilitate the writing of the bath correlation functions. As already mentioned, for the Born approximation to be valid, we need a coarse-graining of time, so that the time step Δt we use to resolve the dynamics is longer than the typical decay time of the bath coherences τ_{b}. Since in general t will be a multiple of Δt, the time difference τ will be as well. Thus, except for the trivial case $\tau = 0$, the coarse-graining applies also to τ, *i.e.*, $\tau \geq \Delta t \gg \tau_{\mathrm{b}}$. This tells us that, during the time scale used to look at the open system, the correlations of the environment should have mostly decayed, $c_{ij}(\tau) \simeq 0$. Therefore, the contribution to the integral in eq. (IV.18) will be negligible for $\tau \gg \tau_{\mathrm{b}}$. Here enters the *Markov approximation*. As a first step, we assume that for such a brief time interval defined by the memory of the environment (τ_{b}) the value of the system density matrix in the interaction picture remains approximately constant, such that we can substitute $\tilde{\rho}(t')$ with $\tilde{\rho}(t)$. The equation we obtain is now a time-local master equation known as the *Redfield equation with time-dependent coefficients* [11]

---

[2] The important relation in eq. (IV.17) can be demonstrated by recalling the definition of the equilibrium density matrix of the environment at inverse temperature β, eq. (IV.7), and using the cyclic property of the trace:

$$\begin{aligned} c_{ij}(t-t'-\mathrm{i}\beta) &= \mathrm{Tr_b}\left\{\tilde{B}_i^{\dagger}(t-t'-\mathrm{i}\beta)B_j\rho_{\mathrm{b}}^{\mathrm{eq}}\right\} = \mathrm{Tr_b}\left\{e^{H_{\mathrm{b}}\beta}\tilde{B}_i^{\dagger}(t-t')e^{-H_{\mathrm{b}}\beta}B_j\rho_{\mathrm{b}}^{\mathrm{eq}}\right\} \\ &= \mathrm{Tr_b}\left\{e^{H_{\mathrm{b}}\beta}\tilde{B}_i^{\dagger}(t-t')e^{-H_{\mathrm{b}}\beta}B_j e^{-H_{\mathrm{b}}\beta}\right\}\Big/Z \\ &= \mathrm{Tr_b}\left\{\tilde{B}_i^{\dagger}(t-t')\rho_{\mathrm{b}}^{\mathrm{eq}}B_j\right\} = \mathrm{Tr_b}\left\{B_j\tilde{B}_i^{\dagger}(t-t')\rho_{\mathrm{b}}^{\mathrm{eq}}\right\} = c_{ji}(t'-t) = c_{ij}^{*}(t-t') \end{aligned}$$

$$\frac{d\tilde{\rho}_{\mathrm{s}}(t)}{dt} = -\int_0^t d\tau \sum_{i,j} c_{ij}(\tau)\left[\tilde{S}_i^{\dagger}(t), \tilde{S}_j^{\dagger}(t-\tau)\tilde{\rho}_{\mathrm{s}}(t)\right] + \text{h.c.}. \tag{IV.19}$$

At this point, the equation is local in time, but not yet Markovian, since it explicitly depends on the initial state of the dynamics [12]. To obtain the Markovian version, we extend the upper limit of the time integral to infinity, obtaining what is normally intended as the *Redfield equation*

$$\frac{d\tilde{\rho}_{\mathrm{s}}(t)}{dt} = -\int_0^{\infty} d\tau \sum_{i,j} c_{ij}(\tau)\left[\tilde{S}_i^{\dagger}(t), \tilde{S}_j(t-\tau)\tilde{\rho}_{\mathrm{s}}(t)\right] + \text{h.c.}. \tag{IV.20}$$

If $\tau \gg \tau_{\mathrm{b}}$, this should not have much influence since, as already said, the integral is expected to become approximately constant.

Both forms of the Redfield equation, eqs. (IV.19) and (IV.20), are known to give non-completely positive dynamical maps, which means that they do not ensure the density matrix of the open system stays positive (a necessary condition for a physical evolution[3]). Thus, in general, the Redfield equation cannot be written in Lindblad form. One of the most common problems using eq. (IV.20) is the non-positivity during the first instances of the dynamics. This happens for example when the dynamics is resolved with a time step Δt smaller than or comparable to the relaxation time of the environment (see section IV.3.5.2), a regime where the Redfield equation does not guarantee any accurate result [13,14]. In the same range of small times, eq. (IV.19) is known to give better results [6,15]. The application of a "slippage" superoperator which describes the intrinsically non-Markovian dynamics of the open system during the initial relaxation of the bath was proposed in ref. [10] to correct for this inconvenience.

It is worth noting that when the system and the environment evolves with different time scales and a sufficiently large Δt is chosen to resolve the dynamics, the Markovian approximation is valid, and the problem mentioned above does not occur.

IV.1.5 Eigenstate basis

The Redfield equation can be solved as presented above but, both for an easier computation and to introduce further approximations, it is usually rewritten in the eigenstate basis of the system Hamiltonian $H_{\mathrm{s}} = \sum_{\alpha} E_{\alpha} |\alpha\rangle\langle\alpha|$. We will use Greek letters to identify the eigenstate basis $|\alpha\rangle$ and their corresponding eigenvalues E_{α}. System interaction operators can be decomposed into a linear combination as follows

$$S_i = \sum_{\alpha,\beta} |\alpha\rangle\langle\alpha|S_i|\beta\rangle\langle\beta| = \sum_{\omega} S_i(\omega), \tag{IV.21}$$

[3] However, the other necessary conditions for a physical result, *i.e.*, the Hermiticity and norm of the density matrix, are always preserved by the Redfield evolution.

where $\omega = E_\beta - E_\alpha$ are the frequencies of the system Hamiltonian spectrum and $S_i(\omega)$ are the system interaction operators evaluated at frequency ω, that is the sum over all the states whose eigenvalue difference corresponds to the given frequency, *i.e.*,

$$S_i(\omega) = \sum_{\substack{\alpha,\beta \\ E_\beta - E_\alpha = \omega}} |\alpha\rangle\langle\alpha|S_i|\beta\rangle\langle\beta| . \tag{IV.22}$$

In the interaction picture, the system operators $\tilde{S}_i(t)$ can be decomposed as

$$\tilde{S}_i(t) = e^{\mathrm{i}H_s t} S_i e^{-\mathrm{i}H_s t} = \sum_\omega e^{-\mathrm{i}\omega t} S_i(\omega) . \tag{IV.23}$$

Note that, since S_i is Hermitian, it holds the symmetry relation

$$S_i^\dagger(\omega) = S_i(-\omega) \tag{IV.24}$$

in the Schrödinger picture, and

$$\tilde{S}_i(t) = \sum_\omega e^{-\mathrm{i}\omega t} S_i(\omega) = \sum_\omega e^{\mathrm{i}\omega t} S_i^\dagger(\omega) = \tilde{S}_i^\dagger(t) \tag{IV.25}$$

in the interaction picture.

On the system eigenstate basis, eq. (IV.20) reads

$$\frac{d\tilde{\rho}_\mathrm{S}(t)}{dt} = -\sum_{i,j}\sum_{\omega,\omega'} \Gamma_{ij}(\omega')\left[S_i^\dagger(\omega), S_j(\omega')\tilde{\rho}_\mathrm{S}(t)\right] e^{\mathrm{i}(\omega-\omega')t} + \mathrm{h.c.} \tag{IV.26}$$

where we have introduced

$$\Gamma_{ij}(\omega) = \int_0^\infty d\tau c_{ij}(\tau) e^{\mathrm{i}\omega\tau} \tag{IV.27}$$

to account for the remaining terms in the time integral. Note that $\Gamma_{ij}(\omega)$ has the form of the Fourier-Laplace transform of the correlation function of the environment evaluated at the system frequency ω.

IV.1.6 Spectral and dispersion functions of the environment

As we have already seen, all the information about the environment was reduced to its correlation functions. However, for practical reasons, it is convenient to define the Fourier transform of the correlation functions of the environment, which will be called the spectral functions here[4]

$$C_{ij}(\omega) = \int_{-\infty}^\infty d\tau c_{ij}(\tau) e^{\mathrm{i}\omega\tau} = \int_0^\infty d\tau \left[c_{ij}(\tau) e^{\mathrm{i}\omega\tau} + c_{ji}^*(\tau) e^{-\mathrm{i}\omega\tau}\right] = \Gamma_{ij}(\omega) + \Gamma_{ji}^*(\omega) . \tag{IV.28}$$

[4] The correlation functions are then obtained as $c_{ij}(t) = \frac{1}{2\pi}\int_{-\infty}^\infty d\omega C_{ij}(\omega) e^{-\mathrm{i}\omega t}$.

Due to the symmetry relation of the correlation functions, we have that $C_{ij}^{*}(\omega)=C_{ji}(\omega)$, *i.e.*, the matrix $C(\omega)$ is Hermitian. Furthermore, being the Fourier transform of positive functions, Bochner's theorem ensures that the matrix $C(\omega)$ is always positive defined [11,16].

As for the correlation functions, a relevant feature of the spectral function is that it satisfies the KMS condition, which in the frequency domain reads

$$C_{ji}(-\omega)=e^{-\omega\beta}C_{ij}(\omega). \tag{IV.29}$$

We remind the reader that this relation plays an important role in maintaining the detailed balance [11,17].

Due to the KMS condition, the spectral function is not symmetric with respect to ω, so it can be split into a symmetric $C_{ij}^{\mathrm{sym}}(-\omega)=C_{ji}^{\mathrm{sym}}(\omega)$ and an antisymmetric $C_{ij}^{\mathrm{asym}}(-\omega)=-C_{ji}^{\mathrm{asym}}(\omega)$ component, such that

$$C_{ij}(\omega)=C_{ij}^{\mathrm{sym}}(\omega)+C_{ij}^{\mathrm{asym}}(\omega), \tag{IV.30}$$

where

$$C_{ij}^{\mathrm{sym}}(\omega)=\frac{C_{ij}(\omega)+C_{ji}(-\omega)}{2}=\frac{1+e^{-\omega\beta}}{2}C_{ij}(\omega), \tag{IV.31}$$

and

$$C_{ij}^{\mathrm{asym}}(\omega)=\frac{C_{ij}(\omega)-C_{ji}(-\omega)}{2}=\frac{1-e^{-\omega\beta}}{2}C_{ij}(\omega). \tag{IV.32}$$

The antisymmetric part is also known as the spectral density $J_{ij}(\omega)$ of the environment

$$J_{ij}(\omega)=C_{ij}^{\mathrm{asym}}(\omega). \tag{IV.33}$$

The above relations are very useful for practical applications. In fact, the direct measure of the correlation function of a quantum environment with an experimental setup is often very difficult, so in most cases, the spectral density is assumed or computed from quantum mechanics/molecular mechanics (QM/MM) or molecular dynamics (MD) approaches [17]. In this second case, the obtained spectral density is classical $J_{ij}^{\mathrm{cl}}(\omega)$ and needs to be carefully converted *a posteriori* to $J_{ij}(\omega)$. Then, the spectral function is recovered using eq. (IV.32). See for example [18] for more details.

In our derivation, $c_{ij}(\tau)$ has emerged as the correlation functions of a quantum environment, but the same results apply also in the case of classical correlation functions. In this easier case, we have $c_{ij}(\tau)=\langle B_i(\tau)B_j(0)\rangle_{\mathrm{eq}}$, where $B(\tau)$ is a classical (stochastic) process and the angular brackets denote the ensemble (statistical) average at equilibrium (see previous Chapters)[5]. Since classical correlation functions are

[5] Note that we used the overbar to indicate the same ensemble average in the previous Chapters.

real and even, the spectral function will be real and even too, that is $C_{ij}(\omega)=C_{ij}(-\omega)$, and corresponds directly to the spectral density of the classical processes $J_{ij}^{\mathrm{cl}}(\omega)$. In this regard, note that the spectral function of a general quantum environment becomes symmetric with respect to ω in the limit of high temperature, $\beta\to 0$ (cf. eq. (IV.29)).

The spectral function is connected through the Kramers-Kroning relation to the dispersion function of the environment

$$\Lambda_{ij}(\omega)=\frac{1}{2\pi}\mathcal{P}\int_{-\infty}^{\infty}d\omega'\frac{C_{ij}(\omega')}{\omega-\omega'}, \tag{IV.34}$$

where $\mathcal{P}$ denotes the principal value of the integral[6]. Again, it holds the symmetry relation $\Lambda_{ij}^{*}(\omega)=\Lambda_{ji}(\omega)$ that guarantees the Hermiticity of the matrix $\Lambda(\omega)$. It could also be shown that $\Lambda_{ij}(\omega)$ is related to $\Gamma_{ij}(\omega)$ through

$$\Lambda_{ij}(\omega)=\frac{1}{2\mathrm{i}}\int_{0}^{\infty}d\tau\left[c_{ij}(\tau)e^{\mathrm{i}\omega\tau}-c_{ji}^{*}(\tau)e^{-\mathrm{i}\omega\tau}\right]=\frac{\Gamma_{ij}(\omega)-\Gamma_{ji}^{*}(\omega)}{2\mathrm{i}}. \tag{IV.35}$$

As we will later see, the dispersion function is primarily related to the renormalization of the energetics of the system because of the interaction with the environment. Although it is evaluated at the system frequencies ω, the values of the dispersion functions depend explicitly on the entire spectral function, eq. (IV.34). This means that it includes the contribution of the high-frequency modes and the cutoff of the environment. Still, in most situations, when the Born-Markov approximation is valid the dispersion function slightly affects the dynamics. For this reason, it is completely disregarded in most applications of the Redfield theory and related algorithmic routines (*e.g.*, in the popular QuTiP Python library [19,20]). However, few work discuss the critical role of this term in the dynamics. Notably, Ishizaki *et al* have shown that the exclusion of these terms from the Redfield equation significantly change the transfer dynamics in a molecular dimer as the system-bath coupling increases [3]. On the other hand, Alicki emphasized that the renormalization implies some consistency problems in the theory, as the thermal equilibrium dictated by the KMS condition, eq. (IV.29), is based on the system Hamiltonian and not on the renormalized one [21]. In the following, we will pay special attention to the role of this imaginary contribution to the Redfield tensor.

---

[6] To avoid divergence in the numerical computation of the principal value, it could be convenient to use the relation $P\int_{-h}^{h}dx\frac{f(x)}{x}=\int_{0}^{h}dx\frac{f(x)-f(-x)}{x}$.

With the new definitions, we can write $\Gamma_{ij}(\omega)$ as a combination of the spectral and dispersion functions

$$\Gamma_{ij}(\omega)=\frac{1}{2}C_{ij}(\omega)+\mathrm{i}\Lambda_{ij}(\omega), \tag{IV.36}$$

and its conjugated complex

$$\Gamma_{ij}^{*}(\omega)=\frac{1}{2}C_{ji}(\omega)\text{-}\mathrm{i}\Lambda_{ji}(\omega)\neq\Gamma_{ji}(\omega). \tag{IV.37}$$

This last inequality shows that the matrix $\Gamma(\omega)$ is not Hermitian.

IV.1.7 Back to the Schrödinger picture

Eq. (IV.26) still relies on the interaction picture. So, for better readability, it is worth converting it into the Schrödinger picture through the transformation

$$\begin{aligned}\frac{d\rho_{\mathrm{S}}(t)}{dt}&=\frac{de^{-\mathrm{i}H_{\mathrm{s}}t}}{dt}\tilde{\rho}_{\mathrm{S}}(t)e^{\mathrm{i}H_{\mathrm{s}}t}+e^{-\mathrm{i}H_{\mathrm{s}}t}\tilde{\rho}_{\mathrm{S}}(t)\frac{de^{\mathrm{i}H_{\mathrm{s}}t}}{dt}+e^{-\mathrm{i}H_{\mathrm{s}}t}\frac{d\tilde{\rho}_{\mathrm{S}}(t)}{dt}e^{\mathrm{i}H_{\mathrm{s}}t}\\&=-\mathrm{i}\left[H_{\mathrm{S}},\rho_{\mathrm{S}}(t)\right]+e^{-\mathrm{i}H_{\mathrm{s}}t}\frac{d\tilde{\rho}_{\mathrm{S}}(t)}{dt}e^{\mathrm{i}H_{\mathrm{s}}t}\end{aligned} \tag{IV.38}$$

In this way, one obtains the most common form of the Redfield equation, that is

$$\begin{aligned}\frac{d\rho_{\mathrm{S}}(t)}{dt}&=-\mathrm{i}\left[H_{\mathrm{S}},\rho_{\mathrm{S}}(t)\right]-\sum_{i,j}\sum_{\omega,\omega'}\Gamma_{ij}(\omega')\left[S_i^{\dagger}(\omega),S_j(\omega')\rho_{\mathrm{S}}(t)\right]+\mathrm{h.c.}\\&=-\mathrm{i}\left[H_{\mathrm{S}},\rho_{\mathrm{S}}(t)\right]-\sum_{i,j}\left[S_i,Q_{ij}\rho_{\mathrm{S}}(t)\right]+\left[\rho_{\mathrm{S}}(t)Q_{ij}^{\dagger},S_i\right]\end{aligned} \tag{IV.39}$$

where to get the last line, we need to recall that S_i is Hermitian and define the operator

$$Q_{ij}=\sum_{\omega'}\Gamma_{ij}(\omega')S_j(\omega'), \tag{IV.40}$$

which is not usually Hermitian. Even if it is possible to rewrite the Redfield equation in a formal structure that is similar to the Lindblad form [15], it is impossible to guarantee *a priori* the positivity of the relaxation rates, leading to the already mentioned positivity problem. So, to force the conversion into a Lindblad equation further approximations must be applied. There is a rich literature about Lindblad forms mimicking Redfield evolution (see for example Chapter V). In the following, we discuss two particular cases where the Redfield equation naturally assume a Lindblad form.

IV.1.8 Secular approximation

The *secular approximation* (also known as the *rotating wave approximation*), introduced by Davies in 1974 [22], is probably the first attempt to take the Redfield equation to Lindblad form. Differently from the phenomenological Lindblad equation, the result of the secular approximation is a master equation that still presents the characteristic quantities of a microscopic derivation, and is usually named the Davies-Lindblad or quantum optical or secular Redfield master equation.

When the time scale used to look at the dynamics is larger than the inverse of system frequency separation, *i.e.*, $\Delta t \gg 1/\min|\omega-\omega'|$ with $\omega \neq \omega'$, the rapid oscillating terms in the interaction picture (eq. (IV.26)) typically cancel out during integration due to destructive interference [17]. So, the strongest approximation one can do, sometimes referred to as the *full* secular approximation, consists in neglecting any contribution from terms that have $\omega \neq \omega'$. This strong approximation is justified in principle only for large Δt. It is easy to show that the resulting equation is in Lindblad form. However, if the system does not have accidental degenerations, the effect of the full secular approximation is to completely decouple the relaxation of the population from the coherences [17].

There exist other (softer) definitions of the secular approximation in which the contribution of frequencies satisfying $\Delta t \leq 1/\min|\omega-\omega'|$ is maintained. Here, we call this category the *partial* secular approximation. An example of partial secular approximation is to consider clusters of frequencies $\bar{\omega}$ for which a constant spectral function is assumed $C_{ij}(\bar{\omega})$ [23]. Usually, the value of the spectral function is taken at the average frequency of the cluster. Then a full secular approximation is applied at the cluster level. Eq. (IV.39) then becomes

$$\frac{d\rho_{\mathrm{s}}(t)}{dt} = -\mathrm{i}\left[H_{\mathrm{s}} + H_{\mathrm{LS}}, \rho_{\mathrm{s}}(t)\right] + \sum_{i,j}\sum_{\bar{\omega}} C_{ij}(\bar{\omega})\left\{S_j(\bar{\omega})\rho_{\mathrm{s}}(t)S_i^{\dagger}(\bar{\omega}) - \frac{1}{2}\left[S_i^{\dagger}(\bar{\omega})S_j(\bar{\omega}), \rho_{\mathrm{s}}(t)\right]_+\right\}, \quad \text{(IV.41)}$$

where

$$H_{\mathrm{LS}} = \sum_{i,j}\sum_{\bar{\omega}} \Lambda_{ij}(\bar{\omega})S_i^{\dagger}(\bar{\omega})S_j(\bar{\omega}) \quad \text{(IV.42)}$$

is the so-called Lamb shift Hamiltonian involving the dispersion functions at cluster frequencies $\bar{\omega}$ and the operators $S_i(\bar{\omega}) = \sum_{\omega\in\bar{\omega}} S_i(\omega)$. In [24], Davidović calls the partial secular approximation by the evocative name of frequency coarse-graining. Note that, the partial secular approximation is reduced to the full one when the frequency width of the clusters is smaller than the minimum distance between the open system frequencies.

Within the secular approximation, the role of the dispersion function, entering the Lamb shift Hamiltonian, is to renormalize the system energies (eventually also changing the system eigenstates) due to the interactions established with the environment.

IV.1.9 Redfield with a δ-correlated environment

As mentioned in the derivation, in the Redfield equation we assume the environment to have very fast correlation times with respect to the system evolution. So, one can in principle enforce this assumption and treat the environment correlations functions as instantaneous, $c_{ij}(t) \propto \delta(t)$. In this case, the relative spectral function is real, $C_{ij}(\omega) = C_{ji}(\omega)$, and completely flat on the whole frequency domain, $C_{ij}(\omega) = C_{ij}(0)$. Thus, the spectral function is symmetric with respect to ω, $C_{ij}(-\omega) = C_{ij}(\omega)$, which means that the equilibrium condition will be at infinite temperature, $\beta \to 0$. We recall that this case corresponds to a classical reservoir with a white noise spectrum, which is exactly the case we considered in Chapter II.

Using a δ-correlated environment, the dispersion function of the environment vanishes (cf. eq. (IV.34)), so we do not have any Lamb shift in this case. The corresponding equation is

$$\begin{aligned}\frac{d\rho_{\mathrm{S}}(t)}{dt} &= -\mathrm{i}\left[H_{\mathrm{S}},\rho_{\mathrm{S}}(t)\right]+\sum_{i,j}\sum_{\omega,\omega'}C_{ij}\left\{S_j(\omega')\rho_{\mathrm{S}}(t)S_i^{\dagger}(\omega)-\frac{1}{2}\left[S_i^{\dagger}(\omega)S_j(\omega'),\rho_{\mathrm{S}}(t)\right]_+\right\}\\ &= -\mathrm{i}\left[H_{\mathrm{S}},\rho_{\mathrm{S}}(t)\right]+\sum_{i,j}C_{ij}\left\{S_j\rho_{\mathrm{S}}(t)S_i^{\dagger}-\frac{1}{2}\left[S_i^{\dagger}S_j,\rho_{\mathrm{S}}(t)\right]_+\right\}\end{aligned} \tag{IV.43}$$

where we used a more compact notation for $C_{ij}=C_{ij}(0)$.

One of the main advantages of using eq. (IV.43), instead of the Redfield or the secular Redfield, is that there is no need to diagonalize the system, so that one can work in the original basis without spending time in diagonalization routines.

IV.2 Exciton transport in an overdamped vibrational environment

For a long time, exciton transport in light-harvesting chromophoric systems has been described with incoherent hopping models (Förster theory). However, about a decade ago, the use of new instrumentation and more advanced spectroscopic techniques made it possible to measure long-lived coherences in exciton transport of light-harvesting complexes [25–27]. This observation conflicted with the incoherent models proposed for transport up to that time and triggered intense research aimed at proposing more accurate descriptions of the coherences and reliable estimations of transport efficiency (there is a vast literature on the subject, see for example [3,4,28–36]).

Although a complete study of the coherent properties has been shown to require the inclusion of non-Markovian effects, using time convolution [37,38] or convolutionless equations [39] or numerical exact methods [40,41], the Redfield equation is not of little use. In fact, in its simplicity (compared to more sophisticated approaches) it gives accurate insights into the dynamics in its range of applicability, which can be used as the starting point for more advanced descriptions.

The target of this section is thus to obtain a Markovian perturbative equation for the dynamics of the exciton, paying attention to its microscopic environment composed of the vibrational degrees of freedom of the chromophores. For the moment, we will follow a generic derivation for a prototypical system made of N molecules. Then, in the next section, we will contextualize the case of the Fenna-Matthews-Olson protein complex.

IV.2.1 Born-Oppenheimer approximation

We start by assuming the *Born-Oppenheimer approximation*, so that the electronic and vibrational degrees of freedom of each chromophore are separated. We further limit our molecules to only two accessible electronic levels: the ground state $|0\rangle$ and the excited state $|1\rangle$. The Hamiltonian of the complex system then reads

$$H = \sum_{i=1}^{N} H_i^{\mathrm{I}} + \sum_{\langle i,j \rangle} H_{ij}^{\mathrm{II}} \,, \tag{IV.44}$$

where the first sum on the right-hand side is over the single-molecule Hamiltonians

$$H_i^{\mathrm{I}} = H_i^{\mathrm{nuc},0}(q_i)|0_i\rangle\langle 0_i| + H_i^{\mathrm{nuc},1}(q_i)|1_i\rangle\langle 1_i|, \tag{IV.45}$$

while the second one, which runs over all the interacting pairs of molecules, regulates the electronic coupling between two different molecules

$$H_{ij}^{\mathrm{II}} = V_{ij}\left(|1_i 0_j\rangle\langle 0_i 1_j| + |0_i 1_j\rangle\langle 1_i 0_j|\right). \tag{IV.46}$$

In our model, we assume it to be independent of the nuclear degrees of freedom.

In eq. (IV.45), $q_i = \left\{q_{1,i},...,q_{3N_i^{\mathrm{nuc}},i}\right\}$ are the (dimensionless) coordinates associated with the $3N_i^{\mathrm{nuc}}$ phonon modes of molecule i, being N_i^{nuc} the number of nuclei for that molecule. Then, $H_i^{\mathrm{nuc},0/1} = T_i^{\mathrm{nuc}} + V_i^{\mathrm{nuc},0/1}(q_i)$ is the nuclear Hamiltonian for the chromophore in its ground/excited state, and it is composed of the kinetic T_i^{nuc} and potential $V_i^{\mathrm{nuc},0/1}(q_i)$ energies of the nuclei. The potential is itself the sum of two contributions: the nuclei-nuclei interaction $V_i^{\text{nuc-nuc}}(q_i)$ and the potential energy $E_i^{0/1}(q_i)$ due to the electrons, so that

$$V_i^{\mathrm{nuc},0/1}(q_i) = V_i^{\text{nuc-nuc}}(q_i) + E_i^{0/1}(q_i). \tag{IV.47}$$

IV.2.2 The displaced harmonic oscillator model

At this point, we assume the potential energy $V_i^{\mathrm{nuc},0/1}(q_i)$ in the ground and excited states to be described by a harmonic potential centred at the respective equilibrium configurations $q_i^{\mathrm{eq},0/1} = \left\{q_{1,i}^{\mathrm{eq},0/1},...,q_{3N_i^{\mathrm{nuc}},i}^{\mathrm{eq},0/1}\right\}$. To account for the difference between the equilibrium coordinates of the two states, we introduce the (dimensionless[7]) displacement $d_i = \left\{d_{1,i},...,d_{3N_i^{\mathrm{nuc}},i}\right\}$. This formalism is known as the *displaced harmonic oscillator model*. Furthermore, we assume the k-th phonon mode to have the same frequency $\omega_{k,i}$ in both the ground and excited state, which means, the harmonic potentials are identical but shifted. Eq. (IV.47) now takes the form

[7] Both the position q and displacement d are here assumed to be dimensionless to simplify the discussion. One can recover the original quantities by multiplying the reduced ones by a factor $\sqrt{\hbar/(m\omega)}$, where m is the mass of the harmonic oscillator.

$$V_i^{\text{nuc},0/1}(q_i) = E_i^{0/1}\left(q_i^{\text{eq},0/1}\right) + \frac{1}{2}\sum_k^{3N_i^{\text{nuc}}} \hbar\omega_{k,i}\left(q_{k,i} - q_{k,i}^{\text{eq},0/1}\right)^2, \tag{IV.48}$$

where $E_i^{0/1}\left(q_i^{\text{eq},0/1}\right)$ is the energy of the electronic ground and excited states in their equilibrium configurations. To simplify the notations, we define the zero of the coordinates to be the equilibrium configuration of the ground state, that is $q_{k,i}^{\text{eq},0} = 0$. As a direct consequence, $q_{k,i}^{\text{eq},1} = d_{k,i}$ and in order to avoid redundancy, we will omit the explicit dependence from the equilibrium coordinates in the following, *i.e.*, $E_i^{0/1} = E_i^{0/1}\left(q_i^{\text{eq},0/1}\right)$. Furthermore, since the energy difference between the equilibrium configurations in the ground and excited state is the only thing that matters, we can arbitrarily choose a common value for the ground state for every molecule E^0, and shift the excited state accordingly.

By separating the different contributions, Hamiltonian in eq. (IV.44) becomes

$$H = H^{\text{sys}} + H^{\text{reorg}} + H^{\text{ph}} + H^{\text{exc-ph}}, \tag{IV.49}$$

where we have a term that regulates the electronic energy and the coupling between the chromophores (it is responsible for the exciton transport through the system network even in absence of interactions with the vibrations)

$$\begin{aligned} H^{\text{sys}} &= H^{\text{ground}} + H^{\text{exc}} \\ &= E^0\sum_{i=1}^{N}|0_i\rangle\langle 0_i| + \sum_{i=1}^{N}E_i^1|1_i\rangle\langle 1_i| + \sum_{\langle i,j\rangle}H_{ij}^{\text{II}} \\ &= E^0\sum_{i=1}^{N}|0_i\rangle\langle 0_i| + \sum_{i=1}^{N}E_i^1|1_i\rangle\langle 1_i| + \sum_{\langle i,j\rangle}V_{ij}\left(|1_i0_j\rangle\langle 0_i1_j| + |0_i1_j\rangle\langle 1_i0_j|\right) \end{aligned} \tag{IV.50}$$

a correction to the exciton site energies due to the displacement between ground and excited state configurations

$$H^{\text{reorg}} = \frac{1}{2}\sum_{i=1}^{N}\sum_{k=1}^{3N_i^{\text{nuc}}}\hbar\omega_{k,i}d_{k,i}^2|1_i\rangle\langle 1_i| = \sum_{i=1}^{N}\lambda_i|1_i\rangle\langle 1_i|, \tag{IV.51}$$

the phonon Hamiltonian

$$H^{\text{ph}} = \sum_{i=1}^{N}\left\{T_i^{\text{nuc}} + \frac{1}{2}\sum_{k=1}^{3N_i^{\text{nuc}}}\hbar\omega_{k,i}q_{k,i}^2\right\}, \tag{IV.52}$$

and the Hamiltonian that regulates the interaction between the electronic degrees of freedom and the vibrational ones

$$H^{\text{exc-ph}} = -\sum_{i=1}^{N}\sum_{k=1}^{3N_i^{\text{nuc}}}\hbar\omega_{k,i}d_{k,i}q_{k,i}|1_i\rangle\langle 1_i|, \tag{IV.53}$$

The characteristic feature of this model is that the coupling is linear both in the oscillator coordinate and the system operators.

In the view of a Redfield equation, the system operators of the interaction are represented by $S_i = |1_i\rangle\langle 1_i|$, while the environment operators are $B_i = -\sum_{k=1}^{3N_i^{\text{nuc}}} \hbar\omega_{k,i} d_{k,i} q_{k,i}$. Please note that when eq. (IV.52) and (IV.53) are written in second quantization they take exactly the form we have used in section III.3 of Chapter III for the derivation of the pseudomode theory.

In eq. (IV.51), we have defined the so-called reorganization energy λ_i of the phonons of the i-th molecule as

$$\lambda_i = \sum_{k=1}^{3N_i^{\text{nuc}}} \lambda_{k,i} = \frac{1}{2} \sum_{k=1}^{3N_i^{\text{nuc}}} \hbar\omega_{k,i} d_{k,i}^2 , \tag{IV.54}$$

with $\lambda_{k,i}$ the reorganization energy of a single harmonic mode. The reorganization energy, that will play a central role in the following, corresponds to the amount of extra energy one has to account for a Franck-Condon transition, *i.e.*, a vertical transition starting from the equilibrium configuration, from the ground to the excited electronic state (see Figure 1).

For our present study, we will always consider a single excitation as the starting point, ignoring the (unlikely) case of double excitations or double-excited states. To simplify the notation above, we define the collective ground state as the tensor product between molecules in their ground states $|0\rangle = \bigotimes_{i=1}^{N} |0_i\rangle$, and the state with a single excitation localized at molecule i as $|i\rangle = |0_1\rangle \otimes ... |1_i\rangle \otimes ... |0_N\rangle$.

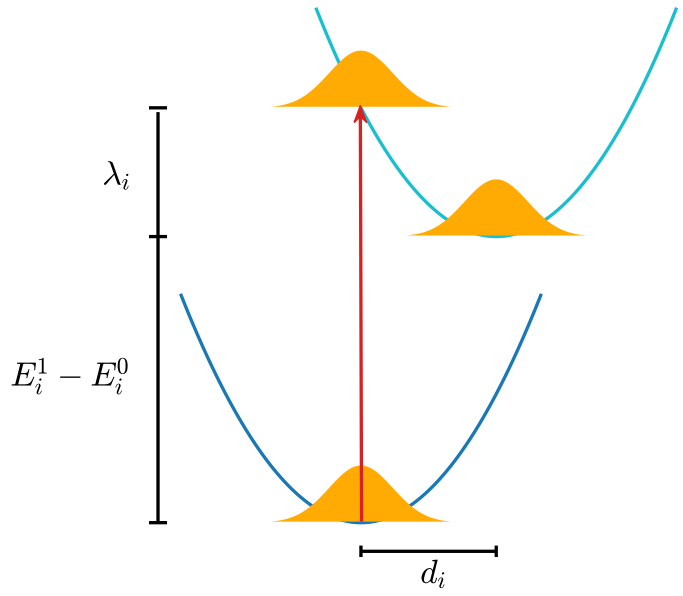

Figure 1. Schematic representation of a Franck-Condon (vertical) transition (red arrow) from the ground (blue line) to the excited (light blue line) electronic state of a chromophore coupled to a phonon environment. The final state is not the equilibrium position in the excited states, since the two potentials are displaced by d_i. The extra energy for the transition is known as the reorganization energy λ_i of the phonons.

IV.2.3 From discrete modes to continuous spectrum

As we have seen in the derivation of the Redfield equation, the correlation function of the environment interaction operators $\left\langle \tilde{B}_i(t) B_j \right\rangle_{\text{eq}}$ is a fundamental quantity for the dynamics of the reduced system. Here, for the sake of simplicity, we will consider the oscillations between different sites to be uncorrelated, *i.e.*, $\left\langle \tilde{B}_i(t) B_j \right\rangle_{\text{eq}} = \left\langle \tilde{B}_i(t) B_i \right\rangle_{\text{eq}} \delta_{ij}$, although this assumption can be easily relaxed.

In the case study we are considering, the calculation of the correlation functions of operators B reduce to the evaluation of the correlation function of the configurations of the harmonic oscillators

$$\begin{aligned} \left\langle \tilde{B}_i(t) B_i \right\rangle_{\text{eq}} &= \sum_{k=1}^{3N_i^{\text{nuc}}} \sum_{l=1}^{3N_i^{\text{nuc}}} \hbar^2 \omega_{k,i} \omega_{l,i} d_{k,i} d_{l,i} \left\langle \tilde{q}_{k,i}(t) q_{l,i} \right\rangle_{\text{eq}} \\ &= \sum_{k=1}^{3N_i^{\text{nuc}}} \hbar^2 \omega_{k,i}^2 d_{k,i}^2 \left\langle \tilde{q}_{k,i}(t) q_{k,i} \right\rangle_{\text{eq}} \end{aligned} \tag{IV.55}$$

where, with the second equivalence, we remarked the fact that different phonon modes are independent of each other. To have a physical interpretation of the meaning of the exciton-phonon coupling, one can think about the presence of the phonons as an external agent that causes a (generally quantum) fluctuation $\delta E_i^1(t)$ in the energies of the exciton levels (see previous Chapters), of which we know the mean $\left\langle B_i \right\rangle_{\text{eq}} = 0$ and the correlation function $\left\langle \tilde{B}_i(t) B_i \right\rangle_{\text{eq}}$ [42].

At this point, we have to model the correlation function. As anticipated, it can be done in different ways, from experimental data [43–46], by running QM/MM or MD calculations [18,28,47–55] or phenomenologically assuming a certain model. For example, in the past Chapters, we used δ-correlation and exponential decay that allowed for a (classical) stochastic implementation of dephasing assisted transport in generic networks. Here, we will use a quantum environment which allows us to account for the finite temperature effect in the dynamics. To do it, it is useful to introduce the spectral density of the exciton-phonons interaction [56]

$$J_i(\omega) = \frac{\pi}{2} \sum_{k=1}^{3N_i^{\text{nuc}}} \frac{\left(\hbar \omega_{k,i} d_{k,i}\right)^2}{\hbar} \delta\left(\omega - \omega_{k,i}\right), \tag{IV.56}$$

where $\delta\left(\omega - \omega_{k,i}\right)$ denotes the Dirac delta function.

The spectral density gives us the combined information about the strength of the coupling between the system (the exciton) and the environment (the phonons), and the density of environmental modes,

$W_i(\omega)=\sum_{k=1}^{3N_i^{\text{nuc}}}\delta(\omega-\omega_{k,i})$.[8] From the spectral density, one can recover the reorganization energy through the relation

$$\lambda_i=\frac{1}{\pi}\int_0^\infty d\omega\frac{J_i(\omega)}{\omega}=\sum_{k=1}^{3N_i^{\text{nuc}}}\frac{\hbar\omega_{k,i}^2d_{k,i}^2}{2}\int_0^\infty d\omega\frac{\delta(\omega-\omega_{k,i})}{\omega}=\frac{1}{2}\sum_{k=1}^{3N_i^{\text{nuc}}}\hbar\omega_{k,i}d_{k,i}^2\,. \tag{IV.57}$$

From eq. (IV.56), one may think of the spectral density as a discrete function of the frequency. However, if the number of normal modes is very high (formally $N_i^{\text{nuc}}\to\infty$), we can assume the spectral density to be a continuum [57], and the environment becomes actually a *bath*.[9] Since the number of nuclei is fixed, this can seem an unrealistic situation. However, there are at least two valid reasons to do it: The first one is that in solution, the number of modes is increased by the presence of solvent modes, which can be treated in the same way as we did for the nuclear ones. The second one is that, even if there are no other modes to add to the count, this is a way to obtain a reduced equation for the dynamics of the sole system (easy to handle), that can then be compared with the results obtained explicitly considering environment (on this topic see for example [57]).

We set as our target a Drude-Lorentz spectral density, *i.e.*, an Ohmic spectral density $J_i(\omega)\propto\omega$ with Lorentzian cutoff at high frequencies [3,31,40]. This spectral density corresponds to the so-called *overdamped Brownian oscillator model* of the vibrational modes [31,58]. The presence of a cutoff is natural in a realistic model of an environment, and it is formally required to prevent certain integrals from diverging, *e.g.*, the dispersion function.

To get our continuous spectral density, it is convenient to assume also a continuous density of modes

$$W_i(\omega)\xrightarrow{\text{continuum}}w_i(\omega)\,. \tag{IV.58}$$

This allows redefining the other quantities with the generic procedure

$$\sum_k f_{k,i}=\sum_{\omega_{k,i}}f_i(\omega_{k,i})W_i(\omega_{k,i})\xrightarrow{\text{continuum}}\int_0^\infty d\omega f_i(\omega)w_i(\omega)\,, \tag{IV.59}$$

where we passed from a discrete sum over all the mode frequencies of the environment, to a continuum of modes.

Using eq. (IV.59), the reorganization energy can then by written in terms of $w_i(\omega)$ as

---

[8] Note that, as expected, its integral gives the number of harmonic modes $\int_0^\infty d\omega W_i(\omega)=\sum_{k=1}^{3N_i^{\text{nuc}}}\int_0^\infty d\omega\delta(\omega-\omega_{k,i})=\sum_{k=1}^{3N_i^{\text{nuc}}}1=3N_i^{\text{nuc}}$.

[9] We obtain something equivalent to the so-called spin-boson model [56] used to study the dynamics of spin-½ systems coupled to a quantum harmonic bath.

$$\lambda_i = \sum_k \lambda_{k,i} = \sum_{\omega_{k,i}} \lambda_i\left(\omega_{k,i}\right) W_i\left(\omega_{k,i}\right) \xrightarrow{\text{continuum}} \int_0^\infty d\omega \lambda_i(\omega) w_i(\omega), \tag{IV.60}$$

while the spectral density becomes

$$\begin{aligned} J_i(\omega) &= \frac{\pi}{2}\sum_k \hbar\omega_{k,i}^2 d_{k,i}^2 \delta\left(\omega-\omega_{k,i}\right) = \pi \sum_{\omega_{k,i}} \lambda_i\left(\omega_{k,i}\right)\omega_{k,i}\delta\left(\omega-\omega_{k,i}\right) W_i(\omega) \\ &\xrightarrow{\text{continuum}} \pi \int_0^\infty d\omega_{k,i}\lambda_i\left(\omega_{k,i}\right)\omega_{k,i}\delta\left(\omega-\omega_{k,i}\right) w_i\left(\omega_{k,i}\right) = \pi\lambda_i(\omega)\omega w_i(\omega) \end{aligned} \tag{IV.61}$$

where in the second equivalence we made use of the definition of the reorganization energy of a single mode. This equation gives us an explicit expression for the two contributions that characterize the spectral density: the strength of the coupling, $\pi\lambda_i(\omega)\omega$, and the distribution of modes, $w_i(\omega)$. To obtain our desired Drude-Lorentz spectral density, we need to impose their product to be

$$J_i(\omega) = 2\lambda_i\omega\frac{\Omega_i}{\omega^2+\Omega_i^2}. \tag{IV.62}$$

A possible condition that satisfies the above spectral density is a Lorentzian density on modes

$$w_i(\omega) = \frac{2}{\pi}\frac{\Omega_i}{\Omega_i^2+\omega^2} N_i, \tag{IV.63}$$

with an Ohmic coupling with the system

$$\pi\lambda_i(\omega)\omega = \frac{\pi\lambda_i\omega}{N_i}, \tag{IV.64}$$

where N_i is the number of harmonic modes (nuclear + extra). Note that in this example $\lambda_i(\omega)$ is assumed to be constant for every mode.

In eq. (IV.62), Ω_i is called the cutoff frequency and corresponds to the inverse of the characteristic relaxation time of the phonons $\tau_i^{\text{ph}} = 1/\Omega_i$. It is thus a measure of the memory time of the environment, *i.e.*, we have an indicator for the Markovianity of the process. The cutoff frequency also gives us a parameter for the identification of the weak coupling regime that is crucial for the correct application of the Redfield equation. In general, for Markovian cases, the cutoff frequency should be larger than the relevant frequencies of the system, that is $\Omega \gg \omega$.

IV.2.4 Details of the spectral function

Differently to the spectral density defined in eq. (IV.33), the one we have introduced above is defined only in the positive semiaxis (see for example the extremes of integration in eq. (IV.61)). It has come out naturally as the frequencies of the harmonic modes are positives. To make them coincide, since we know that the spectral density is equal to the antisymmetric part of the spectral function, it is sufficient to impose the condition

$J_i(-\omega) = -J_i(\omega)$, which incidentally, in the case under consideration, leaves eq. (IV.62) unchanged but extends its limits to the entire real axis.

Now that the antisymmetric part of the spectral function is known, we can easily obtain the spectral function $C_i(\omega)$ as

$$C_i(\omega) = \frac{2}{1-e^{-\hbar\omega\beta}} C_i^{\text{asym}}(\omega) = \frac{2}{1-e^{-\hbar\omega\beta}} J_i(\omega) = 4\lambda_i \omega \frac{\Omega_i}{\omega^2 + \Omega_i^2} \frac{1}{1-e^{-\hbar\omega\beta}}. \tag{IV.65}$$

This expression contains all that we need to know about the environment-system coupling for the construction of our Redfield equation: the reorganization energy λ_i of the phonons, the cutoff frequency Ω_i of environment correlation functions and the (inverse) temperature β that we assume to be constant for all the environments. The most important range of values of the spectral function is in the region that comprehends the relevant frequencies of the system, $[-\omega_{\max}, \omega_{\max}]$, since they are directly connected with the relaxation operators in the Redfield equation.

In the following, we analyse the role of each of the three parameters characterising the spectral function determined by the Drude-Lorentz spectral density.

IV.2.4.1 Reorganization energy

The contribution to the spectral function due to the reorganization energy is the easiest to understand. Figure 2 reports the spectral functions for three different values of this parameter while maintaining constant the temperature and cutoff frequency. Notice how the reorganization energy controls the slope of the spectral function in the low-frequency range of the positive semiaxis. At higher reorganization energy correspond higher value of the curve, while the overall profile is only slightly perturbed. We can conclude that the reorganization energy is mostly involved in regulating the amplitude of the relaxation coefficients $C_i(\omega = E_\beta - E_\alpha)$, where E_α and E_β are two eigenenergies of the system. In other words, higher reorganization energies imply a quicker dephasing and relaxation dynamics.

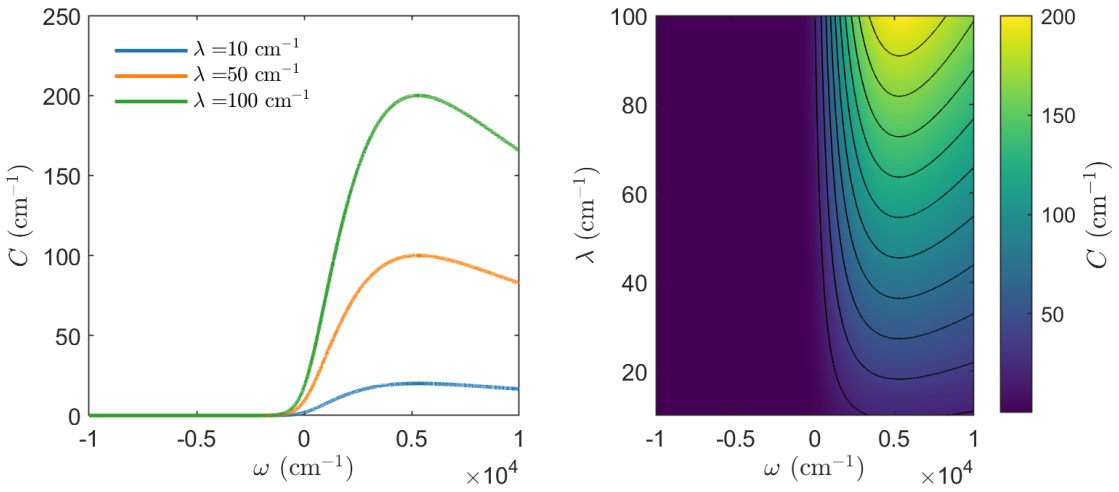

Figure 2. Left panel: Spectral function at different reorganization energies: $\lambda = 10\ \mathrm{cm}^{-1}$ (blue), $\lambda = 50\ \mathrm{cm}^{-1}$ (orange) and $\lambda = 100\ \mathrm{cm}^{-1}$ (green). The reorganization energy primarily influences the slope of the curve and the value of the maximum. Right panel: Dependence of the spectral function (colour gradient) on the reorganization energy λ. The other parameters are: $\Omega = 5300\ \mathrm{cm}^{-1}$ ($\tau^{\mathrm{ph}} \approx 1$ fs) and $\beta^{-1} \approx 241\ \mathrm{cm}^{-1}$ ($T = 347$ K). We have set $\hbar = 1$.

IV.2.4.2 Temperature

The variation of the temperature leads to two interesting limits of eq. (IV.65), that we can evince by looking at Figure 3. At low temperatures, $\beta \to \infty$, we have

$$\lim_{\beta\to\infty} C_i(\omega) = \lim_{\beta\to\infty} 4\lambda_i\omega \frac{\Omega_i}{\omega^2+\Omega_i^2}\frac{1}{1-e^{-\hbar\omega\beta}} = \begin{cases} 0 & \omega \le 0 \\ 4\lambda_i\omega\dfrac{\Omega_i}{\omega^2+\Omega_i^2} & \omega > 0 \end{cases} \tag{IV.66}$$

where the spectral function vanishes in the negative semiaxis, while is identical to the spectral density in the positive one. This completely asymmetrical situation is highly critical for the Redfield equation (note for example that the dispersion function, eq. (IV.34), tends to diverge). As a matter of fact, it is known that the Born-Markov approximation does not hold in this regime [3,13,41,59], therefore the master equation should not be used to describe the dynamics at extremely low temperatures.

On the other hand, in the high-temperature regime, $\beta \to 0$, we have that the spectral function becomes classical and approaches the Lorentzian shape also used in Chapter III

$$\lim_{\beta\to 0} C_i(\omega) = \lim_{\beta\to 0} 4\lambda_i\omega \frac{\Omega_i}{\omega^2+\Omega_i^2}\frac{1}{1-e^{-\hbar\omega\beta}} = 4\frac{\lambda_i}{\beta}\frac{\Omega_i}{\omega^2+\Omega_i^2}. \tag{IV.67}$$

Note that, keeping the reorganization energy and the cutoff frequency fixed, at very high temperatures the spectral function can assume large values and the weak-coupling approximation can consequently fail in this case [13].

In essence, the primary role of the temperature is to influence the symmetry of the spectral function of the quantum environments, by increasingly damping the values at negative frequencies for decreasing temperatures. This results underline the temperature dependence of the populations of the eigenstates at equilibrium, namely, the detailed balance.

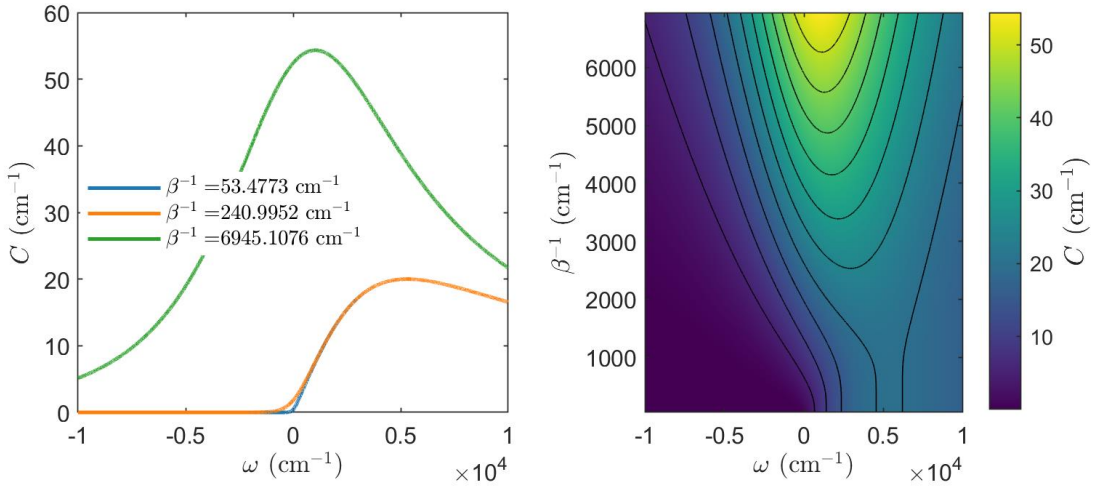

Figure 3. Left panel: Spectral function at different temperatures $\beta^{-1} \approx 53.5$ cm^{-1} ($T = 77$ K, blue), $\beta^{-1} \approx 241$ cm^{-1} ($T = 347$ K, orange) and $\beta^{-1} \approx 6945$ cm^{-1} ($T = 10^4$ K, green). The temperature primarily influences the symmetry of the curve, that is connected to the detailed balance, and the value in $\omega = 0$. Right panel: Dependence of the spectral function (colour gradient) on the temperature β. The other parameters are: $\lambda = 10$ cm^{-1} and $\Omega = 5300$ cm^{-1} ($\tau^{\text{ph}} \approx 1$ fs). We have set $\hbar = 1$.

IV.2.4.3 Cutoff frequency

The last parameter entering the definition of the spectral function is the cutoff frequency, whose influence is reported in Figure 4. Notice that the cutoff frequency influences the position, the value and even the width of the maximum of the spectral function. Incidentally, in the reported cases, the position of the maximum occurs in the proximity of the cutoff frequency, so one may wrongly think that in general there is a direct correlation between the position of the maximum and the Markovianity of the environment. However, this is not true, as the position of the maximum is also influenced by the temperature (see for example the spectral function represented as a green line in Figure 3 that has the same cutoff frequency as the others).

The cutoff also influences the spectral function in the low frequency range of the positive semiaxis. In fact, in the limit $\Omega_i \to \infty$, that corresponds to the Markovian situation in which $\omega_{\max} \ll \Omega_i$, we have

$$\lim_{\Omega_i \to \infty} C_i(\omega) = \lim_{\Omega_i \to \infty} 4\lambda_i \omega \frac{\Omega_i}{\omega^2 + \Omega_i^2} \frac{1}{1 - e^{-\hbar\omega\beta}} = 4\frac{\lambda_i \omega}{\Omega_i} \frac{1}{1 - e^{-\hbar\omega\beta}}. \tag{IV.68}$$

Here it is evident that the relaxation coefficients increase linearly both with the reorganization energy and the correlation time of the bath. Sometimes the ratio λ_i/Ω_i is treated as a single term which gives the effective coupling strength in Ohmic spectral densities (cf. Chapter III).

In this situation, when the temperature is sufficiently low ($\beta^{-1} \ll \hbar\Omega_i$), we can distinguish three regions of the spectral function depicted in Figure 5. For $\hbar\omega \ll -\beta^{-1}$ (negative semiaxis), we have the exponential suppression of the spectral function

$$\lim_{\Omega_i\to\infty} C_i(\omega)\big|_{\hbar\omega\ll-\beta^{-1}} = -4\frac{\lambda_i\omega}{\Omega_i}e^{\hbar\omega\beta} = 4\frac{\lambda_i|\omega|}{\Omega_i}e^{-\hbar|\omega|\beta}. \tag{IV.69}$$

In the region $-\beta^{-1} \ll \hbar\omega \ll \beta^{-1}$, that is around $\omega = 0$, the temperature term diverges hyperbolically as $1/(\hbar\omega\beta)$, but because of the linear coupling strength, the spectral function becomes constant

$$\lim_{\Omega_i\to\infty} C_i(\omega)\big|_{-\beta^{-1}\ll\hbar\omega\ll\beta^{-1}} = 4\frac{\lambda_i}{\hbar\Omega_i\beta} = C(\omega=0). \tag{IV.70}$$

When the system frequencies fall within this high-temperature and strongly Markovian regime, the correlation functions of the environment are well approximated by Dirac δ-functions (see also Chapter II).

The last region is $\beta^{-1} \ll \hbar\omega$, where we have that the spectral function is linear with the frequency and independent of the temperature

$$\lim_{\Omega_i\to\infty} C_i(\omega)\Big|_{\beta^{-1}\ll\hbar\omega} = \frac{4\lambda_i\omega}{\Omega_i}. \tag{IV.71}$$

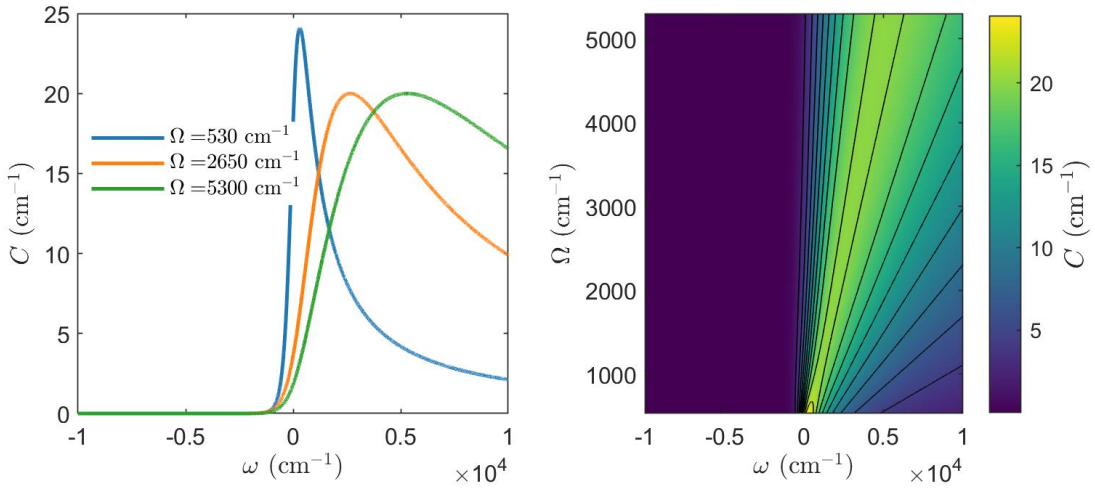

Figure 4. Left panel: Spectral function at different cutoff frequencies: $\Omega = 530$ cm^{-1} ($\tau^{\mathrm{ph}} \approx 10$ fs, blue), $\Omega = 2650$ cm^{-1} ($\tau^{\mathrm{ph}} \approx 5$ fs, orange) and $\Omega = 5300$ cm^{-1} ($\tau^{\mathrm{ph}} \approx 1$ fs, green). The cutoff frequency influences the slope of the curve and the position and value of the maximum. Right panel: Dependence of the spectral function (colour gradient) on the cutoff frequency Ω. The other parameters are: $\lambda = 10$ cm^{-1} and $\beta^{-1} \approx 241$ cm^{-1} ($T = 347$ K). We have set $\hbar = 1$.

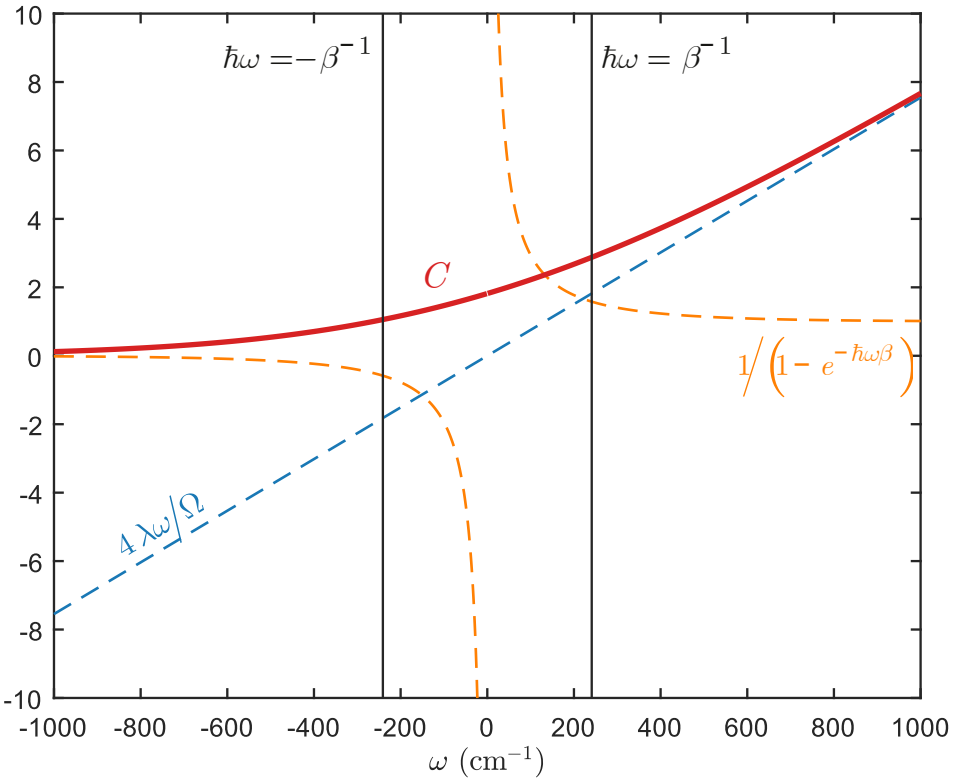

Figure 5. Detail of the spectral function $C(\omega)$ (red) in the region $\omega \ll \Omega$ (Markovian regime). We have separated the linear term (blue) from the temperature-dependent one (orange). Parameters are: $\lambda = 10$ cm^{-1}, $\Omega = 5300$ cm^{-1} ($\tau^{\mathrm{ph}} \approx 1$ fs) and $\beta^{-1} \approx 241$ cm^{-1} ($T = 347$ K). We have set $\hbar = 1$.

IV.3 Different shades of the Redfield equation

IV.3.1 Details of the system: the FMO protein complex

At this point, it is time to introduce the open system whose dynamics will be taken as the case-study for this Chapter and the next one. We choose the popular Fenna-Matthews-Olson (FMO) complex [60], a protein trimer composed of 8 bacteriochlorophylls (BChl) *a* per subunit, involved in the photosynthesis process of green sulfur bacteria. The spatial structure of a monomer of the FMO is reported in Figure 3 of Chapter I. The FMO complex is physically located between the chlorosome/baseplate, responsible for the light-harvesting process, and the bacteria reaction centre located on the membrane. FMO acts like a very efficient wire that transfers the excitation from the antenna pigments to the reaction centre in the very first instances of photosynthesis [61]. The FMO is one of the most studied complexes for exciton transport, and its fame is due to the fact that it has been the first protein where coherent oscillations were observed using optical spectroscopies [25,26,62].

The FMO complex is divided into three identical and well-spaced monomers so that there is not exciton exchange between different subunits during the dynamics. Each monomer can thus be considered an independent system. For about 20 years, since the first determination of the crystallographic structure of the FMO, each monomer was believed to consist of 7 BChl *a*, with BChl *a* 1 oriented toward the baseplate, and BChl *a* 3 interacting with the reaction centre [63,64]. The numbering we use has been chosen according to Fenna's original one reported in [60]. Now, we know the presence of an eighth chlorophyll placed between BChl *a* 1 and the baseplate that seems to be the contact point for the exciton transfer to the network [63]. Since BChl *a* 8 is far from the rest of the chlorophyll, its effect on the dynamics is negligible and it is usually ignored [65]. For this reason, and in order to be able to compare our results with those published, we will only consider the 7-chlorophyll model of the FMO complex in our analysis. We will refer to the electronic excited states of each BChl as the *sites* where the excitation can be found. Following this route, we take the Hamiltonian of the system in the site basis given by Adolphs and Renger in [64] for the FMO of the *Chlorobium tepidum* bacterium

$$H^{\mathrm{exc}} = \begin{pmatrix} 200 & -96.0 & 5.0 & -4.4 & 4.7 & -12.6 & -6.2 \\ -96.0 & 320 & 33.1 & 6.8 & 4.5 & 7.4 & -0.3 \\ 5.0 & 33.1 & 0 & -51.1 & 0.8 & -8.4 & 7.6 \\ -4.4 & 6.8 & -51.1 & 110 & -76.6 & -14.2 & -67.0 \\ 4.7 & 4.5 & 0.8 & -76.6 & 270 & 78.3 & -0.1 \\ -12.6 & 7.4 & -8.4 & -14.2 & 78.3 & 420 & 38.3 \\ -6.2 & -0.3 & 7.6 & -67.0 & -0.1 & 38.3 & 230 \end{pmatrix} \mathrm{cm}^{-1}. \qquad \text{(IV.72)}$$

The Hamiltonian diagonal terms E_i^1 are shifted in order to match the zero of the energetics with site 3 (the lowest in energy). In this case, the ground state energy is estimated to be $E^0 = -12210\ \mathrm{cm}^{-1}$. A graph-like representation of the above Hamiltonian is reported in the left panel of Figure 6, where the width of the edges is proportional to the coupling between the chromophores. From the coupling strength, a defined structure emerges that can be expected to be the favoured path for coherent energy transport in absence of interactions with the environment. This path corresponds to a linear chain connecting site 1 to site 4 and a cyclic network comprehending sites from 4 to 7 (see the right panel of Figure 6). This simplified graph has been used, for example, by Hoyer *et al* to compare the differences in the quantum speedup in the presence or absence of environmental interactions [66].

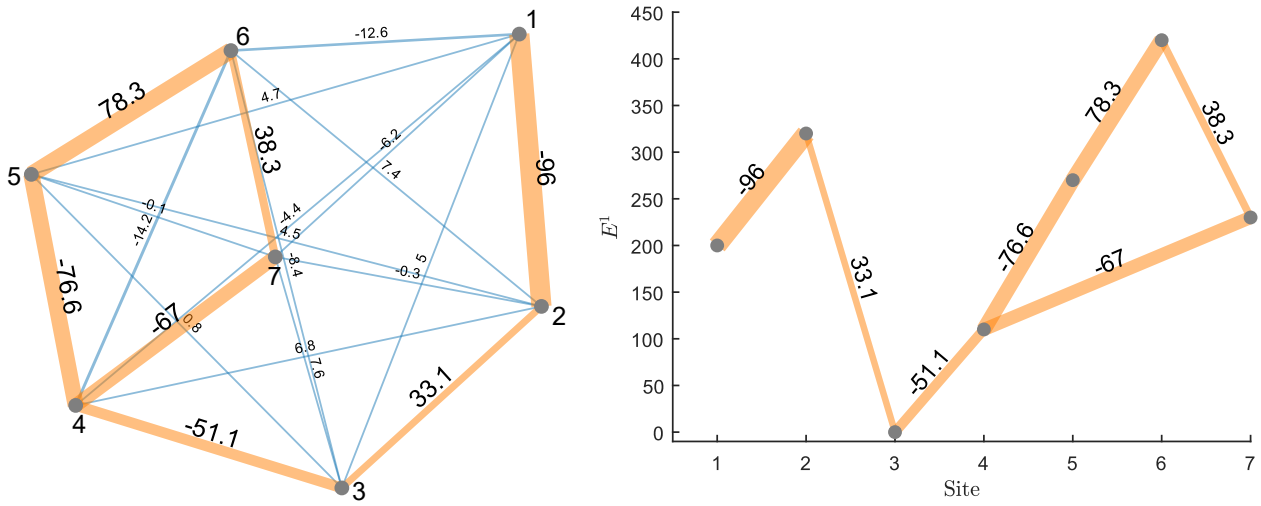

Figure 6. Left panel: The FMO connectivity is represented as an undirected graph. The width of the edges is proportional to the coupling strength between the BChls. Right panel: Only the main couplings (orange lines) are reported and the vertical position of the vertex of the graph is in relation to the exciton energy on that site. Every energy is reported in units of cm^{-1}.

In the FMO Hamiltonian, the standard deviation of the site energies is $\sqrt{\mathrm{var}\left\{E_i^1\right\}} \approx 127\ \mathrm{cm}^{-1}$, greater than the maximum coupling strength of the network, *i.e.*, $\max\left|V_{ij}\right| = 96.0\ \mathrm{cm}^{-1}$. Moreover, in general, the coupling between different chromophores is always smaller than the energy difference between them. With these observations, it is natural to expect that the eigenstates of the excitonic Hamiltonians will be mostly localized, *i.e.*, extended to a very limited number of sites. We briefly report and visualize them in Appendix A.

IV.3.2 Additional relaxation channels

To complete the characterization of our system, we add extra relaxation channels to describe the exciton recombination $\mathcal{L}^{\mathrm{R}}$ and the trapping from site 3 to the reaction centre $\mathcal{L}^{\mathrm{T}}$. We will treat these terms phenomenologically, *i.e.*, we express them as dissipative contributions in the Lindblad form, namely

$$\mathcal{L}^{\mathrm{R}}\left[\rho(t)\right] = \gamma^{\mathrm{R}} \sum_{i=1}^{N} \left\{ |0\rangle\langle i|\rho(t)|i\rangle\langle 0| - \frac{1}{2}\left[|i\rangle\langle i|, \rho(t)\right]_+ \right\}, \tag{IV.73}$$

$$\mathcal{L}^{\mathrm{T}}\left[\rho(t)\right] = \gamma^{\mathrm{T}} \left\{ |\mathrm{r.c.}\rangle\langle 3|\rho(t)|3\rangle\langle \mathrm{r.c.}| - \frac{1}{2}\left[|3\rangle\langle 3|, \rho(t)\right]_+ \right\} \tag{IV.74}$$

where γ^{R} is the (radiative + non-radiative) recombination rate that we assume to be the same for every chromophore, and γ^{T} is the trapping rate to the reaction centre $|\mathrm{r.c.}\rangle$. In this case, with $\rho(t)$ we indicate the density matrix of the (open) exciton system plus the ground state and reaction centre.

We consider both processes (IV.73) and (IV.74) as unidirectional. For the trapping, this is natural since the excitation is assumed to never come back from the reaction centre. For the recombination, it is justified by the

optical separation in energy ($\sim 12210\ \mathrm{cm}^{-1}$) that is widely larger than the typical temperature range of the environment ($53.5 \div 241\ \mathrm{cm}^{-1}$). If we exclude extra sources for radiative-induced excitations, at thermal equilibrium most of the population will be on the ground state. For the rest of the Chapter, we will assume $\gamma^{\mathrm{R}} = 1\ \mathrm{ns}^{-1}$ and $\gamma^{\mathrm{T}} = 1\ \mathrm{ps}^{-1}$ as estimated, for example, in ref [67].

As the FMO acts like a bridge to carry the photoinduced excitation from the antenna chromophore to the reaction centre the goal of the complex is to transfer the greatest amount of energy to the final destination. So, we can define the efficiency η of the light-harvesting process as the amount of population that has been transferred to the reaction centre at the end of the process (formally at time $t \to \infty$) [67,68][10]

$$\eta = \lim_{t\to\infty} \langle \mathrm{r.c.}|\rho(t)|\mathrm{r.c.}\rangle . \tag{IV.75}$$

However, since the reaction centre is connected to site 3 only, we can also write the efficiency as

$$\eta = \gamma^{\mathrm{T}} \int_0^\infty dt \langle 3|\rho(t)|3\rangle , \tag{IV.76}$$

which very much resembles the definition of the efficiency of transport given in Chapters II and III.

Since the population of the excited states of the FMO can be lost only through recombination or trapping, η will be determined by the kinetic competition between these two processes. To highlight this concept, the efficiency of trapping can be written in terms of the "efficiency of recombination" as

$$\eta = 1 - \lim_{t\to\infty} \langle 0|\rho(t)|0\rangle = 1 - \gamma^{\mathrm{R}} \sum_{i=1}^{N} \int_0^\infty dt \langle i|\rho(t)|i\rangle . \tag{IV.77}$$

Thus, high efficiency is not possible if the trapping time is slow compared to the recombination time. To extend our look at the problem, we introduce also this companion indicator that gives us a measure of the average transfer time it takes to populate the reaction centre [67,68], defined as

$$\tau = \frac{1}{\eta} \int_0^\infty dt \frac{d\langle \mathrm{r.c.}|\rho(t)|\mathrm{r.c.}\rangle}{dt} t = \frac{\gamma^{\mathrm{T}}}{\eta} \int_0^\infty dt \langle 3|\rho(t)|3\rangle t . \tag{IV.78}$$

[10] In the references, authors use non-Hermitian terms in the Hamiltonian to account for the recombination and trapping, while we decide to include both explicitly, so that we can easily look at the ground and reaction centre states.

IV.3.3 Redfield forms for the exciton dynamics in the FMO

As a modelling choice, in the following, we will always assume that all the molecules of our network have equal reorganization energy $\lambda_i = \lambda$ and cutoff frequency $\Omega_i = \Omega$. Moreover, we will assume the phonons of a chromophore to be uncorrelated from the phonons of the others, that is $C_{ij}(\omega) = C(\omega)\delta_{ij}$.

Now that we have the Hamiltonian and the eigenstates of the system, a model to describe the effects of exciton-phonon coupling and the extra relaxation channels, we can finally write the master equation that governs the transport in the FMO network as

$$\frac{d\rho(t)}{dt} = \mathcal{L}\left[\rho(t)\right] = \mathcal{L}^{\mathrm{H}}\left[\rho(t)\right] + \mathcal{R}\left[\rho(t)\right] + \mathcal{L}^{\mathrm{R}}\left[\rho(t)\right] + \mathcal{L}^{\mathrm{T}}\left[\rho(t)\right], \tag{IV.79}$$

where $\mathcal{L}^{\mathrm{H}}\left[\rho(t)\right] = -\mathrm{i}\left[H^{\mathrm{sys}} + H^{\mathrm{reorg}}, \rho(t)\right]$ and $\mathcal{R}\left[\rho(t)\right]$ is the Redfield superoperator. We will consider four variants of this operator to investigate the corresponding dynamics: the original Redfield superoperator (sometimes called "full" Redfield here)

$$\mathcal{R}^{\mathrm{R}}\left[\rho(t)\right] = \sum_i \sum_{\omega,\omega'} \Gamma(\omega')\left[S_i(\omega), S_i(\omega')\rho(t)\right] + \mathrm{h.c.}, \tag{IV.80}$$

the secular Redfield superoperator, where we neglect the elements of the Redfield tensor connecting transitions with different frequencies $\omega \neq \omega'$,

$$\mathcal{R}^{\mathrm{sec}}\left[\rho(t)\right] = \sum_i \sum_{\omega} \Gamma(\omega)\left[S_i(\omega), S_i(\omega)\rho(t)\right] + \mathrm{h.c.}, \tag{IV.81}$$

the Redfield "without imaginary part" (R-imag) [3] superoperator, that we use to study the effects of the dispersion function $\Lambda(\omega)$,[11]

$$\mathcal{R}^{\text{R-imag}}\left[\rho(t)\right] = \frac{1}{2}\sum_i \sum_{\omega,\omega'} C(\omega')\left[S_i(\omega), S_i(\omega')\rho(t)\right] + \mathrm{h.c.}, \tag{IV.82}$$

and the δ-correlated Redfield superoperator, that we will call the Haken-Strobl (HS) superoperator as it coincides with the Lindblad dissipator obtained in Chapter II for the Haken-Strobl model,

$$\mathcal{R}^{\mathrm{HS}}\left[\rho(t)\right] = C\sum_i S_i\rho(t)S_i - \frac{1}{2}\left[S_iS_i, \rho(t)\right]_+ . \tag{IV.83}$$

In this last case, we set $C = C(\omega = 0) = 4\lambda/\beta\Omega$ in eq. (IV.83), so that the spectral function is determined by the parameters used in the spectral density of the full Redfield.

In all the above equations, the system operators are

---

[11] The name "Redfield without imaginary part" originates from the fact that we impose here $\Lambda(\omega) = 0$, neglecting the imaginary contributions from $\Gamma(\omega) = C(\omega)/2 + \mathrm{i}\Lambda(\omega)$.

$$S_i = |i\rangle\langle i| . \tag{IV.84}$$

Note that in this section we reintroduced $\hbar = 1$ and we will maintain this choice from now on.

In the following, we will investigate how the above equations behave, when they fail to reproduce the system dynamics and why it happens. The ranges of parameters we will use are reported in Table 1 and includes the typical values used for multichromophore systems in physiological environments.

Table 1. Ranges of parameters we used in our investigation.

Parameter	Range
γ^{R}	1 ns^{-1}
γ^{T}	1 ps^{-1}
λ	0÷1000 cm^{-1}
Ω / τ^{ph}	80÷5300 cm^{-1} / ~66÷1 fs
β^{-1} / T	~53.5÷241 cm^{-1} / 77÷347 K

IV.3.4 Efficiency and trapping time

As a first analysis, we investigate the effects of changing λ and Ω on the efficiency and trapping time. To do so, we keep the temperature fixed at $\beta^{-1} \approx 241\ \mathrm{cm}^{-1}$ ($T = 347$ K), and propagate the dynamics with a coarse-graining in time of $\Delta t = 10$ fs for a total time of $t_{\max} = 1$ ns. We choose an initial state localized at site 1, which is the site closest to the injector. The efficiency η is quantified by the value of the population of the reaction centre at the end of the simulation. The value of the transfer time τ is calculated numerically through a trapezoidal integration.

Results are reported in Figure 7 (Redfield), Figure 8 (secular Redfield), Figure 9 (Redfield without imaginary part), and Figure 10 (Haken-Strobl). On the left panel, we have the surface of efficiency and transfer time to the reaction centre versus the reorganization energy λ and the cutoff frequency Ω of the environment varying independently. On the right panel, we show the calculated efficiencies corresponding to a particular ratio λ/Ω. This is because the ratio represents in this context an analogous of the *equivalent noise strength* that we used in Chapter III. Note that, the same ratio can be realized by different combinations of the reorganization energy and cutoff frequency, leading to a range of efficiencies corresponding to the same value of λ/Ω. Nevertheless, Figures 7-10 clearly show that it remains a good control parameter for the transport efficiency. The colour gradient is such that regions with high efficiency and fast transport are yellow, while non-efficient transport fades to purple. Although the trapping time and the efficiency quantify slightly different

aspects of the transport, both have similar profiles (inverse to each other) that are favoured approximately in the same areas.

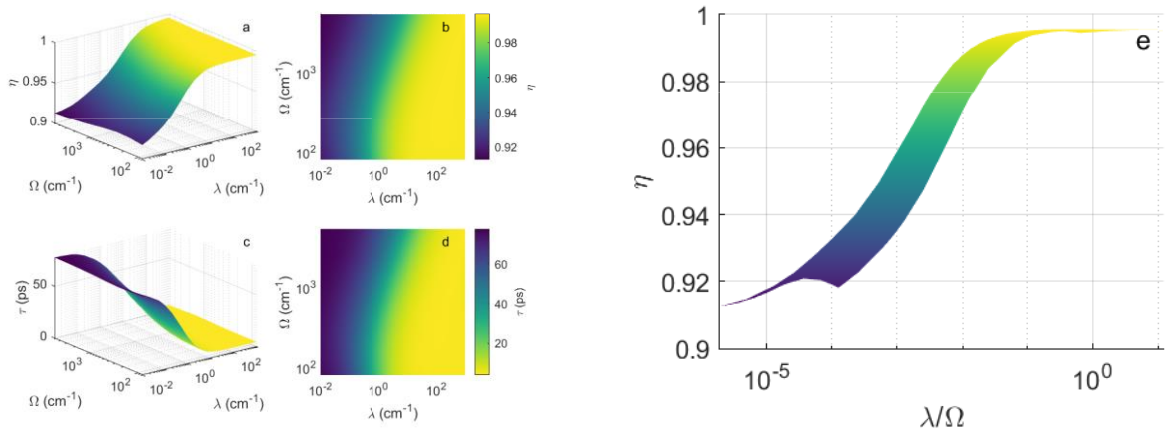

Figure 7. Results of the Redfield dynamics on the FMO complex at $\beta^{-1} \approx 241\ \mathrm{cm}^{-1}$ ($T = 347\ \mathrm{K}$). Left panel: Efficiency (a)(b) and transfer time (c)(d) to the reaction centre versus the reorganization energy λ and the cutoff frequency Ω. Favourable values (high efficiency and fast transport) are yellow, while unfavourable ones are purple. Right panel: Efficiency of the transport to the reaction centre versus the ratio λ/Ω (e).

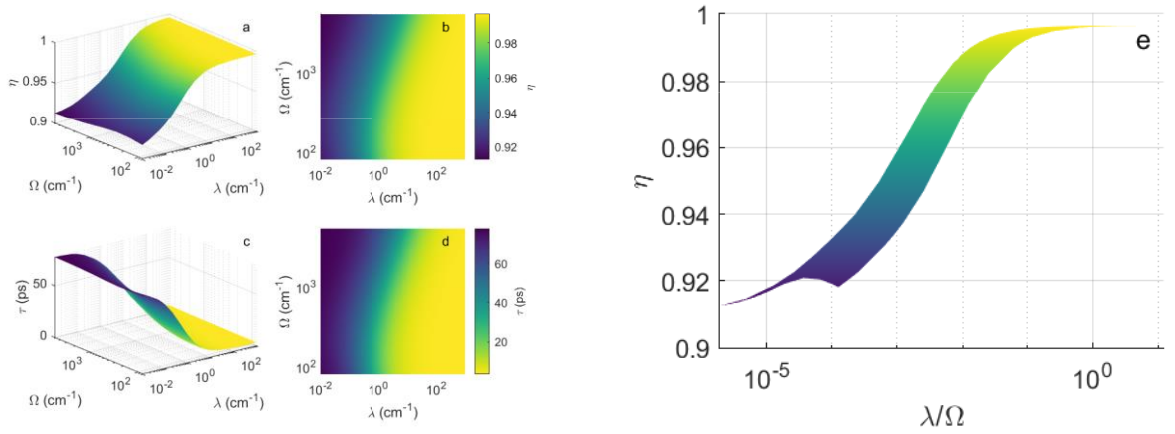

Figure 8. Results of the secular Redfield dynamics on the FMO complex at $\beta^{-1} \approx 241\ \mathrm{cm}^{-1}$ ($T = 347\ \mathrm{K}$). Left panel: Efficiency (a)(b) and transfer time (c)(d) to the reaction centre versus the reorganization energy λ and the cutoff frequency Ω. Favourable values (high efficiency and fast transport) are yellow, while unfavourable ones are purple. Right panel: Efficiency of the transport to the reaction centre versus the ratio λ/Ω (e).

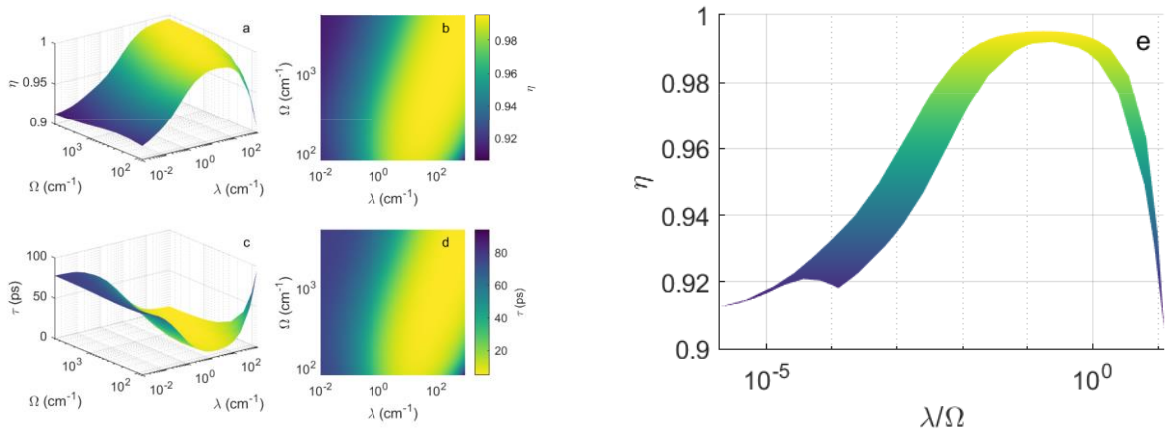

Figure 9. Results of the dynamics of the Redfield without imaginary part on the FMO complex at $\beta^{-1} \approx 241\ \mathrm{cm}^{-1}$ ($T = 347$ K). Left panel: Efficiency (a)(b) and transfer time (c)(d) to the reaction centre versus the reorganization energy λ and the cutoff frequency Ω. Favourable values (high efficiency and fast transport) are yellow, while unfavourable ones are purple. Right panel: Efficiency of the transport to the reaction centre versus the ratio λ/Ω (e).

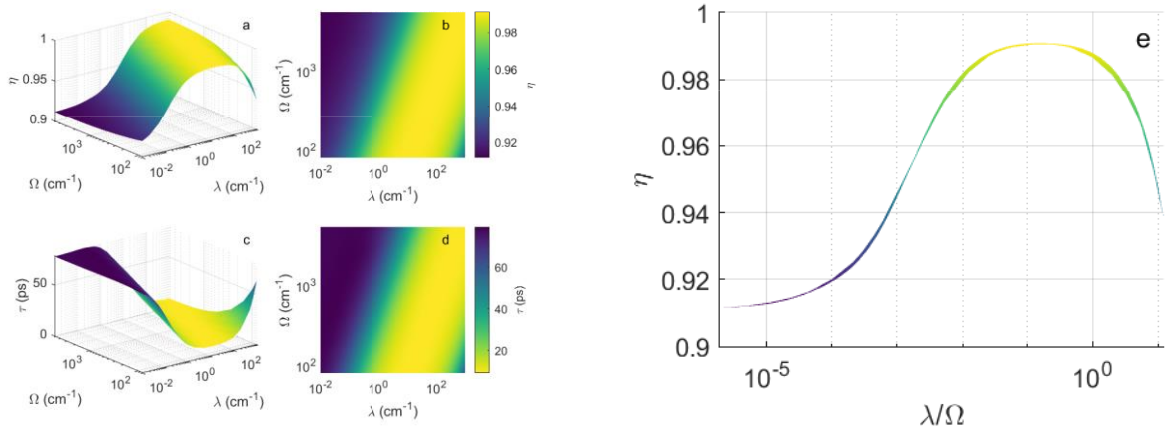

Figure 10. Results of the Haken-Strobl dynamics on the FMO complex at $\beta^{-1} \approx 241\ \mathrm{cm}^{-1}$ ($T = 347$ K). Left panel: Efficiency (a)(b) and transfer time (c)(d) to the reaction centre versus the reorganization energy λ and the cutoff frequency Ω. Favourable values (high efficiency and fast transport) are yellow, while unfavourable ones are purple. Right panel: Efficiency of the transport to the reaction centre versus the ratio λ/Ω (e).

From the study of the transport efficiency as a function of the spectral density parameters, we should highlight two main conclusions:

i. In the low λ/Ω region, the secular approximation and the omission of the imaginary contribution of the Redfield tensor do not significantly change the efficiency nor the typical trapping time. In

particular, all the versions of the dynamics produce an increasing sigmoidal trend in the plot of the efficiency versus λ/Ω, predicting a positive contribution of the environment to an efficient transport. The value of the efficiency at vanishing coupling is $\eta \approx 91\%$, achieved by the dynamics of the isolated system, and it reaches a maximum of $\eta \approx 99.6\%$ in the moderately strong coupling regime. Such a maximum is approached when the dephasing rate due to the phonons is around the same order of magnitude of the coupling strength between sites: $V \approx 4\lambda/\beta\Omega$, this is the condition in which the Hamiltonian and the dissipations cooperate to optimize the transport [37].

ii. The second important point to make is the profile of the transfer efficiency approaching the strong coupling limit. In particular, as already discussed in Chapters II and III, it is well known that, in the strong coupling regime, the transport is expected to be approximated by a hopping mechanism between the sites of the molecular network whose rates decreases as the coupling increases [3,69]. This slower transport should be reflected in a lower efficiency that is not correctly predicted by neither the full nor the secular form of the Redfield master equation. By omitting the imaginary part of the Redfield tensor, we recover the bell shape of the efficiency which is typical of ENAQT (see Figure 9). The issue of the behaviour of the transfer rates at high coupling and in particular the crucial role of the commonly neglected imaginary contribution to the Redfield tensor has been raised in a seminal paper by Ishizaki and Fleming [3] considering a molecular dimer. Here we recover the same phenomenology in a multichromophore setting.

The overall profile of the Redfield without imaginary part resembles that obtained with the Haken-Strobl equation, which differs from the others because of its narrow shape. This should not be surprising since from its definition in eq. (IV.83), HS equations that have a constant λ/Ω ratio give the same dynamics. Differently from the other variants, the HS equation is exact in all the range of parameters, since the Markov and Born conditions are always valid.[12] This is not true for the other equations, for which there are values of Ω and λ that cause the Born-Markov approximations to be violated and the predictions made to be no longer consistent with the underlying theory. We will come back to this issue in section IV.3.5.4 below. On the other hand, unfortunately, Haken-Strobl only represents a limiting case, and its assumptions are more stringent compared to the omission of non-secular terms or setting $\Lambda(\omega) = 0$.

IV.3.5 Results from the observation of the dynamics

We will now discuss the features of the dynamics obtained for the different equations as the λ, Ω and β parameters vary. In general, we will change only one parameter at a time to see how it affects the dynamics.

[12] By definition, the HS equation has correlation function that decays instantaneously (Markovian). Consequently, the environment is always relaxed in its thermal state and there is not entanglement with the state of the system (Born condition is naturally satisfied).

When they do not change, parameters are kept fixed at: $\lambda = 35\ \mathrm{cm}^{-1}$, $\Omega = 150\ \mathrm{cm}^{-1}$ ($\tau^{\mathrm{ph}} \approx 35.4$ fs) and $\beta^{-1} \approx 241\ \mathrm{cm}^{-1}$ ($T = 347$ K). The values of λ and Ω have been chosen by taking as a reference the estimations of Adolphs and Renger [64] for a realistic environment for the FMO complex [32,68]. Incidentally, this also reveals to be the most interesting position in the parameter space, as it allows us to see where the Redfield equation succeeds and fails. The temperature has been chosen from [4], which served us to initially benchmark the results of our software routine; however, we noted that comparable effects on the dynamics are obtained at room temperature.

For all the simulations, we set $\Delta t = 10$ fs the time we use to observe the dynamics. In some cases, the choice of Δt could produce artefacts in the observed dynamics (as introduced in the derivation of the Redfield equation) that will be discussed. Plots of the dynamics discussed in this section are reported in the Supplementary Information at the end of the thesis.

IV.3.5.1 The effects of the reorganization energy

We start our discussion by commenting on the dynamics of the populations of the density matrix at the variation of the reorganization energy λ. In most of the works focusing on the efficiency of transport, the discussion is only based on the dynamics of the site populations, which describe how the excitation moves through space, starting with an excitation localized at site 1. We take a more comprehensive approach by looking also at the exciton basis (*i.e.*, the eigenstates of H^{exc}), since it is the natural representation to interpret the different processes represented in the Redfield tensor. Moreover, we argue that the eigenstate population also allows identifying unphysical situations that may be hidden by looking at site populations only, indeed we could observe how the positivity issue clearly emerged in the energy representation while still generating legitimate positive site populations.

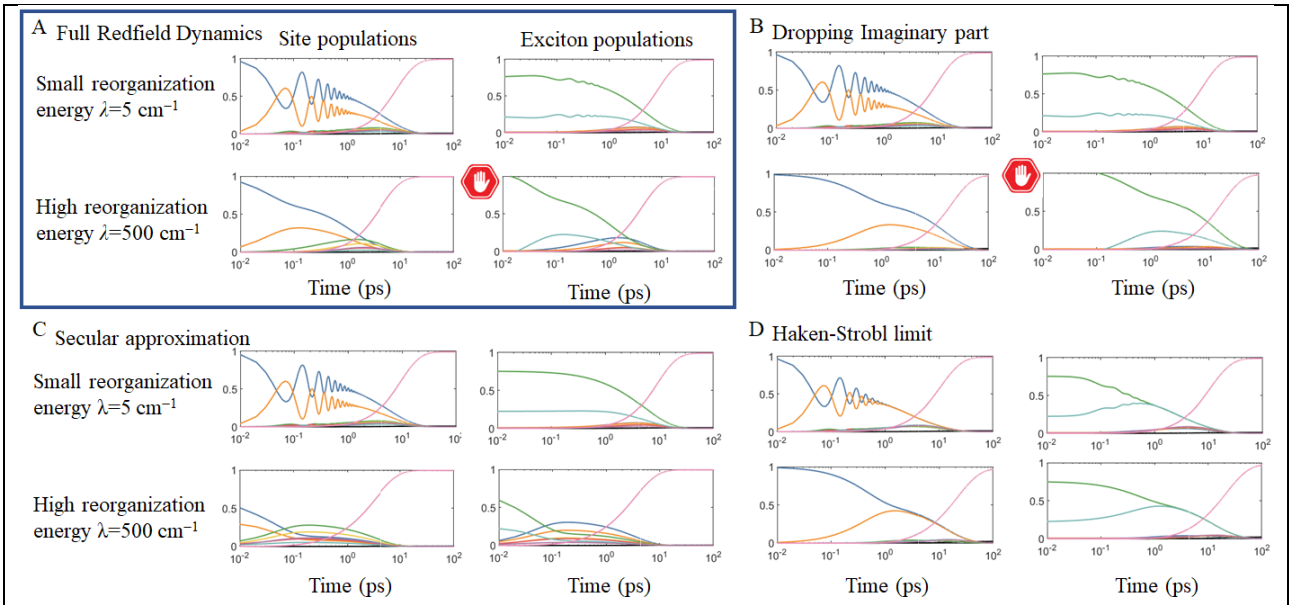

Figure 11. Dynamics of the site and exciton populations of the FMO molecular complex. The full Redfield dynamics is represented in panel A (surrounded by a blue contour), in panel B we drop the imaginary contribution in the Redfield tensor, the effect of secular approximation is reported in panel C, while in panel D we show the Haken-Strobl limit. Every panel is composed of four plots, two for the site populations and two for the exciton populations, in the small and high reorganization energy regime. For the Redfield equation with and without imaginary contributions, the emergence of negative exciton populations at high λ is a typical alarm bell that we are using the equations outside their range of validity, and is marked with an alert signal.

Figure 11 shows the time evolution of site and energy populations, in the case of small and high reorganization energies, calculated with the full Redfield equation, dropping the imaginary part of the Redfield tensor, applying the secular approximation and in the HS limit. Several observations are in order:

i. Let us first explain the general features of the dynamics by referring to the case of small reorganization energy (first line of panel A). The initial condition of the simulation is a state fully localized in chromophore 1 (blue line). As site 1 in mainly coupled to site 2 (orange, see Figure 6 for the coupling pattern), the initial dynamics is characterized by a coherent exchange between these two sites. According to the structure of the eigenstates shown in Figure 18, the dynamics starts with a significant initial population on the third (green) and the sixth (aquamarine) energy eigenstates. We can see that, when the dynamics escapes the "coherent trap" of sites 1-2 and spreads over the other sites (and eigenstates), reaching in particular site 3, the excitation starts to be captured by the reaction centre (pink line).

ii. Comparing the results generated by the different versions of the Redfield equations in the limit of small reorganization energy, we can appreciate some differences even though they predict practically the same transport efficiency. In particular, the secular form of the equation (panel C) does not

reproduce the small oscillations on the population of the eigenstates that are visible in the full Redfield equation and that persist by dropping the imaginary contribution on the Redfield tensor (panel B) and in the HS limit (panel D). This is the effect of the decoupling between populations and coherences (see section IV.1.8). For the specific FMO Hamiltonian model, the effect is small and leaves practically unaffected the pattern of the population dynamics on the site representation. This is because the eigenenergies of the model are well separated. However, it appears clear that when the model admits eigenstates that lie close in energy, the omission of non-secular contributions can deeply affect the dynamics. The other, even more visible, difference is observed in the HS limit, where the tendency toward the equalization of all the populations, corresponding to the infinite temperature condition, is clearly visible both in the site and in the energy representation.

iii. By increasing the value of the reorganization energy, we encounter a more complex scenario where the different approximations to the Redfield dynamics behaves differently. Let us take the depopulation rate of the initial state as representative of the rate at which the excitation is transfer from site-to-site. While all the equations describe an initial increasing of such transfer rate with increasing reorganization energy λ, in the intermediate regime (say λ between 10 cm^{-1} and 100 cm^{-1}) the full Redfield equation reach a maximum transfer rate which become independent on the value of λ. On the contrary, the secular version of the Redfield equation predicts a transfer rate which continues to increase linearly with the reorganization energy while by dropping the imaginary contribution and in the HS limit we assist to a lowering of the transfer rate.

These different behaviours can be observed in the second line of panels A-D in Figure 11, which shows the dynamics in a strong coupling regime ($\lambda = 500$ cm^{-1}), by looking at the depopulation of the initial state in chromophore one (blue line). The depopulation rate has reached a plateau in the full Redfield description, it is very fast when the secular approximation is applied, and it is slower in panel B and D. While the slow transfer rate predicted by the R-imag and HS equation reflects on a lower transport efficiency in the strong coupling regime as discussed in the previous section (see Figure 9 and Figure 10), the different dynamics predicted by the secular form does not imply a difference in the calculated efficiency compared to the full Redfield solution (see Figure 7 and Figure 8). This happens simply because in this regime the intersite redistribution rate is much higher than the trapping rate γ^{T}, which therefore become the bottleneck for the process of transfer to the reaction centre.

iv. Notice that while the site populations predicted by the full Redfield equation do not look “suspicious” even in this high coupling condition, by switching to the energy representation we quickly discover that something is wrong, as exciton 3 features a population exceeding 1 while other eigenstates are assigned a negative population. This is a warning that we are applying the theory outside its range of validity. The same warning pops up even by dropping the imaginary part (panel B). On the contrary, it will never happen by using the secular form (panel C) or in the HS limit (panel) D because these master equations have a Lindblad form (therefore preserving complete positivity by construction).

Before moving on, we are now in the position to summarize some important observations on the role of the non-secular contributions and imaginary contribution to the Redfield tensor: we can state that the secular terms in the Lamb-shift, present both in the full Redfield and the secular Redfield, do not give significant contributions to the dynamics in any regime. On the contrary, the secular relaxation terms play a predominant role in the low-coupling regime, increasing transport between sites as λ increases. Outside this regime, the inclusion of nonsecular terms in the real part of the relaxation superoperator (as in the Redfield without imaginary part) creates relevant connections between populations and coherences. This has the effect of slowing down the transport between sites of the FMO. In the full Redfield equation, the effect is compensated by the imaginary nonsecular terms. To better understand this, we report in Figure 12 heat maps of the real and imaginary parts of the tensor $\mathcal{L}^{\mathrm{H}}+\mathcal{R}^{\mathrm{R}}$ in the eigenstate basis at various values of λ.[13] As can be noted, the structure of the real part, *i.e.*, the relative weights of the tensor terms, remains fixed for different λ, while their value increases linearly. This is because only $\mathrm{Re}\left\{\mathcal{R}^{\mathrm{R}}\right\}$ contributes to the real part, which is influenced by $C(\omega)$. Differently, the imaginary part changes its structure with λ, passing from a (mostly) diagonal matrix to a structured one. This is due to the fact that it comprehends both the Hamiltonian contribution $\mathcal{L}^{\mathrm{H}}$, that is independent on λ, and the imaginary contribution $\mathrm{Im}\left\{\mathcal{R}^{\mathrm{R}}\right\}$, that is linear with λ due to $\Lambda(\omega)$. The differences in the behaviour of the Redfield equation with and without the imaginary part of $\mathcal{R}^{\mathrm{R}}$ can thus be understood based on this observation: At low λ values, the imaginary part of Redfield is dominated by the $\mathcal{L}^{\mathrm{H}}$ terms and behaves like R-imag equation, while at higher λ the emergence of $\mathcal{R}^{\mathrm{R}}$ contributions affects the dynamics. But what is the role of the imaginary terms $\mathrm{Im}\left\{\mathcal{R}^{R}\right\}$? In ref. [3], Ishizaki and Fleming argue they are responsible for the dissipation process of the environment. Because of the Markov approximation, the phonon modes of the environment are required to be always relaxed to their equilibrium state and the imaginary part of the Redfield superoperator is responsible for this equilibrium. At low λ/Ω, this approximation is valid. However, as the ratio increases, this implies that the mechanism of energy transfer between two chromophores (de-excitation of the donor and excitation of the acceptor), involves only the equilibrium states of the phonons, in a process that is thus independent of the reorganisation energy [3]. For this reason, the results of the Redfield dynamics are independent of λ in the strong coupling regime.

[13] To do so, we have to represent superoperators as matrices. This is possible by passing from the Hilbert space to the Liouville space [75]. When this change in space is applied, the density matrix in Hilbert space is represented as a vector in Liouville space, through a process known as *vectorization*. This technique is particularly useful for the numerical computation of the dynamics.

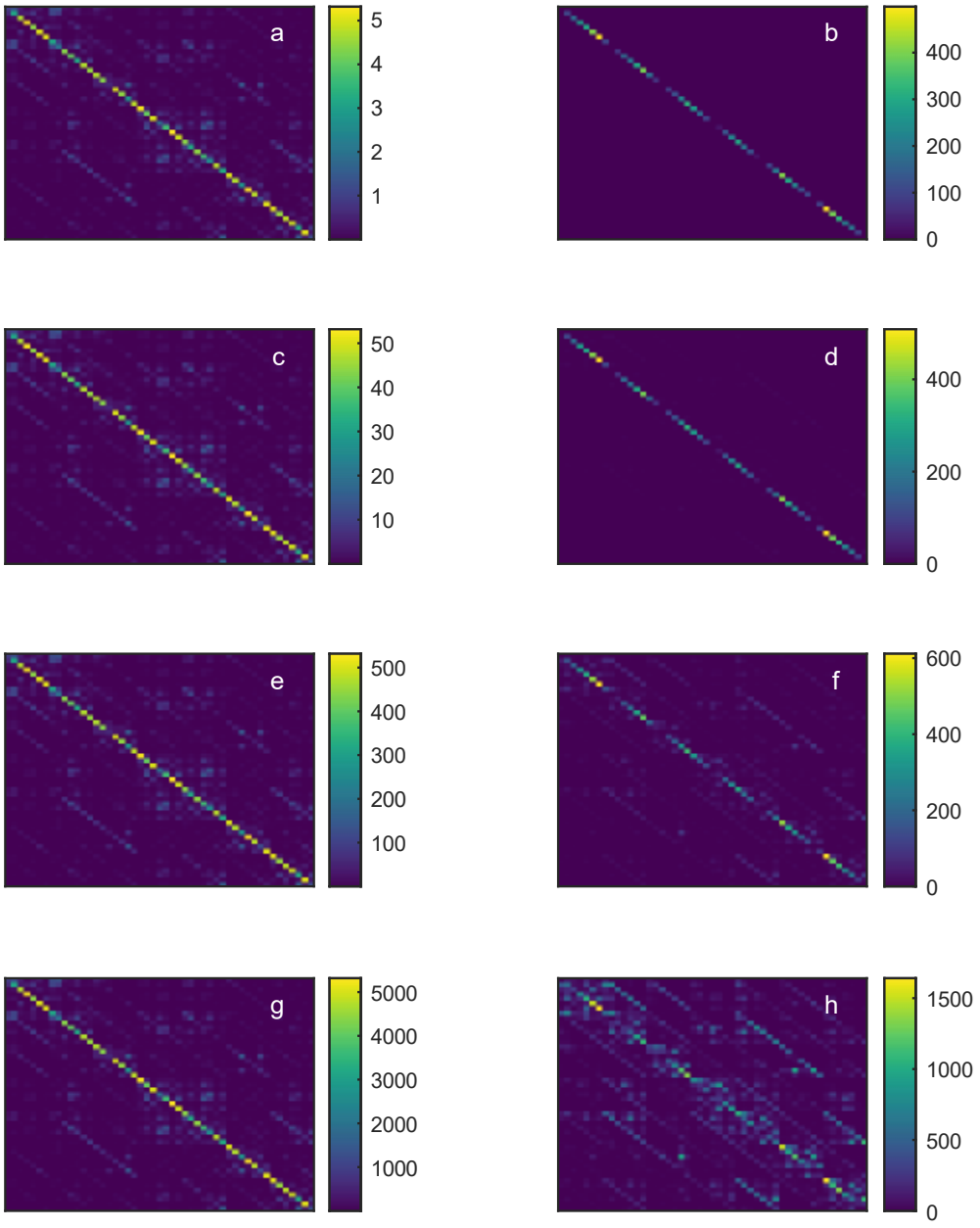

Figure 12. Heat maps of the terms of the tensor $\mathcal{L}^{\mathrm{H}} + \mathcal{R}^{\mathrm{R}}$ in the exciton basis. The absolute values (units of cm^{-1}) of the real component are reported in (a, c, e, g), while the absolute values (units of cm^{-1}) of the imaginary terms are in (b, d, f, h). Tensors have been calculated for the following values of the reorganization energy: $\lambda = 1\ \mathrm{cm}^{-1}$ (a, b), $\lambda = 10\ \mathrm{cm}^{-1}$ (c, d), $\lambda = 100\ \mathrm{cm}^{-1}$ (e, f) and $\lambda = 1000\ \mathrm{cm}^{-1}$ (g, h). Other parameters are: $\Omega = 150\ \mathrm{cm}^{-1}$ and $\beta^{-1} \approx 241\ \mathrm{cm}^{-1}$.

IV.3.5.2 The effects of the cutoff frequency

What happens to the dynamics as the cutoff frequency changes is more complex. For this study, we will limit ourselves to investigating the effects this parameter has on the (Markovian) Redfield dynamics, leaving a reference to Chapter III for a more complete analysis of the effects of non-Markovianity on the dynamics of

a system. In the derivation of the Redfield equation, we introduced a series of conditions for the Born-Markov to be valid. In particular, it is required that the time step Δt with which we look at the dynamics must be greater than the coherence time τ^{ph} of the environment, which we recall is the inverse of the cutoff frequency Ω. If this is not the case, memory effects come into play in the first few instants of the dynamics that must be considered explicitly [10,13], and the Redfield equation, which in general never guarantees the positivity of the density matrix, can easily return unphysical situations. We can observe examples of this phenomenon in the Redfield (and R-imag) dynamics when the relaxation time of the environment becomes longer than the chosen time step $\Delta t = 10$ fs (figures in Sup. Info.). In Figure 13, we follow the dynamics of the smallest eigenvalue of the density matrix, which should be positive semi-definite for valid physical systems, at values of $\tau^{\text{ph}} \approx 10$ fs, 35.4 fs and 66 fs. As we can see, times $t < \tau^{\text{ph}}$ result in an invalid eigenvalue, and the non-positivity gets worst as the correlation time increases. The effect is of course absent when the secular approximation is applied since the corresponding equation is in Lindblad form (so it always implements a positive map). The HS equation is also immune because of its δ - correlated environment.

Another feature related to the cutoff frequency is that, as we know, the ratio λ/Ω is very important for the dynamics. So we can expect to obtain the same trends observed in the previous paragraph by changing Ω, and in practice, it is exactly what we observed. However, since we have set $\lambda = 35$ cm^{-1} and a threshold of $\Omega = 80$ cm^{-1} to have not relevant problems with non-Markovianity, we cannot see the typical trend inversion in transport rate in the R-imag and HS dynamics, as we never reach the turning point. Furthermore, while reorganization energy acts only as a multiplicative factor for spectral function, a variation of the cutoff modifies the shape of $C(\omega)$, as seen in the previous section. Dynamics with different Ω will therefore exhibit differences between them due to the different mutual weights of the relaxation channels at the various frequencies ω of the system. This difference is responsible for the broadening of the efficiency profiles in Figure 7e, Figure 8e and Figure 9e. So we have one more element to understand those efficiency profiles: for small λ/Ω the profile is narrow because the environment only perturbs the dynamics, which then behaves similarly to what Schrödinger predicts. Where there is maximum efficiency, the profile is again narrow because, as seen previously, the transfer to the reaction centre becomes the bottleneck. In the remaining zones, the shape of the spectral function, influenced by the value of the cutoff frequency, results in differences in the relaxation process that are reflected in the broadening of the efficiency profile.

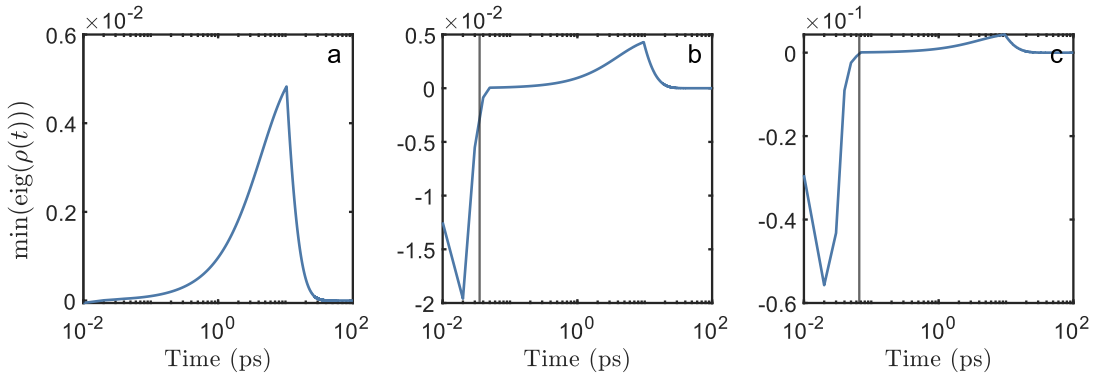

Figure 13. Redfield dynamics of the lowest eigenvalue of the density matrix $\rho(t)$ for $\Omega = 530$ cm^{-1} ($\tau^{\mathrm{ph}} \approx 10$ fs) (a), $\Omega = 150$ cm^{-1} ($\tau^{\mathrm{ph}} \approx 35.4$ fs) (b) and $\Omega = 80$ cm^{-1} ($\tau^{\mathrm{ph}} \approx 66$ fs) (c). For time steps less that the environment correlation time τ^{ph} (vertical lines), the Redfield equation does not guarantee that the dynamics are physically acceptable.

IV.3.5.3 The effects of the temperature

The FMO complex of green sulfur bacteria can operate in a very large range of temperatures in nature, from a hundred meters deep in the Black Sea to the hot springs in New Zealand (*e.g.*, the *Chlorobium tepidum*) [70]. Moreover, under experimental conditions, it can be cooled down to 77 K or work at room temperature. In the Sup. Info., we report the dynamics of the populations of the Redfield variants for temperatures in the range $T = 77 \div 347$ K. The other parameters are kept fixed at $\lambda = 35$ cm^{-1} and $\Omega = 150$ cm^{-1}.

From the dynamics, we note that as temperature decreases the initial coherent beatings are maintained for a longer time. Since this phenomenology is also evident for the Haken-Strobl case, for which temperature is merely a fictitious parameter that changes the strength of dephasing, the explanation lies in the fact that as the temperature decreases, the $C(\omega)$ coefficients that regulate the inter-site equilibration in the FMO also decrease. In other words, environmental fluctuations diminish with decreasing temperature. Note that, since the Hamiltonian is not temperature dependent, the frequency of the beatings is not affected.
All the dynamics of the Redfield with and without the imaginary part are very similar, suggesting that the temperature gives a small contribution to the dispersion function in this range. They are also very similar to the secular Redfield results, with the only difference being that it overestimates the initial site beatings with respect to Redfield, and neglects the rapid oscillations of the exciton populations.

In the examined cases, the efficiencies and trapping times are very similar in all the temperature ranges, suggesting that temperature plays a little role under these conditions of reorganization energy and cutoff.

Temperature can also cause problems with non-positivity (see section IV.2.4.2). In fact, besides the impossibility of correctly reproducing the dynamics in the first instants (due to the finite memory time of the environment), the Redfield equation faces difficulties in guaranteeing fully physical evolution at very low

temperatures. In Figure 14, the lowest eigenvalue of the density matrix $\rho(t)$ is evolved *via* Redfield equation at the temperature of 77 K. To verify that the problem is not dependent on the initial condition, the reported dynamics start from a localization on site 1 and from the 5th eigenstate of the FMO Hamiltonian (the most delocalized on sites, see Appendix A). In both cases, the non-positivity persists for all, or nearly all, of the duration of the dynamics, returning to an acceptable value (i.e., to zero) only at long times when the population has been transferred to the reaction centre and the ground state. Curiously, the omission of the Lamb-shift seems to solve the problems associated with this non-physical behaviour, which in any case turns out to be quite small with peaks in the order of 10^{-3}.

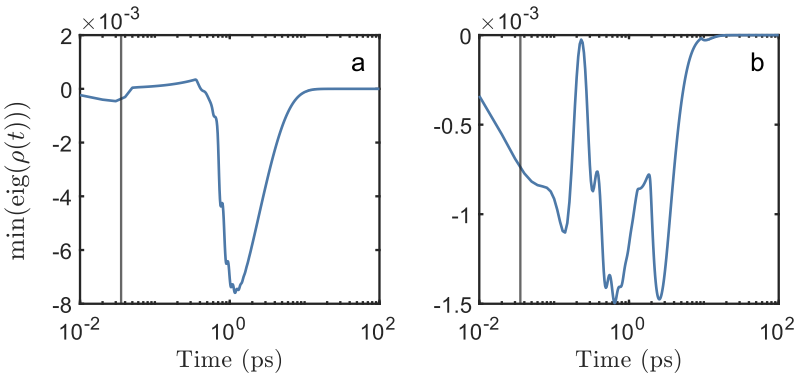

Figure 14. Redfield dynamics of the lowest eigenvalue of the density matrix $\rho(t)$ for $\beta^{-1} = 53.5$ cm^{-1}, *i.e.*, $T = 77$ K. Initial state localized at site 1 (a), or at the eigenstate 5 (b). At this low temperature, Redfield has problems in the predicting a physical evolution also at times that are longer than the environment correlation time τ^{ph} (vertical lines).

IV.3.5.4 Physical and non-physical dynamics in the strong-coupling regime

In sections IV.3.4 and IV.3.5.1, we have noted that the Redfield without imaginary part seems to reproduce the trend of the Haken-Strobl equation at high λ. However, so far, we have only discussed the dynamics of the populations, but, since quantum states are defined by the presence of coherences, it is also fundamental to look at their behaviour to understand something more about the undergoing processes.

We need to highlight that four factors regulate the dynamics: the Hamiltonian, that is responsible for the coherence modulation, the phonon relaxation, that is the main source of dissipations in both bases, the trapping, which acts as a damping term for the coherences involving site 3, and the recombination that damps all the coherences in the site basis, but with a longer time scale. In Sup. Info., we report the dynamics of the coherences at different reorganization energies λ starting with localization at site 1. We keep the other parameters fixed at $\Omega = 150$ cm^{-1} and $\beta^{-1} \approx 241$ cm^{-1}.

In ref. [3], Ishizaki and Fleming (implicitly) suggest that the similarities between the R-imag and HS results are due to the lack of $\Lambda(\omega)$ contributions in both equations, associated with the dissipation of the environment.

However, a part from some similarities, the two equations have some fundamental differences. The first reason is that in the case of the R-imag equation, the absence of such terms is the result of a user's choice (we are neglecting terms that appear in the original Redfield equation), while for the Haken-Strobl it is a natural consequence of its δ-correlated environment. The second reason stays in the observation of the behaviour of the coherences. In fact, differently from the populations, where the main discrepancies can be traced to the effects of finite temperature, the coherences differ remarkably in the two cases. For example, let us look at the formation of the site coherences in the first instances of the dynamics. In both cases, the maximum value is reached more quickly as λ increases in the strong coupling regime. However, if for Haken-Strobl it diminishes with increasing λ, for the R-imag the amplitude remains constant. This sounds particularly strange if one looks at the site populations. In fact, in the strong coupling regime, populations remain practically unchanged in the first instances of the dynamics, so how is such a fast and intense formation of coherences possible? By looking at numbers, it becomes clear that some of the coherences exceed the threshold value fixed by the populations (*i.e.*, it must always hold that $\left|\rho_{ij}\right| \leq \sqrt{\rho_{ii}\rho_{jj}}$). In practice, this confirms once again that we cannot trust the evolution of the equation in large reorganization energy regions.

Another proof of the difference between R-imag and HS equations is in the passage from quantum to classical transport. It is well known that, when the electronic coupling V_{ij} becomes perturbative in comparison with the dissipations, the dynamics of the transport can be described with a good approximation by the Förster theory [3,17,40,71], which predict an incoherent jumping process whose kinetic rates get smaller for large reorganization energies (cf. Chapter III). In [3,40], Ishizaki clearly shows that the Redfield transfer rates, whether in the secular or non-secular form, with or without the $\Lambda(\omega)$ contributions, are never compatible with the Förster ones. This is emblematic of the fact that, although the R-imag equation has "acceptable" phenomenological profiles for the efficiency, the trapping rate and the dynamics of the site populations, it predicts (for the large λ) unphysical coherences and does not match with Förster predictions.

The case is very different for the Haken-Strobl equation. In [66], Whaley and co-workers demonstrate that the Haken-Strobl dynamics on an infinite linear chain reduces to a classical diffusion transport in the asymptotic limit of large dephasing rates ($\lambda \to \infty$ in our analysis). In general, by calculating the fluxes between sites [65], it is possible to see that in the strong coupling regime the local currents derived from the off-diagonal elements of the density matrix (coherences), *i.e.,* quantum fluxes [65]

$$J^{\mathrm{Q}}_{i\neq j}(t) = -2V_{ij}\,\mathrm{Im}\left\{\rho_{ij}(t)\right\}, \tag{IV.85}$$

matches the classical ones calculated using just the diagonal elements (populations) [65]

$$J^{\mathrm{C}}_{i\neq j}(t) = \kappa^{\mathrm{F}}_{ij}\left(\rho_{ii}(t) - \rho_{jj}(t)\right), \tag{IV.86}$$

where κ^{F}_{ij} is the Förster rate between sites i and j [71–73] (see Appendix B for more details). We give an example of the excellent agreement for $\lambda = 1000\ \mathrm{cm}^{-1}$ in Figure 15. This demonstrates that the HS results are consistents also when the process passes from quantum to classical-like transport.

In conclusion, one might ask why, if the transport becomes classical-like, we still see coherences in the dynamics of the Haken-Strobl. The answer stays in the form of the dissipator. A classical master equation (Förster) is made of real terms that directly connect site populations with other site populations. In the HS equation (excluding trapping and recombinations), these terms do not exist since the dissipator acts only on the site coherences. On the other hand, coherences mediate the populations to populations transport orchestrated by the Hamiltonian. Thus, in non-equilibrium situations, there is an interplay between the creation and the damping of the coherences that is responsible for the actual transport. However, in the strong coupling regime, coherences do not add any additional information to that already provided by populations, as can be seen from the equivalence between quantum and classical fluxes [29].

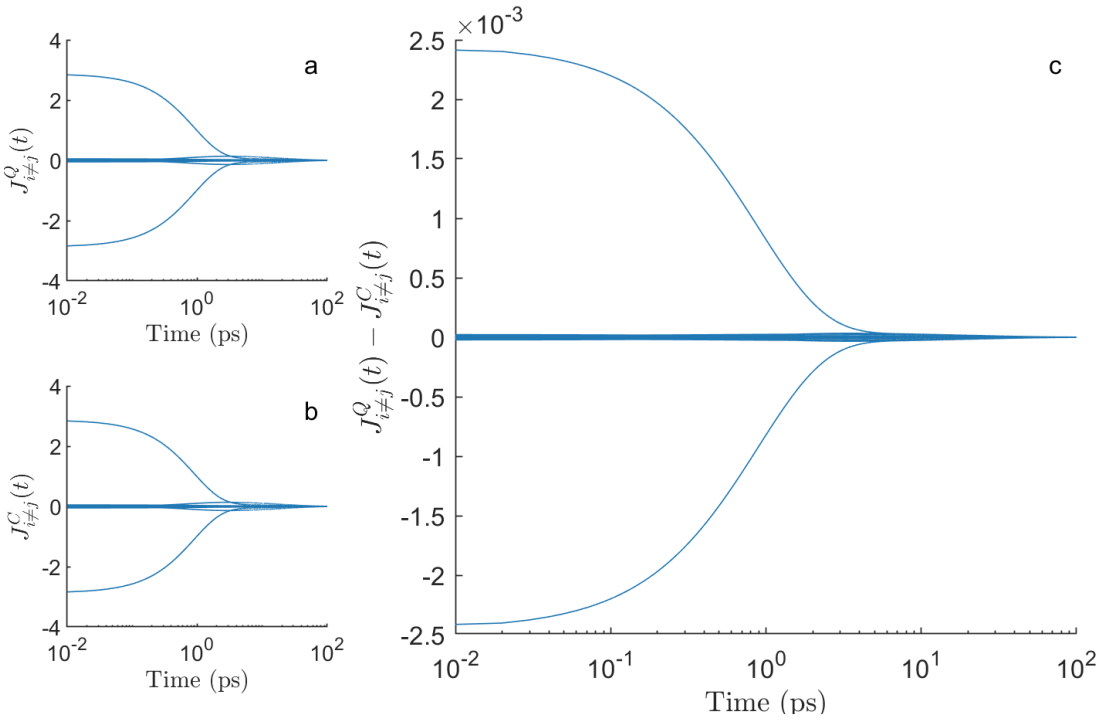

Figure 15. Quantum (a) and classical (b) fluxes and their difference (c) for a Haken-Strobl dynamics. The difference is three orders of magnitude smaller than the fluxes, demonstrating excellent agreement. Parameters of the simulation are: $\lambda = 1000\ \mathrm{cm}^{-1}$, $\Omega = 150\ \mathrm{cm}^{-1}$ and $\beta^{-1} \approx 241\ \mathrm{cm}^{-1}$.

IV.3.5.5 Inverse participation ratio, purity of the state and the efficiency of transport

We conclude our investigation with some observations we made about the correlation between the efficiency and some dynamical indicators, namely, the dynamical inverse participation ratio (dynamical IPR) and the purity of the density matrix.

IPR is commonly used as a measure of how much delocalized an eigenstate α of the Hamiltonian is on the sites. The definition reads

$$\mathrm{IPR}(\alpha) = \sum_i \left|\langle i|\alpha\rangle\right|^4 .$$

The result is a real number between 1, when the eigenstate is localized only on one site, and $1/N$, when it is equally delocalized over the entire network. Here, we use an extension of the IPR, according to [74], to use it as a dynamical quantity that can test the number of states that participate to the density matrix at time t. We define it as

$$\mathrm{IPR}(t) = \mathrm{Tr}\left[\rho(t) \circ \rho(t)\right] = \sum_i \rho_{ii}^2(t), \tag{IV.87}$$

where $\circ$ denotes the Hadamard (elementwise) product. Note that, by definition, the dynamical IPR strictly depends on the basis set used to expand the density matrix. Differently from [74], where they express it on the site basis, we will take it on the exciton basis, including in the density matrix also the reaction centre and the ground state. The reason for our choice is that, in our case study, the two bases behave quite similarly, but the dynamical IPR on the site basis sometimes has disturbing fluctuations, while on the eigenstates the profile is always smooth.

The question is, how do we expect the IPR to behave during dynamics? According to what we have already seen in the previous paragraphs, we expect an initial transient in which the number of excitons involved in the system state increases (IPR decreases) because of the redistribution due to the interaction with the vibrational environment. Subsequently, the trapping and the recombination processes localize the population into 2 states (reaction centre, mainly, and ground state), leading to an increase in the IPR.

The other quantity we will use, is the purity the system that is defined as

$$\mathrm{purity}(t) = \mathrm{Tr}\left[\rho^2(t)\right] = \sum_{i,j} \left|\rho_{ij}(t)\right|^2 . \tag{IV.88}$$

The purity has a value of 1 for pure states that can be described by a statevector, and intermediate values between 1 and $1/N$ for mixed states. Differently from the dynamical IPR, the purity is base-independent. Its meaning is usually associated with the measure of the degree of entanglement between a system and its environment. However, because of the Born assumption, it would be improper to speak about entanglement in our case, as the system and the environment are assumed to be always separable. So, in our simulation, it represents more generically a measure of the level of decoherence in the system state. We expect its value to start from 1 when the dynamics is in the initial pure state (localization at site 1), diminishing as the environment introduces decoherences in the system, and then rising as the population gets transferred (mainly) on the reaction centre. While the descending part is quite intuitive, since the density matrix loses its coherences, the turnover may be difficult to understand. However, it is just a consequence of the relaxation channels we are using. At the end of the dynamics, the density matrix will be an incoherent state with population present only at the reaction centre and the ground state of the FMO complex. In this case, the purity could take every value between 1, when the final state is localized on one of them, and 1/2, when the population is equally parted. Since, as we have seen so far, the population of the reaction centre at the end of the dynamics is usually >90%, it is very intuitive that the purity will be high.

By looking at eqs. (IV.87) and (IV.88), one can notice the similarity between the two definitions that differ only in the way one takes the product between the density matrix and itself. So, it is natural to imagine that in some cases the two indicators can give the same results. In particular, we noted that when the coherences in the exciton basis get mostly damped, the purity approaches the IPR (see Sup. Info. for the dynamics). This is because purity contains the same contributions due to exciton populations as IPR, with the addition of extra terms related to the squared norm of the coherences.

From the dynamics reported in the Sup. Info., we observe that the position (time and value) of the minima of the purity and the IPR change with the reorganization energy. Such minima represent the turning point between the part of the dynamics mostly characterized by the redistribution of the excitation in the exciton manifold and the subsequent part characterized by the trapping and recombination. In Figure 16 and Figure 17, we show how the value of the minimum and its time position are correlated with the efficiency in the case of the IPR and the purity, respectively. Every dot represents a result obtained for a different reorganization energy from $\lambda = 0$ (no coupling with dephasing environment) to $\lambda = 1000\ \mathrm{cm}^{-1}$. The cutoff was set at $\Omega = 150\ \mathrm{cm}^{-1}$ and temperature $\beta^{-1} \approx 241\ \mathrm{cm}^{-1}$. The dynamics have been initiated with an excitation at site 1, but we obtained similar results starting from eigenstate 5, proving the robustness of observations. The results with both parameters give a comparable trend. In particular, in the region of high efficiency, they superpose very well because in this regime in the dynamics the purity and IPR match before getting the minimum. The most important observation is that both the value and the time required to reach the minimum of both indicators is inversely correlated to the trapping efficiency. For all kinds of equations, IPR ranges from a value of ~ 0.35 (delocalization on ~ 3 states)[14] and a time of ~ 30 ps for an efficiency of $\eta \approx 0.91 \div 0.92$, to value of ~ 0.15 (delocalization on ~ 7 states) and times on the order of picosecond for efficiencies close to unity. Purity maintains the same trends with a slight difference in the right side of the graphs, which means that at small reorganization energies, IPR reaches a lower minimum in a shorter time than purity, *i.e.*, delocalization on states occurs faster than the loss of coherences. But why is it convenient for the system to delocalize? Let us start with an intuitive consideration: since efficiency is a race between trapping and recombination, the faster the phenomena that bring population to site 3 occur, the greater the transfer to the reaction centre will be, and, with it, the efficiency. Given this, it seems to be clear that delocalization is a way for the system to consistently bring and maintain population to site 3. Presumably, if we imagined the existence of other types of relaxation channels that transfer population from the initial sites directly to site 3, delocalization to the whole network may play a negative role in the equation. Or, in another scenario, if the network were really very large, but the initial state is close to the site responsible for transfer to the reaction centre, it would be probably not needed

[14] Please note that we used the generic term *states* and not *excitons* because the density matrix also includes the reaction centre and ground state, which are not excitons but are nevertheless included in the state count operated by the IPR.

to delocalize the excitation over the whole complex, but, on the contrary, to localize over a particular portion of it.

As a final note, as we know, the Redfield without imaginary part and the Haken-Strobl exhibit a bell-shaped profile for the trapping efficiency. This can be noted also in Figure 16 and Figure 17 by the presence of a turnover: when the maximum efficiency is reached, for larger values of reorganization energy the minima of the IPR and purity are increased and the time to reach them gets longer.

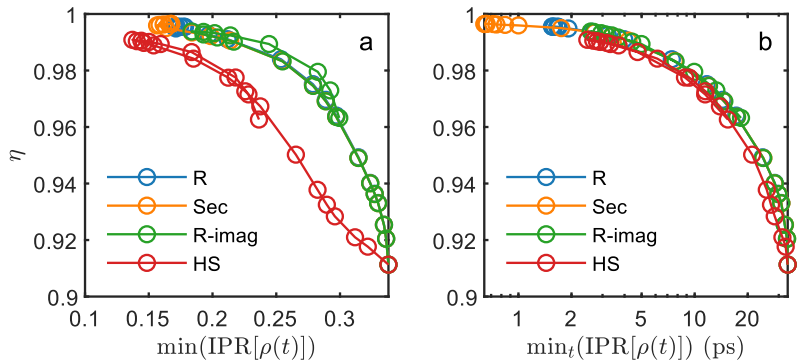

Figure 16. Efficiency of trapping as a function of the minimum of the dynamical IPR on the exciton basis (a) and the time needed to reach the IPR minimum (b). Each point is taken from a simulation at different values of reorganization energy from $\lambda = 0$ to $\lambda = 1000\ \mathrm{cm}^{-1}$. Other simulation parameters: $\Omega = 150\ \mathrm{cm}^{-1}$ and $\beta^{-1} \approx 241\ \mathrm{cm}^{-1}$. Initial state localized at site 1.

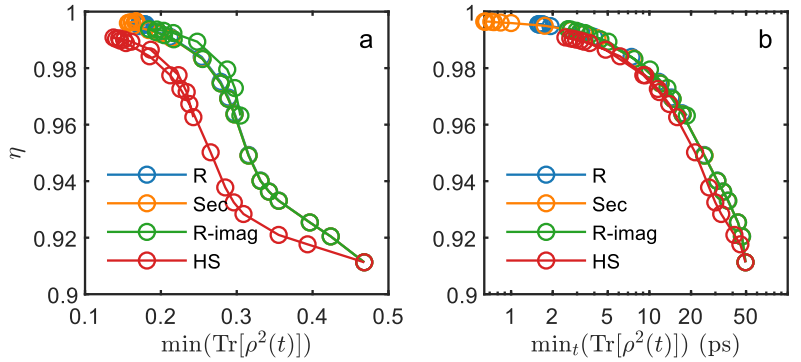

Figure 17. Efficiency of trapping as a function of the minimum of the purity of the density matrix (a) and the time needed to reach the purity minimum (b). Each point is taken from a simulation at different values of reorganization energy from $\lambda = 0$ to $\lambda = 1000\ \mathrm{cm}^{-1}$. Other simulation parameters: $\Omega = 150\ \mathrm{cm}^{-1}$ and $\beta^{-1} \approx 241\ \mathrm{cm}^{-1}$. Initial state localized at site 1.

IV.4 Conclusions

In this Chapter, we have discussed the results of simulating excitonic transport in molecular networks using the Redfield equation in a wide range of environmental conditions, examining what it predicts, when it fails and (possibly) why. To do this, we started with a careful derivation of the Redfield equation, paying attention to the implications of the Born-Markov approximations, like the weak coupling and the coarse-graining in time. We also introduced the definitions of the spectral and dispersion function, quantities that emerge from the system-environment interaction and of fundamental importance for the interpretation of the dynamics.

The formalization of the exciton-vibration interaction in light-harvesting complexes has been presented under the Born-Oppenheimer and displaced harmonic-oscillator approximations. To better understand the features of the Redfield equation, and to compare it with some variants usually adopted in literature, we have studied the dynamics of the FMO molecular complex over a large set of environmental conditions and reported our observations on the Redfield, secular Redfield, Redfield without imaginary part and Haken-Strobl equations.

We have observed an interesting behaviour for the efficiency of transport to the reaction centre as the ratio λ/Ω changes. If at low ratios all the equations predict the same results, at intermediate and high values a sigmoidal shape is observed for the Redfield and secular Redfield equations, while a bell-shaped profile is obtained in the case of the Redfield without imaginary part and Haken-Strobl equations. As seen, this is due to the population dynamics in the strong coupling regime, where the rate of thermalization in the excitonic manifold has completely different behaviour for the various equations: accelerated in the case of secular Redfield, constant in the case of full Redfield and slowed down in the case of Redfield without imaginary part and Haken-Strobl.

We have demonstrated the problems of non-positivity when choosing a time step for the propagation of dynamics that is smaller than the relaxation time of the environment, and eventually when the Redfield equation is propagated at low temperatures.

Since in literature, sometimes, it is said that the Redfield without imaginary part and Haken-Strobl equations are similar except for the temperature effects, we have investigated the similarity and provided evidence of significant differences. In fact, while the populations behave similarly, the dynamics of the coherences as reorganization energy changes are not comparable at all. This is at the base of the impossibility of the Redfield without imaginary part to reach the correct Förster-like transport in the strong coupling regime. The regime is instead correctly reproduced by the Haken-Strobl equation.

Finally, we found a correlation between the transport efficiency towards the reaction centre and the minimum of two indicators: the dynamical IPR and the purity of the density matrix.

IV.5 Appendix A

In Table 2, we report the composition of the eigenstates $|\alpha\rangle = \sum_{i=1}^{7} c_{i,\alpha} |i\rangle$ and their respective eigenenergies for the FMO Hamiltonian in eq. (IV.72). Then, in Figure 18, we show the contribution $|c_{i,\alpha}|^2$ of each excited state (site) on the eigenstates of the FMO Hamiltonian.

Table 2. Eigenenergies and eigenstates of the FMO complex Hamiltonian H^{exc}.

	$\alpha = 1$	$\alpha = 2$	$\alpha = 3$	$\alpha = 4$	$\alpha = 5$	$\alpha = 6$	$\alpha = 7$
$E_\alpha^{\text{exc}} \left(\text{cm}^{-1}\right)$	≈ -28.6	≈ 74.2	≈ 148.5	≈ 244.1	≈ 269.0	≈ 374.1	≈ 468.6
$c_{1,\alpha}$	0,0567	0,0931	0,8682	-0,0573	-0,0404	-0,4739	-0,0697
$c_{2,\alpha}$	0,1093	0,0701	0,4607	-0,0490	-0,0691	0,8686	0,0958
$c_{3,\alpha}$	-0,8833	-0,4239	0,1366	0,0455	-0,1227	0,0646	0,0109
$c_{4,\alpha}$	-0,4308	0,7455	-0,0239	-0,1444	0,4589	0,0522	-0,1546
$c_{5,\alpha}$	-0,1096	0,3268	-0,1053	-0,5181	-0,6566	-0,0828	0,4046
$c_{6,\alpha}$	-0,0041	-0,0926	0,0601	0,0367	0,4648	-0,0812	0,8739
$c_{7,\alpha}$	-0,0836	0,3682	0,0070	0,8376	-0,3475	-0,0238	0,1856

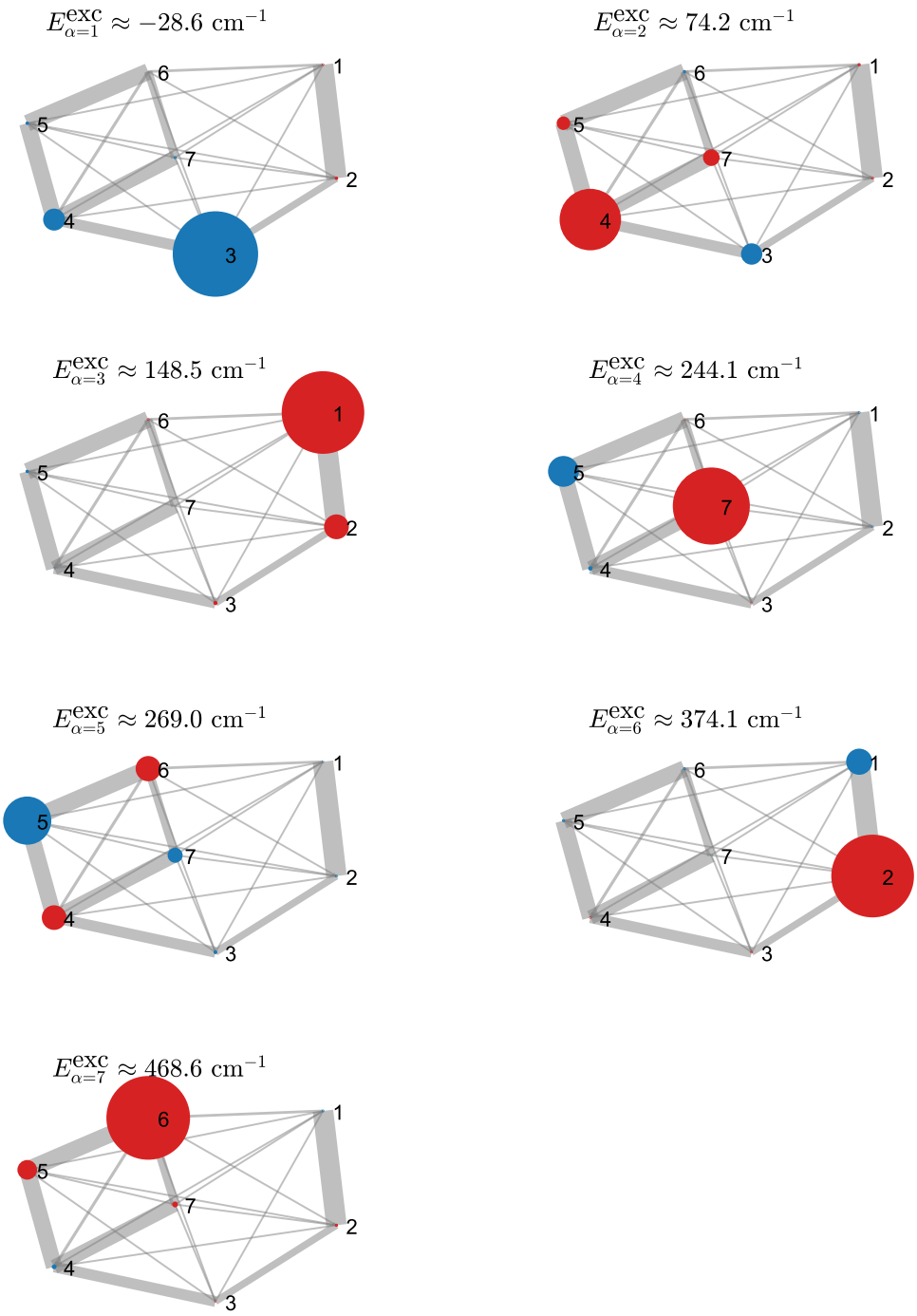

Figure 18. Composition of the eigenstates for the isolated FMO complex. The dimension of the node is proportional to the weight (squared norm of the amplitudes in Table 2) of the site in the eigenstate. The phases are represented in red (positive) and blue (negative).

IV.6 Appendix B

The Förster rates for exciton transport correspond to the Fermi-golden-rule rates when the perturbation is the Coulombic interaction between the sites (*i.e.*, the off-diagonal terms of the exciton Hamiltonian V_{ij}) [65,71,72]. They can be written as

$$\kappa_{i\neq j}^{\mathrm{F}} = 2\left|V_{ij}\right|^2 \mathrm{Re}\int_0^\infty dt F_i^*\left(t\right) A_j\left(t\right) \tag{IV.89}$$

where $F_i\left(t\right)$ and $A_i\left(t\right)$ are the fluorescence and absorption correlation functions of chromophore i (their Fourier transforms are known as the line-shape functions) [71]. For the displaced harmonic oscillator, including recombination and trapping contributions, we have [65]

$$\kappa_{i\neq j}^{\mathrm{F}} = 2\left|V_{ij}\right|^2 \mathrm{Re}\int_0^\infty dt e^{\mathrm{i}\left(E_i^1 - E_j^1\right)t} e^{-\left[g_i^*(t)+g_j(t)\right]} e^{\gamma^{\mathrm{T}} t\left(\delta_{i3}+\delta_{j3}\right)/2} e^{\gamma^{\mathrm{R}} t} \tag{IV.90}$$

where $g_i\left(t\right)$ the line-broadening function [71]

$$g_i\left(t\right) = \int_0^t ds \int_0^s ds' c_{ii}\left(s'\right), \tag{IV.91}$$

with $c_{ii}\left(t\right)$ the correlation function of the environment interacting operators for site i. In general, $g_i\left(t\right)$ is not easy to calculate, but in Haken-Strobl conditions, it is analytical [65]

$$g_i\left(t\right) = \frac{2\lambda}{\beta\Omega} t, \tag{IV.92}$$

so that we obtain [65]

$$\kappa_{i\neq j}^{\mathrm{F}} = 2\left|V_{ij}\right|^2 \frac{\left\{\dfrac{4\lambda}{\beta\Omega} + \dfrac{\gamma^{\mathrm{T}}\left(\delta_{i3}+\delta_{j3}\right)}{2} + \gamma^{\mathrm{R}}\right\}}{\left\{\dfrac{4\lambda}{\beta\Omega} + \dfrac{\gamma^{\mathrm{T}}\left(\delta_{i3}+\delta_{j3}\right)}{2} + \gamma^{\mathrm{R}}\right\}^2 + \left(E_i^1 - E_j^1\right)^2}. \tag{IV.93}$$

IV.7 References

[1] A.G.G. Redfield, On the Theory of Relaxation Processes, IBM J. Res. Dev. 1 (1957) 19–31. https://doi.org/10.1147/rd.11.0019.

[2] A.G. Redfield, The Theory of Relaxation Processes, in: Adv. Magn. Opt. Reson., Academic Press Inc., 1965: pp. 1–32. https://doi.org/10.1016/B978-1-4832-3114-3.50007-6.

[3] A. Ishizaki, G.R. Fleming, On the adequacy of the Redfield equation and related approaches to the study of quantum dynamics in electronic energy transfer, J. Chem. Phys. 130 (2009) 234110. https://doi.org/10.1063/1.3155214.

[4] J. Jeske, D.J. Ing, M.B. Plenio, S.F. Huelga, J.H. Cole, Bloch-Redfield equations for modeling light-harvesting complexes, J. Chem. Phys. 142 (2015) 064104. https://doi.org/10.1063/1.4907370.

[5] B. Palmieri, D. Abramavicius, S. Mukamel, Lindblad equations for strongly coupled populations and coherences in photosynthetic complexes, J. Chem. Phys. 130 (2009) 204512. https://doi.org/10.1063/1.3142485.

[6] R. Hartmann, W.T. Strunz, Accuracy assessment of perturbative master equations: Embracing nonpositivity, Phys. Rev. A. 101 (2020) 012103. https://doi.org/10.1103/PhysRevA.101.012103.

[7] T. Albash, S. Boixo, D.A. Lidar, P. Zanardi, Quantum adiabatic Markovian master equations, New J. Phys. 14 (2012) 123016. https://doi.org/10.1088/1367-2630/14/12/123016.

[8] D.A. Lidar, Lecture Notes on the Theory of Open Quantum Systems, (2019). http://arxiv.org/abs/1902.00967.

[9] M. Cattaneo, G.L. Giorgi, S. Maniscalco, R. Zambrini, Local versus global master equation with common and separate baths: superiority of the global approach in partial secular approximation, New J. Phys. 21 (2019) 113045. https://doi.org/10.1088/1367-2630/ab54ac.

[10] P. Gaspard, M. Nagaoka, Slippage of initial conditions for the Redfield master equation, J. Chem. Phys. 111 (1999) 5668–5675. https://doi.org/10.1063/1.479867.

[11] H.-P. Breuer, F. Petruccione, The Theory of Open Quantum Systems, Oxford University Press, Oxford, 2007. https://doi.org/10.1093/acprof:oso/9780199213900.001.0001.

[12] D. Manzano, A short introduction to the Lindblad master equation, AIP Adv. 10 (2020) 025106. https://doi.org/10.1063/1.5115323.

[13] A. Suárez, R. Silbey, I. Oppenheim, Memory effects in the relaxation of quantum open systems, J. Chem. Phys. 97 (1992) 5101–5107. https://doi.org/10.1063/1.463831.

[14] S. Gnutzmann, F. Haake, Positivity violation and initial slips in open systems, Zeitschrift Für Phys. B Condens. Matter. 101 (1996) 263–273. https://doi.org/10.1007/s002570050208.

[15] R.S. Whitney, Staying positive: going beyond Lindblad with perturbative master equations, J. Phys. A Math. Theor. 41 (2008) 175304. https://doi.org/10.1088/1751-8113/41/17/175304.

[16] E. Mozgunov, D. Lidar, Completely positive master equation for arbitrary driving and small level spacing, Quantum. 4 (2020) 227. https://doi.org/10.22331/q-2020-02-06-227.

[17] V. May, O. Kühn, Charge and Energy Transfer Dynamics in Molecular Systems, 3rd ed., Wiley-Vch, 2011.

[18] S. Valleau, A. Eisfeld, A. Aspuru-Guzik, On the alternatives for bath correlators and spectral densities from mixed quantum-classical simulations, J. Chem. Phys. 137 (2012) 224103. https://doi.org/10.1063/1.4769079.

[19] J.R. Johansson, P.D. Nation, F. Nori, QuTiP: An open-source Python framework for the dynamics of open quantum systems, Comput. Phys. Commun. 183 (2012) 1760–1772. https://doi.org/10.1016/j.cpc.2012.02.021.

[20] J.R. Johansson, P.D. Nation, F. Nori, QuTiP 2: A Python framework for the dynamics of open quantum systems, Comput. Phys. Commun. 184 (2013) 1234–1240. https://doi.org/10.1016/j.cpc.2012.11.019.

[21] M. Winczewski, R. Alicki, Renormalization in the Theory of Open Quantum Systems via the Self-Consistency Condition, (2021) 1–35. http://arxiv.org/abs/2112.11962.

[22] E.B. Davies, Markovian master equations, Commun. Math. Phys. 39 (1974) 91–110. https://doi.org/10.1007/BF01608389.

[23] N. Vogt, J. Jeske, J.H. Cole, Stochastic Bloch-Redfield theory: Quantum jumps in a solid-state environment, Phys. Rev. B. 88 (2013) 174514. https://doi.org/10.1103/PhysRevB.88.174514.

[24] D. Davidović, Completely Positive, Simple, and Possibly Highly Accurate Approximation of the Redfield Equation, Quantum. 4 (2020) 326. https://doi.org/10.22331/q-2020-09-21-326.

[25] G.S. Engel, T.R. Calhoun, E.L. Read, T.-K. Ahn, T. Mančal, Y.-C. Cheng, R.E. Blankenship, G.R. Fleming, Evidence for wavelike energy transfer through quantum coherence in photosynthetic systems, Nature. 446 (2007) 782–786. https://doi.org/10.1038/nature05678.

[26] G. Panitchayangkoon, D. Hayes, K.A. Fransted, J.R. Caram, E. Harel, J. Wen, R.E. Blankenship, G.S. Engel, Long-lived quantum coherence in photosynthetic complexes at physiological temperature, Proc. Natl. Acad. Sci. 107 (2010) 12766–12770. https://doi.org/10.1073/pnas.1005484107.

[27] E. Collini, C.Y. Wong, K.E. Wilk, P.M.G. Curmi, P. Brumer, G.D. Scholes, Coherently wired light-harvesting in photosynthetic marine algae at ambient temperature, Nature. 463 (2010) 644–647. https://doi.org/10.1038/nature08811.

[28] S. Shim, P. Rebentrost, S. Valleau, A. Aspuru-Guzik, Atomistic Study of the Long-Lived Quantum Coherences in the Fenna-Matthews-Olson Complex, Biophys. J. 102 (2012) 649–660. https://doi.org/10.1016/j.bpj.2011.12.021.

[29] E. Zerah Harush, Y. Dubi, Do photosynthetic complexes use quantum coherence to increase their efficiency? Probably not, Sci. Adv. 7 (2021) 1–9. https://doi.org/10.1126/sciadv.abc4631.

[30] Y. Chang, Y.C. Cheng, On the accuracy of coherent modified Redfield theory in simulating excitation energy transfer dynamics, J. Chem. Phys. 142 (2015). https://doi.org/10.1063/1.4905721.

[31] A. Ishizaki, T.R. Calhoun, G.S. Schlau-Cohen, G.R. Fleming, Quantum coherence and its interplay with protein environments in photosynthetic electronic energy transfer, Phys. Chem. Chem. Phys. 12 (2010) 7319. https://doi.org/10.1039/c003389h.

[32] P. Rebentrost, M. Mohseni, A. Aspuru-Guzik, Role of Quantum Coherence and Environmental Fluctuations in Chromophoric Energy Transport, J. Phys. Chem. B. 113 (2009) 9942–9947. https://doi.org/10.1021/jp901724d.

[33] D.M. Wilkins, N.S. Dattani, Why Quantum Coherence Is Not Important in the Fenna–Matthews–Olsen Complex, J. Chem. Theory Comput. 11 (2015) 3411–3419. https://doi.org/10.1021/ct501066k.

[34] A.S. Bondarenko, J. Knoester, T.L.C. Jansen, Comparison of methods to study excitation energy transfer in

molecular multichromophoric systems, Chem. Phys. 529 (2020) 110478. https://doi.org/10.1016/j.chemphys.2019.110478.

[35] E. Zerah-Harush, Y. Dubi, Universal Origin for Environment-Assisted Quantum Transport in Exciton Transfer Networks, J. Phys. Chem. Lett. 9 (2018) 1689–1695. https://doi.org/10.1021/acs.jpclett.7b03306.

[36] H. Hossein-Nejad, C. Curutchet, A. Kubica, G.D. Scholes, Delocalization-Enhanced Long-Range Energy Transfer between Cryptophyte Algae PE545 Antenna Proteins, J. Phys. Chem. B. 115 (2011) 5243–5253. https://doi.org/10.1021/jp108397a.

[37] M. Mohseni, A. Shabani, S. Lloyd, H. Rabitz, Energy-scales convergence for optimal and robust quantum transport in photosynthetic complexes, J. Chem. Phys. 140 (2014) 035102. https://doi.org/10.1063/1.4856795.

[38] A. Shabani, M. Mohseni, H. Rabitz, S. Lloyd, Efficient estimation of energy transfer efficiency in light-harvesting complexes, Phys. Rev. E. 86 (2012) 011915. https://doi.org/10.1103/PhysRevE.86.011915.

[39] P. Rebentrost, R. Chakraborty, A. Aspuru-Guzik, Non-Markovian quantum jumps in excitonic energy transfer, J. Chem. Phys. 131 (2009) 184102. https://doi.org/10.1063/1.3259838.

[40] A. Ishizaki, G.R. Fleming, Unified treatment of quantum coherent and incoherent hopping dynamics in electronic energy transfer: Reduced hierarchy equation approach, J. Chem. Phys. 130 (2009) 234111. https://doi.org/10.1063/1.3155372.

[41] Y. Tanimura, Numerically "exact" approach to open quantum dynamics: The hierarchical equations of motion (HEOM), J. Chem. Phys. 153 (2020) 020901. https://doi.org/10.1063/5.0011599.

[42] A. Tokmakoff, Time-Dependent Quantum Mechanics and Spectroscopy, (2014) 272. http://tdqms.uchicago.edu/ (accessed April 28, 2022).

[43] A. Kell, X. Feng, M. Reppert, R. Jankowiak, On the Shape of the Phonon Spectral Density in Photosynthetic Complexes, J. Phys. Chem. B. 117 (2013) 7317–7323. https://doi.org/10.1021/jp405094p.

[44] M. Wendung, T. Pullerits, M.A. Przyjalgowski, S.I.E. Vulto, T.J. Aartsma, R. Van Grondelle, H. Van Amerongen, Electron-vibrational coupling in the fenna-matthews-olson complex of prosthecochloris aestuarii determined by temperature-dependent absorption and fluorescence line-narrowing measurements, J. Phys. Chem. B. 104 (2000) 5825–5831. https://doi.org/https://doi.org/10.1021/jp000077+.

[45] T.-C. Dinh, T. Renger, Towards an exact theory of linear absorbance and circular dichroism of pigment-protein complexes: Importance of non-secular contributions, J. Chem. Phys. 142 (2015) 034104. https://doi.org/10.1063/1.4904928.

[46] J. Pieper, M. Rätsep, I. Trostmann, F.-J. Schmitt, C. Theiss, H. Paulsen, H.J. Eichler, A. Freiberg, G. Renger, Excitonic Energy Level Structure and Pigment−Protein Interactions in the Recombinant Water-Soluble Chlorophyll Protein. II. Spectral Hole-Burning Experiments, J. Phys. Chem. B. 115 (2011) 4053–4065. https://doi.org/10.1021/jp111457t.

[47] S. Maity, B.M. Bold, J.D. Prajapati, M. Sokolov, T. Kubař, M. Elstner, U. Kleinekathöfer, DFTB/MM Molecular Dynamics Simulations of the FMO Light-Harvesting Complex, J. Phys. Chem. Lett. 11 (2020) 8660–8667. https://doi.org/10.1021/acs.jpclett.0c02526.

[48] S. Saito, M. Higashi, G.R. Fleming, Site-Dependent Fluctuations Optimize Electronic Energy Transfer in the Fenna–Matthews–Olson Protein, J. Phys. Chem. B. 123 (2019) 9762–9772. https://doi.org/10.1021/acs.jpcb.9b07456.

[49] I.P. Mercer, I.R. Gould, D.R. Klug, A Quantum Mechanical/Molecular Mechanical Approach to Relaxation Dynamics: Calculation of the Optical Properties of Solvated Bacteriochlorophyll-a, J. Phys. Chem. B. 103 (1999) 7720–7727. https://doi.org/10.1021/jp990284d.

[50] X. Hu, T. Ritz, A. Damjanović, F. Autenrieth, K. Schulten, Photosynthetic apparatus of purple bacteria, Q. Rev. Biophys. 35 (2002) 1–62. https://doi.org/10.1017/S0033583501003754.

[51] C. Olbrich, U. Kleinekathöfer, Time-Dependent Atomistic View on the Electronic Relaxation in Light-Harvesting System II, J. Phys. Chem. B. 114 (2010) 12427–12437. https://doi.org/10.1021/jp106542v.

[52] G. Tao, W.H. Miller, Semiclassical Description of Electronic Excitation Population Transfer in a Model Photosynthetic System, J. Phys. Chem. Lett. 1 (2010) 891–894. https://doi.org/10.1021/jz1000825.

[53] C. Olbrich, J. Strümpfer, K. Schulten, U. Kleinekathöfer, Theory and Simulation of the Environmental Effects on FMO Electronic Transitions, J. Phys. Chem. Lett. 2 (2011) 1771–1776. https://doi.org/10.1021/jz2007676.

[54] S. Jurinovich, C. Curutchet, B. Mennucci, The Fenna-Matthews-Olson Protein Revisited: A Fully Polarizable (TD)DFT/MM Description, ChemPhysChem. 15 (2014) 3194–3204. https://doi.org/10.1002/cphc.201402244.

[55] F. Häse, S. Valleau, E. Pyzer-Knapp, A. Aspuru-Guzik, Machine learning exciton dynamics, Chem. Sci. 7 (2016) 5139–5147. https://doi.org/10.1039/C5SC04786B.

[56] U. Weiss, Quantum Dissipative Systems, Second, World Scientific Publishing Company, Singapore, 1999.

[57] Á. Rivas, A.D. K Plato, S.F. Huelga, M. B Plenio, Markovian master equations: a critical study, New J. Phys. 12 (2010) 113032. https://doi.org/10.1088/1367-2630/12/11/113032.

[58] S. Mukamel, Principles of nonlinear optical spectroscopy, Oxford University Press, New York, 1995.

[59] Y.C. Cheng, R.J. Silbey, Markovian Approximation in the Relaxation of Open Quantum Systems, J. Phys. Chem. B. 109 (2005) 21399–21405. https://doi.org/10.1021/jp051303o.

[60] R.E. Fenna, B.W. Matthews, Chlorophyll arrangement in a bacteriochlorophyll protein from Chlorobium limicola, Nature. 258 (1975) 573–577. https://doi.org/10.1038/258573a0.

[61] J. Dostál, J. Pšenčík, D. Zigmantas, In situ mapping of the energy flow through the entire photosynthetic apparatus, Nat. Chem. 8 (2016) 705–710. https://doi.org/10.1038/nchem.2525.

[62] S. Savikhin, D.R. Buck, W.S. Struve, Oscillating anisotropies in a bacteriochlorophyll protein: Evidence for quantum beating between exciton levels, Chem. Phys. 223 (1997) 303–312. https://doi.org/10.1016/S0301-0104(97)00223-1.

[63] J. Wen, H. Zhang, M.L. Gross, R.E. Blankenship, Membrane orientation of the FMO antenna protein from Chlorobaculum tepidum as determined by mass spectrometry-based footprinting, Proc. Natl. Acad. Sci. U. S. A. 106 (2009) 6134–6139. https://doi.org/10.1073/pnas.0901691106.

[64] J. Adolphs, T. Renger, How Proteins Trigger Excitation Energy Transfer in the FMO Complex of Green Sulfur Bacteria, Biophys. J. 91 (2006) 2778–2797. https://doi.org/10.1529/biophysj.105.079483.

[65] J. Wu, F. Liu, J. Ma, R.J. Silbey, J. Cao, Efficient energy transfer in light-harvesting systems: Quantum-classical comparison, flux network, and robustness analysis, J. Chem. Phys. 137 (2012) 174111. https://doi.org/10.1063/1.4762839.

[66] S. Hoyer, M. Sarovar, K. Birgitta Whaley, Limits of quantum speedup in photosynthetic light harvesting, New J. Phys. 12 (2010) 065041. https://doi.org/10.1088/1367-2630/12/6/065041.

[67] M. Mohseni, P. Rebentrost, S. Lloyd, A. Aspuru-Guzik, Environment-assisted quantum walks in photosynthetic energy transfer, J. Chem. Phys. 129 (2008) 174106. https://doi.org/10.1063/1.3002335.

[68] P. Rebentrost, M. Mohseni, I. Kassal, S. Lloyd, A. Aspuru-Guzik, Environment-assisted quantum transport, New J. Phys. 11 (2009) 033003. https://doi.org/10.1088/1367-2630/11/3/033003.

[69] C. Kreisbeck, T. Kramer, M. Rodríguez, B. Hein, High-Performance Solution of Hierarchical Equations of Motion for Studying Energy Transfer in Light-Harvesting Complexes, J. Chem. Theory Comput. 7 (2011) 2166–2174. https://doi.org/10.1021/ct200126d.

[70] T.M. Wahlund, C.R. Woese, R.W. Castenholz, M.T. Madigan, A thermophilic green sulfur bacterium from New Zealand hot springs, Chlorobium tepidum sp. nov., Arch. Microbiol. 156 (1991) 81–90. https://doi.org/10.1007/BF00290978.

[71] M. Yang, G.R. Fleming, Influence of phonons on exciton transfer dynamics: comparison of the Redfield, Förster, and modified Redfield equations, Chem. Phys. 275 (2002) 355–372. https://doi.org/10.1016/S0301-0104(01)00540-7.

[72] J. Cao, R.J. Silbey, Optimization of Exciton Trapping in Energy Transfer Processes, J. Phys. Chem. A. 113 (2009) 13825–13838. https://doi.org/10.1021/jp9032589.

[73] J. Wu, J. Cao, Higher-order kinetic expansion of quantum dissipative dynamics: Mapping quantum networks to kinetic networks, J. Chem. Phys. 139 (2013) 044102. https://doi.org/10.1063/1.4812781.

[74] C. Smyth, F. Fassioli, G.D. Scholes, Measures and implications of electronic coherence in photosynthetic light-harvesting, Philos. Trans. R. Soc. A Math. Phys. Eng. Sci. 370 (2012) 3728–3749. https://doi.org/10.1098/rsta.2011.0420.

[75] J.A. Gyamfi, Fundamentals of quantum mechanics in Liouville space, Eur. J. Phys. 41 (2020) 063002. https://doi.org/10.1088/1361-6404/ab9fdd.

Chapter V

Collision models for Markovian dynamics in the weak-coupling regime

In this Chapter, we aim at formulating collision models for an efficient simulation of the Markovian dynamics of an open system in the weak coupling limit with a quantum environment. The reference equation in this regime is the Redfield master equation whose properties and validity range has been investigated in the previous Chapter, together with the explicit form that can be used to model energy transfer in a molecular network [1–7]. However, it turns out that the general Redfield description cannot be reproduced by a collision scheme and this is intimately connected to the positivity issue [8–10]. Therefore the first step is to select a master equation which is based on the same microscopic description of the system-environment but can be reduced to the Lindblad form which guarantees the preservation of positivity. Several Born-Markov master equations in Lindblad form have been proposed to offer alternatives to Redfield, while hopefully maintaining similar accuracy in the same range of applications (Markovian and weak coupling conditions) [11–20]. Many of these equations still rely on the Redfield theory introduced in Chapter IV, proposing modifications to the final structure of the relaxation tensor based on different motivations. Thanks to the analysis performed in the previous Chapter, we can conclude that several approaches can lead to the same dynamics if the environment is chosen in agreement with the assumptions of the theory. Starting from this evidence, we here present the relative collision algorithms. The collision algorithms have been developed having in mind their implementation as quantum circuits, however, they offer an alternative numerical route to compute the open system dynamics also in a classical setting, with the advantage of requiring a set of calculations on the system wavefunction (of dimension N) rather than solving for the density matrix (of dimension N^2).

The Chapter is organized as follows. A very brief recall of the system Hamiltonian and the spectral function of the environment is given in section V.1. Section V.2 will be devoted to the introduction of a generic scheme for implementing Lindblad-type master equations and use some of the aforementioned Born-Markov equations

as the target of our models. In section V.3, we will analyse the results of a classical implementation of the proposed models, finding excellent agreement with the target equations. Then, we will introduce the quantum algorithmic version of the collision models and discuss the scaling of the algorithmic complexity. As already seen in Chapters II, we will make use of the reset gate to reinitialize the state of the qubit ancilla after every interaction to guarantee the Markovianity of the dynamics and preserve the purity of the state. This will result once again in an unravelling of the target equations into trajectories of pure states similar to the Monte Carlo wavefunction methods [21–27]. Since the impossible direct implementation of this famous computational strategy on a quantum computer, here we suggest that our collision scheme can be used as a vehicle to implement already existing algorithms. We conclude in section V.4 giving some perspective for future work.

V.1 A brief recap of the FMO

As a case study for this Chapter, we take the exciton transport between the chromophores of one of the three subunits of the Fenna-Matthews-Olson (FMO) molecular complex. The system has been extensively characterized in the previous Chapter, here we briefly summarize the fundamental quantities useful for the development of the collision model.

Site energies and electronic coupling have been calculated by Adolphs and Renger in [2] for the FMO complex of the *Chlorobium tepidum* bacterium. Here, we will use their data as the reference for the system Hamiltonian

$$H^{\mathrm{exc}} = \begin{pmatrix} 200 & -96 & 5 & -4.4 & 4.7 & -12.6 & -6.2 \\ -96 & 320 & 33.1 & 6.8 & 4.5 & 7.4 & -0.3 \\ 5 & 33.1 & 0 & -51.1 & 0.8 & -8.4 & 7.6 \\ -4.4 & 6.8 & -51.1 & 110 & -76.6 & -14.2 & -67 \\ 4.7 & 4.5 & 0.8 & -76.6 & 270 & 78.3 & -0.1 \\ -12.6 & 7.4 & -8.4 & -14.2 & 78.3 & 420 & 38.3 \\ -6.2 & -0.3 & 7.6 & -67 & -0.1 & 38.3 & 230 \end{pmatrix} \mathrm{cm}^{-1}. \tag{V.1}$$

The environment is represented by the vibrational degrees of freedom of the protein scaffold. Under the Born-Oppenheimer approximation, and using the displaced harmonic oscillator model to describe the state of the phonons, a linear Hamiltonian can be derived to describe the exciton-phonon coupling. Such Hamiltonian reads $H^{\mathrm{int}} = \sum_{i=1}^{N} B_i S_i$ (cf. Chapter IV), where B_i is the environment operator and $S_i = |i\rangle\langle i|$ is the system interacting operator corresponding to the projector operator to site i.

Under the Born-Markov approximations, the fine details about the environment are lost, and the fluctuations of the protein environment that surrounds the chromophores are described by means of a spectral function. Here, we assume it to be a Drude-Lorentz spectral function $C(\omega)$, equally parametrized for all the sites. The expression reads ($\hbar = 1$)

$$C(\omega) = 4\lambda\omega \frac{\Omega}{\omega^2 + \Omega^2} \frac{1}{1 - e^{-\omega\beta}}, \tag{V.2}$$

where λ is the reorganization energy of the environmental phonons, Ω is the cutoff frequency of the environment (the reciprocal of the relaxation time) and β is the inverse temperature. The values of the spectral function at the system frequencies ω correspond to the relaxation rates of the dynamics of the exciton transfer. On the contrary, the renormalization of the Hamiltonian due to the interaction with the environment is described by the dispersion function $\Lambda(\omega)$, which is defined in terms of the spectral functions as

$$\Lambda_i(\omega) = \frac{1}{2\pi} \mathcal{P} \int_{-\infty}^{\infty} \frac{C_i(\omega')}{\omega - \omega'} d\omega', \tag{V.3}$$

where $\mathcal{P}$ denotes the principal value of the integral.

For the present Chapter, we will omit the presence of extra relaxation channels (like recombination and trapping) to focus on the dissipations in the exciton manifold. However, simple implementation strategies for these processes are available and they are reported in Appendix B.

V.2 The collision model

Differently from Chapters II and III, where we implemented algorithms for environments with classical correlation functions, here the collisions must take into consideration the quantum character of the environment, in particular the effect of the finite temperature. In the following, we will introduce a generic scheme to implement Markovian collision models and discuss a proposal for the implementation of trajectories of collisions. Then, we will select two categories of Lindblad-type master equations and propose a collision model for their simulation.

V.2.1 A generic scheme for Markovian collision models

A general framework for Markovian collision models has been proposed by Cattaneo *et al* in ref. [28]. Here, we provide an overview of the method to establish the basic ingredients which will be useful to build and discuss of our algorithmic implementations. Let us consider the evolution of an open system, by neglecting for the moment the self-Hamiltonian, and discretize the dynamics into time steps of length Δt. During each time step, to reproduce the effect of the environment, we allow the system to interact with an ancilla under a certain Hamiltonian, we call this interaction a *collision*. The collision event is represented by a unitary operator $U(\Delta t)$ acting both on the system (or subsystem) and the ancilla degrees of freedom

$$U(\Delta t) = \exp\left(-\mathrm{i} H^{\mathrm{coll}} \Delta t\right), \quad H^{\mathrm{coll}} = cS \otimes A + c^* S^\dagger \otimes A^\dagger, \tag{V.4}$$

where H^{coll} is the (Hermitian) collision Hamiltonian, $|c|$ is the strength of the collision, S is an operator acting on the system and A is an operator acting on the ancilla. For Markovian evolutions, the state of the ancilla before the collision must be uncorrelated with the system. Moreover, an ancilla can interact only once

with the system to ensure there are no backflows of information (non-Markovianity). Given these conditions, each collision must have its dedicated ancilla. In this way, a memoryless collision model is obtained that reproduces the dynamics of a Lindblad master equation in the limit $\Delta t \to 0^+$ as proved in ref. [28]. When this is the case, after the collision, the degrees of freedom of the interacted ancilla can be traced out since they are no more useful for the computation, and the resources devoted to storing its state can be used for a new ancilla that must be initialized to the correct initial state (reset of the ancilla) [29].

The state of the open system after the collision is given by the dynamical map

$$\rho(t+\Delta t) = \Phi\left[\rho(t)\right] = \mathrm{Tr}_{\mathrm{anc}}\left\{U(\Delta t)\left(\rho(t)\otimes\rho^{\mathrm{anc}}\right)U^{\dagger}(\Delta t)\right\}. \tag{V.5}$$

Then, the dynamics of the open system emerges as a consequence of the repeated interactions

$$\rho(n\Delta t) = \Phi_n\left[\rho(0)\right] = \Phi\left[...\Phi\left[\rho(0)\right]...\right]. \tag{V.6}$$

The state of the ancillae can be generally different at every time step (for example to simulate a time-dependent state of the environment), but this will not be the case considered here.

To see how collision models reproduce the Lindblad equation, we make an example. Let us assume the ancilla is a qubit described by a diagonal density matrix $\rho^{\mathrm{anc}} = p_0^{\mathrm{anc}}\left|0^{\mathrm{anc}}\right\rangle\left\langle 0^{\mathrm{anc}}\right| + p_1^{\mathrm{anc}}\left|1^{\mathrm{anc}}\right\rangle\left\langle 1^{\mathrm{anc}}\right|$ and the ancilla operator is simply $A = \sigma_+^{\mathrm{anc}} = \left|1^{\mathrm{anc}}\right\rangle\left\langle 0^{\mathrm{anc}}\right|$. When the collision is perturbative, $|c|\Delta t \ll 1$, *i.e.*, for weak collision strengths and/or for short interaction times Δt, we can expand the collision operator up to second order in Δt

$$U(\Delta t) \approx 1 - \mathrm{i}H^{\mathrm{coll}}\Delta t - \frac{1}{2}\left(H^{\mathrm{coll}}\right)^2\Delta t^2. \tag{V.7}$$

By substitution in eq. (V.5) and considering only terms up to Δt^2, one gets

$$\begin{aligned}
\rho(t+\Delta t) = \rho(t) &- \Delta t\left(\mathrm{i}\left[cS,\rho(t)\right]\mathrm{Tr}_{\mathrm{anc}}\left\{A\rho^{\mathrm{anc}}\right\} + \mathrm{i}\left[c^*S^{\dagger},\rho(t)\right]\mathrm{Tr}_{\mathrm{anc}}\left\{A^{\dagger}\rho^{\mathrm{anc}}\right\}\right) \\
&+ c^2\Delta t^2\,\mathrm{Tr}_{\mathrm{anc}}\left\{A\rho^{\mathrm{anc}}A\right\}\left(S\rho(t)S - \frac{1}{2}\left[SS,\rho(t)\right]_+\right) \\
&+ c^{*2}\Delta t^2\,\mathrm{Tr}_{\mathrm{anc}}\left\{A^{\dagger}\rho^{\mathrm{anc}}A^{\dagger}\right\}\left(S^{\dagger}\rho(t)S^{\dagger} - \frac{1}{2}\left[S^{\dagger}S^{\dagger},\rho(t)\right]_+\right) \\
&+ |c|^2\Delta t^2\,\mathrm{Tr}_{\mathrm{anc}}\left\{A\rho^{\mathrm{anc}}A^{\dagger}\right\}\left(S\rho(t)S^{\dagger} - \frac{1}{2}\left[S^{\dagger}S,\rho(t)\right]_+\right) \\
&+ |c|^2\Delta t^2\,\mathrm{Tr}_{\mathrm{anc}}\left\{A^{\dagger}\rho^{\mathrm{anc}}A\right\}\left(S^{\dagger}\rho(t)S - \frac{1}{2}\left[SS^{\dagger},\rho(t)\right]_+\right)
\end{aligned} \tag{V.8}$$

Now, by inserting the state of the ancilla and the definition of the operator A, the evolution of the density matrix of the open system can be written as

$$\begin{aligned}\frac{\rho(t+\Delta t)-\rho(t)}{\Delta t} &= p_0^{\text{anc}}|c|^2\,\Delta t\left(S\rho(t)S^\dagger-\frac{1}{2}\left[S^\dagger S,\rho(t)\right]_+\right)\\ &+p_1^{\text{anc}}|c|^2\,\Delta t\left(S^\dagger\rho(t)S-\frac{1}{2}\left[SS^\dagger,\rho(t)\right]_+\right)\end{aligned} \tag{V.9}$$

By defining $|c|^2=|\tilde{c}|^2/\Delta t$ and taking the limit $\Delta t\to 0^+$, the above equation approximates a Lindblad equation

$$\begin{aligned}\lim_{\Delta t\to 0^+}\frac{\rho(t+\Delta t)-\rho(t)}{\Delta t} &\approx \frac{d\rho(t)}{dt}\\ &=\gamma_0\left(S\rho(t)S^\dagger-\frac{1}{2}\left[S^\dagger S,\rho(t)\right]_+\right)+\gamma_1\left(S^\dagger\rho(t)S-\frac{1}{2}\left[SS^\dagger,\rho(t)\right]_+\right)\end{aligned} \tag{V.10}$$

with rates $\gamma_0=p_0^{\text{anc}}|\tilde{c}|^2$ and $\gamma_1=p_1^{\text{anc}}|\tilde{c}|^2$. Note that we have not imposed particular constraint to the form of the system collision operator. Therefore, this is a generic and powerful procedure to reproduce general master equations in Lindblad form.

V.2.2 Collision model from trajectories

By starting from the above idea, we now discuss an original collision model that does not rely on the density matrix formalism, rather the dynamics of the open system emerges as the average of pure states trajectories. This is obtained by adopting a suitable collision scheme at the level of the system-ancillae wavefunction and by measuring the ancillae state (collapsing their state) after every interaction. In Appendix A, we show that measuring the state of the ancillae after a single collision is equivalent to tracing over the ancillary degrees of freedom. In fact, by preparing the state $U(\Delta t)\left(\rho(t)\otimes\rho^{\text{anc}}\right)U^\dagger(\Delta t)$ multiple times and measuring the ancilla after every preparation, the statistical density matrix of the system obtained as the ensemble average over different realizations approaches the one expected from eq. (V.5). Moreover, in Appendix A we show that also different realizations of the entire dynamics (trajectories) reproduce on average the dynamics of the open system.

The advantage of a trajectory approach is twofold: on the one hand, it is well-known that trajectory approaches on Hilbert space have a more favourable resource scaling of $\mathcal{O}\left(N^2\right)$ with respect to Liouville evolutions such as the Lindblad one that scales with $\mathcal{O}\left(N^4\right)$. On the other hand, compared to other trajectories approaches, this implementation based on unitary operations can be easily implemented both on classical and quantum computers without any need to modify the proposed algorithm. Indeed, we stress once again that for their formulation in terms of system and ancillae evolving under unitary interactions, collision models suit the idea of a digital quantum computer implementation, as also demonstrated in Chapters II and III, and refs. [29–31].

To work with pure states only, we prepare our collision model in a way that the initial state of the ancilla qubits is the ground state in the computational basis of the quantum computer, *i.e.*, $\left|\phi^{\text{anc}}\right\rangle = \left|0^{\text{anc}}\right\rangle$. As the initial state of the system, we consider an excitation localized at site 1, that is $\left|\psi\right\rangle = \left|1\right\rangle$ (we will assume here to work under the algorithmic mapping proposed in Chapter II for simplicity). In the spirit of a collision model, we decompose the time evolution in small time steps Δt, so that we can write the unitary evolution operator as

$$U(\Delta t) = U_H(\Delta t) U_{\text{exc-ph}}(\Delta t), \tag{V.11}$$

where

$$U_H(\Delta t) = \exp\left[-\text{i}\left(H^{\text{exc}} + H^{\text{LS}}\right)\Delta t\right] \tag{V.12}$$

denotes the unitary evolution of the system governed by the exciton Hamiltonian H^{exc}, eventually renormalized by the Lamb shift H^{LS}. Note that it does not involve any collision with the ancillae. Then, $U_{\text{exc-ph}}(\Delta t)$ represents the evolution due to the interaction with the phononic environment. This is driven by collision Hamiltonians for the system-ancillae interaction that have different forms depending on the Lindblad equation and on the collision scheme we want to implement. In our case, we will Trotterize it into many contributions by implementing the various relaxation channels acting on the system. In this way, we will be able to use only one ancilla qubit, reducing the resource requirements, with the reset technique already mentioned.

The collision model is very flexible, so further collisions can be added at will to implement extra relaxation channels. In Appendix B, we show the collision operators that one can add to take into account the exciton recombination and the trapping to the reaction centre. However, these extra channels will not be considered in the rest of the Chapter.

V.2.3 Target dynamics

Our aim in this section is to contextualize the collision model depicted above to simulate the dissipative dynamics of a chromophore network as discussed in the previous Chapter, according to the Redfield equation. However, it turns out that the general Redfield description is not suited to be reproduced by a collision scheme. In fact, a correct algorithmic scheme for the Redfield dynamics should be able to return also the (eventually) non-positive density matrices that can be generated during the evolution. Contrarily, collision models are the result of unitary operations and measurements, which makes it impossible to obtain non-positive density matrices from positive initial states. So, the general Redfield tensor cannot be cast into a collision model.

Therefore, the first step is to select a master equation which is based on the same microscopic description of the system-environment but can be reduced to the Lindblad form which guarantees the preservation of the

positivity. This problem has been long considered in the literature and many different techniques have been proposed over the years, based on various approaches like the use of secular approximation [32], δ-correlated environments [12], explicit coarse-graining [13–16], different Markovian approximations [17], a geometrical average of the relaxation rates [18] or phenomenological assumptions [19,20]. Without the ambition of choosing the best method to reproduce the accuracy of Redfield results (see for example the discussions in refs [9,18]), we will select two different categories of master equations and present the collision operators that can be used to propagate them.

V.2.3.1 The secular Redfield equation

The secular Redfield equation has been already introduced and examined in the previous Chapter. We recall here that it is obtained by neglecting rapid oscillating terms in the Redfield tensor in the interaction picture. This can be done by a complete cancellation (full secular approximation) of terms connecting transitions with different frequencies, $\omega \neq \omega'$, or by creating clusters of frequencies $\bar{\omega}$ in which the mixing is allowed and the separation is imposed at the cluster level (partial secular approximation). In any case, the equation can be written as

$$\frac{d\rho(t)}{dt} = -\mathrm{i}\left[H^{\mathrm{exc}} + H^{\mathrm{LS,sec}}, \rho(t)\right] + \sum_{i=1}^{N}\sum_{\bar{\omega}} C(\bar{\omega})\left\{S_i(\bar{\omega})\rho(t)S_i^{\dagger}(\bar{\omega}) - \frac{1}{2}\left[S_i^{\dagger}(\bar{\omega})S_i(\bar{\omega}), \rho(t)\right]_+\right\}, \quad \text{(V.13)}$$

where $H^{\mathrm{LS,sec}} = \sum_{i=1}^{N}\sum_{\bar{\omega}} \Lambda(\bar{\omega}) S_i^{\dagger}(\bar{\omega}) S_i(\bar{\omega})$ is the Lamb shift Hamiltonian involving the dispersion functions at cluster frequencies $\bar{\omega}$ and $S_i(\bar{\omega}) = \sum_{\omega\in\bar{\omega}} S_i(\omega)$. The spectral function $C(\bar{\omega})$ is usually evaluated at the average frequency of the cluster, but there is some freedom in the definition.

When the full approximation is used there is only one frequency per cluster, and the total number of clusters is $\#(\bar{\omega}) = \mathcal{O}\left(N^2\right)$. On the other hand, by changing the number of clusters, the number of terms in the sum decreases. However, as we are going to see, this does not necessarily imply a computational advantage in the case of the collision model we propose. Note that, in the extreme case of a single cluster, eq. (V.13) becomes identical to the Haken-Strobl equation, for which a dedicated collision model has been presented in Chapter II.

For the partial secular Redfield, we propose a collision model that implements each one of the dissipation processes in eq. (V.13) as a stand-alone collision. The collision operators and Hamiltonians read in this case

$$U^{\text{p-sec}}(\Delta t) = \prod_{i=1}^{N}\prod_{\bar{\omega}} \exp\left(-\mathrm{i}H_i^{\text{p-sec}}(\bar{\omega})\Delta t\right), \quad H_i^{\text{p-sec}}(\bar{\omega}) = \sqrt{\frac{C(\bar{\omega})}{\Delta t}}\left(S_i(\bar{\omega})\sigma_+^{\text{anc}} + S_i^{\dagger}(\bar{\omega})\sigma_-^{\text{anc}}\right). \quad \text{(V.14)}$$

Note that the number of collisions in a single time step is determined by the number of clusters, $\#(\bar{\omega})$, multiplied by the number of molecules in the network, *i.e.*, a total of $\#(\bar{\omega})N$ collisions.

In principle, we could implement also the full secular Redfield with the collision operators defined above. However, it would result in a scaling of $\mathcal{O}(N^3)$ collision operators to apply for each time step. Since the FMO Hamiltonian has no accidental frequency degeneration, it is convenient to rewrite the full secular Redfield equation as (see Appendix C for the details)

$$\begin{aligned}\frac{d\rho(t)}{dt} = &-\mathrm{i}\left[H^{\mathrm{exc}} + H^{\mathrm{LS,sec}}, \rho(t)\right] + \sum_{i=1}^{N} C(0)\left\{S_i(0)\rho(t)S_i(0) - \frac{1}{2}\left[S_i(0)S_i(0), \rho(t)\right]_+\right\} \\ &+ \sum_{\substack{\alpha,\beta \\ \alpha\neq\beta}} C\left(\varepsilon_\beta - \varepsilon_\alpha\right) w_{\alpha\beta}\left\{|\alpha\rangle\langle\beta|\rho(t)|\beta\rangle\langle\alpha| - \frac{1}{2}\left[|\beta\rangle\langle\beta|, \rho(t)\right]_+\right\}\end{aligned} \tag{V.15}$$

where $w_{\alpha\beta} = \sum_{i=1}^{N}\langle\alpha|S_i|\beta\rangle\langle\beta|S_i|\alpha\rangle$, in order to reduce the number of collisions from $\mathcal{O}(N^3)$ to $\mathcal{O}(N^2)$. Then the collision operator for the system-environment interaction can be defined as $U^{\text{f-sec}}(\Delta t) = U^{\text{f-sec,II}}(\Delta t)U^{\text{f-sec,I}}(\Delta t)$, where

$$U^{\text{f-sec,I}}(\Delta t) = \prod_{i=1}^{N}\exp\left(-\mathrm{i}H_i^{\text{f-sec,I}}\Delta t\right), \quad H_i^{\text{f-sec,I}} = \sqrt{\frac{C(0)}{\Delta t}}\left(S_i(0)\sigma_x^{\text{anc}}\right) \tag{V.16}$$

are the collision operators and Hamiltonians for the $\omega = 0$ frequencies and

$$U^{\text{f-sec,II}}(\Delta t) = \prod_{\substack{\alpha,\beta \\ \alpha\neq\beta}}\exp\left(-\mathrm{i}H_{\alpha\beta}^{\text{f-sec,II}}\Delta t\right), \quad H_{\alpha\beta}^{\text{f-sec,II}} = \sqrt{\frac{C\left(\varepsilon_\beta - \varepsilon_\alpha\right)w_{\alpha\beta}}{\Delta t}}\left(|\alpha\rangle\langle\beta|\sigma_+^{\text{anc}} + |\beta\rangle\langle\alpha|\sigma_-^{\text{anc}}\right) \tag{V.17}$$

are the collision operators and Hamiltonians for the remaining terms of eq. (V.45). In the above eq. (V.16), $\sigma_x = \sigma_+ + \sigma_-$ is the Pauli x-operator. The two classes of collision operators in (V.16) and (V.17) corresponds to different incoherent processes, indeed (V.16) causes pure dephasing in the system, which is an adiabatic incoherent process, while (V.17) induces transitions between the eigenstates of the system thus introducing energy dissipation.

V.2.3.2 Geometric mean master equations

Surprisingly, in the attempt to derive Lindblad-form equations that could compete with the Redfield results within its range of validity, several authors, following very different approaches, arrived at a similar result [17–19], that reads

$$\frac{d\rho(t)}{dt} = -\mathrm{i}\Big[H^{\mathrm{exc}} + H^{\mathrm{LS},\kappa}, \rho(t)\Big] + \sum_{i=1}^{N}\sum_{\omega,\omega'}\sqrt{C(\omega)C(\omega')}\left\{S_i(\omega)\rho(t)S_i^{\dagger}(\omega') - \frac{1}{2}\Big[S_i^{\dagger}(\omega')S_i(\omega), \rho(t)\Big]_{+}\right\} \tag{V.18}$$

The dissipation terms of this equation are similar but not equivalent to the original Redfield tensor. The difference is that the relaxation rates $C(\omega)$ of the Redfield equation relative to the operator pair $S_i(\omega)$ and $S_i^{\dagger}(\omega')$ are replaced by the geometric mean $\sqrt{C(\omega)C(\omega')}$. The mathematical structure induced by this simple substitution ensures that the resulting equation is always writable in Lindblad form with positive Lindblad rates. Because of the curious form of the relaxation rates, here we identify this group of equations under the name of *geometrical-mean master equations* (GMME). Different GMMEs characterize themselves only in the way the Lamb shift Hamiltonian is defined.

The first appearance of a GMME, namely the *position and energy resolving Lindblad equation* (PERLind) [19], is due to Kiršanskas et al. who phenomenologically assumed this form on the base of a heuristic argument in an attempt to reproduce Redfield results, beyond the secular approximation, with a completely-positive master equation. In their original paper, the Lamb shift is completely neglected, so we set $H^{\mathrm{LS,PERLind}} = 0$ for the PERLind master equation.

Another GMME is the *universal Lindblad equation* (ULE). In this case, Nathan *et al* propose a formal microscopic derivation similar to the Redfield one, but with a different definition of the Markovian approximation [17,33]. From the derivation, the Lamb shift Hamiltonian for ULE results in

$$H^{\mathrm{LS,ULE}} = \frac{1}{2\pi}\sum_{i=1}^{N}\sum_{\omega,\omega'} S_i^{\dagger}(\omega)S_i(\omega')\mathcal{P}\int_{-\infty}^{\infty}\frac{\sqrt{C(\omega-\omega")C(\omega'-\omega")}}{\omega"}d\omega". \tag{V.19}$$

Since it is based on a formal derivation, authors of the ULE claim the universality of this equation in low coupling and Markovian regime, having the same accuracy and range of applicability as the Redfield equation [17,33]. However, the question of whether microscopically derived Lindblad-type equations can take the place of the Redfield equation is still under debate [34,35].

Finally, we mention also the *geometric-arithmetic master equation* (GAME) introduced in [18] by Davidović. The equation is obtained in a quite sophisticated approximation procedure in which terms that average out over a time scale typical of the quantum system are eliminated from the Redfield equation. The Lamb shift Hamiltonian of GAME in this case reads

$$H^{\mathrm{LS,GAME}} = -\frac{\mathrm{i}}{2}\sum_{i=1}^{N}\Big(S_iK_i - K_i^{\dagger}S_i\Big), \tag{V.20}$$

where $K_i = \sum_\omega \left(\Lambda(\omega) + C(\omega)/2\right) S_i(\omega)$.[1] In Ref. [18], Davidović also shows a comparison of the results of the GMME and other Lindblad equations, finding the best agreement with Redfield dynamics for the GAME and ULE. Curiously, when the secular approximation is adopted, both the ULE and GAME reduce exactly to the secular Redfield equation, which means that they include all the typical contributions of that equation.

The collision operators for the GMMEs have the same form for all the various equations since the only difference between them is in the Hamiltonian evolution carried out by the operator (V.12). To reduce the computational effort of our collision model, it is convenient to diagonalize the dissipator of eq. (V.18) as

$$\frac{d\rho(t)}{dt} = -\mathrm{i}\left[H^{\mathrm{exc}} + H^{\mathrm{LS},\kappa}, \rho(t)\right] + \sum_{i=1}^{N}\left\{Q_i \rho(t) Q_i^\dagger - \frac{1}{2}\left[Q_i^\dagger Q_i, \rho(t)\right]_+\right\}, \tag{V.21}$$

where the Lindblad jumps operators are defined as $Q_i = \sum_\omega \sqrt{C(\omega)} S_i(\omega)$. Now, the collision operator and Hamiltonian can be defined as

$$U^{\mathrm{GMME}}(\Delta t) = \prod_{i=1}^{N} \exp\left(-\mathrm{i} H_i^{\mathrm{GMME}} \Delta t\right), \quad H_i^{\mathrm{GMME}} = \sqrt{\frac{1}{\Delta t}}\left(Q_i \sigma_+^{\mathrm{anc}} + Q_i^\dagger \sigma_-^{\mathrm{anc}}\right). \tag{V.22}$$

Note that we need here only N collisions per time step.

V.3 Results and discussion

V.3.1 Results of the collision model

In light of what has been observed in the previous Chapter, we test our collision model within the regime of validity of the Born-Markov condition, *i.e.*, $\lambda = 35\ \mathrm{cm}^{-1}$, $\Omega^{-1} = 1\ \mathrm{fs}$ and $T = 347\ \mathrm{K}$, so that the reproduced dynamics can be considered physically reliable. In this regime, the strength of coupling with the environment is sufficiently weak, the decay of the correlations is fast compared to the frequency of the system and the spectral function has a perfect Ohmic behaviour in the range of frequencies typical of the FMO Hamiltonian. However, as should be expected, the proposed collision schemes would correctly reproduce the target equations in all the possible range of parameters, also outside the validity region of the equations themselves. This is possible because, differently from the Redfield equation that usually becomes negative outside the Born-Markov boundaries, these Lindblad equations do not.

[1] Interestingly, in the GAME equation the Lamb shift that renormalize the system Hamiltonian depends not only on the dispersion function, but also in the spectral function. This is the only case in which we have observed this.

In Figure 1, we present the master equation results and the dynamics generated by the collision models of the full secular Redfield, PERLind, ULE and GAME. The simulation started with an excitation localized at site 1. For the collision models, we average over 10^4 trajectories propagating the algorithms using a time step of $\Delta t = 1$ fs . We first observe as the dynamics generated by the different master equations are practically indistinguishable for the chosen spectral density and system. On the basis of the analysis presented in the previous Chapter, we also know that such dynamics is the same generated by the full Redfield equation.[2]

The second point is to assess the capability of the collision algorithm to reproduce the average dynamics. As proof of the excellent agreement obtained by our dynamics, we also report in the last column of Figure 1 both the fidelity $\mathrm{F}\left(\rho^{\text{target}},\rho^{\text{coll}}\right)$ and the trace distance $\mathrm{T}\left(\rho^{\text{target}},\rho^{\text{coll}}\right)$ between the target (ρ^{target}) and the simulated (ρ^{coll}) density matrices at each time step. These quantities, defined as

$$\mathrm{F}\left(\rho^{\text{target}},\rho^{\text{coll}}\right)=\left(\mathrm{Tr}\left\{\sqrt{\sqrt{\rho^{\text{target}}}\rho^{\text{coll}}\sqrt{\rho^{\text{target}}}}\right\}\right)^2, \tag{V.23}$$

$$\mathrm{T}\left(\rho^{\text{target}},\rho^{\text{coll}}\right)=\frac{1}{2}\left\|\rho^{\text{target}}-\rho^{\text{coll}}\right\|_1=\frac{1}{2}\mathrm{Tr}\left\{\sqrt{\left(\rho^{\text{target}}-\rho^{\text{coll}}\right)^2}\right\}, \tag{V.24}$$

measure the degree of distinguishability of two density matrices. Results can be read by remembering that the two indicators have the same boundaries $0\le \mathrm{F}\left(\rho^{\text{target}},\rho^{\text{coll}}\right),\mathrm{T}\left(\rho^{\text{target}},\rho^{\text{coll}}\right)\le 1$ but with the opposite meaning, *i.e.*, the fidelity and trace distance of two identical states are $\mathrm{F}(\rho,\rho)=1$ and $\mathrm{T}(\rho,\rho)=0$, respectively. Results show an optimally high fidelity and low trace distance, confirming the goodness of our collisional models. However, the agreement between the result of the collision algorithm and the resolution of the master equation could be further improved by increasing the number of trajectories and diminishing the time step of the simulation (in our case the time step was small enough and could even have been increased).

[2] Based on the comparison between the original Redfield form and the secular Redfield in this range of parameters.

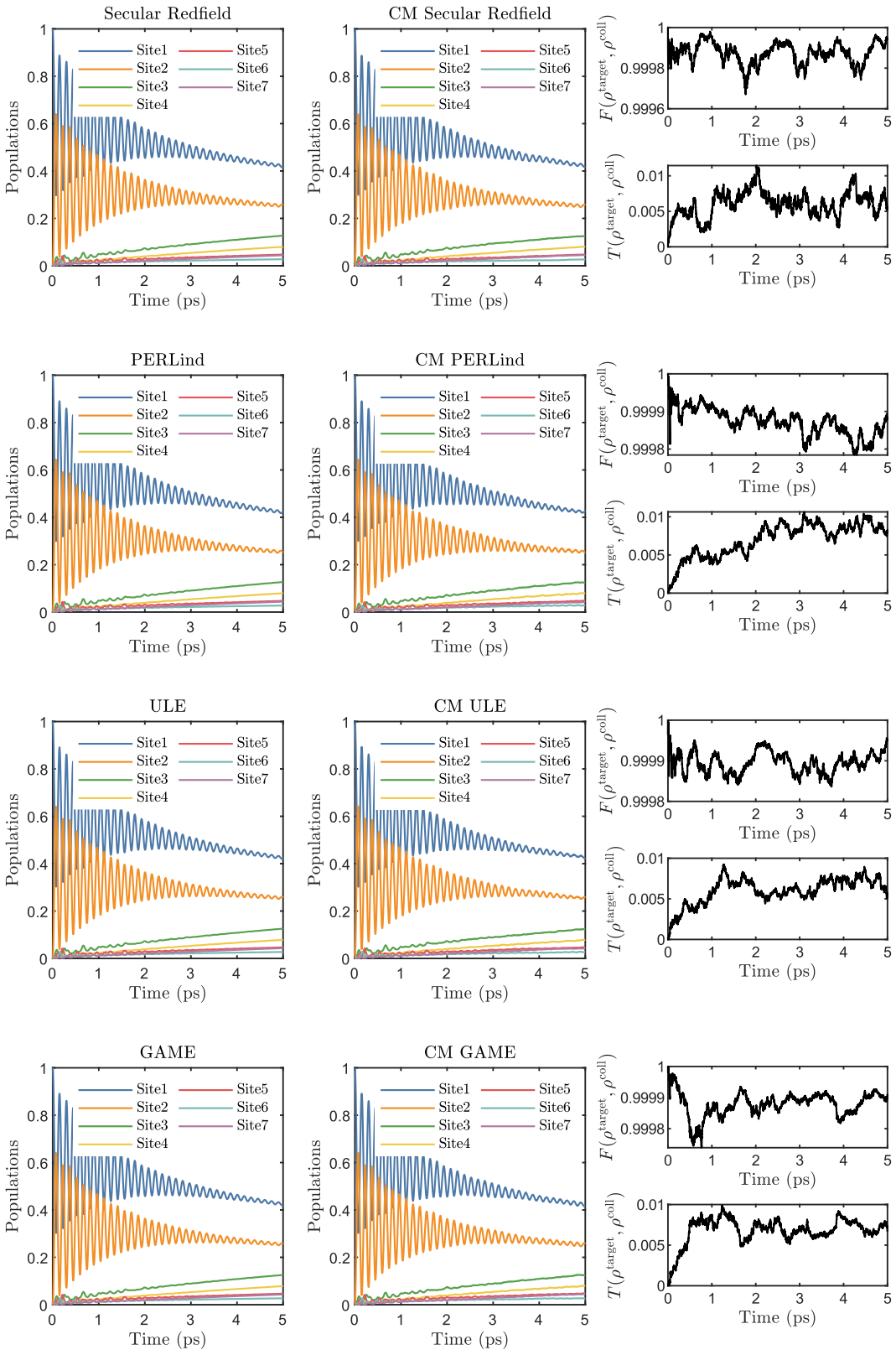

Figure 1. Results of the collision model (central column) compared with the target dynamics (left column). The fidelity and trace distance between the dynamics of the target density matrix and the collision (right column) show excellent agreement, proving the goodness of our collision algorithms. Parameters of the simulation: $\lambda = 35\ \text{cm}^{-1}$, $\Omega^{-1} = 1\ \text{fs}$, $T = 347\ \text{K}$, $\Delta t = 1\ \text{fs}$, 10^4 trajectories.

V.3.2 Scaling of the algorithms on a digital quantum computer

Here we briefly discuss the possible implementation of the algorithms on a digital quantum computer. The first aspect to be decided is the mapping of the states of the system into the qubits of the quantum register. Since the dynamics we want to implement does not involve multi-excitons, the most efficient and simple mapping on a quantum computer is in this case the binary mapping. The binary mapping allows for the implementation of the N sites of the simulated open system on N states of the computational basis, requiring a number of qubits that scales logarithmically, $q = \lceil \log_2(N) \rceil$.[3] For the FMO complex, $q = 3$ qubits are sufficient. Another aspect is how to implement the ancillae that are necessary for the dynamics. There are two possible ways to do it. One way, which is the most expensive, requires mapping the ancilla of each collision as a qubit of the quantum register. The other way is to dedicate only one qubit of the register as the ancilla qubit, which must be reset after every interaction. The advantage of using the second method is evident, but, it can be argued that, in the current generation of quantum computers, the noise introduced for a reset gate is so high that the computation quickly loses coherence [31]. This motivation was used for example by Cattaneo *et al*. used to justify the use of the first approach in their recent simulation of a collision model on (noisy) IBM quantum computers. However, we must say that current quantum computers are not the target of our proposed collision models, as the noise is so high that simulations would fail to correctly reproduce dynamics also for small systems [31]. Depending on the technical characteristic of the future quantum hardware, it is an open question whether better results will be obtained by using a larger quantum register with few reset operations or with a single ancilla qubit undergoing multiple reset operations. Here, we decide to stay with the option requiring less controllable qubits and therefore we repeatedly reset a single ancilla qubit.

The algorithmic steps are similar to the ones we have already reported in Chapters II and III. A schematic example of the circuit is reported in Figure 2. The system must be initially prepared in order to reproduce the presence of an excitation in the chromophoric network. Because of the algorithmic mapping, this can require a gate that operates on the whole quantum register of the system, *i.e.*, that can be implemented in the worst case with $\mathcal{O}\left(4^q\right) = \mathcal{O}\left(N^2\right)$ CNOT gates. However, for simple initial states (like initial localization on a single site) very few operations are needed without requiring any CNOT.[4]

Then, since the collision Hamiltonians of our algorithms rely on the system operators on the exciton basis, it is convenient to apply a gate D to change the state of the system quantum register from the site basis to the

[3] The number of states becomes $N+2$ if we insert also the reaction centre and the ground state. However, the scaling analysis reported here is still valid also in that case.

[4] If the dynamics starts with an excitation at site 1, and we map that site as $|000\rangle$, we do not even need to apply any gate.

excitons basis. This approach has also been used by Gupta and Chandrashekar in [36] and requires up to $\mathcal{O}\left(4^q\right)=\mathcal{O}\left(N^2\right)$ CNOT gates. At the end of the circuit, the inverse operator $D^\dagger$ can be implemented if one desires to read the results on the site basis.

The central part of the circuit is occupied by the repetition of gates implementing the Hamiltonian free-evolution (on the exciton basis) $U_{\mathrm{H}}\left(\Delta t\right)$ and the collisions $U_{\text{exc-ph}}\left(\Delta t\right)$. In general, to obtain the populations at time $t=n\Delta t$, it will be necessaire to repeat the block of instructions for n times.

$U_{\mathrm{H}}\left(\Delta t\right)$ is a unitary operation acting on the system quantum register that can be transpiled in general using $\mathcal{O}\left(4^q\right)=\mathcal{O}\left(N^2\right)$ CNOT gates. However, since H^{exc} is diagonal in the exciton basis, if the Lamb shift is null or diagonal as well, then it requires only $\mathcal{O}\left(2^q\right)=\mathcal{O}\left(N\right)$ CNOT gates for the decomposition.

The decomposition of the circuit block implementing $U_{\text{exc-ph}}\left(\Delta t\right)$ is the one that characterizes the different collision models proposed and gives the overall scaling of the quantum circuit. In Figure 3, we show that it is composed of gates implementing the collision operators, followed by a reset gate on the ancilla qubit. A single collision operator can be implemented by $\mathcal{O}\left(4^q\right)=\mathcal{O}\left(N^2\right)$ CNOT gates. Thus, the final scaling must take into account the number of these collision operators reported in the previous section for the partial/full secular Redfield and the GMMEs. Results are reported in Table 1 along with the scaling of the Haken-Strobl equation found in Chapter II. We can see that the quantum algorithm for the collision model of the partial secular equation has a scaling that depends on the number of frequency clusters used. It ranges from $\mathcal{O}\left(N^5\right)$ if we use one cluster per frequency or $\mathcal{O}\left(N^3\right)$ if we use only one cluster that comprehends all the frequencies. Note that these limit situations correspond to the full secular Redfield and the Haken-Strobl cases respectively, for which we have proposed alternative algorithms resulting in a better scaling. It is precisely the collision algorithm for Haken-Strobl that presents the best scaling for the Markovian equations examined in this thesis. The algorithm for GMME is the best performing of those presented in this chapter. However, all the proposed algorithms scale better than the $\mathcal{O}\left(N^6\right)$ often required by the Stinespring dilation [37]. In [36], the algorithm proposed by Gupta and Chandrashekar for the full secular Redfield requires $\mathcal{O}\left(N^2\log_2 N\right)$ CNOTs to be executed. This is definitely a better scaling compared to our collision algorithm for the secular Redfield. However, in their derivation, they assumed a particular form for the interaction between the bath of each chromophore (we assumed separated baths instead). Counter-intuitively, this makes the number of independent dissipation channels an order of magnitude smaller than the one we considered, which is probably the reason for their advantage.

To conclude, we highlight that also for the collision algorithms proposed in this Chapter, by exploiting the correspondence between measurement and trace, the demand for trajectories into which the algorithms are decomposed is naturally satisfied by the need for a digital quantum computer to run a circuit several times to obtain information on qubit populations (cf. Chapters II and III).

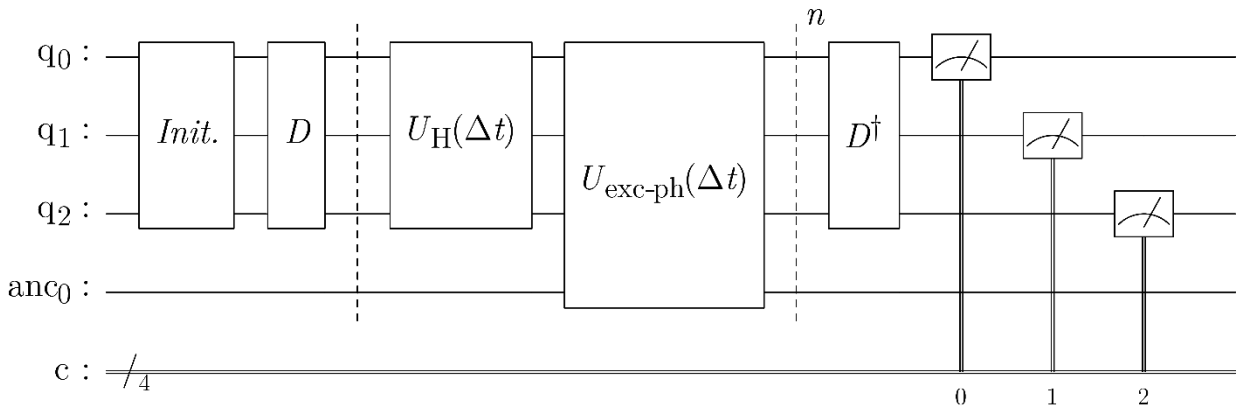

Figure 2. Scheme of the quantum circuit for the execution of the proposed algorithms. The quantum register of the system is mapped on the FMO states on the site basis. The first gate initializes the register. D and $D^\dagger$ change the basis from site to exciton and *vice versa*. The circuit between the barriers must be repeated n times to get the result at time $n\Delta t$. To save resources of the quantum device, the ancilla qubit is reset after every execution of the gates involving it.

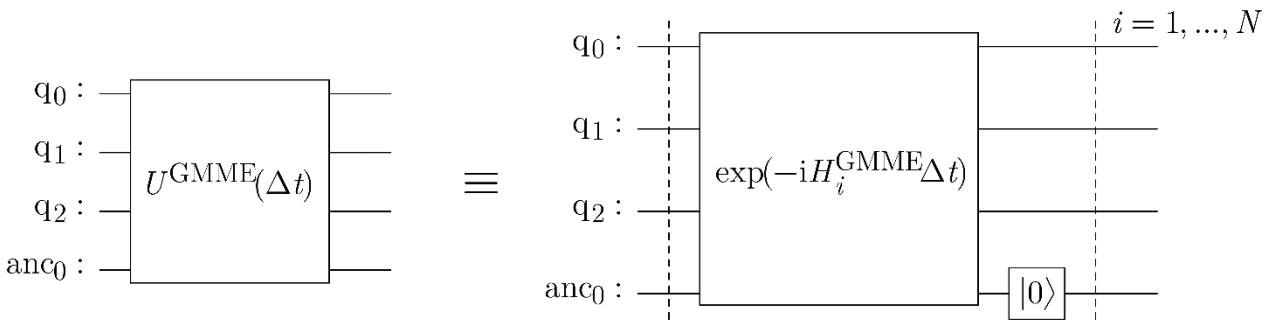

Figure 3. $U_{\text{exc-ph}}(\Delta t)$ circuit block ($U^{\mathrm{GMME}}(\Delta t)$ in this figure) represent in a compact notation the sequence of gates (collision operators followed by a reset of the ancilla) that implements the various dissipation channels. The decomposition of the collision operator in 1- and 2-qubit gates is not univocal and depends on the device used for the execution.

Table 1. The algorithmic complexity of the Markovian collision algorithms proposed in this thesis.

Algorithm	# CNOT gates, # reset gates
Full secular Redfield equation	$\mathcal{O}\left(N^4\right)$, $\mathcal{O}\left(N^2\right)$
Partial secular Redfield equation	$\mathcal{O}\left(N^3\right) \leq \mathcal{O}\left(\#(\bar{\omega})N^3\right) \leq \mathcal{O}\left(N^5\right)$, $\mathcal{O}\left(\#(\bar{\omega})N\right)$
GMMEs	$\mathcal{O}\left(N^3\right)$, $\mathcal{O}(N)$
Haken-Strobl (Chapter II)	$\mathcal{O}\left(N^2\right)$, $\mathcal{O}(N)$

V.3.3 Trajectories and similarities with Monte Carlo wavefunction methods

In this last part, we discuss the trajectories that are produced by our algorithms. In Figure 4, we take as an example the dynamics of the full secular Redfield equation simulated with our collision model at an increasing number of trajectories (results for the other equations are similar). To appreciate better the results, we show both the population of site 1 and site 3 during time. The purple line represents the dynamics of a single (random) trajectory produced by the collision model we propose. Focusing on this line, it can be clearly seen, especially looking at site 1, that at time $t \approx 1$ ps the dynamics change unexpectedly. A phenomenological explanation for this observation is that a collision has occurred between the system and the ancilla. By increasing the number of trajectories, the probability to see a collision increases (it is very clear for example from the dynamics originated by the average of 10 trajectories). Then, when the number of trajectories is very high, the collision spots of the individual trajectories can no longer be distinguished by looking at the average dynamics, and the result of the master equation is asymptotically recovered.

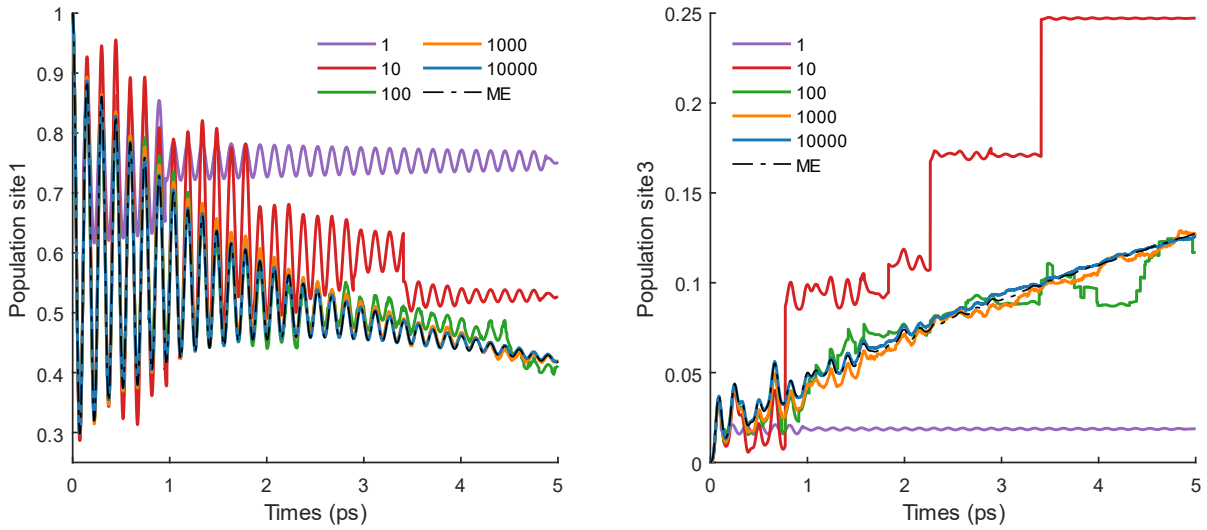

Figure 4. Simulation of the populations of site 1 (left panel) and site 3 (right panel) obtained by the collision model for the full secular Redfield are compared with the master equation results (dashed black line). The violet line corresponds to a single trajectory. Red, green, orange and blue lines are computed as the average of 10, 100, 1000 and 10000 trajectories, respectively. Parameters of the simulations are $\lambda = 35\ \mathrm{cm}^{-1}$, $\Omega^{-1} = 1\ \mathrm{fs}$, $T = 347\ \mathrm{K}$ and $\Delta t = 1\ \mathrm{fs}$.

The argument that a collision occurred is certainly plausible and, for certain collision models, it is also exact (see Chapter II). In the following we will substantiate this intuition by looking closer at a single trajectory and its probabilistic measure. Without complicating things too much, let us take a simple target equation, where we have only one Lindblad operator in the dissipator, that reads

$$\frac{d\rho(t)}{dt} = -\mathrm{i}\left[H, \rho(t)\right] + c^2\left(O\rho(t)O^\dagger - \frac{1}{2}\left[O^\dagger O, \rho(t)\right]_+\right), \tag{V.25}$$

so that propagator (cf. eq. (V.11)) can be written as the product of system Hamiltonian propagation and a collision operator

$$U(\Delta t) = U_{\mathrm{coll}}(\Delta t)U_{\mathrm{H}}(\Delta t) = \exp\left(-\mathrm{i}H_{\mathrm{coll}}\Delta t\right)\exp\left(-\mathrm{i}H\Delta t\right) \tag{V.26}$$

where $H_{\mathrm{coll}} = c/\sqrt{\Delta t}\left(O\sigma_{\mathrm{anc}}^{+} + O^\dagger\sigma_{\mathrm{anc}}^{-}\right)$. The initial state of the ancillae is the desired state $\left|0^{\mathrm{anc}}\right\rangle$. Let us follow the system state evolution step by step. We recall that in Appendix A, we demonstrated the parallelism between repeated measures and trace of the ancillae, so the evolution

$$\rho(0) = \left|\psi(0)\right\rangle\left\langle\psi(0)\right| \xrightarrow{U_{\mathrm{H}}(\Delta t)} \rho' \xrightarrow[2)\ \text{trace anc}]{1)\ U_{\mathrm{coll}}(\Delta t)} \rho(\Delta t)$$

can be approximated by averaging over different trajectories of pure states

$$\left|\psi(0)\right\rangle \xrightarrow{U_{\mathrm{H}}(\Delta t)} \left|\psi'\right\rangle \xrightarrow[\text{2) measure anc}]{\text{1) } U_{\mathrm{coll}}(\Delta t)} \left|\psi_k(\Delta t)\right\rangle \xrightarrow{\text{average over trajectories}} \rho(\Delta t).$$

The first step is Hamiltonian propagation. This transforms the initial state into

$$\left|\psi'\right\rangle = U_{\mathrm{H}}(\Delta t)\left|\psi(0)\right\rangle = \left|\psi(0)\right\rangle - \mathrm{i}\Delta t H\left|\psi(0)\right\rangle + \mathcal{O}\left(\Delta t^2\right). \tag{V.27}$$

Then we have the collision event and subsequent measure of the ancilla resulting in state $\left|\phi_k^{\mathrm{anc}}\right\rangle$ with $k=0$ or 1 with probability $p_{k=0}^{\mathrm{anc}}$ and $p_{k=1}^{\mathrm{anc}}$, respectively. The system statevector results in

$$\begin{aligned}\left|\psi_k(\Delta t)\right\rangle &= \frac{\left\langle\phi_k^{\mathrm{anc}}\right|U_{\mathrm{coll}}(\Delta t)\left|\psi'\right\rangle\otimes\left|0^{\mathrm{anc}}\right\rangle}{\sqrt{p_k^{\mathrm{anc}}}} \\ &= \begin{cases} \dfrac{1}{\sqrt{p_{k=0}^{\mathrm{anc}}}}\left(1-\mathrm{i}\Delta t H-\dfrac{1}{2}\Delta t c^2 O^\dagger O\right)\left|\psi(0)\right\rangle+\mathcal{O}\left(\Delta t^2\right), & \left|\phi_k^{\mathrm{anc}}\right\rangle=\left|0^{\mathrm{anc}}\right\rangle \\ -\dfrac{\mathrm{i}}{\sqrt{p_{k=1}^{\mathrm{anc}}}}\sqrt{\Delta t}cO\left|\psi(0)\right\rangle+\mathcal{O}\left(\Delta t^{3/2}\right), & \left|\phi_k^{\mathrm{anc}}\right\rangle=\left|1^{\mathrm{anc}}\right\rangle \end{cases}\end{aligned} \tag{V.28}$$

where $p_{k=0}^{\mathrm{anc}} = 1 - p_{k=1}^{\mathrm{anc}}$ and $p_{k=1}^{\mathrm{anc}} = c^2\Delta t + \mathcal{O}\left(\Delta t^2\right)$. Averaging over trajectories, one obtains the density matrix $\rho(\Delta t)$ that is

$$\begin{aligned}\rho(\Delta t) &= \sum_{k=0,1} p_k^{\mathrm{anc}}\left|\psi_k(\Delta t)\right\rangle\left\langle\psi_k(\Delta t)\right| \\ &= \rho(0) - \mathrm{i}\Delta t\left[H,\rho(0)\right] + c^2\Delta t\left(O\rho(0)O^\dagger - \frac{1}{2}\left[O^\dagger O,\rho(0)\right]_+\right) + \mathcal{O}\left(\Delta t^2\right)\end{aligned} \tag{V.29}$$

It is easy to show that the corrections of order $\mathcal{O}\left(\Delta t^{3/2}\right)$ vanish in the averaging step. Now writing the equation as

$$\frac{\rho(\Delta t)-\rho(0)}{\Delta t} = -\mathrm{i}\left[H,\rho(0)\right] + c^2\left(O\rho(0)O^\dagger - \frac{1}{2}\left[O^\dagger O,\rho(0)\right]_+\right) + \mathcal{O}(\Delta t) \tag{V.30}$$

and taking the limit of $\Delta t \to 0^+$ the desired target eq. (V.25) is obtained. Note that the fundamental condition $c^2\Delta t \ll 1$ for deriving a valid collision model (cf. section V.2) reflects here in a remote probability of measuring the state 1 of the ancilla. It follows that in presence of a more complex collision scheme than the ones we have analyzed here, the probability of multiple samplings of state 1 of the ancillae during the same time interval Δt must be very small.

Eq. (V.28) closely resembles the typical propagation scheme of a Monte Carlo wavefunction method (also known as quantum jump algorithm) [21–27]. In that algorithm, the evolution of the trajectory is based on the

calculation of a (jump) probability (the equivalent of our $p_{k=1}^{\mathrm{anc}}$), and then a Monte Carlo sampling decides if the system evolves under a "non-Hermitian Hamiltonian" [27] (corresponding to measuring state 0 of the ancilla in our case) or if a jump has occurred (corresponding to measuring state 1). After applying the respective operator, the state of the system must be renormalized. Because of the use of non-unitary operators, that require to force renormalization, Monte Carlo wavefunction methods cannot be directly implemented as quantum algorithms for digital quantum computers. On the contrary, our collision scheme is completely based on unitary operations and measurements. So, incidentally, our collision model is an interesting and immediate alternative for the application of quantum jump algorithms on digital quantum devices, with the extra cost of a single ancilla qubit.

V.4 Conclusions and perspectives

In this last Chapter of the thesis, we have introduced some strategies based on collision models to reproduce the dynamics of the FMO molecular complex using the secular Redfield equation (both in the full or partial approximation) and the GMMEs (namely, the PERLind, the ULE and the GAME). These Lindblad-form equations offer an alternative to the original Redfield equation for the description of the dynamics of an open quantum system in contact with a perturbative environment at finite temperature. The resulting collision models are defined in terms of microscopic quantities like the spectral and dispersion functions of the environment, besides the system Hamiltonian.

In our derivation, we pose particular attention to proposing collision models that generate trajectories of pure states, in order to permit an efficient classical and quantum simulation. The results of a classical simulation of the collision algorithms for the dynamics of the FMO have been shown, and the high accuracy of our collision models has been assessed using the fidelity and the trace distance as indicators of the indistinguishability of the obtained states from the target states.

We have presented the circuit for a possible quantum implementation of the proposed algorithms and discussed their algorithmic complexity. The GMMEs result in better scaling, $\mathcal{O}\left(N^3\right)$, with respect to both variants of the secular Redfield form. Combined with the fact that benchmarks in the literature show they can reproduce Redfield dynamics beyond the possibility of the secular equations [18], GMMEs are probably the best alternative offered in this Chapter.

In the final part, we showed that the particular formulation of the collision model leads to a propagation scheme that is very similar to the well-known Monte Carlo wavefunction methods (*i.e.*, the quantum jump unravelling of the master equation). Since these methods require the use of non-unitaries operators, it is not possible to implement quantum jump schemes directly on a quantum computer. So incidentally, our collision schemes offer a platform to translate Monte Carlo wavefunction methods to quantum algorithms.

We noted that in literature there exists also some quantum jump models that implement the full Redfield equation [38,39]. A correct unravelling scheme in this case has to be able to follow also the (eventual)

nonphysical behaviour, *i.e.*, the ensemble average over the trajectories should correctly reproduce the solution of the target equation, and also its pathological situations. However, an average over (physically acceptable) pure states will never result in negative populations. In [39] (and similarly in [38]), the problem of dealing with non-positivity is handled by using two distinct wavefunctions $|\psi\rangle$ and $|\phi\rangle$, whose total dimension is twice the Hilbert space of the open system, to represent the trajectories. Then the density matrix is obtained as the ensemble average $\rho = \overline{|\psi\rangle\langle\phi|} + \overline{|\phi\rangle\langle\psi|}$, which can assume negative values. Whether it is possible to implement collision models that can carry out the same kind of unravelling is still unknown to us, and could be the object of future investigations.

V.5 Appendix A

Here we demonstrate that the dynamics of the density matrix of the open system, computed as the average over the trajectories obtained by measuring the ancillae after every interaction, corresponds to the one obtained by tracing over the ancillary degrees of freedom.

The first step is to show the density matrix of the open system at time $t+\Delta t$ in eq. (V.6) can be obtained by repeated measurements of the state $\rho^{\text{tot}}(t+\Delta t) = U\left(\rho(t)\otimes\rho^{\text{anc}}\right)U^{\dagger}$. For this purpose, we call $\left|\phi_k^{\text{anc}}\right\rangle = \left\{\left|0^{\text{anc}}\right\rangle, \left|1^{\text{anc}}\right\rangle\right\}$ the states on which we measure the ancillae, and we remove the time dependency from $U(\Delta t) = U$ to simplify the notation. Every ancilla state will have a probability

$$p_k^{\text{anc}} = \text{Tr}\left\{\left\langle\phi_k^{\text{anc}}\right|\rho^{\text{tot}}(t)\left|\phi_k^{\text{anc}}\right\rangle\right\} \tag{V.31}$$

to be measured after the collision with the system. Now, let us suppose that state $\left|\phi_l^{\text{anc}}\right\rangle$ is observed. The total state (system + ancillae) becomes the normalized product state

$$\rho_l^{\text{tot}}(t+\Delta t) = \frac{\left\langle\phi_l^{\text{anc}}\right|\rho^{\text{tot}}(t)\left|\phi_l^{\text{anc}}\right\rangle \otimes \left|\phi_l^{\text{anc}}\right\rangle\left\langle\phi_l^{\text{anc}}\right|}{p_l^{\text{anc}}}, \tag{V.32}$$

from which it is easy to see that the state of the open system is

$$\rho_l(t+\Delta t) = \frac{\left\langle\phi_l^{\text{anc}}\right|\rho^{\text{tot}}(t)\left|\phi_l^{\text{anc}}\right\rangle}{p_l^{\text{anc}}}. \tag{V.33}$$

If one prepares and measures many times the initial state $\rho^{\text{tot}}(t+\Delta t)$, the resulting average state for the system will be

$$\begin{aligned}\rho(t+\Delta t) &= \sum_k p_k^{\text{anc}} \rho_k (t+\Delta t) \\ &= \sum_k \left\langle \phi_k^{\text{anc}} \middle| \rho^{\text{tot}}(t) \middle| \phi_k^{\text{anc}} \right\rangle = \sum_k \left\langle \phi_k^{\text{anc}} \middle| U\left(\rho(t)\otimes\rho^{\text{anc}}\right)U^\dagger \middle| \phi_k^{\text{anc}} \right\rangle \\ &= \text{Tr}_{\text{anc}} \left\{ U\left(\rho(t)\otimes\rho^{\text{anc}}\right)U^\dagger \right\}\end{aligned} \tag{V.34}$$

where in the last equivalence we used the definition of trace.

Now, we show that the result is valid at all times by demonstrating the validity at $t+2\Delta t$. Using the same formalism of eq. (V.34), we can write

$$\rho(t+2\Delta t) = \sum_k \sum_l p_l^{\text{anc}} p_{lk}^{\text{anc}} \rho_{lk}(t+2\Delta t), \tag{V.35}$$

where p_l^{anc} is the probability of measuring $\left|\phi_l^{\text{anc}}\right\rangle$ at time $t+\Delta t$, p_{lk}^{anc} is the conditional probability of measuring $\left|\phi_k^{\text{anc}}\right\rangle$ at time $t+2\Delta t$ when state $\left|\phi_l^{\text{anc}}\right\rangle$ was measured in the previous step of the dynamics and

$$\rho_{lk}(t+2\Delta t) = \frac{\left\langle \phi_k^{\text{anc}} \middle| U\left(\left\langle \phi_l^{\text{anc}} \middle| U\left(\rho(t)\otimes\rho^{\text{anc}}\right)U^\dagger \middle| \phi_l^{\text{anc}} \right\rangle \otimes \rho^{\text{anc}}\right)U^\dagger \middle| \phi_k^{\text{anc}} \right\rangle}{p_l^{\text{anc}} p_{lk}^{\text{anc}}} \tag{V.36}$$

is the correspondent density matrix of the system. Then, eq. (V.35) can be simplified as

$$\begin{aligned}\rho(t+2\Delta t) &= \sum_k \sum_l \left\langle \phi_k^{\text{anc}} \middle| U\left(\left\langle \phi_l^{\text{anc}} \middle| U\left(\rho(t)\otimes\rho^{\text{anc}}\right)U^\dagger \middle| \phi_l^{\text{anc}} \right\rangle \otimes \rho^{\text{anc}}\right)U^\dagger \middle| \phi_k^{\text{anc}} \right\rangle \\ &= \sum_k \left\langle \phi_k^{\text{anc}} \middle| U\left(\sum_l \left\langle \phi_l^{\text{anc}} \middle| U\left(\rho(t)\otimes\rho^{\text{anc}}\right)U^\dagger \middle| \phi_l^{\text{anc}} \right\rangle \otimes \rho^{\text{anc}} \right)U^\dagger \middle| \phi_k^{\text{anc}} \right\rangle \\ &= \sum_k \left\langle \phi_k^{\text{anc}} \middle| U\left(\rho(t+\Delta t)\otimes\rho^{\text{anc}}\right)U^\dagger \middle| \phi_k^{\text{anc}} \right\rangle \\ &= \text{Tr}_{\text{anc}} \left\{ U\left(\rho(t+\Delta t)\otimes\rho^{\text{anc}}\right)U^\dagger \right\}\end{aligned} \tag{V.37}$$

The results shown in this Appendix are of course valid also when the states of the system and ancillae are described by pure states at the initial time t. In this particular case, it is trivial to demonstrate that the density matrix of a trajectory ($\rho_l(t+\Delta t)$, $\rho_{lk}(t+2\Delta t)$ and so on) is still a pure state [40], *i.e.*, it is possible to write the state of the system in terms of statevectors without the need of considering a density matrix evolution.

V.6 Appendix B

To complete the characterization of our system, we could add extra relaxation channels to describe the exciton recombination $\mathcal{L}^{\text{R}}$ and the trapping from site 3 to the reaction centre $\mathcal{L}^{\text{T}}$ (cf. with Chapter IV). We have already shown the Lindblad-type form of these channels in the previous Chapter, to which we refer for more details. However, for the completeness of the discussion, we report them here as

$$\mathcal{L}^{\mathrm{R}}\left[\rho(t)\right]=\gamma^{\mathrm{R}}\sum_{i=1}^{N}\left\{|0\rangle\langle i|\rho(t)|i\rangle\langle 0|-\frac{1}{2}\left[|i\rangle\langle i|,\rho(t)\right]_{+}\right\}, \tag{V.38}$$

$$\mathcal{L}^{\mathrm{T}}\left[\rho(t)\right]=\gamma^{\mathrm{T}}\left\{|\mathrm{r.c.}\rangle\langle 3|\rho(t)|3\rangle\langle \mathrm{r.c.}|-\frac{1}{2}\left[|3\rangle\langle 3|,\rho(t)\right]_{+}\right\} \tag{V.39}$$

where γ^{R} is the recombination rate that we have assumed to be constant for every chromophore, and γ^{T} is the trapping rate to the reaction centre $|\mathrm{r.c.}\rangle$.

When these extra channels are inserted in the description of the system, eq. takes the form

$$U(\Delta t)=U_{\mathrm{T}}(\Delta t)U_{\mathrm{R}}(\Delta t)U_{\text{exc-ph}}(\Delta t)U_{H}(\Delta t), \tag{V.40}$$

Where $U_{\mathrm{R}}(\Delta t)$ is the collision operator for the recombination of the exciton, defined as

$$U_{\mathrm{R}}(\Delta t)=\prod_{i=1}^{N}\exp\left(-\mathrm{i}H_{i}^{\mathrm{R}}\Delta t\right),\quad H_{i}^{\mathrm{R}}=\sqrt{\frac{\gamma^{\mathrm{R}}}{\Delta t}}\left(|0\rangle\langle i|\sigma_{\text{anc}}^{+}+|i\rangle\langle 0|\sigma_{\text{anc}}^{-}\right), \tag{V.41}$$

while $U_{\mathrm{T}}(\Delta t)$ is the collision operator for the trapping to the reaction centre, defined as

$$U_{\mathrm{T}}(\Delta t)=\exp\left(-\mathrm{i}H^{\mathrm{T}}\Delta t\right),\quad H^{\mathrm{T}}=\sqrt{\frac{\gamma^{\mathrm{T}}}{\Delta t}}\left(|\mathrm{r.c.}\rangle\langle 3|\sigma_{\text{anc}}^{+}+|3\rangle\langle \mathrm{r.c.}|\sigma_{\text{anc}}^{-}\right). \tag{V.42}$$

We stress once again that, in the propagation scheme we propose, each collision must involve an ancilla initially prepared in state $|0^{\text{anc}}\rangle$, and the state of the ancilla must be reset after every collision.

For the implementation on a digital quantum computer, the inclusion of extra states for the reaction centre and the ground state requires a total number of qubits $q=\lceil\log_2(N+2)\rceil$ for the enlarged system register (exciton states plus 2 extra states) using an algorithmic mapping. Then, each collision operator the form $U_{\mathrm{R}}(\Delta t)$ can be decomposed in 1- and 2-qubit gates using $\mathcal{O}\left(4^{q+1}\right)=\mathcal{O}\left(N^{2}\right)$ CNOTs and a subsequent reset gate for the ancilla. Since there are N collision operators that implement the recombination channels acting on different sites, $U_{\mathrm{R}}(\Delta t)$ requires a total number of $\mathcal{O}\left(N^{3}\right)$ CNOTs gates and N resets for the execution. The same reasoning can be applied also for $U_{\mathrm{T}}(\Delta t)$, that requires $\mathcal{O}\left(4^{q+1}\right)=\mathcal{O}\left(N^{2}\right)$ CNOT and 1 reset for the implementation.

V.7 Appendix C

To allow a more agile implementation of the collision model of the full secular Redfield, we propose here a revisited writing of eq. (V.13). Since the FMO Hamiltonian has not degenerate frequencies except for $\omega=0$

, operators $S_i(\omega)$ take the simple form of $S_i(\omega)=\langle\alpha|S_i|\beta\rangle|\alpha\rangle\langle\beta|$, where $\varepsilon_\beta-\varepsilon_\alpha=\omega$. Thus the full secular equation for systems with non-degenerate frequencies can be rewritten as

$$\begin{aligned}\frac{d\rho(t)}{dt}=&-\mathrm{i}\Big[H^{\mathrm{exc}}+H^{\mathrm{LS,sec}},\rho(t)\Big]+\sum_{i=1}^{N}C(0)\Big\{S_i(0)\rho(t)S_i(0)-\frac{1}{2}\Big[S_i(0)S_i(0),\rho(t)\Big]_+\Big\}\\&+\sum_{i=1}^{N}\sum_{\substack{\alpha,\beta\\ \alpha\neq\beta}}C\left(\varepsilon_\beta-\varepsilon_\alpha\right)\langle\alpha|S_i|\beta\rangle\langle\beta|S_i|\alpha\rangle\Big\{|\alpha\rangle\langle\beta|\rho(t)|\beta\rangle\langle\alpha|-\frac{1}{2}\Big[|\beta\rangle\langle\beta|,\rho(t)\Big]_+\Big\}\end{aligned}\tag{V.43}$$

where we have separated the $\omega=0$ terms from the rest. Now, if we define

$$w_{\alpha\beta}=\sum_{i=1}^{N}\langle\alpha|S_i|\beta\rangle\langle\beta|S_i|\alpha\rangle,\tag{V.44}$$

the full secular Redfield becomes

$$\begin{aligned}\frac{d\rho(t)}{dt}=&-\mathrm{i}\Big[H^{\mathrm{exc}}+H^{\mathrm{LS,sec}},\rho(t)\Big]+\sum_{i=1}^{N}C(0)\Big\{S_i(0)\rho(t)S_i(0)-\frac{1}{2}\Big[S_i(0)S_i(0),\rho(t)\Big]_+\Big\}\\&+\sum_{\substack{\alpha,\beta\\ \alpha\neq\beta}}C\left(\varepsilon_\beta-\varepsilon_\alpha\right)w_{\alpha\beta}\Big\{|\alpha\rangle\langle\beta|\rho(t)|\beta\rangle\langle\alpha|-\frac{1}{2}\Big[|\beta\rangle\langle\beta|,\rho(t)\Big]_+\Big\}\end{aligned}\tag{V.45}$$

The advantage of using eq. (V.45) instead of eq. (V.43) in a collision model is in the number of collision operators to compute that reduces from $\mathcal{O}\left(N^3\right)$ to $\mathcal{O}\left(N^2\right)$.

V.8 References

[1] D. Abramavicius, S. Mukamel, Exciton dynamics in chromophore aggregates with correlated environment fluctuations, J. Chem. Phys. 134 (2011) 174504. https://doi.org/10.1063/1.3579455.

[2] J. Adolphs, T. Renger, How Proteins Trigger Excitation Energy Transfer in the FMO Complex of Green Sulfur Bacteria, Biophys. J. 91 (2006) 2778–2797. https://doi.org/10.1529/biophysj.105.079483.

[3] P. Kjellberg, T. Pullerits, Three-pulse photon echo of an excitonic dimer modeled via Redfield theory, J. Chem. Phys. 124 (2006) 024106. https://doi.org/10.1063/1.2150447.

[4] V.I. Novoderezhkin, A.G. Yakovlev, R. van Grondelle, V.A. Shuvalov, Coherent Nuclear and Electronic Dynamics in Primary Charge Separation in Photosynthetic Reaction Centers: A Redfield Theory Approach, J. Phys. Chem. B. 108 (2004) 7445–7457. https://doi.org/10.1021/jp0373346.

[5] T. Renger, R.A. Marcus, On the relation of protein dynamics and exciton relaxation in pigment–protein complexes: An estimation of the spectral density and a theory for the calculation of optical spectra, J. Chem. Phys. 116 (2002) 9997–10019. https://doi.org/10.1063/1.1470200.

[6] T. Renger, V. May, Ultrafast Exciton Motion in Photosynthetic Antenna Systems: The FMO-Complex, J. Phys. Chem. A. 102 (1998) 4381–4391. https://doi.org/10.1021/jp9800665.

[7] P. Rebentrost, M. Mohseni, A. Aspuru-Guzik, Role of Quantum Coherence and Environmental Fluctuations in Chromophoric Energy Transport, J. Phys. Chem. B. 113 (2009) 9942–9947. https://doi.org/10.1021/jp901724d.

[8] J. Jeske, D.J. Ing, M.B. Plenio, S.F. Huelga, J.H. Cole, Bloch-Redfield equations for modeling light-harvesting complexes, J. Chem. Phys. 142 (2015) 064104. https://doi.org/10.1063/1.4907370.

[9] R. Hartmann, W.T. Strunz, Accuracy assessment of perturbative master equations: Embracing nonpositivity, Phys. Rev. A. 101 (2020) 012103. https://doi.org/10.1103/PhysRevA.101.012103.

[10] B. Palmieri, D. Abramavicius, S. Mukamel, Lindblad equations for strongly coupled populations and coherences in photosynthetic complexes, J. Chem. Phys. 130 (2009) 204512. https://doi.org/10.1063/1.3142485.

[11] F.E. van Dorsselaer, G. Nienhuis, Quantum trajectories, J. Opt. B Quantum Semiclassical Opt. 2 (2000) R25–R33. https://doi.org/10.1088/1464-4266/2/4/201.

[12] P. Rebentrost, M. Mohseni, I. Kassal, S. Lloyd, A. Aspuru-Guzik, Environment-assisted quantum transport, New J. Phys. 11 (2009) 033003. https://doi.org/10.1088/1367-2630/11/3/033003.

[13] G. Schaller, T. Brandes, Preservation of positivity by dynamical coarse graining, Phys. Rev. A. 78 (2008) 022106. https://doi.org/10.1103/PhysRevA.78.022106.

[14] J.D. Cresser, C. Facer, Coarse-graining in the derivation of Markovian master equations and its significance in quantum thermodynamics, (2017) 1–21. http://arxiv.org/abs/1710.09939.

[15] E. Mozgunov, D. Lidar, Completely positive master equation for arbitrary driving and small level spacing, Quantum. 4 (2020) 227. https://doi.org/10.22331/q-2020-02-06-227.

[16] C. Majenz, T. Albash, H.-P. Breuer, D.A. Lidar, Coarse graining can beat the rotating-wave approximation in quantum Markovian master equations, Phys. Rev. A. 88 (2013) 012103. https://doi.org/10.1103/PhysRevA.88.012103.

[17] F. Nathan, M.S. Rudner, Universal Lindblad equation for open quantum systems, Phys. Rev. B. 102 (2020) 115109. https://doi.org/10.1103/PhysRevB.102.115109.

[18] D. Davidović, Completely Positive, Simple, and Possibly Highly Accurate Approximation of the Redfield Equation, Quantum. 4 (2020) 326. https://doi.org/10.22331/q-2020-09-21-326.

[19] G. Kiršanskas, M. Franckié, A. Wacker, Phenomenological position and energy resolving Lindblad approach to quantum kinetics, Phys. Rev. B. 97 (2018) 035432. https://doi.org/10.1103/PhysRevB.97.035432.

[20] E. Kleinherbers, N. Szpak, J. König, R. Schützhold, Relaxation dynamics in a Hubbard dimer coupled to fermionic baths: Phenomenological description and its microscopic foundation, Phys. Rev. B. 101 (2020) 125131. https://doi.org/10.1103/PhysRevB.101.125131.

[21] N. Vogt, J. Jeske, J.H. Cole, Stochastic Bloch-Redfield theory: Quantum jumps in a solid-state environment, Phys. Rev. B. 88 (2013) 174514. https://doi.org/10.1103/PhysRevB.88.174514.

[22] K. Mølmer, Y. Castin, J. Dalibard, Monte Carlo wave-function method in quantum optics, J. Opt. Soc. Am. B. 10 (1993) 524. https://doi.org/10.1364/JOSAB.10.000524.

[23] J. Dalibard, Y. Castin, K. Mølmer, Wave-function approach to dissipative processes in quantum optics, Phys. Rev. Lett. 68 (1992) 580–583. https://doi.org/10.1103/PhysRevLett.68.580.

[24] N. Gisin, I.C. Percival, The quantum state diffusion picture of physical processes, J. Phys. A. Math. Gen. 26 (1993) 2245–2260. https://doi.org/10.1088/0305-4470/26/9/019.

[25] H.M. Wiseman, G.J. Milburn, Interpretation of quantum jump and diffusion processes illustrated on the Bloch sphere, Phys. Rev. A. 47 (1993) 1652–1666. https://doi.org/10.1103/PhysRevA.47.1652.

[26] M.B. Plenio, P.L. Knight, The quantum-jump approach to dissipative dynamics in quantum optics, Rev. Mod. Phys. 70 (1998) 101–144. https://doi.org/10.1103/RevModPhys.70.101.

[27] M. Kornyik, A. Vukics, The Monte Carlo wave-function method: A robust adaptive algorithm and a study in convergence, Comput. Phys. Commun. 238 (2019) 88–101. https://doi.org/10.1016/j.cpc.2018.12.015.

[28] M. Cattaneo, G. De Chiara, S. Maniscalco, R. Zambrini, G.L. Giorgi, Collision Models Can Efficiently Simulate Any Multipartite Markovian Quantum Dynamics, Phys. Rev. Lett. 126 (2021) 130403. https://doi.org/10.1103/PhysRevLett.126.130403.

[29] F. Gallina, M. Bruschi, B. Fresch, Strategies to simulate dephasing-assisted quantum transport on digital quantum computers, New J. Phys. 24 (2022) 023039. https://doi.org/10.1088/1367-2630/ac512f.

[30] G. García-Pérez, M.A.C. Rossi, S. Maniscalco, IBM Q Experience as a versatile experimental testbed for simulating open quantum systems, Npj Quantum Inf. 6 (2020) 1. https://doi.org/10.1038/s41534-019-0235-y.

[31] M. Cattaneo, M.A.C. Rossi, G. García-Pérez, R. Zambrini, S. Maniscalco, Quantum simulation of dissipative collective effects on noisy quantum computers, (2022) 1–25. http://arxiv.org/abs/2201.11597.

[32] V. May, O. Kühn, Charge and Energy Transfer Dynamics in Molecular Systems, 3rd ed., Wiley-Vch, 2011.

[33] F. Nathan, M.S. Rudner, Erratum: Universal Lindblad equation for open quantum systems [Phys. Rev. B 102 , 115109 (2020)], Phys. Rev. B. 104 (2021) 119901. https://doi.org/10.1103/PhysRevB.104.119901.

[34] D. Davidovic, Systematic Gorini, Kossakowski, Sudarshan and Lindblad Equation for Open Quantum Systems, (2021) 1–20. http://arxiv.org/abs/2112.07863.

[35] D. Tupkary, A. Dhar, M. Kulkarni, A. Purkayastha, Fundamental limitations in Lindblad descriptions of systems

weakly coupled to baths, Phys. Rev. A. 105 (2022) 032208. https://doi.org/10.1103/PhysRevA.105.032208.

[36] P. Gupta, C.M. Chandrashekar, Digital quantum simulation framework for energy transport in an open quantum system, New J. Phys. 22 (2020) 123027. https://doi.org/10.1088/1367-2630/abcdc9.

[37] Z. Hu, R. Xia, S. Kais, A quantum algorithm for evolving open quantum dynamics on quantum computing devices, Sci. Rep. 10 (2020) 3301. https://doi.org/10.1038/s41598-020-60321-x.

[38] H.-P. Breuer, B. Kappler, F. Petruccione, Stochastic wave-function method for non-Markovian quantum master equations, Phys. Rev. A. 59 (1999) 1633–1643. https://doi.org/10.1103/PhysRevA.59.1633.

[39] I. Kondov, U. Kleinekathöfer, M. Schreiber, Stochastic unraveling of Redfield master equations and its application to electron transfer problems, J. Chem. Phys. 119 (2003) 6635–6646. https://doi.org/10.1063/1.1605095.

[40] M.A. Nielsen, I.L. Chuang, Quantum Computation and Quantum Information, 10th ed., Cambridge University Press, 2000. http://www.tandfonline.com/doi/abs/10.1080/00107514.2011.587535.

Supporting information

In the following, we report the plots of the dynamics analysed in Chapter IV.

Due to the lack of space in the figures, we report here the colour scheme that is maintained for all plots:

- Site (or exciton) 1: blue ■■■
- Site (or exciton) 2: orange ■■■
- Site (or exciton) 3: green ■■■
- Site (or exciton) 4: yellow ■■■
- Site (or exciton) 5: red ■■■
- Site (or exciton) 6: aquamarine ■■■
- Site (or exciton) 7: violet ■■■
- Reaction centre: pink ■■■
- Ground state: black ■■■

S.1 Dynamics of the populations at the variation of the reorganization energy

The dynamics of the populations of the FMO, in the site and exciton (*i.e.*, the eigenvalues of H^{exc}) basis, are shown at the variation of the reorganization energy. The results of the Redfield equation are reported in Figures 1-2, the secular Redfield equation is shown in Figures 3-4, the Redfield equation without the imaginary part is in Figures 5-6 and the Haken-Strobl is reported in Figures 7-8.

The fixed parameters are: initial state localized at site 1, $\Omega = 150\ \mathrm{cm}^{-1}$, $T = 347\ \mathrm{K}$ and $\Delta t = 10\ \mathrm{fs}$.

The values of the reorganization energy are: $\lambda = 1\ \mathrm{cm}^{-1}$ (a), $\lambda = 5\ \mathrm{cm}^{-1}$ (b), $\lambda = 10\ \mathrm{cm}^{-1}$ (c), $\lambda = 50\ \mathrm{cm}^{-1}$ (d), $\lambda = 100\ \mathrm{cm}^{-1}$ (e), $\lambda = 500\ \mathrm{cm}^{-1}$ (f) and $\lambda = 1000\ \mathrm{cm}^{-1}$ (g).

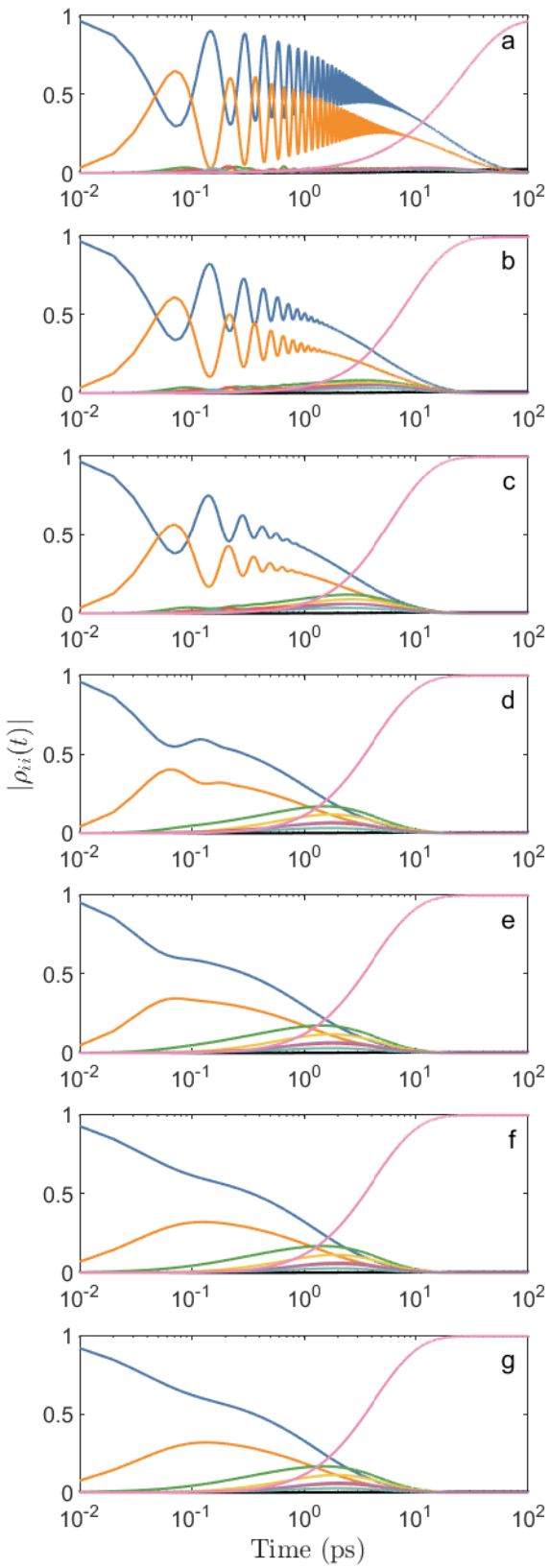

Figure 1. Dynamics of the site populations at the variation of the reorganization energy. Full Redfield equation.

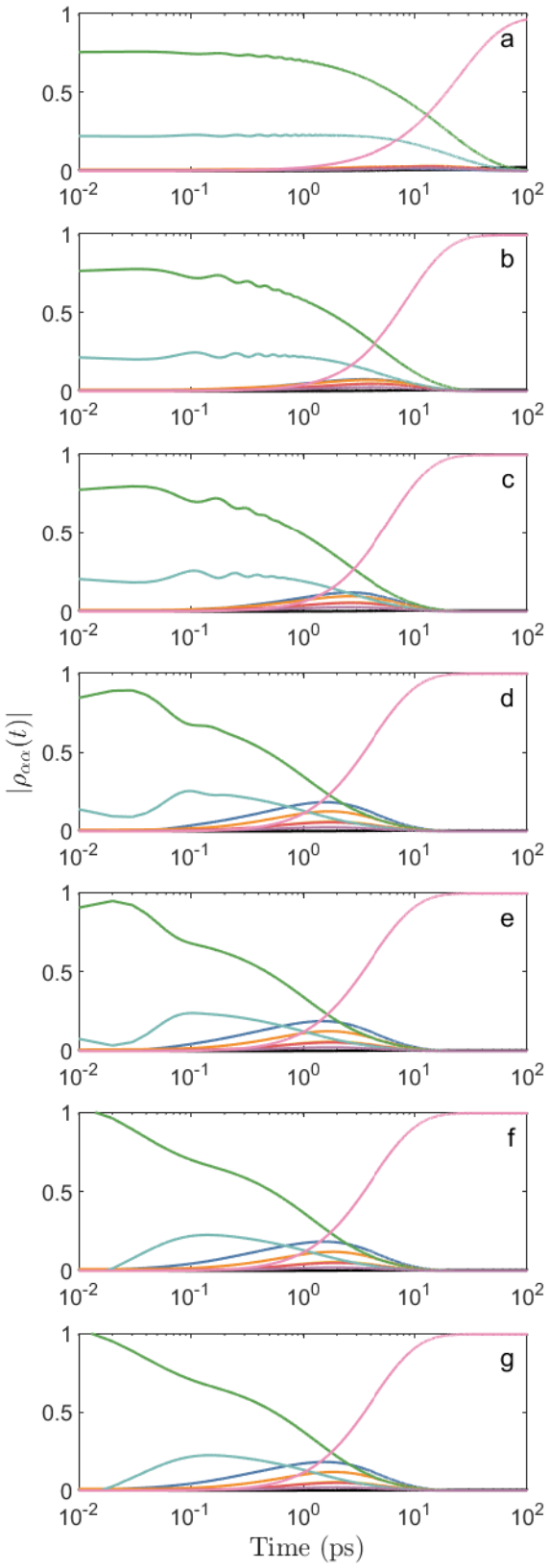

Figure 2. Dynamics of the exciton populations at the variation of the reorganization energy. Full Redfield equation.

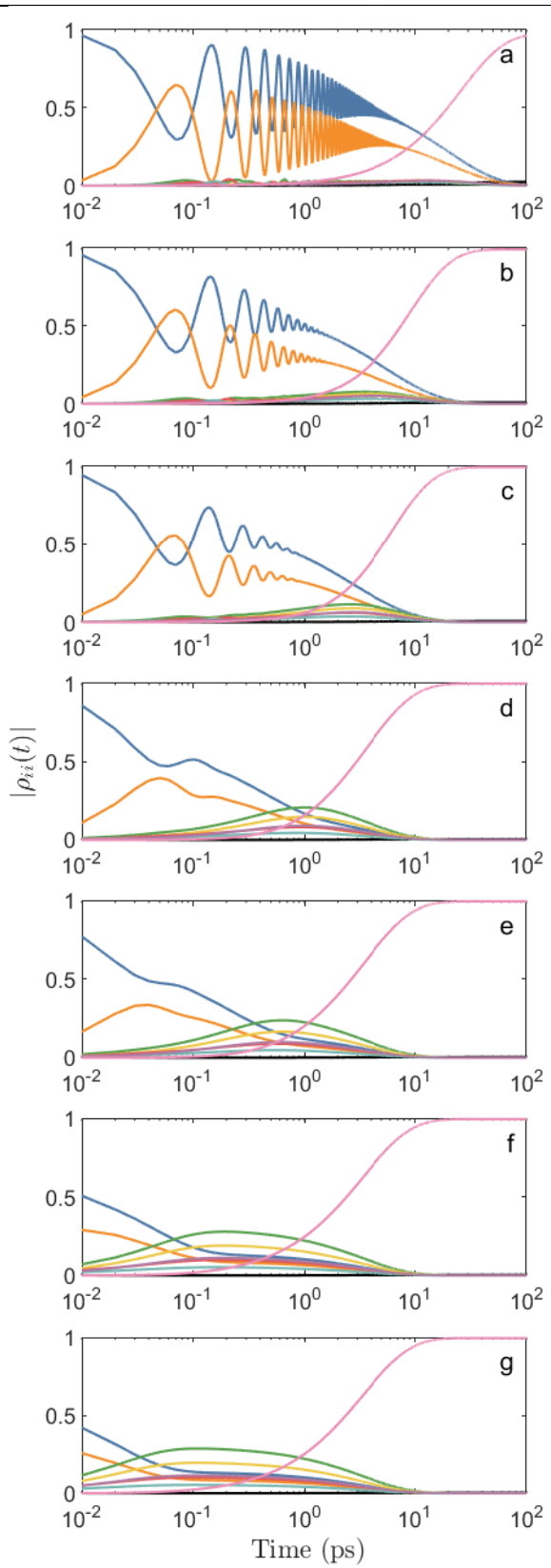

Figure 3. Dynamics of the site populations at the variation of the reorganization energy. Secular Redfield equation.

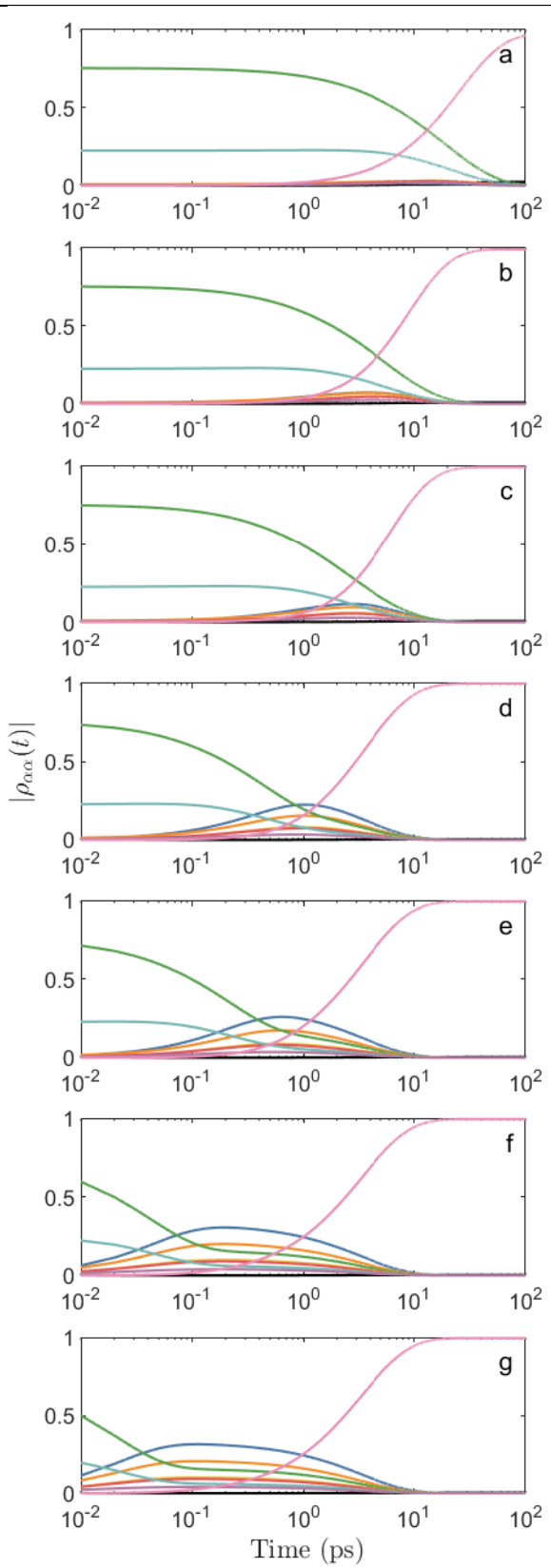

Figure 4. Dynamics of the exciton populations at the variation of the reorganization energy. Secular Redfield equation.

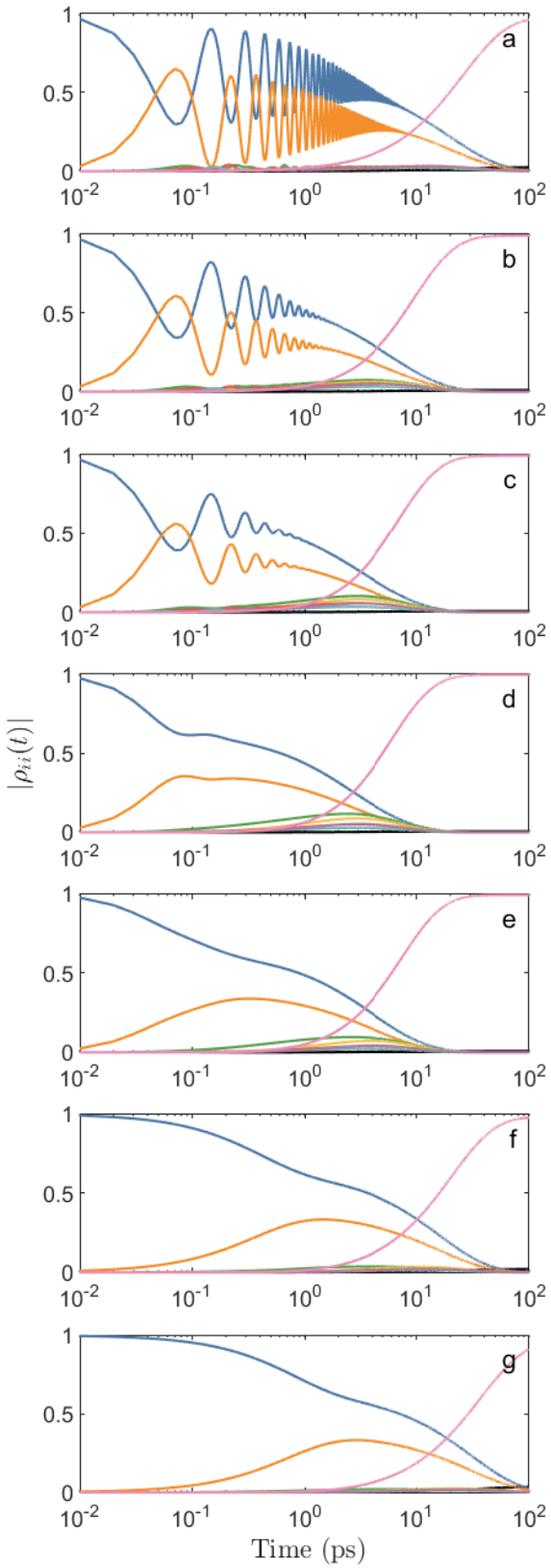

Figure 5. Dynamics of the site populations at the variation of the reorganization energy. Redfield equation without imaginary part.

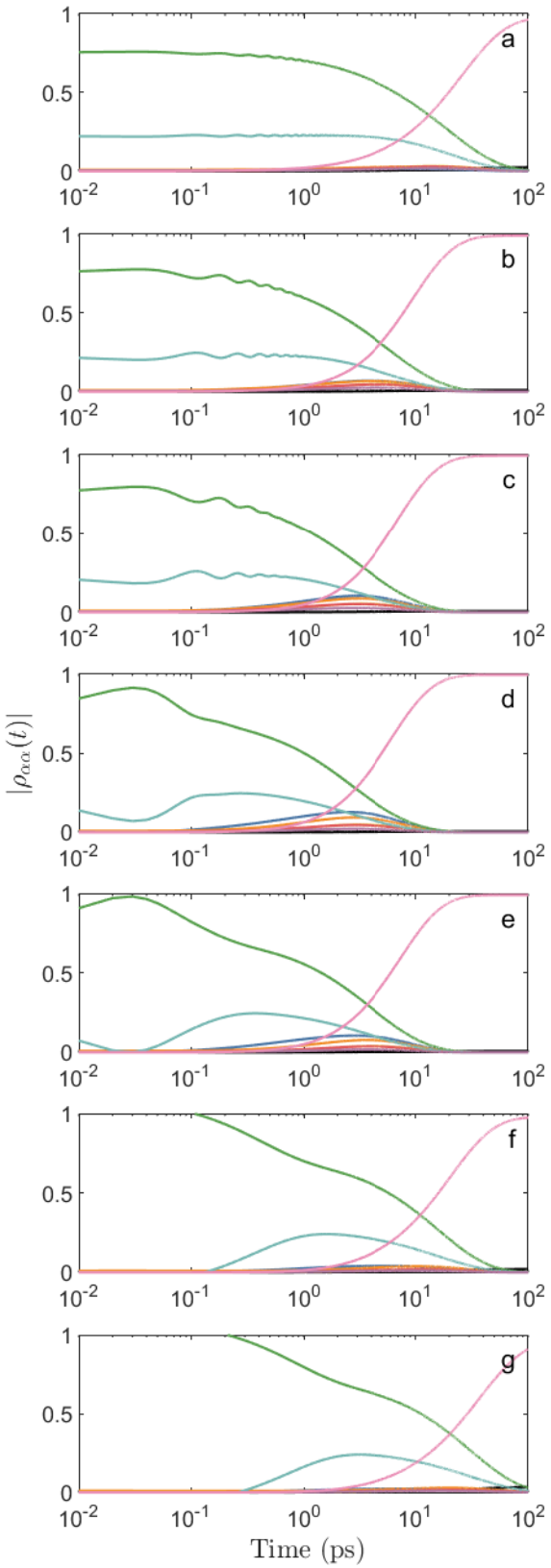

Figure 6. Dynamics of the exciton populations at the variation of the reorganization energy. Redfield equation without imaginary part.

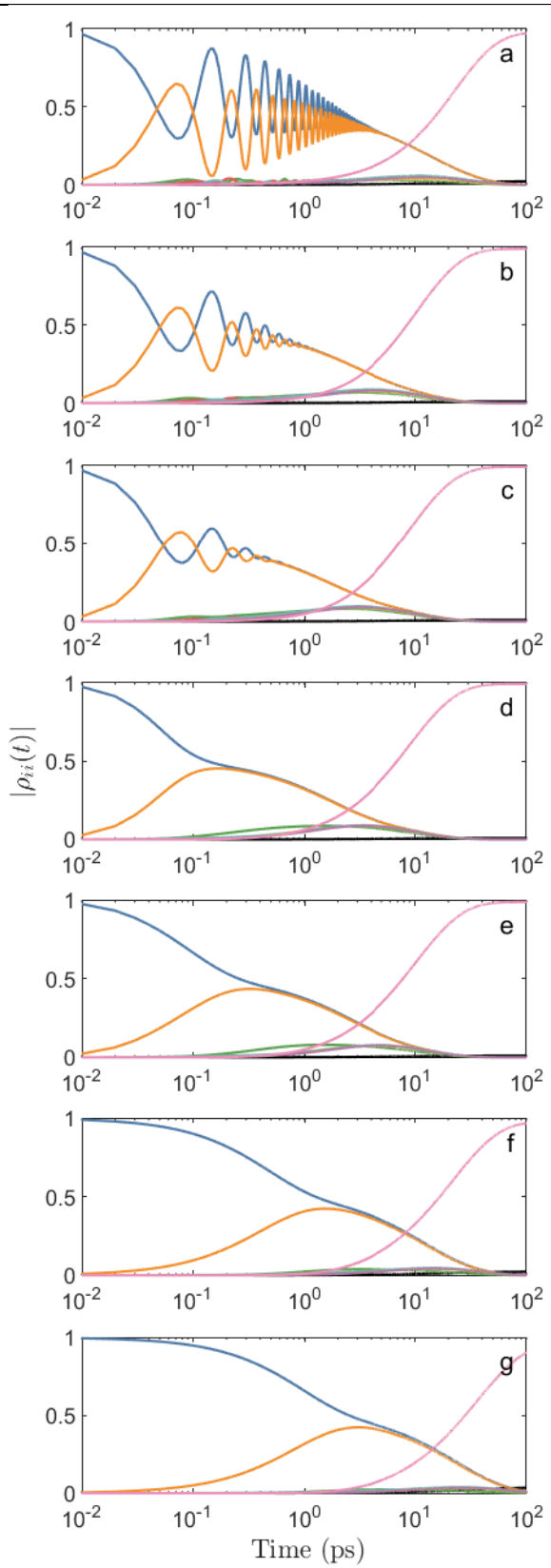

Figure 7. Dynamics of the site populations at the variation of the reorganization energy. Haken-Strobl equation.

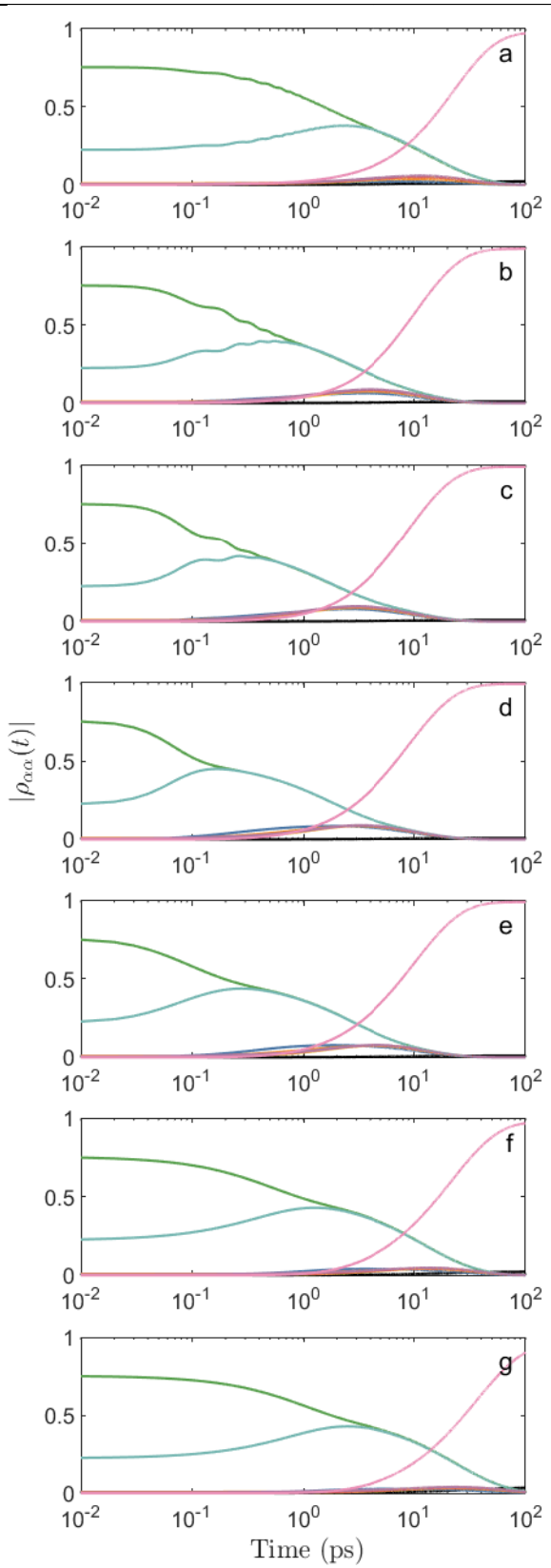

Figure 8. Dynamics of the exciton populations at the variation of the reorganization energy. Haken-Strobl equation.

S.2 Dynamics of the populations at the variation of the cutoff frequency

The dynamics of the populations of the FMO, in the site and exciton basis, are shown at the variation of the cutoff frequency. The results of the Redfield equation are reported in Figures 9-10, the secular Redfield equation is shown in Figures 11-12, the Redfield equation without the imaginary part is in Figures 13-14 and the Haken-Strobl is reported in Figures 15-16.

The fixed parameters are: initial state localized at site 1, $\lambda = 35\ \mathrm{cm}^{-1}$, $T = 347\ \mathrm{K}$ and $\Delta t = 10\ \mathrm{fs}$.

The values of the cutoff frequency are: $\Omega = 5300\ \mathrm{cm}^{-1}$ (a), $\Omega = 1500\ \mathrm{cm}^{-1}$ (b), $\Omega = 530\ \mathrm{cm}^{-1}$ (c), $\Omega = 150\ \mathrm{cm}^{-1}$ (d) and $\Omega = 80\ \mathrm{cm}^{-1}$ (e).

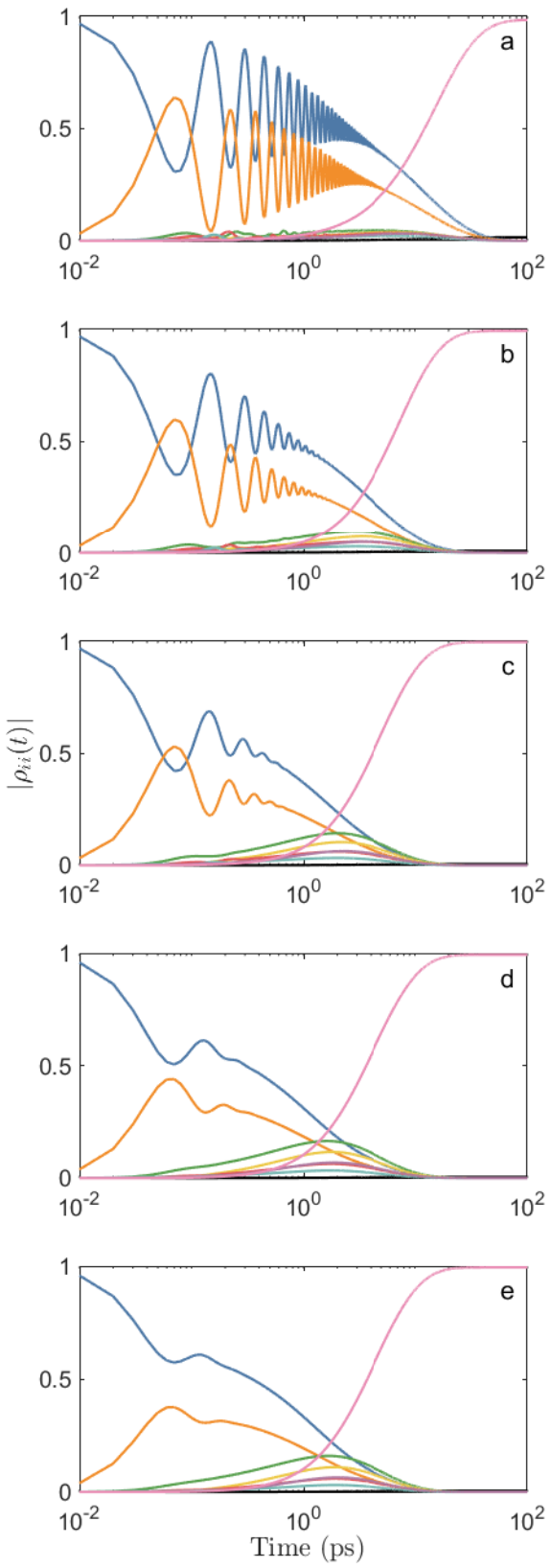

Figure 9. Dynamics of the site populations at the variation of the cutoff frequency. Full Redfield equation.

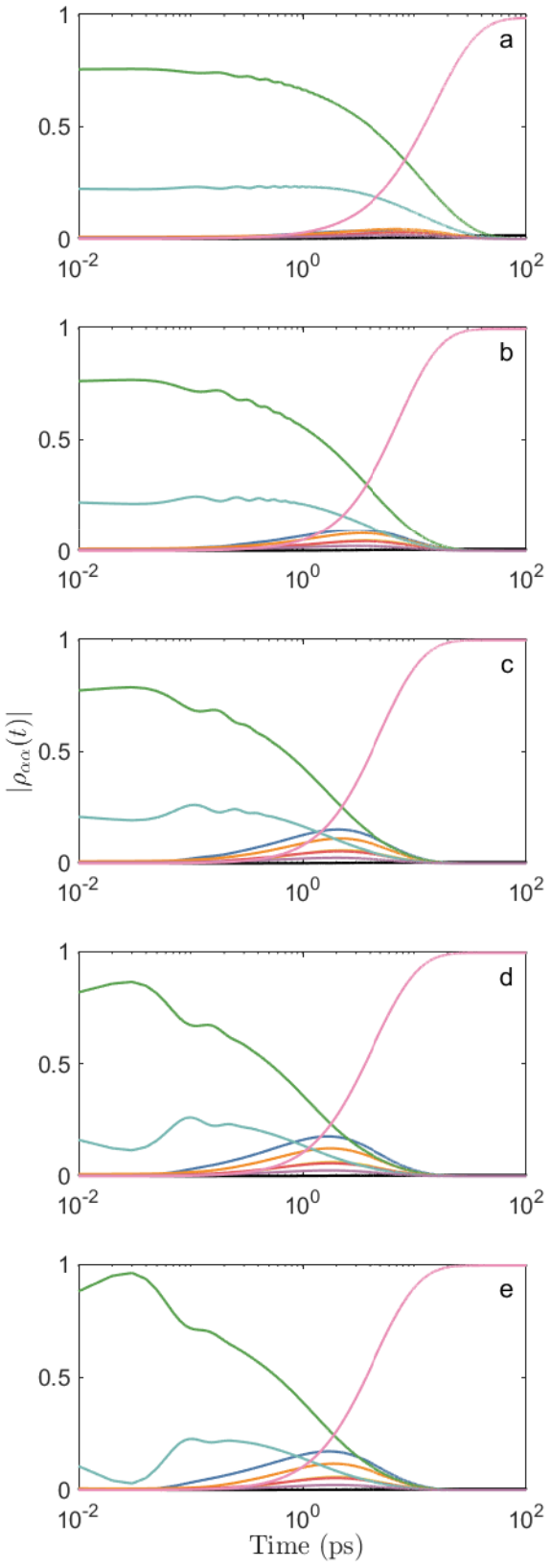

Figure 10. Dynamics of the exciton populations at the variation of the cutoff frequency. Full Redfield equation.

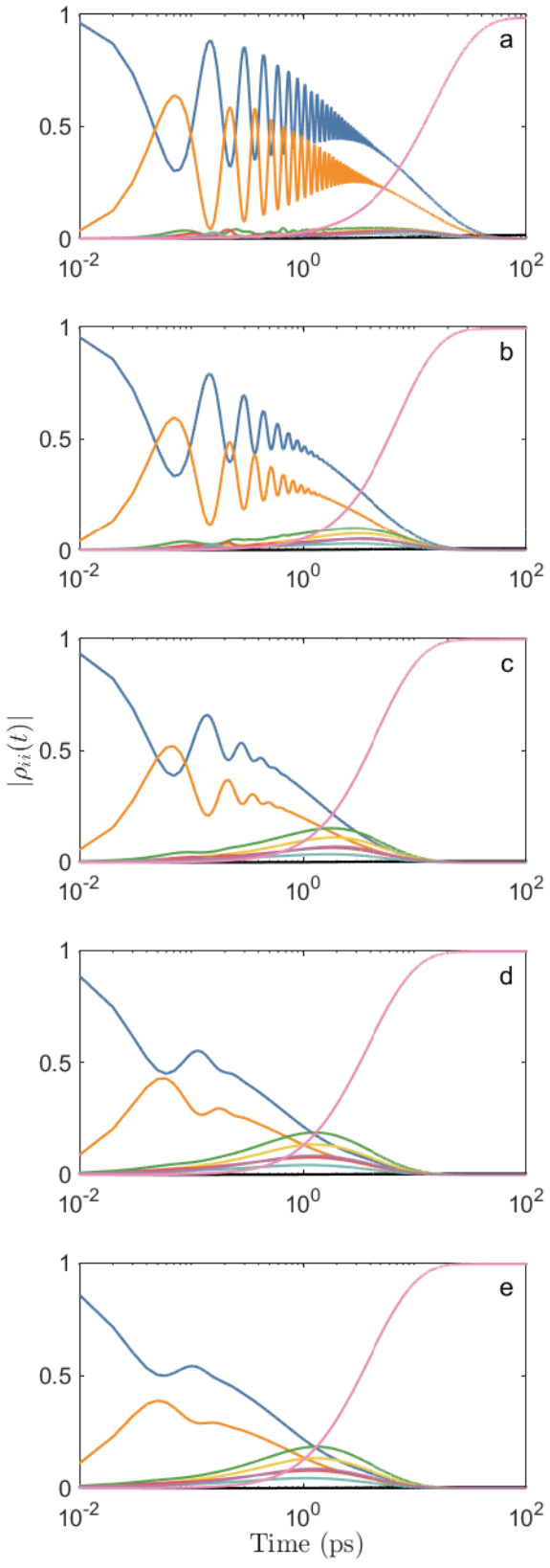

Figure 11. Dynamics of the site populations at the variation of the cutoff frequency. Secular Redfield equation.

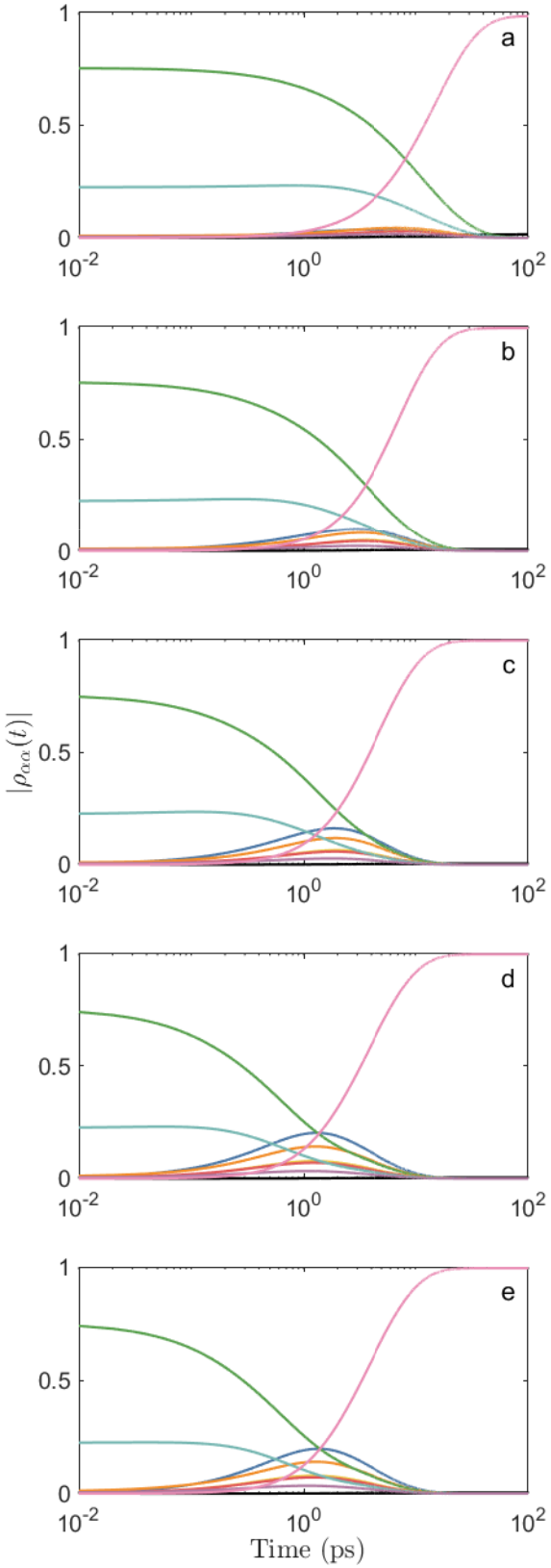

Figure 12. Dynamics of the exciton populations at the variation of the cutoff frequency. Secular Redfield equation.

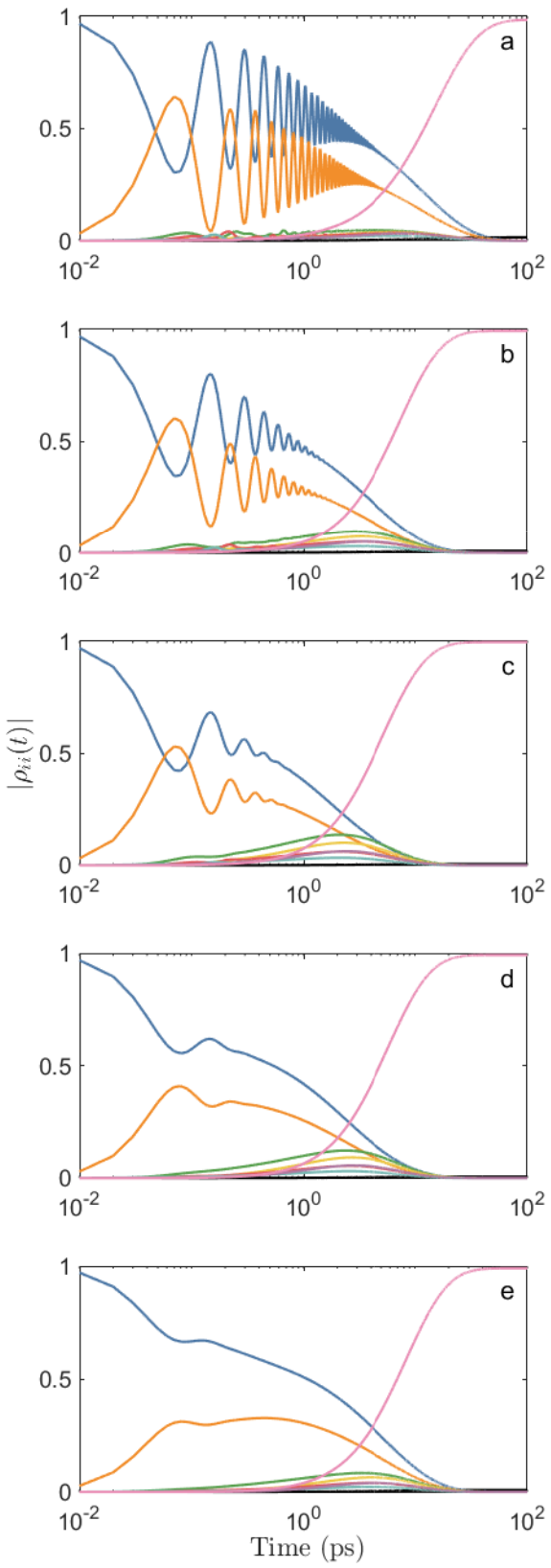

Figure 13. Dynamics of the site populations at the variation of the cutoff frequency. Redfield equation without imaginary part.

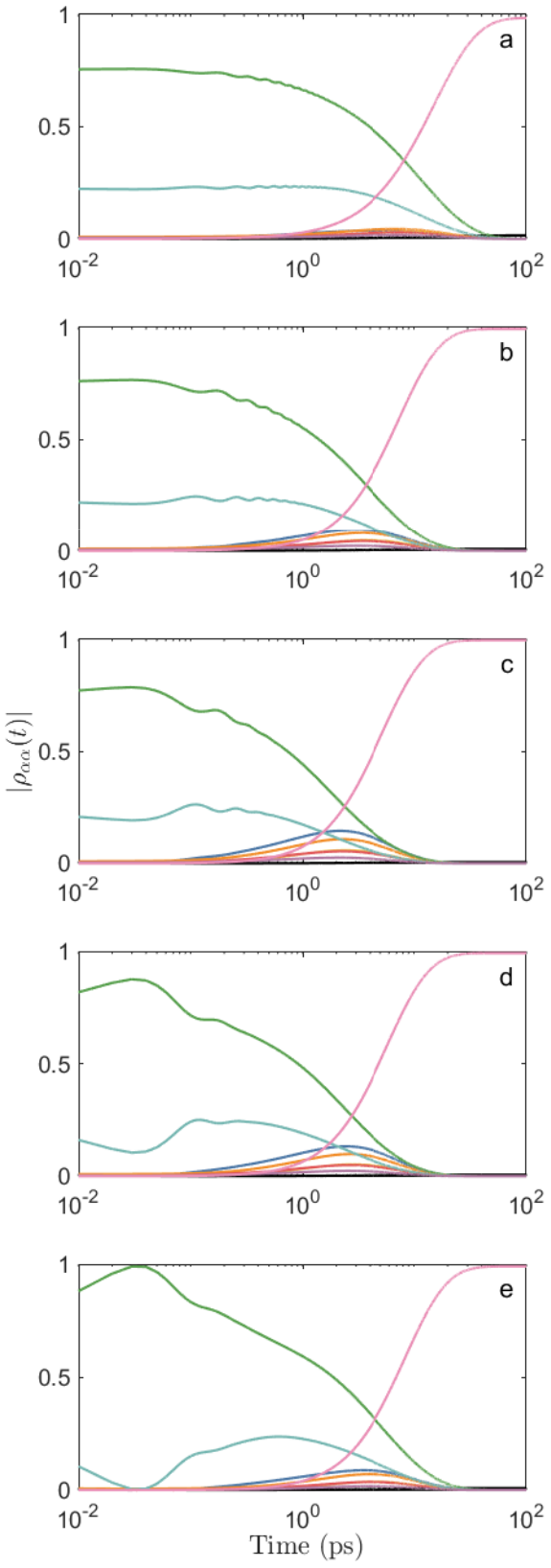

Figure 14. Dynamics of the exciton populations at the variation of the cutoff frequency. Redfield equation without imaginary part.

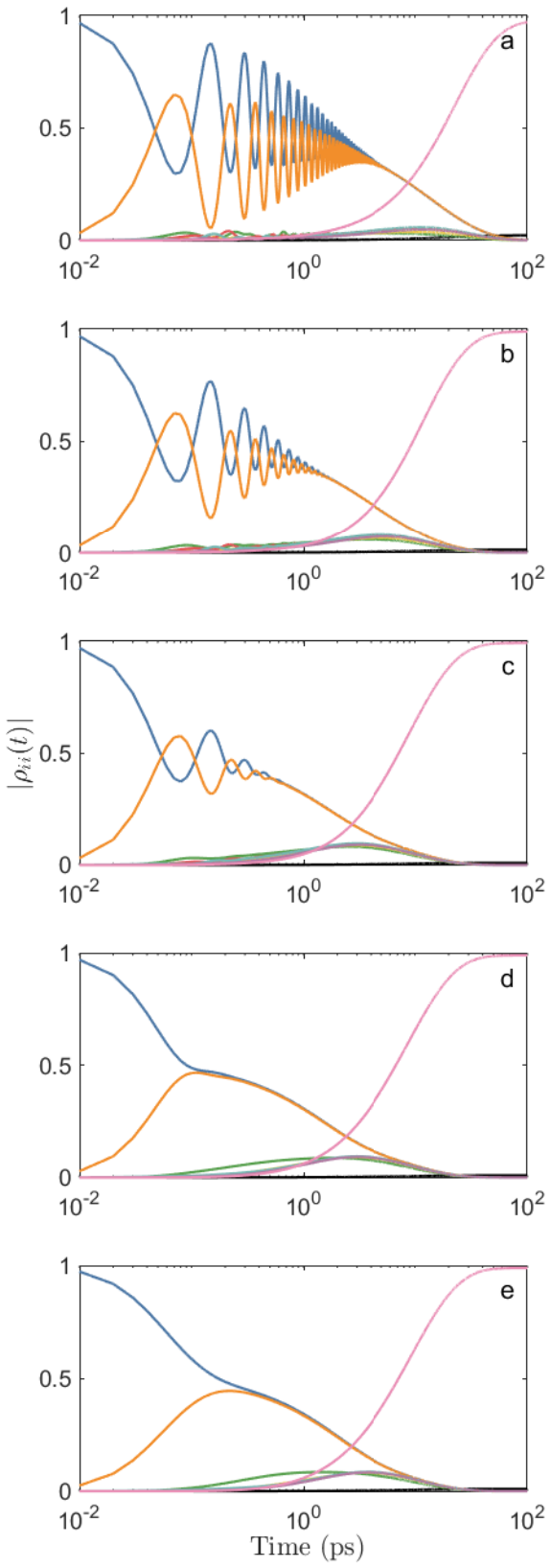

Figure 15. Dynamics of the site populations at the variation of the cutoff frequency. Haken-Strobl equation.

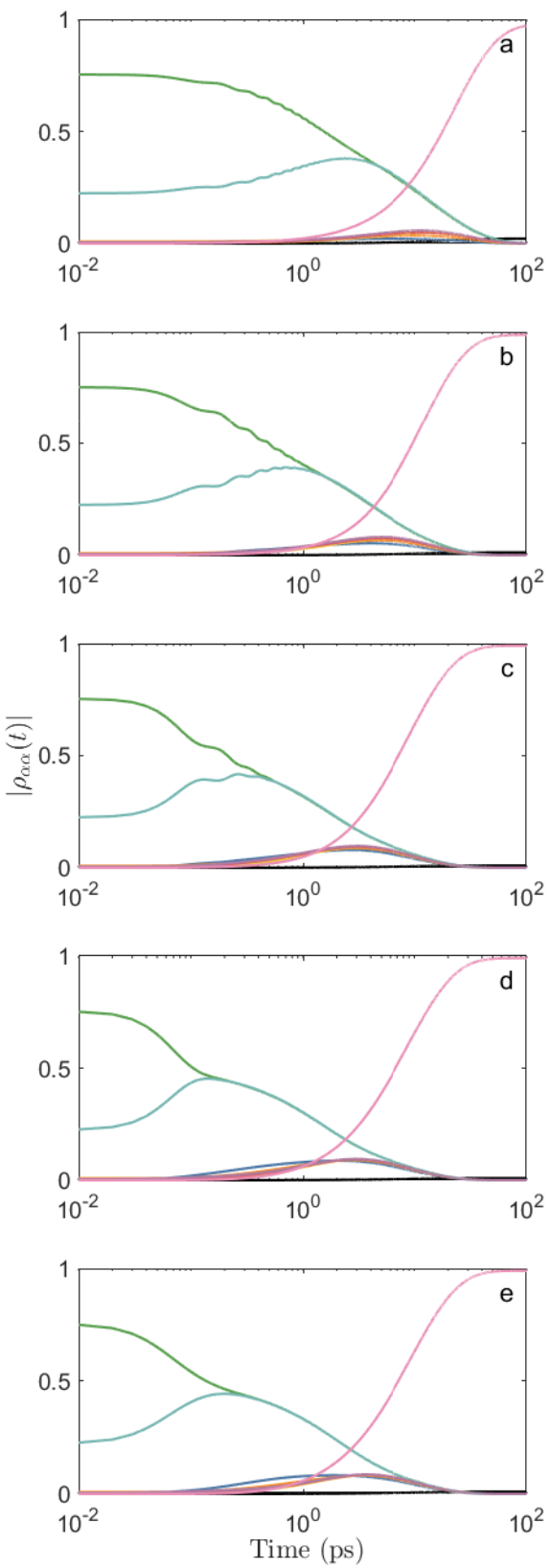

Figure 16. Dynamics of the exciton populations at the variation of the cutoff frequency. Haken-Strobl equation.

S.3 Dynamics of the populations at the variation of the temperature

The dynamics of the populations of the FMO, in the site and exciton basis, are shown at the variation of the temperature. The results of the Redfield equation are reported in Figures 17-18, the secular Redfield equation is shown in Figures 19-20, the Redfield equation without the imaginary part is in Figures 21-22 and the Haken-Strobl is reported in Figures 23-24.

The fixed parameters are: initial state localized at site 1, $\lambda = 35\ \mathrm{cm}^{-1}$, $\Omega = 150\ \mathrm{cm}^{-1}$ and $\Delta t = 10\ \mathrm{fs}$.

The values of the temperature are: $T = 77\ \mathrm{K}$ (a), $T = 131\ \mathrm{K}$ (b), $T = 239\ \mathrm{K}$ (c) and $T = 347\ \mathrm{K}$ (d).

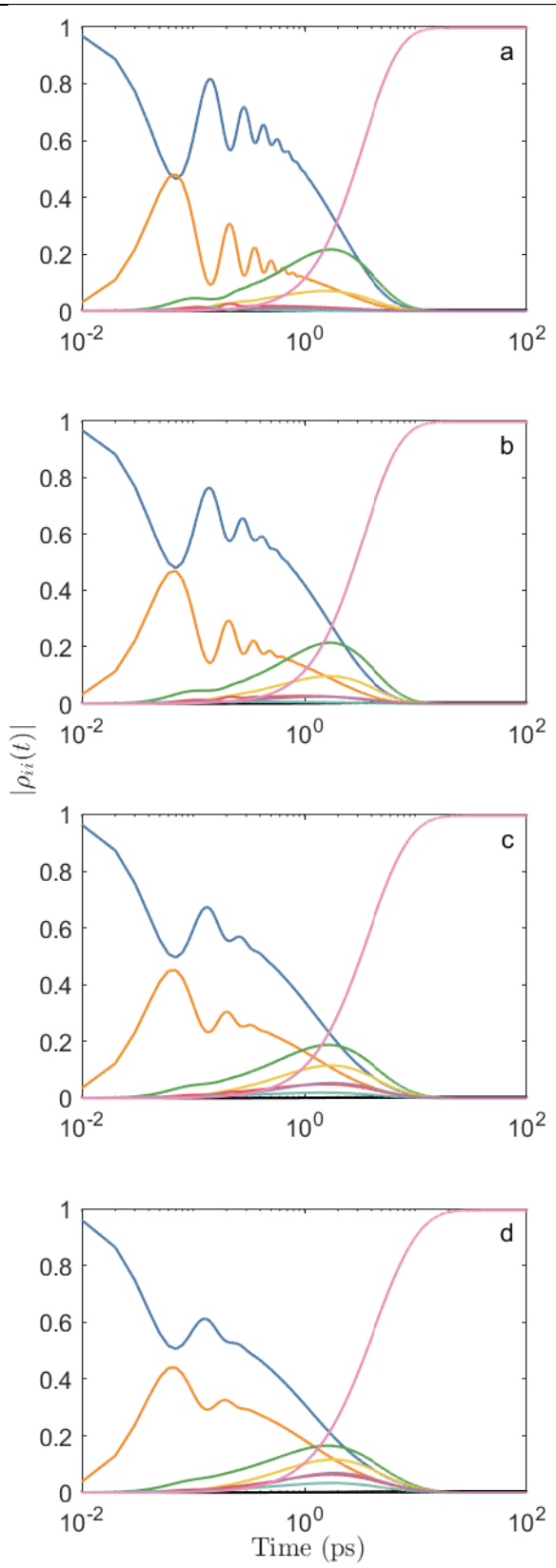

Figure 17. Dynamics of the site populations at the variation of the temperature. Full Redfield equation.

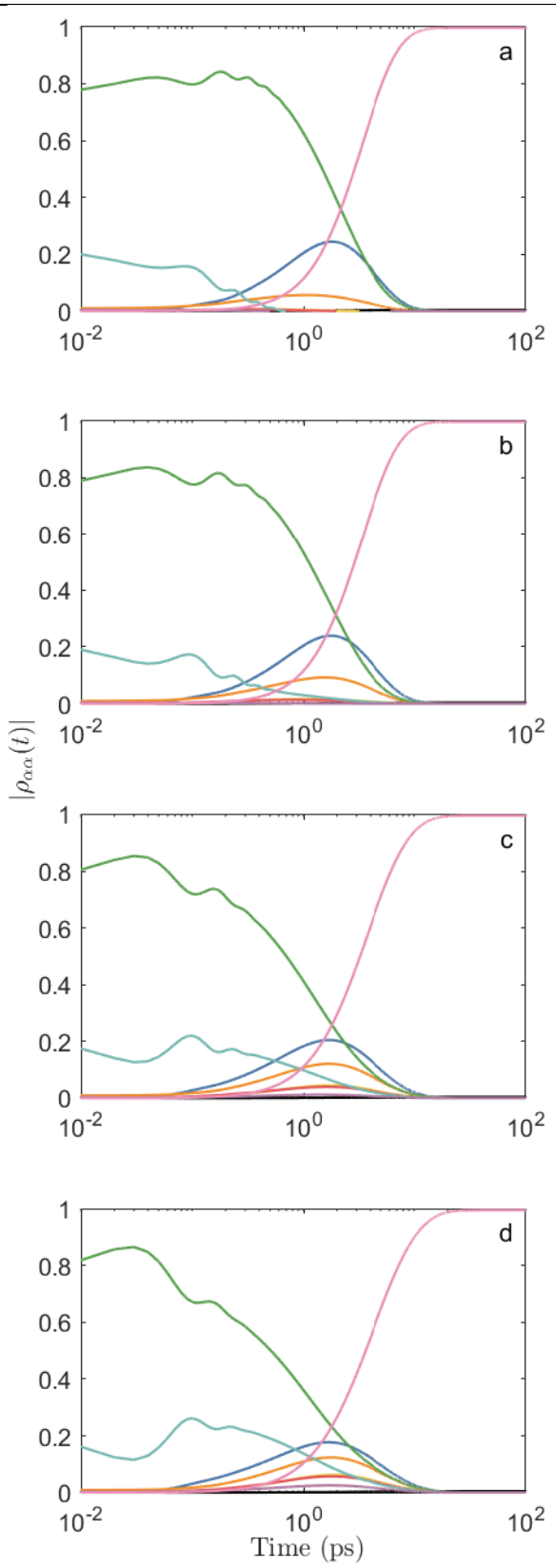

Figure 18. Dynamics of the exciton populations at the variation of the temperature. Full Redfield equation.

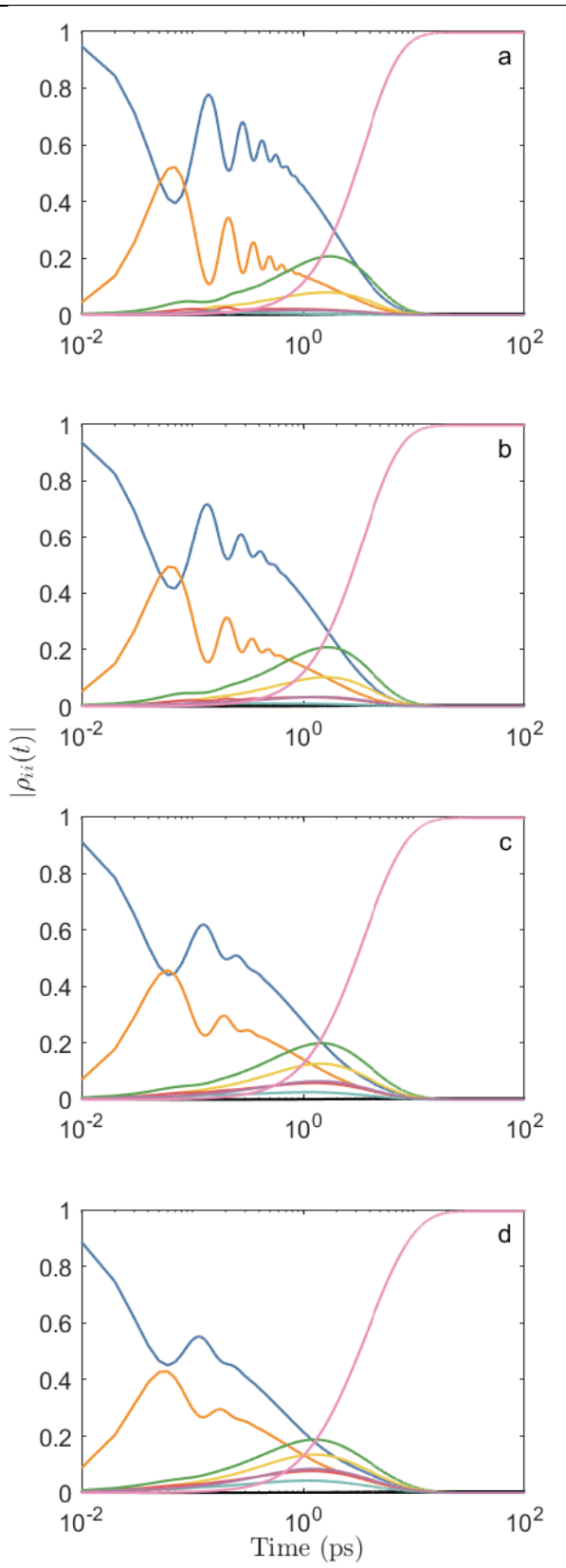

Figure 19. Dynamics of the site populations at the variation of the temperature. Secular Redfield equation.

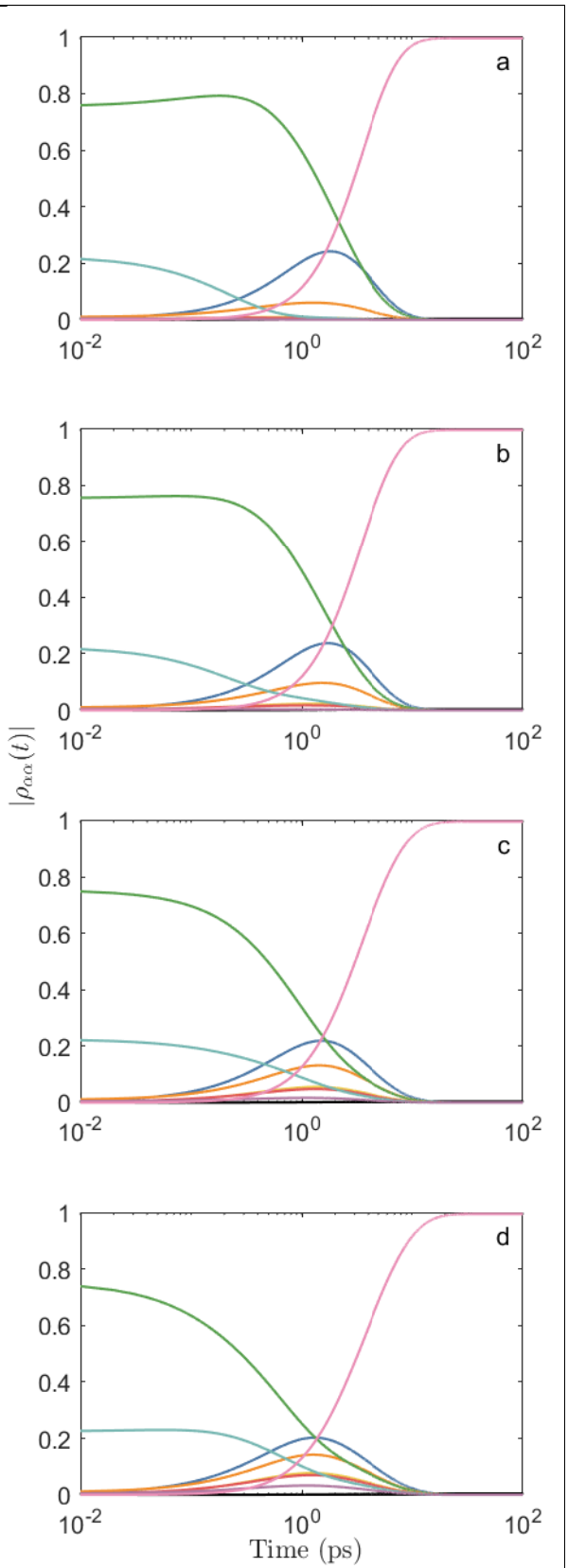

Figure 20. Dynamics of the exciton populations at the variation of the temperature. Secular Redfield equation.

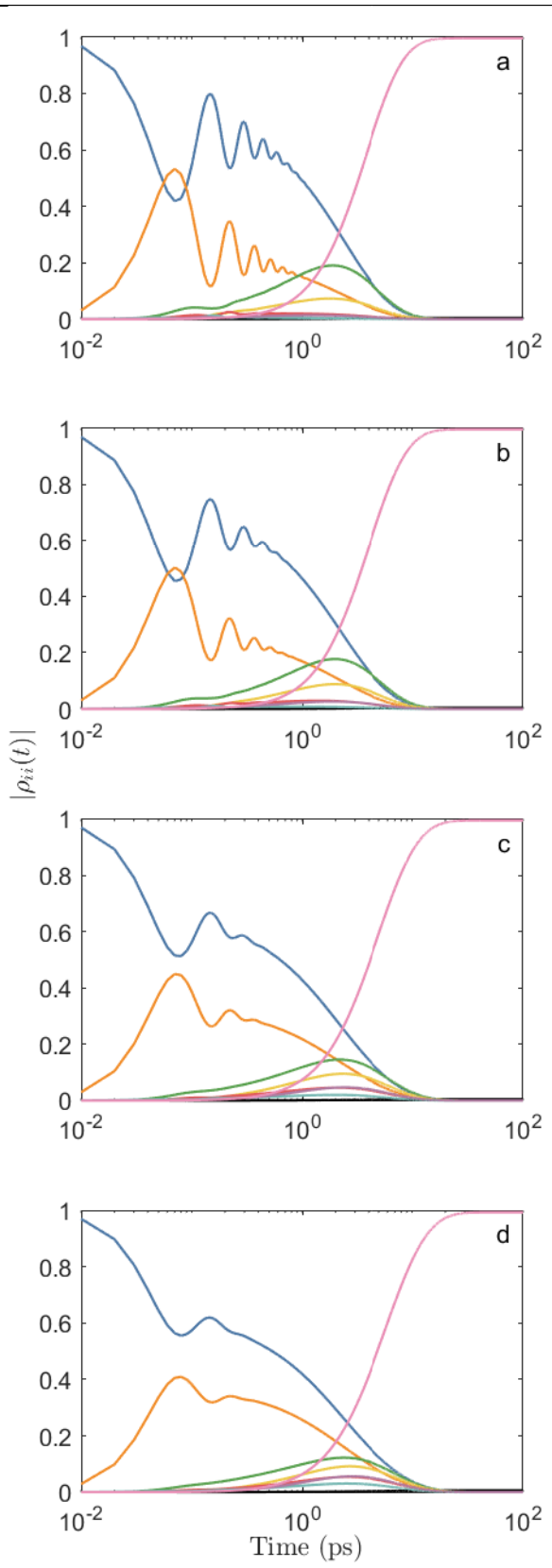

Figure 21. Dynamics of the site populations at the variation of the temperature. Redfield equation without the imaginary part.

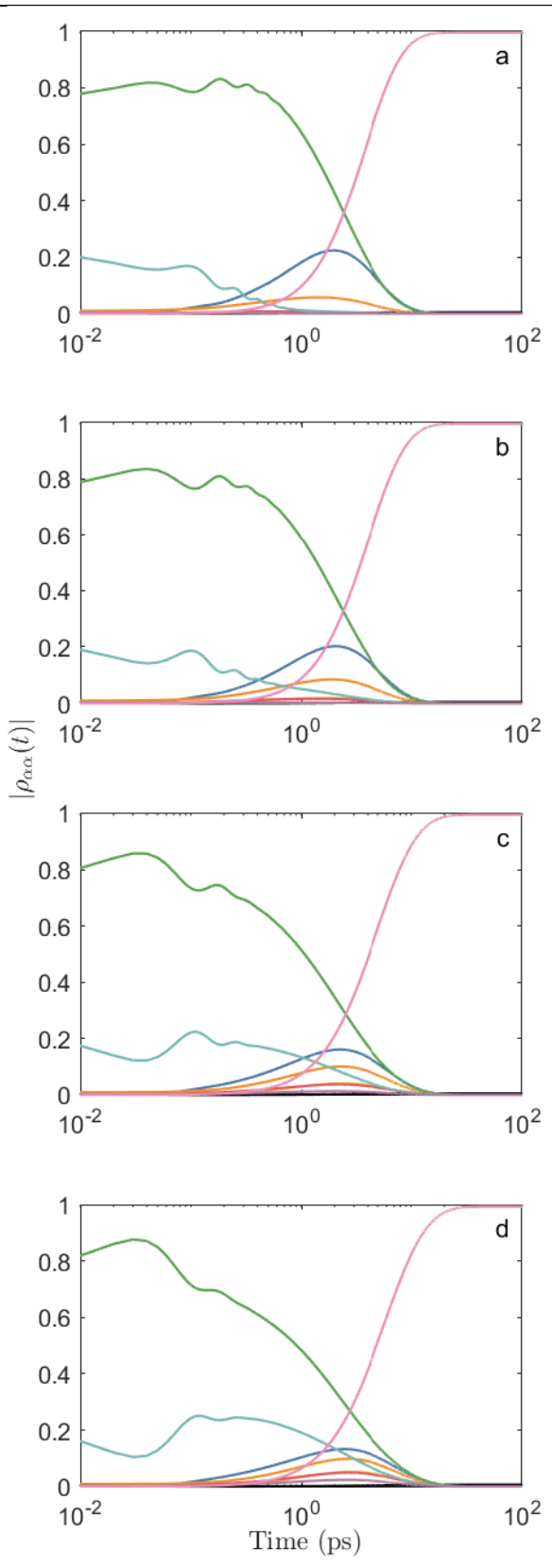

Figure 22. Dynamics of the exciton populations at the variation of the temperature. Redfield equation without the imaginary part.

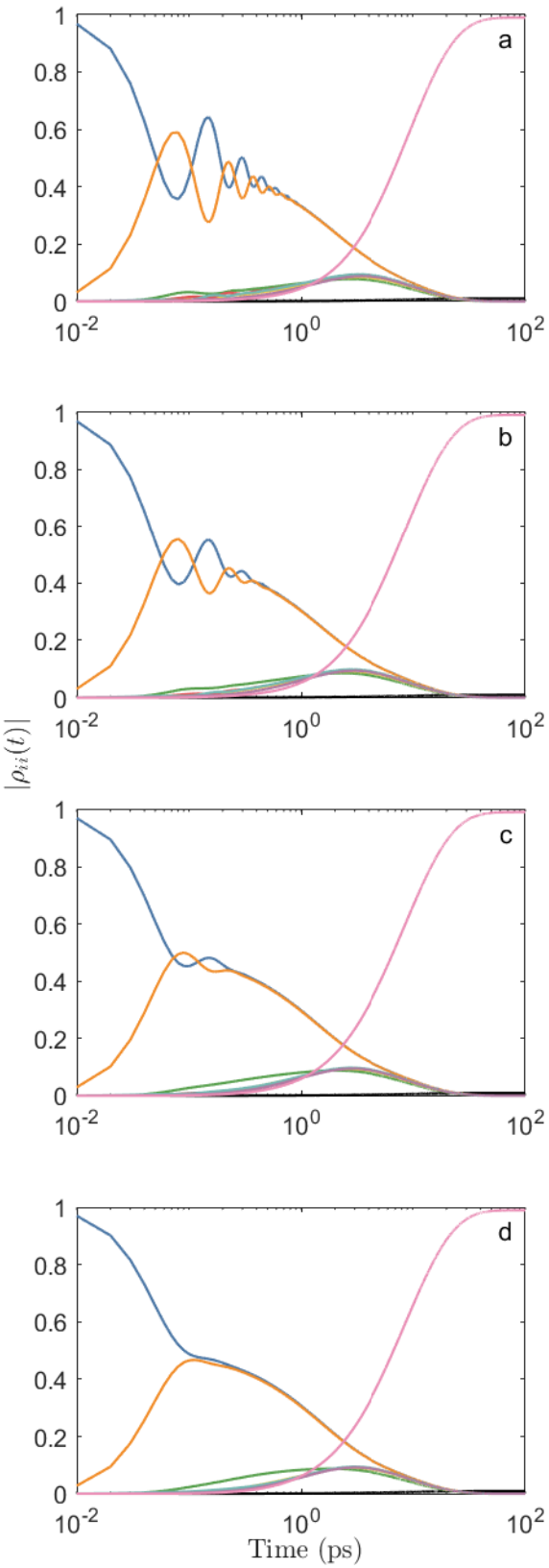

Figure 23. Dynamics of the site populations at the variation of the temperature. Haken-Strobl equation.

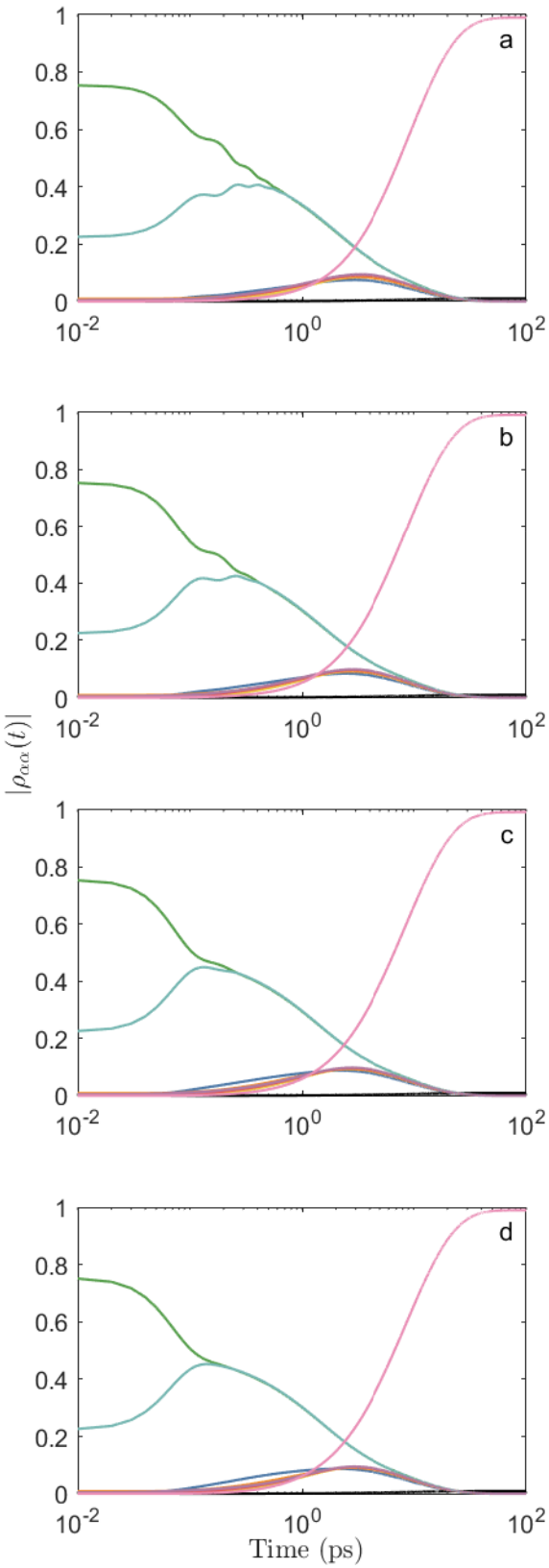

Figure 24. Dynamics of the exciton populations at the variation of the temperature. Haken-Strobl equation.

S.4 Dynamics of the coherences at the variation of the reorganization energy

The dynamics of the absolute values of the coherences of the FMO, in the site and exciton basis, are shown at the variation of the reorganization energy. The results of the Redfield equation are reported in Figures 25-26, the secular Redfield equation is shown in Figures 27-28, the Redfield equation without the imaginary part is in Figures 29-30 and the Haken-Strobl is reported in Figures 31-32.

The fixed parameters are: initial state localized at site 1, $\Omega = 150\ \mathrm{cm}^{-1}$, $T = 347\ \mathrm{K}$ and $\Delta t = 10\ \mathrm{fs}$.

The values of the reorganization energy are: $\lambda = 1\ \mathrm{cm}^{-1}$ (a), $\lambda = 5\ \mathrm{cm}^{-1}$ (b), $\lambda = 10\ \mathrm{cm}^{-1}$ (c), $\lambda = 50\ \mathrm{cm}^{-1}$ (d), $\lambda = 100\ \mathrm{cm}^{-1}$ (e), $\lambda = 500\ \mathrm{cm}^{-1}$ (f) and $\lambda = 1000\ \mathrm{cm}^{-1}$ (g).

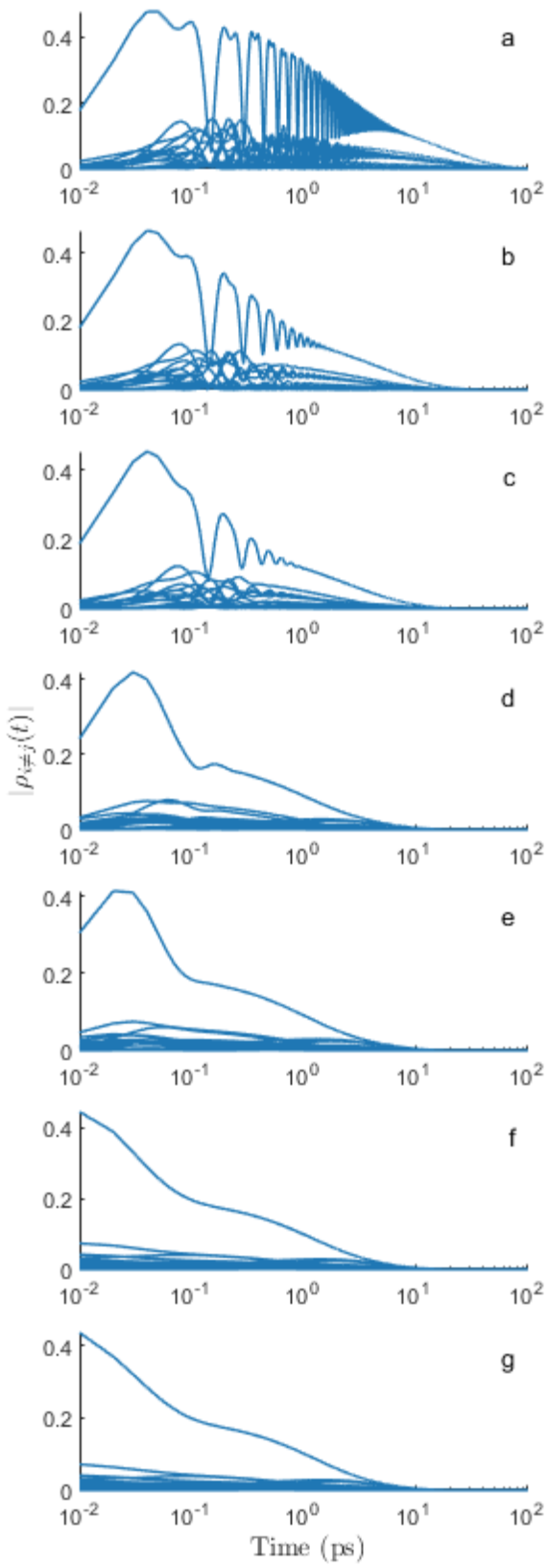

Figure 25. Dynamics of the site coherences at the variation of the reorganization energy. Full Redfield equation.

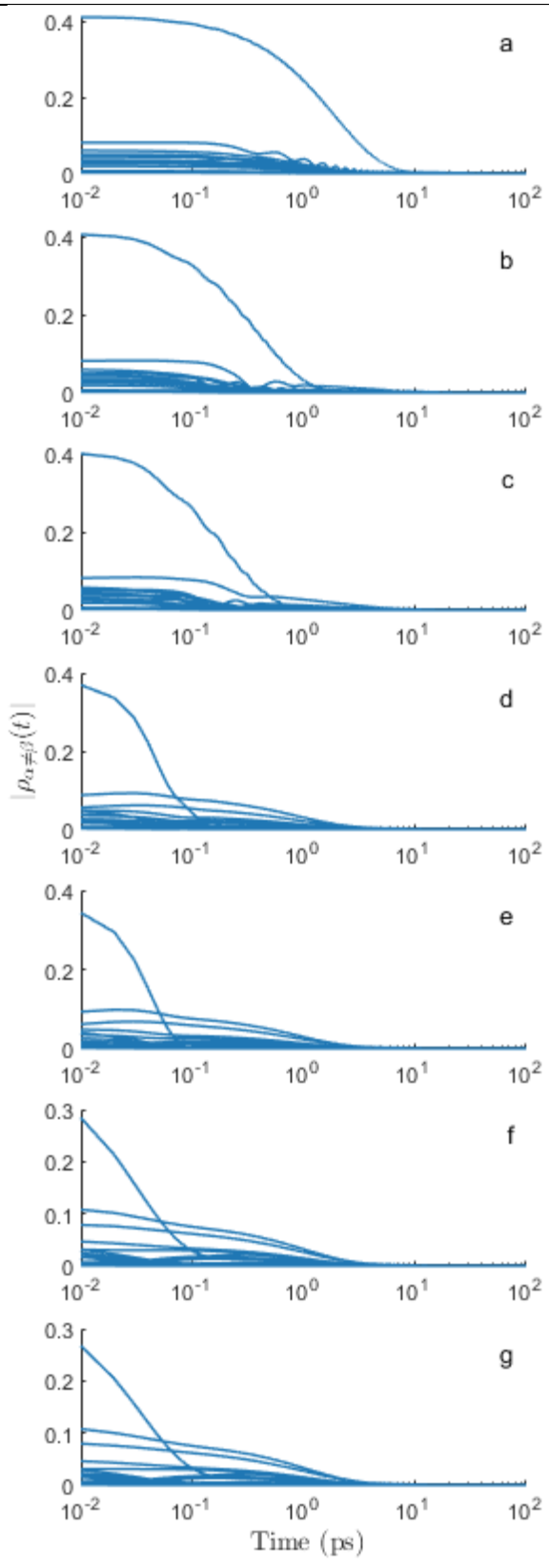

Figure 26. Dynamics of the exciton coherences at the variation of the reorganization energy. Full Redfield equation.

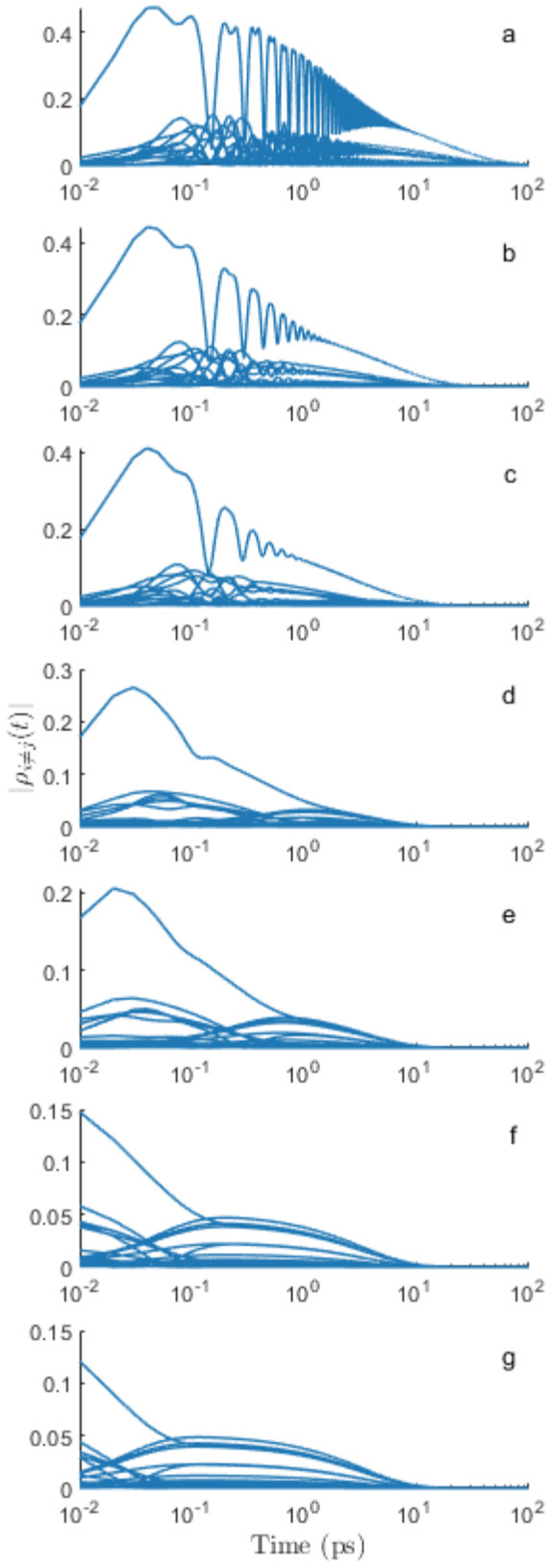

Figure 27. Dynamics of the site coherences at the variation of the reorganization energy. Secular Redfield equation.

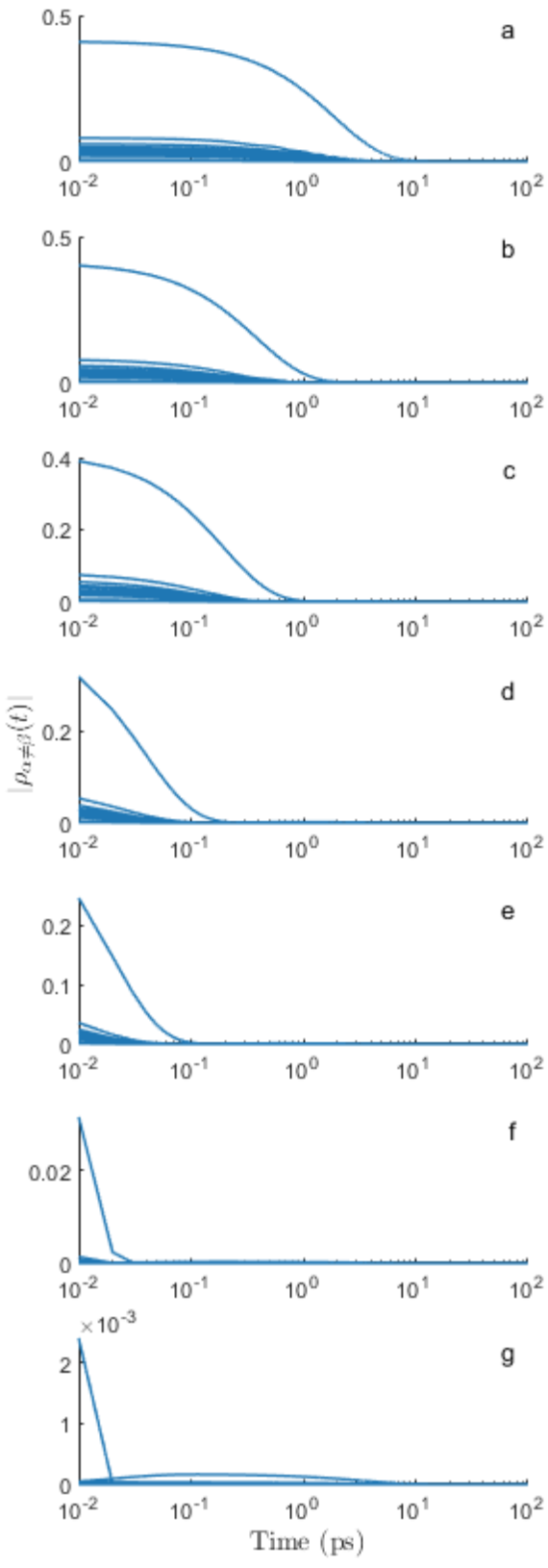

Figure 28. Dynamics of the exciton coherences at the variation of the reorganization energy. Secular Redfield equation.

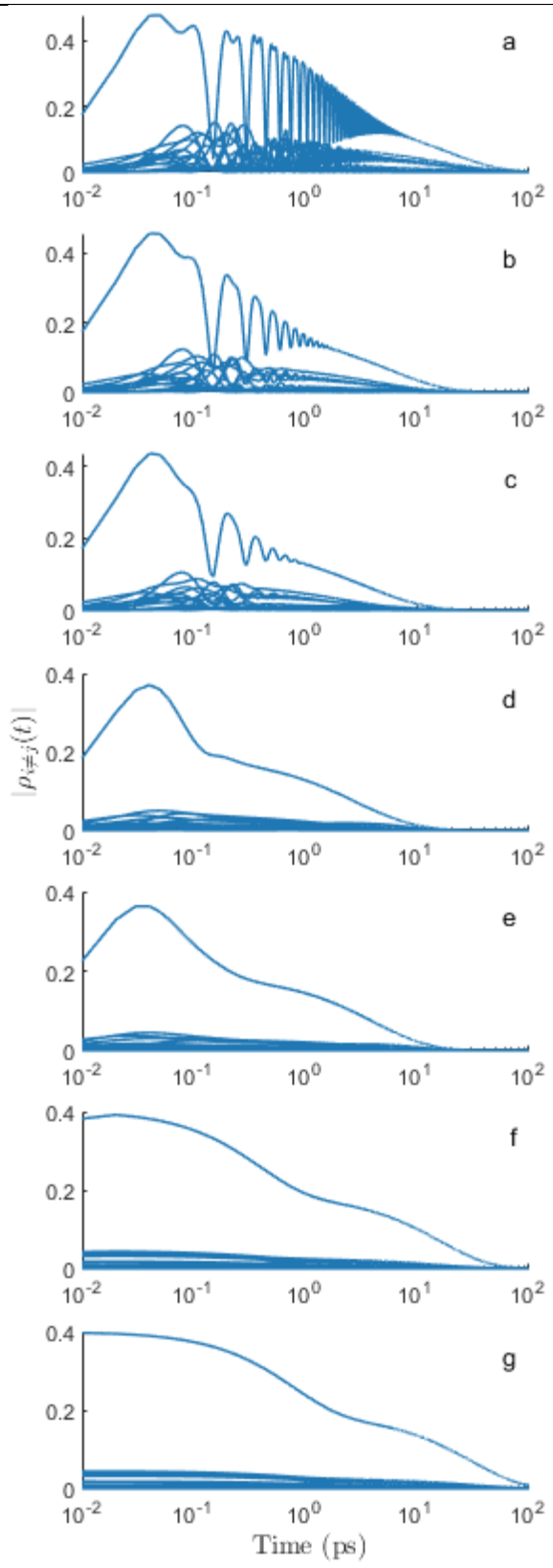

Figure 29. Dynamics of the site coherences at the variation of the reorganization energy. Redfield equation without the imaginary part.

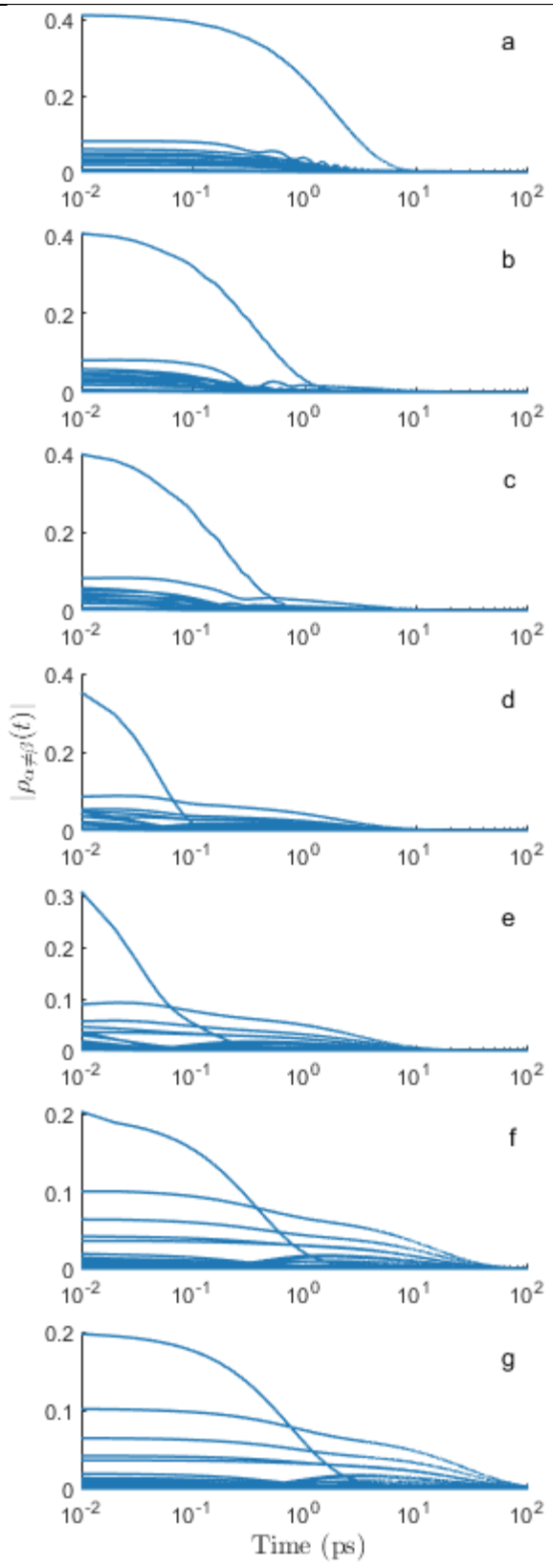

Figure 30. Dynamics of the exciton coherences at the variation of the reorganization energy. Redfield equation without the imaginary part.

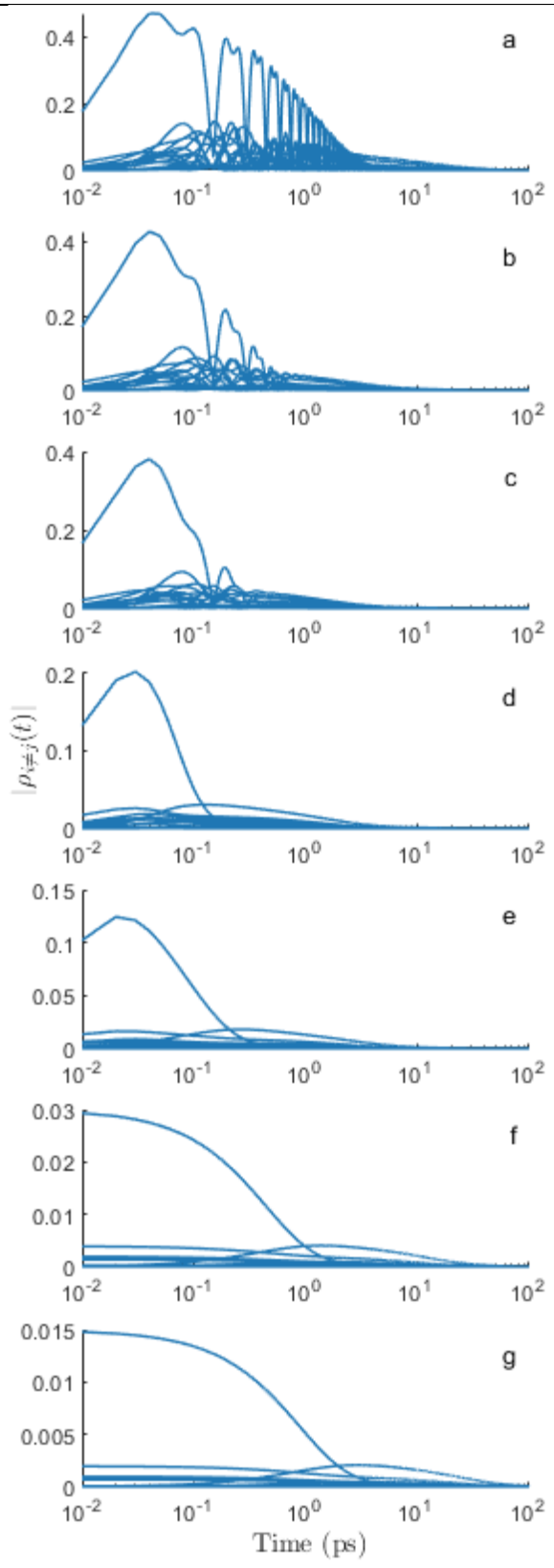

Figure 31. Dynamics of the site coherences at the variation of the reorganization energy. Haken-Strobl equation .

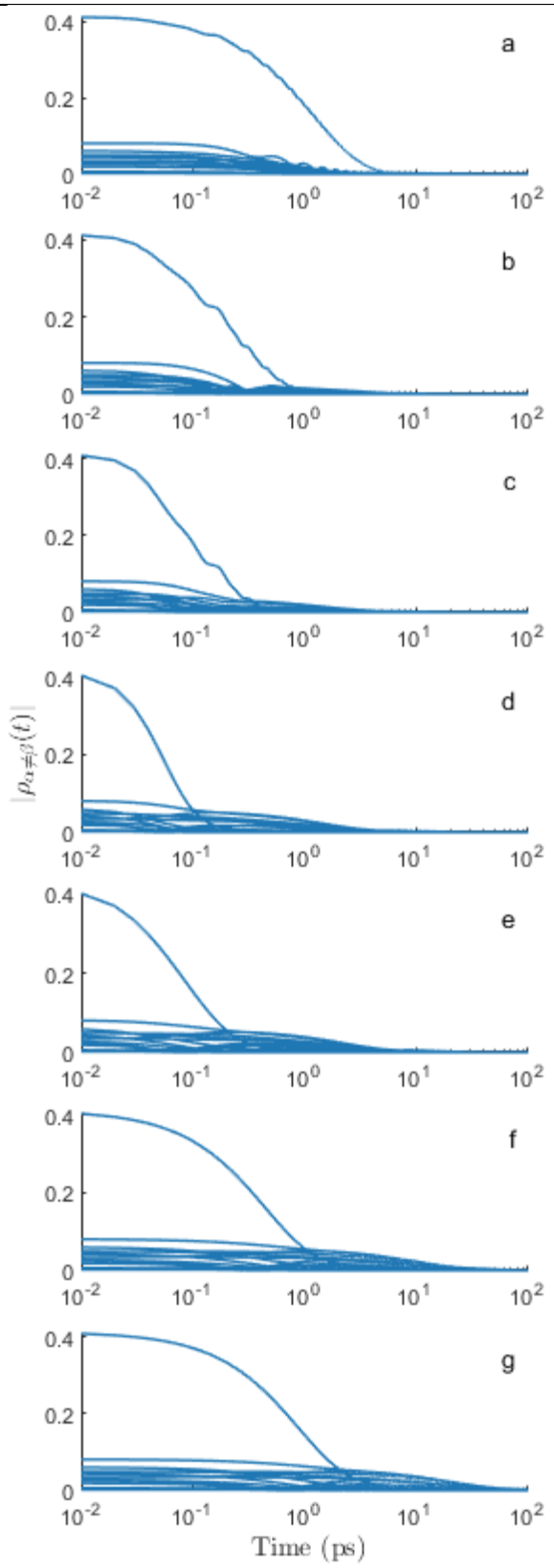

Figure 32. Dynamics of the exciton coherences at the variation of the reorganization energy. Haken-Strobl equation.

S.5 Dynamics of the dynamical IPR and purity

The dynamics of the dynamical IPR on the exciton basis and the dynamics of the purity of the density matrix are shown at the variation of the reorganization energy. The results of the Redfield equation are reported in Figure 33, the secular Redfield equation is shown in Figure 34, the Redfield equation without the imaginary part is in Figure 35 and the Haken-Strobl is reported in Figure 36.

The fixed parameters are: initial state localized at site 1, $\Omega = 150\ \mathrm{cm}^{-1}$, $T = 347\ \mathrm{K}$ and $\Delta t = 10\ \mathrm{fs}$.

The values of the reorganization energy are: $\lambda = 1\ \mathrm{cm}^{-1}$ (a), $\lambda = 5\ \mathrm{cm}^{-1}$ (b), $\lambda = 10\ \mathrm{cm}^{-1}$ (c), $\lambda = 50\ \mathrm{cm}^{-1}$ (d), $\lambda = 100\ \mathrm{cm}^{-1}$ (e), $\lambda = 500\ \mathrm{cm}^{-1}$ (f) and $\lambda = 1000\ \mathrm{cm}^{-1}$ (g).

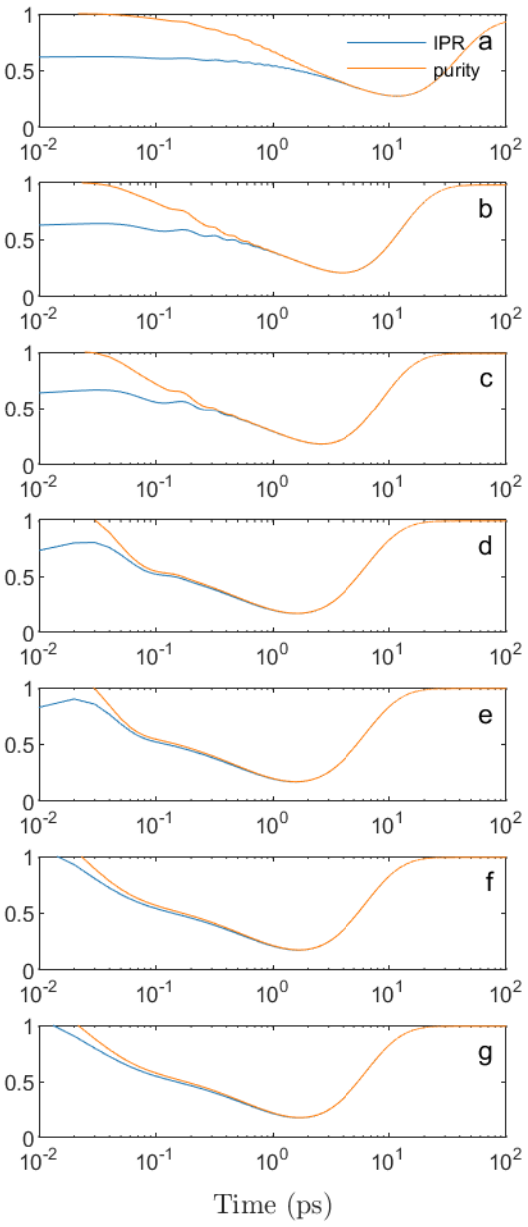

Figure 33. Dynamics of the dynamical IPR and purity at the variation of the reorganization energy. Full Redfield equation.

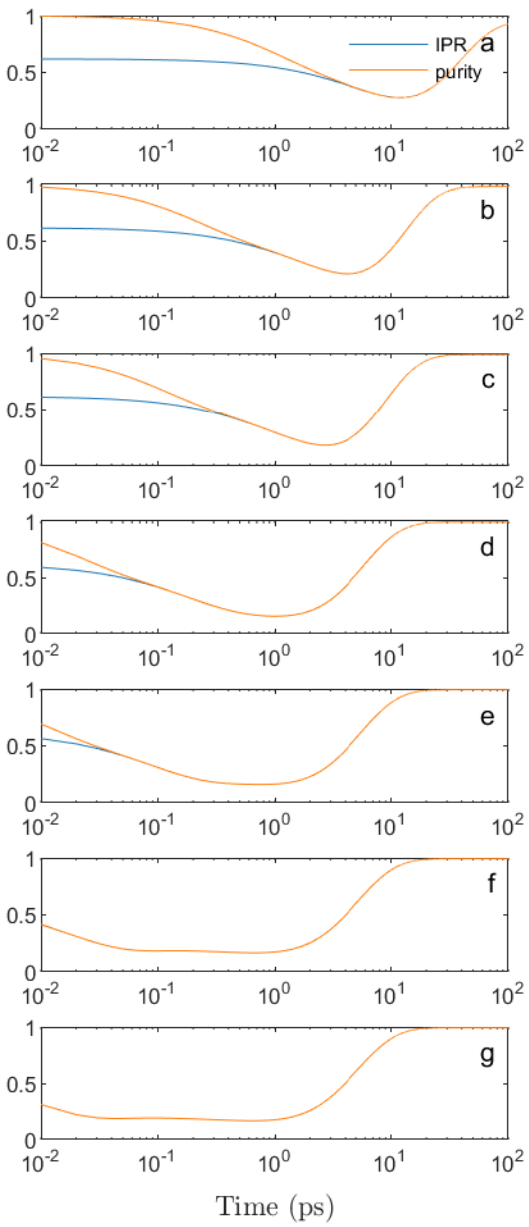

Figure 34. Dynamics of the dynamical IPR and purity at the variation of the reorganization energy. Secular Redfield equation.

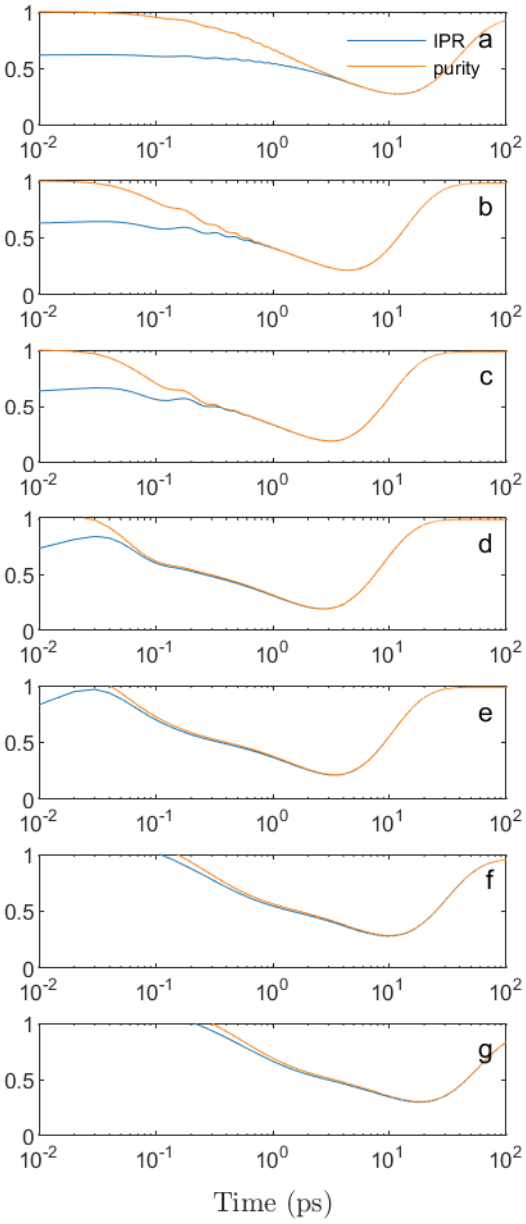

Figure 35. Dynamics of the dynamical IPR and purity at the variation of the reorganization energy. Redfield equation without the imaginary part.

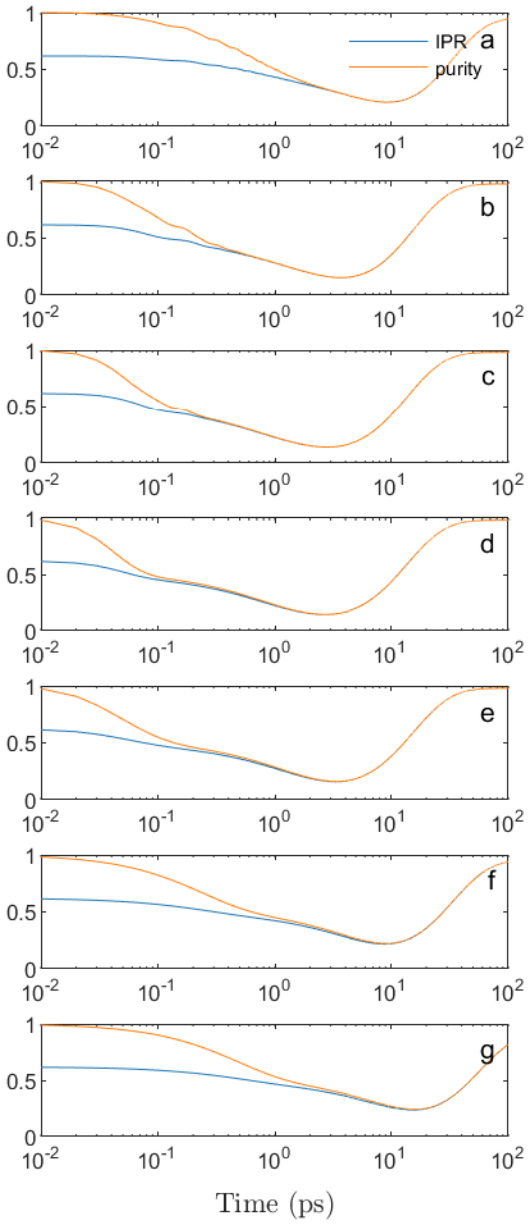

Figure 36. Dynamics of the dynamical IPR and purity at the variation of the reorganization energy. Haken-Strobl equation.